Author(s):

Title: Progress in Paper Physics Seminar : Abstract book of the PPPS2020 seminar September 1-3, 2020 in Jyväskylä, Finland

Year: 2020

Version: Published version

Copyright: © 2020 VTT

Rights: In Copyright

Rights url: http://rightsstatements.org/page/InC/1.0/?language=en

Please cite the original version:

Kouko, J., Lehto, J., & Tuovinen, T. (Eds.). (2020). Progress in Paper Physics Seminar : Abstract
book of the PPPS2020 seminar September 1-3, 2020 in Jyväskylä, Finland. VTT. VTT Technology,
378. https://www.vttresearch.com/sites/default/files/pdf/technology/2020/T378.pdf

Progress in Paper Physics Seminar

Abstract book of the PPPS2020 seminar on September 1-3, 2020 in Jyväskylä, Finland

Jarmo Kouko | Jani Lehto | Tero Tuovinen (eds.)

Progress in Paper Physics Seminar PPPS2020

Book of abstracts

Jarmo Kouko (ed.)

VTT

Jani Lehto (ed.)

VTT

Tero Tuovinen (ed.)

University of Jyväskylä and
JAMK Jyväskylä University of Applied Sciences

Cover image: City of Jyväskylä

In association with

VTT Technical Research Centre Of Finland Ltd

VTT is a visionary research, development and innovation partner. We drive sustainable growth and tackle the greatest global challenges of our time and turn them into growth opportunities. We go beyond the obvious to help society and companies to grow through technological innovations. We have over 75 years of experience of top-level research and science-based results. VTT´s turnover and other operating income is 258 M€. VTT is at the sweet spot where innovation and business come together.

University of Jyväskylä (JYU)

The University of Jyväskylä is the fourth largest university in Finland and offers education and research in various fields. The special expertise areas of the university include Natural Sciences, Human Sciences, Sports and Health Sciences, as well as Teacher education. In the field of Information Technology, the university focuses on the areas of Computational Sciences, Software and Telecommunication Technology, Information Systems, Cognitive Science and Educational Technology, and Cyber Security.

Metsä Fibre

Metsä Fibre is a leading producer of bioproducts, bioenergy and sawn timber. The company's brand in the pulp business is Botnia, and in sawn timber, Nordic Timber. Metsä Fibre is the world's leading producer of bleached softwood pulp and a major producer of sawn timber. Currently employing approximately 1,200 people, the company's sales in 2018 totaled EUR 2.5 billion. Metsä Fibre is part of Metsä Group.
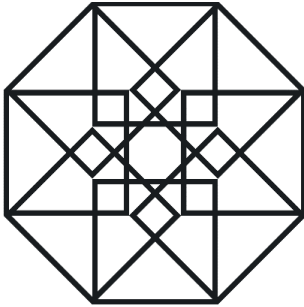
The Federation of Finnish Learned Societies

The Federation of Finnish Learned Societies, established in 1899, is a national co-operative body for learned societies in Finland. It contributes to the co-operation between learned societies, supports and develops scholarly communication and publishing, and promotes awareness and usage of research results. It also supports and develops the role of its members in science policy discussion.

The Federation has a membership of 275 societies and four academies from all branches of arts and sciences, in total 250,000 individual members. Every year these learned societies arrange hundreds of meetings and conferences, attended by the academic community and the general public. The societies and academies are among the foremost academic publishers in Finland: they issue more than 100 periodicals and some 250 new book titles each year. Publications issued by the member societies are sold in the Bookstore Tiedekirja, the shop and webstore maintained by the Federation. The Exchange Centre for Scientific Literature is in charge of the exchange of publications of learned societies and other scientific publishing bodies.

FEDERATION OF FINNISH
LEARNED SOCIETIES

Table of Contents

Session 1 Plenary talk 1
Douglas W. Coffin

Session 2A Compression behavior of fiber networks
Erik Prume, Sebastian Felder, & Jaan-Willem Simon

Marcus Pfeiffer, Robert Götzinger, Benjamin Hiller, Stefan Kolling, & Samuel Schabel

Pedro Godinho, Thomas Bader, Josef Eberhardsteiner, & Christian Hellmich

Jukka Ketoja, Sara Paunonen, Elina Pääkkönen, Tiina Pöhler, Tero Mäkinen, Juha Koivisto, & Mikko Alava

Session 2B Novel measurement methods
Yakov Kazakov, Anastasiia Romanova, & Dmitry Chukhchin

Laura Resch, Anna Karner, Wolfgang Sprengel, Roland Würschum, & Robert Schennach

Elias Henögl, & Robert Schennach

Lisa Hoffellner & Erich Leitner

Welcome to Jyväskylä

Welcome to Jyväskylä, a Central Finnish town surrounded by beautiful lakes and forests! This lively town will be the setting of the PPPS2020 conference. Due to its compact size and warm atmosphere, Jyväskylä is easily reachable and ideal for networking.

Jyväskylä is a lively, versatile city of sport, movement and well-being in which over 5000 events are staged annually. Jyväskylä is situated in the middle of Finland, right in the heart of Urban Finnish Lakeland. The city that follows in the footsteps of the world-famous architect and designer Alvar Aalto can offer visitors some amazing encounters with nature in the middle of the city as well as a variety of thought-provoking culture.

The town is home to 140,000 people and very friendly to international visitors. The people in Jyväskylä have excellent language skills and customer service attitudes. Jyväskylä is especially known for education and sports, and offers a unique combination of urban life and proximity of nature.

Organizers and Committees

The conference is organized by the University of Jyväskylä together with VTT Technical Research Centre of Finland Ltd.

Chairmen of the seminar

Jarmo Kouko
Research team leader at VTT
Vice Chairman of Tappi Paper Physics Committee

Dr. Kouko been involved in research of cellulose pulp, paper, board and most recently in fiber foams and extensible papers. He has 30 peer-reviewed scientific publications and more than 20 scientific conference presentations at field of viscoelastic material behaviour of paper and materials that contain natural fibers.

Jani Lehto
Vice President at VTT

Dr. Lehto is currently in charge of VTT's biomass processing and products research area. Earlier he has also been in charge of VTT's bioenergy and biofuels related research. He has published several scientific articles and conference publications on those fields. He also holds more than 10 patents and have 10+ year career in industry before moving to VTT.

Tero Tuovinen
Adjunct Professor at University of Jyväskylä and Researcher at JAMK University of Applied Science

He has studied computational mechanics and more precisely moving materials (paper webs) and industrial processes more than 15 years. In his career Tuovinen has been organized 29 conferences and supervised 9 M.Sc.'s. He has written 3 monographs, 23 peer-reviewed journal articles, 7 chapters in the book and 16 conference articles. Moreover, he has been editor of 13 books. Today, Tuovinen is a member of ECCOMAS (European Community of Computational Methods in Applied Sciences) managing board and member of Computational Solids and Structural Mechanics committee.

Local Organizing Committee
- Jarmo Kouko, VTT
- Tero Tuovinen, JAMK & JYU
- Jani Lehto, VTT
- Niina Holviala, VTT
- Jaana Räisänen, JYU
- Päivi Vahala-Partanen, VTT
- Tuomo Hokkanen, VTT

Scientific Committee
- Nikolay Banichuk (Moscow State University, Russia)
- Warren Batchelor (Australian Pulp and Paper Institute, Monash University)
- Jean-Francis Bloch (Universite de Grenoble Alpes, France)
- Douglas W. Coffin (Miami University, Ohio, USA)
- Ulrich Hirn (Graz University of Technology, Austria)
- Steven Keller (Miami University, Ohio, USA)
- Artem Kulachenko (KTH Royal Institute of Technology, Sweden)
- Thad Maloney (Aalto University, Finland)
- Mark Martinez (University of British Columbia, Canada)
- Konrad Olejnik (Lodz University of Technology, Poland)
- Joel Pawlak (North Carolina State University, USA)
- Jaan-Willem Simon (RWTH Aachen University)
- Elias Retulainen (VTT Technical Research Centre of Finland Ltd, Finland)
- William Sampson (University of Manchester, UK)
- Samuel Schabel (Technische Universität Darmstadt, Germany)
- Sören Östlund (KTH Royal Institute of Technology, Sweden)

From the Organizing Committee

It is our great pleasure and honor to welcome you to the Progress in Paper Physics Seminar 2020. The Progress in Paper Physics Seminar 2020 will take place in the amazing city of Jyväskylä, from the 1st to the 3rd of September, 2020. We chose Original Sokos Hotel Alexandra (Hannikaisenkatu 35), as the meeting venue. Venue is located in the the city centre of Jyväskylä.

The topics addressed by the seminar will cover a wide range of topics in the field of paper physics and chemistry Besides three plenary speakers, we have selected 37 oral presentations and 12 poster presentations. The Seminar will provide a delightful forum for the attendees arriving at the scene and remotely involved to improve their scientific knowledge and explore the latest outcomes and trends in the field. It will offer plenty of networking opportunities, interaction with leading scientists, and stimulating creative exchange among researches and people working in the respective industries.

We hope you will join us for this outstanding scientific event, the PPPS2020, and take a little extra time to enjoy the remarkable and exceptional beauty of Jyväskylä!

With best wishes,

On behalf of the whole Organizing Committee

Jarmo Kouko

Scope and topics of the Progress in Paper Physics Seminar

The scope of the Progress in Paper Physics Seminar is to discuss the broad scope of physical properties of paper, paperboard and new cellulose containing materials. In addition to contributions centered on traditional paper grades and product, investigations of other materials produced from natural fibers, biocomposites and nanostructured materials are welcome. The program will contain presentations reporting on the latest experimental, theoretical and computational developments. Recent development of fundamental and applied contributions are welcomed to the seminar. In addition to the general topics listed below, there will be three invited plenary speakers aiming at bringing industry and academia together for in-depth discussions on selected topics in paper physics the potential impact on industry.

The major categories and subtopic examples for the PPPS 2020

Paper structure and performance
- Converting performance such as folding, creasing and deep drawing
- Printing performance such as ink-paper interactions and dimensional stability
- Package performance such as lifetime, degradation, vapor/liquid transport
- Tissue performance
- Theories/developments/insights: Fibers and fiber bonds, variability and heterogeneity, strength and failure.

Experimental and computational methods
- Application of classical physics: Electromagnetism, friction, etc.
- Constitutive properties/equations
- End-use properties
- Fibers and fiber-fiber bonds
- Optical characterization methods
- Process and converting simulations
- Structure
- Transport phenomena (Fluid-structure interaction, Heat and Mass transfers)

New cellulose based applications
- Additive manufacturing (3D printing)
- Architecture and interior applications
- Composites
- Filter and barrier materials
- Extensible papers
- Foam-laid structures

Plenary speakers

Professor Douglas Coffin
Faculty member at Miami University

Professor Douglas Coffin has extensive experience in Paper Physics, with a primary focus on the mechanics of fibers, paper, paperboard, and products. He has advanced the understanding of the mechanosorptive response, dimensional stability, constitutive behavior, and fracture of cellulose-based materials. Doug has made contributions to segments of the industry ranging from tissue paper to corrugated boxes.

Doug has been a faculty member at Miami University (Ohio, USA) since 2002. Before that he was on the faculty of the Institute of Paper Science and Technology in Atlanta, Georgia and spent a sabbatical year at the Swedish Pulp and Paper Research Institute in Stockholm, Sweden.

He was awarded the Van den Akker Prize in Paper Physics in 2001 and the TAPPI Corrugated Division Award and Bettendorf Prize in 2011 for his contributions to the field. He is also a recipient of the Dennis and Bridgette Orwig Family Outstanding Research Award (2006) and the Author Olson Generational Teaching Excellence Award (2010). He currently serves on the editorial board of TAPPI Journal. Doug is an active member of the Fundamental Research Committee of the Pulp and Paper Fundamental Research Society.

Professor Tom Lindström
Senior advisior at BiMaC Innovation and FPIRC at KTH

Professor Tom Lindström has a wide experience in most sectors of the Forest Products Industry, such as Pulp and Paper Technology and Wood Technology. His experience encompasses academic, institutional and industrial activities. Lindström´s scientific and technical interests include the physical and surface science of cellulosic fibers and wood-based materials and the physiochemical swelling behavior of cellulose/lignin gels, and a focus has for long been on various paper chemistries such as dry/wet strengthening materials, retention/formation aids, sizing agents etc. Lindström has also worked on forming, wet pressing and drying and consolidation phenomena of paper structures and surface modifications of cellulosic fibers. During recent years, his focus has been on manufacture and upscaling of nanocellulosic materials and various industrial applications of these materials.

Tom Lindström is currently a senior advisor to the boards of Biofibre Materials Research Centre (BiMaC Innovation) and the Forest Products Research College (FPIRC) at the Royal Institute of Technology (KTH).

He was honored to Tappi Fellow 1995 and a Fellow of the International Academy of Wood Science in 1996. He also became a George Jayme medalist in 2007 (ZellCheming), and an Ekman medalist in 2008 (SPCI), and received the William H. Aiken Technical Award in 2016 for outstanding contributions to the Forest Products Industry.

Dr. Anna Suurnäkki
Vice President of Research at Metsä Fibre Oy

Anna Suurnäkki graduated from the Department of Process and Material Technology, Helsinki University of Technology, with a major in biotechnology. Her own research expertise is in pulp and paper biotechnology, especially in enzymatic fibre engineering for industrial applications. Anna Suurnäkki has extensive experience in carrying out and steering the research of fibre processing and novel wood-based materials. While working for the VTT Technical Research Centre of Finland, she coordinated both national and European R&D projects and programs related to forest-based biorefineries.

ABSTRACTS FOR

ORAL

PRESENTATIONS

Tuesday 1.9.2020 at 8:45 - 9:30

Session 1 Plenary talk by Douglas W. Coffin

On the founding of the corrugated board Industry and the introduction of box compression testing: 1871 - 1914

Session chair: Jarmo Kouko

On the founding of the corrugated board industry and the introduction of box compression testing: 1871-1914

Douglas W. Coffin

Miami University, Oxford, Ohio, USA

Corresponding author: *Douglas Coffin <coffindw@miamioh.edu>*

Keywords: Corrugated board, box compression strength, history

Introduction

During an interview by filmmaker Ken Burns, the American essayist Gerald Early stated:

> *I think there are only three things that America will be known for 2,000 years from now when they study this civilization: The Constitution, jazz music and baseball. They're the three most beautifully designed things this culture has ever produced.*

This statement conjures a romantic view of the American spirit and these three items capture some of the best attributes of our culture. Yet, there are countless other developments and inventions that were critical to shaping the society we live in today each one having its own story intertwined with the others. Emanating from the paper industry, corrugated board and the regular slotted container represent two of the "most beautifully designed things" that have helped shape our society. Just like the Constitution, jazz, and baseball, corrugated board is inherently imperfect yet has constantly evolved to meet the demands of the times. Perhaps in 2000 years, the corrugated box will be forgotten, but today it stands as one of the most important paper-based products in the world. With the rise of e-commerce and a broader social awareness of sustainability, corrugated board is enjoying a period of growth with renewed interest in research and development. Few today are familiar with the rich history behind this product. Recently, I[1] reviewed some of the history of the early days of corrugated board industry with a specific focus on testing from 1913 to1925. In this

companion article, I add additional information covering the years from 1871 to 1914, with a specific discussion of the earliest "tests" of stacking strength that I found in the open literature.

In the 1946 Harry Bettendorf, a publisher in the packaging industry, issued his history of paperboard and paperboard containers[2], and in the preface he stated:

> *…the romance of paperboard and mass-production paperboard packages is little known. The mass-production paperboard package is a phantom genie that touches each of us perhaps more intimately than most of man's other developments.*

Seventy-five years separate us from Bettendorf's suggestion that his peers knew little about the founding of the paperboard package industry. Today that history is even more pertinent than in the years directly following World War II. The period from 1871 to 1914 covers the first patented invention of a corrugated packaging material to the 1914 Pridham decision. The Pridham decision insured that east and west bound freight rates were the same and reinforced the Western Classification rule 14-b that fiber-based packaging was charged the same rate as other certified containers. This Pridham decision, finally leveled the playing field for paper-based shipping containers, which ultimately allowed corrugated to dominate the business; yet, most of the elements that led to this success were put into to play before 1914.

The birth of an industry

The invention of corrugated board is attributed to Albert L. Jones of New York City[3] The year was 1871. It was the Gilded Age; a name based on the based on the novel of Mark Twain and Charles Dudley Warner[4]. Before, we describe how this patent triggered the development of a new industry, some other events of the day that are aligned with Early's three most important American inventions: The Constitution, jazz, and baseball. At this time, America was recovering from the Civil War. It was the beginning of a time of major economic growth and industrialization. The 15th Amendment of the US Constitution (stating that the right to "vote shall not be denied or abridged by the United States or by any State on account of race, color, or previous condition of servitude") had recently been ratified (03/30/1870). The ratification immediately triggered efforts to circumnavigate the amendment and suppress voters; efforts which still occurs today. In 1871, the sisters of the late Louis Moreau Gottschalk, born in New Orleans and considered a forefather of Jazz, gave a recital of his music at St. George's Hall (Liverpool, UK). It was reported that his music "embodying the eccentric negro and creole rhythms and tunes … deserve(s) to live." [5]. During that same year, the *National Association of Professional Base Ball Players* was established and on May 4 the first professional baseball game was played in Fort Wayne, Indiana,

marking the start of Major League Baseball. During this same era, tobacco companies had taken up the practice of putting images on the protective paperboard card inserts of cigarette packages, and a few years later, 1886, the players of the New York Giants were featured on the first set of baseball cards.

This era was marked with the creation of great wealth for industrialists, large income growth for skilled labor, but abject poverty for many. Of special interest given today's COVID-19 pandemic with New York being hit so hard, there were 805 deaths in New York City in 1871 from the smallpox pandemic: much fewer deaths than experienced in Europe or even Boston[6]. That same year marked the beginning of the downfall of William Magear Tweed (Boss Tweed) who had often been the subject of Thomas Nast's editorial cartoons in Harper's Weekly. Again, this seems especially poignant today considering the current contentious relationship between the media and President Trump. Finally, in 1871 the Metropolitan Museum of Art acquired its first pieces of Art. Although the Met is currently closed because of the pandemic, it plans to reopen in August of 2020 under a new set of operating procedures that ensures social distancing.

Jones's patent for corrugated board arrived during this time of great change in America, which was also known as the Paper Age[7]:

> *This is the age of paper. Everything is made from paper nowadays, from wheels of railroad cars to costumes for fancy dress parties, and from bonbonieres to underclothing. …. and in fact, there are few things which cannot be, have not been or will not yet be made of paper.*

Even recycling was a critical component of the paper industry in 1871[8] as evidenced by the following statement about New York City.

> *A competent authority calculates that at least 1000 persons in this city derive their means of subsistence from the occupation of buying, trading, selling, collecting, sorting, packing, and shipping old rags and wastepaper. The principal dealers enjoy a handsome income from the business, and several have made fortunes.*

Jones's patent for corrugated board[3] covered just a single layer of paperboard "which is corrugated, crimped, or bossed, so as to present an elastic surface by reason of such corrugated, crimped, or bossed surface." Graphic examples from the patent are shown in Figure 1.1.
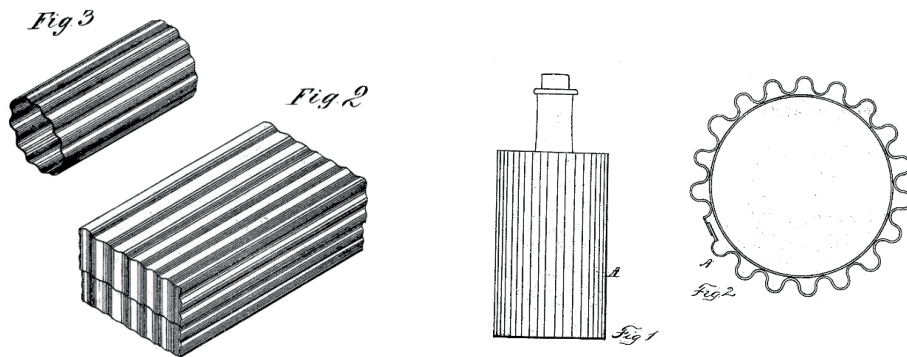
Figure 1.1. First corrugated packaging [3].   Figure 1.2. First Corrugated Board [11]

It is the rare invention that is entirely a new idea. Baseball was just a modification of the game of rounders. The Constitution was inspired by the Magna Carta. Jazz music epitomizes the idea of reinvention and constant evolution. Likewise, Jones's invention used the existing idea of fluting a material and applied it to packaging. In fact, it was later ecognized that the 1856 English patent of Healy and Allen[9] covered the corrugation of sheet materials although their application was for vented hatbands. Corrugated iron had been invented in 1829 and was probably readily observed in New York City in 1871.

In 1873, Henry Norris acquired Jones's patent and began to produce corrugated fluting for packing glassware. The following year, Oliver Long was granted two patents[7,8] covering single-face and double-face packing material with a core of shredded material and the second that replaced the shredded core with a fluted paper. This second patent[8] thus marked the invention of corrugated board as shown for single-face in Figure 1.2. Shortly after this, Robert Gair appears to have acquired some interest in the Long patents, as did Albert Jones[2]. Gair had started printing and selling paper in 1864 and grew the business to one making an assortment of bags and boxes. Jones[12] was granted another patent in 1875, in which he introduced creasing to the fluted material to form corners. Thus, corrugated box was invented.

In 1875, Norris teamed up with Robert Thompson to form Thomson & Norris, and in 1878 they sued Gair for patent infringement. It took years to settle the case, but due to the discovery of the Healy and Allen patent[9], a compromise was made and Thomson and Norris and Gair enjoyed a relative monopoly on producing corrugated board as a packing material. During this time, they developed the methods and machines to mass produce corrugated board and boxes.

Whereas the corrugated box was new, paperboard boxes and folding cartons had been previously developed and were in high demand in this era. It was estimated that Chicago's annual consumption of paper boxes in 1902 was 21 million[13]. A google

patent search with the words "paper box" in the title revealed over 900 patents were issued between 1850 and 1900. Many of these dealt with the scoring and cutting of blanks to produce various types of boxes. An example of an 1883 patented box blank[14] that closely resembles that of a regular slotted container is shown in Figure 1.3. The combined simplicity of the box design, the high stiffness to weight ratio, and the great cushioning capacity of corrugated board made it a wonderful engineered structure for packaging. These material and structural advantages combined with cost effective means of mass production led to a new industry destined to dominate the shipment of goods.
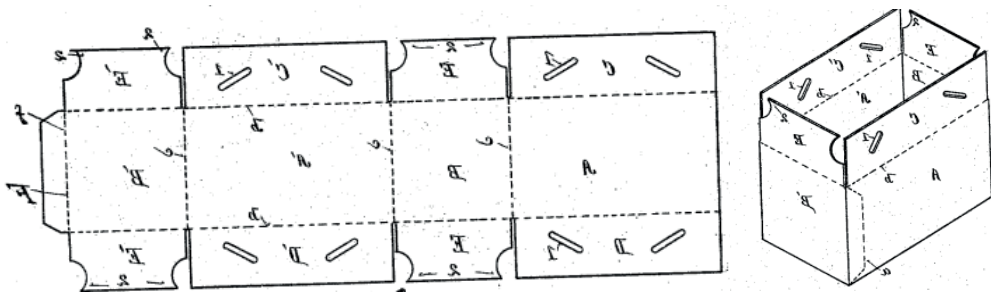
Figure 1.3. Box blank patent from 1893 [14]

The expansion of the industry

As his business in corrugated and folding cartons grew, Robert Gair relocated to Brooklyn, New York in 1888. The Robert Gair Company was incorporated in 1903 and by 1909 it consisted of a series of multi-story buildings including a nine-story factory made from concrete. In 1914, he constructed a 16-story building, the tallest reinforced concrete building in the world at that time. By 1909, Thompson & Norris, also headquartered in Brooklyn, had additional box plants in Boston MA, Brookville IN, France, Germany, and England.

By the end of the nineteenth century, the original patents had expired, and other companies began producing corrugated board. In 1906, the Hinde & Dauch Company of Sandusky, OH was reported as "one of the largest factors in the corrugated board industry in America"[15]. They had started out supplying straw, bought a straw mill, and in 1906 had four plants in the US and were building two mills in Europe. It is important to note, that most corrugated board at this time was made from strawboard. The J. W. Sefton Manufacturing Company started in 1888 in Anderson, IN originally making wooden butter dishes[16]. They began to produce paper products, acquired a plant in Chicago, and started making corrugated board. They developed machines for producing and converting corrugated board.

One reason for the growth of corrugated shipping containers was their inclusion in Railroad shipping regulations. In 1903, a cereal manufacturer obtained an exclusion

from the Central Freight Association to ship their product in corrugated containers[17]. E. W. Bonfield provided a first-person account[2] of the inclusion of corrugated boxes in a proposal at the meeting of the Western Classification Committee held at Frankfort Michigan, July 17-21, 1906. Mr. Bonfield had not considered corrugated board in his original proposal, but a third party asked for its inclusion prompting Mr. Bonfield to add corrugated to his proposal. So as not to hamper the proceedings and having no knowledge of safe load limits for corrugated, Bonfield's team limited gross weight to 100 pounds. By October 1, 1907 Rule 14-b of the Western Classification, "Pulp, Fibre or Double Faced Corrugated Boxes" was adopted.

In 1912, the R. W. Pridham & Company, a producer of paper boxes, brought a case against the railroads because rule 14-b was not being applied to eastbound freight as it was for westbound freight. The railroads were charging higher rates for eastbound freight packed in paper containers compared to those packed in wood containers. The wooden box manufacturer had hoped the railroads would prevail and they could use this case to remove rule 14-b all together. In 1914, the case was decided in favor of Pridham by the Interstate Commerce Commission. The Commission had been established in 1887 by an act of Congress, which applied the Constitution's clause "to regulate commerce with foreign nations, and among the several states."; thus, making the railroads the first regulated industry in the USA. The Commission's decision was a major victory for the paper-box industry.

In his discussion, Bonfield stated that in the process of getting rule 14-b approved they were asked by the committee to find a standard test that could be used to measure the strength to resist damage. Not having any knowledge of a corrugated strength test, Mr. Bonfield mentioned the only strength tester for paper he knew, the Mullen tester. Afterwards, he acquired a jumbo Mullen tester used for book cover stock and started bringing it to the meetings to demonstrate its use with corrugated board. Thus, the Mullen or burst test became a standard measure for the quality of corrugated board. There was no science behind the adoption of the Mullen test; rather, it was simply the only paper strength test known to those promoting the adoption of new shipping rules for paper-based packaging. This marks the beginning of the long love-hate relationship of the industry with the burst test. The reader can find further discussion of the Mullen and a rival, the Webb tester, in the companion article[1]. Needless, to say the inclusion of corrugated board in rule 14-b helped stimulated the growth of the industry. It offered a needed alternative to wooden crates, and by 1910 the corrugated box industry was firmly established[18]:

> *The increasing scarcity of wood in recent years has compelled the use of some other materials for shipping cases. This has brought into use the heavy cardboard container or shipping case, the economical manufacture of which has been made possible by the invention of special machinery.*

In 1907, Charles Cristadoro[19], an outspoken wood-box-man, stated that the production of packing boxes consumed fifty percent of the lumber in the US. He suggested that wooden crates were critical to the US economy and diverting word for other uses such as for pulp were creating a problem. In hindsight, given that the answer was already apparent, it is interesting that he asked:

> *With all these drains of the forests what will be the future box and of what will it be made!*
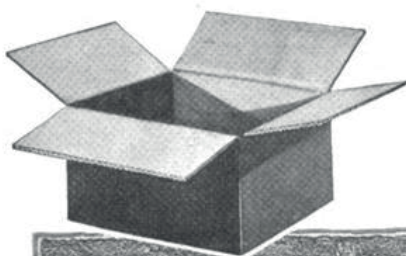
He does not mention the corrugated box in his article, but shortly afterwards Cristadoro and others begin to call corrugated and fiberboard boxes inferior substitute containers. Perhaps even in 1907, Cristadoro knew paper would supplant wood, and his article foretold of the war of sorts between the industries of wood and paper containers. The Pridham decision of 1914 was one victory for paper, but as outlined in[1] it was not until the 1920's that producers of corrugated boxes claimed victory.

In 1914, a full-page advertisement placed by Hinde & Dauch appeared in the September issue of *Factory*[20] asking "Which would you rather unpack". As shown in Figure 1.4 it has a corrugated box with the top flaps open in the top left corner and the broken pieces of a wooden crate strewn across the right side of the page. This advertisement summed up the battle between corrugated and wooden boxes:
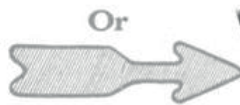
> *No matter how we argue, a container that creates disorder – that admits road dust to come in contact with the product -that frequently arrives "damaged" – creates serious dissatisfaction. Glance at the Illustrations. You instantly choose to unpack the fibre container because its clean – there's no litter – it's easier. Why then, when your preference is so strong, can you afford to disregard the attitude of others toward your packed-in-a-wooden-box product?*
>
> *Besides gaining and holding trade, you will save in every department where packing is done by using boxes of Hinde-Dauch corrugated fibre board.*

Figure 1.4. An Advertisement from 1914 capturing the essence of the war between wood and corrugated containers[20].

The rise of performance testing for corrugated materials

As stated in the last section, the Mullen test was not chosen because it had any inherent and known capability to predict box performance but was chosen only as a

practical means to an end. Yet, today the measurement still persists; mainly because it is still specified in shipping regulations. The newer alternative rule specifying the magnitude of the edge crush test is performance based. The companion article[1] provides additional history surrounding the use of Mullen, the adoption of performance testing developed from wooden boxes, and eventually the characterization of corrugated board as an engineering material. Interestingly, box compression testing was not fully investigated until the second half of the 1920's, the Jazz age. On the other hand, it was obvious to those dealing with corrugated boxes in the first decade of the twentieth century that compression strength was important for performance.

To set a historical frame around the early awareness of box compression, first we provide some interesting connections between packaging Early's choice of the three most beautiful American inventions. From 1900 to 1910, baseball was fast becoming America's pastime, ragtime music was popular, and the 16th Amendment introducing income taxes was passed by congress. The widespread popularity of baseball was perfectly captured in the August 1905 issue of *Packages*[21] stating "all devotees of the game of baseball, which so far as *Packages* knows, includes pretty much every normally constituted American citizen…" In another section of that same issue it was reported that "a baseball nine" (team) composed of employees of a boxboard manufacturer "walloped" employees of a strawboard manufacturer. A third section featured the baseball team of the Greif Brothers Company from Cleveland, OH (Figure 1.5). This was when Greif was a cooperage and before the produced corrugated materials.

Figure 1.5. Greif Bros. baseball team 1905[21]
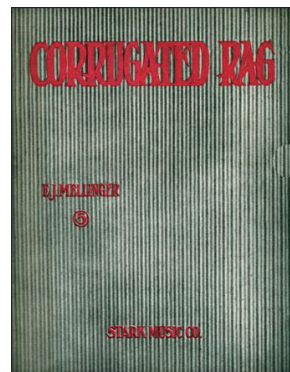
Figure 1.6. That Corrugated Rag, 1911[23]

It was reported in the July 1909 Issue of *Packages*[22] that US senate had adopted an amendment to the tariff bill which provided for a tax on corporations presumably in an effort to head off legislation on a federal income tax. They mused that holders of stock in corporations will see this as a very one-sided affair and they sated:

> *The ways of the senate sometimes are Gevious (*devious or grievous?*)*
> *and hard of understanding. Maybe the result isn't far from what is desired.*

Perhaps not known to *Packages* when they wrote this news brief, but that legislation also had the 16th amendment of the constitution attached to it. This eventually led to the federal corporate and individual income tax system we have today.

Corrugated packaging had even infiltrated the music world as evidenced by the song composed by Edward J. Mellinger called *That Corrugated Rag*, published in 1911[23]. As shown in Figure 1.6, the cover appears to be made from corrugated paperboard.

The start of the twentieth century was also a time when the advantages of corrugated board as a shipping container were being discovered by many industries as discussed below with examples from the apiculture, floriculture and pharmaceutical industries. These new potential customers questioned if corrugated could perform well. In response, ad hoc testing was completed to give assurance to the potential users of these containers.

In a 1902 article in *The Beekeepers' Record*[24], corrugated containers are listed as a novel and economical choice for shipping honey. The article reveals perhaps the first publicly recorded compression strength evaluation:

> *No fear need be entertained with regard to the strength of these boxes, for*
> *we have personally tested the point by standing on one, and a weight of*
> *twelve stone* (168 lbs.) *made no impression whatever.*

Standing on a box seemed to be the preferred early method of evaluation for strength. In 1904[25], it was reported that paper boxes made from heavy stock at the Lewis Paper Box plant in Toledo, OH would support the weight of a man jumping on it.

One of the advantages of corrugated board and boxes were that they could be designed to meet the requirements of the package. Strength was a consideration in this design as captured by an article in *Pharmaceutical Age*[26] touting the advantage of corrugated containers made by Thompson & Norris, which read:

> *Express boxes are made of double-faced corrugated board. The company explains that it makes all styles, suiting the selection to the goods of each customer. Some enclosures naturally require less protection than others and in these cases the company does not furnish as strong a box as it would where the article is particularly fragile and requires maximum protection in order to prevent breakages.*

In an advertisement for the Sefton Manufacturing Company appearing in the *Florists' Review*[27], the key attributes of corrugated were listed as "Strong, Light, Convenient". Again, the strength was determined relative to a man's weight:

> *A Paper box strong enough to support a man's weight. The arched construction of corrugated fibre board gives the strength to a box with the least weight and also provides a dead air cell which helps to preserve flowers.*

In 1910, the Hinde & Dauch company ran a series of advertisements in *Factory* touting the advantages of corrugated board over wood for shipping containers. It seems that this campaign was in response to the pressure being applied by the wooden box industry to suppress the use of corrugated containers. In the March issue, an advertisement[28] (Figure 1.7) showed perhaps the first official test of top-to-bottom compression strength in a corrugated container. The advertisement explained that the test was conducted by the Macbeth & Evans Glass Co. in the presence of a Pennsylvania R. R. official to prove the strength of H&D corrugated slotted cartons used to ship glassware. It was a reported that a 12 in x 12 in x 17 in carton did not collapse until a load of 4,230 lbs. had been reached by placing pigs of lead on top of it as shown in Figure 1.7. The strength value of 4230 lbs. for a box of this size this is extra ordinally high indicating that the corrugated box was likely heavy weight, and probably had inserts, which carried significant load. None the less, the image clearly shows what can be considered a scientific compressive strength test of a corrugated box.

In follow up advertisements, in the April 1910[29], February 1911[30] (Figure 1.8), and May 1911[31] issues of *Factory*, strength and resilience were emphasized with a focus on how the lack of through-the-thickness-direction stiffness gives resilience from shock. This concept stems from the original patent idea of Jones: "so as to present an elastic surface by reason of such corrugated, crimped, or bossed surface." These concepts highlight the true brilliance of corrugated board for packaging.

Although stacking performance did not become a major focus until after World War II, it was much appreciated in the early days of the corrugated industry. Figure 1.9 shows corrugated boxes containing mason jars stacked up to thirty feet high at the Ball

Brothers Glass Manufacturing Company. Stacking strength or the ability of the bottom box to support the weight of those stacked above it is clearly articulated in the caption of the original article: "…proof of the strength of the boxes in the lower tiers" [32].

Even if your packing boxes had to stand as great a strain as this—

H & D Corrugated Fibre would serve the purpose better than wood. And would save you freight bills, save you storage room in your plant, save time in packing. Regardless of what your product is, if it goes in reasonably-sized boxes, we can design a better, more economical packing for it, with

H & D Corrugated Fibre Board Boxes

This is your chance to learn why this new and better way for packing your goods in Fibre Board would be better for your own use. Strong, tough, light—it is a packing that use in hundreds of large plants has proved a saver of packers' time, a saver of freight bills, a saver of damage in transit—a saver at every turn. And now will you not learn about it—will you not simply express your willingness to examine this modern packing device, and judge of it?

Let Us Send You a Free Sample

Without costing you a cent and without obligation, let us, at our own risk, design a sample package for you. This will give you an exact idea of the efficiency and economy of H & D Corrugated Fibre Board Boxes for your use.

Better Than Wood Boxes

Wood boxes are expensive. They are expensive the day you buy them, because lumber is high and going higher, they are expensive all the while you keep them on hand because they occupy valuable space, they are expensive when you use them because they make useless work in make-ready, they are expensive in shipment because they cost pound-freight-rates, they are expensive after shipment because they so often break open and damage contents. H & D Corrugated Fibre Board Boxes are convenient, light, tough—they stand hard wear better than wood, and cost less at every turn.

H & D Boxes are easy to get and are surprisingly inexpensive. We make them up in specific sizes to meet your requirements. Because they are in collapsible form, thousands may be stored away in but little space. And they can be brought out, packed and made ready for shipment in half the time it takes to handle wood boxes.

Saves Freight

Ten H &, D boxes will travel for the freight charges you now pay on one wooden case. Our corrugated board is the only practical substitute for wood—and it is vastly superior. Our experience studying and improving packing and shipping methods will help you to plan an H & D box that once tried will revolutionize your shipping methods. Our free book, "How to Pack It" contains valuable information for your shipping room.

Send Today for Your Sample

No matter what your business is—no matter where located, write us today for a sample of H & D and the book "How to Pack It." We will gladly extend expert help in designing a box for your product that will save time in packing and save danger of breakage—colors printed without extra charge. Write today to our nearest office for sample and particulars.

The Hinde & Dauch Paper Co.

NEW YORK   CHICAGO   ST. LOUIS   BOSTON
PITTSBURG   PHILADELPHIA   CINCINNATI
SAN FRANCISCO   SANDUSKY, OHIO

4230 lbs. on a Small H & D Package

This cut represents a test made by The Macbeth-Evans Glass Co. in the presence of a Pennsylvania R. R. Official, to prove the strength of H & D CORRUGATED SLOTTED CARTON—the Carton measures 12x12x17 inches and did not break down until after the 47 pigs of lead with a combined weight of 4230 lbs. had been piled upon it, thus proving CORRUGATED BOXES to have greater strength than ordinary wood boxes.

Figure 1.7. Hinde & Dauch advertisement showing perhaps the first recorded box compression test from 1910[28].

It is obvious that by 1914, the industry understood many of the performance issues of corrugated board. In all likelihood, testing protocols were being carried out by companies to aid in design. The concept that compressive strength is a key indicator for box performance would not be well established until the 1930's[33], although

advertisements during the period in between indicate the growing acceptance that compressive strength was important. These advertisements also suggest that the corrugated box industry was as vibrant and exciting as a circus. For example, the advertisement from 1918[34] shown in Figure 1.10 suggested that a corrugated box was strong enough to support a hippopotamus. The Sefton Manufacturing Company had a marketing campaign in 1923, showing "Five big men on a Sefton box" (Figure 1.11)[35]. It stated that the compressive strength of a 12 in x 12 in x 12 in corrugated box was 1000 lbs.

Figure 1.8. Hinde & Dauch advertisement from 1911 showing the how through-the-thickness compliance allows for absorption of energy from shock[30]

Summary

The origins and initial development of the corrugated board industry have all the elements of a story worth telling. There were fascinating characters such as Gair and Cristadoro. There was conflict such as the war between the wood and paper box-men. There were setbacks such as the dealings with the railways, and finally triumph with the dominance of corrugated board's use in shipping. This subject would make great storyline for a Ken Burns documentary. More importantly, those working in the field should be mindful of this story.

Many of the influences that drove the origins of the corrugated industry, are still reflected in driving factors of today's industry, and we realize that our challenges are not as new as we tend to imagine. Our understanding of box compression strength slowly developed and came to dominate the research of our community. Clearly, it is not the only indicator of performance. Now in the age of e-commerce we must return

back to the other important attributes of corrugated that were noted so well in 1911[29]; the ability to withstand shock and rough handling. The early history of this aspect was further discussed in the companion paper[1], and the conclusion was that our challenges are closer to the challenges faced by our predecessors from 1910 to 1930 than those in the interceding years.

Figure 1.9. Photo from 1911 showing corrugated boxes packed with mason jars stacked up to 30 feet tall[32]

Figure 1.10. Compression strength implied by image[34]

Figure 1.11. A 1000 lb. strength box[35]

Corrugated board, one of the great inventions of the *Paper Age*, is just as important in the digital age due to the rise of e-commerce and the consumer's focus on sustainability and recyclability. To summarize, the words of J. L. Thompson[36], Vice President of Thompson & Norris in 1913 should resonate with those in the industry today.

> *The present controversy between the wood box and the fiber box interest renders a few remarks on the subject not inappropriate at this particular time…..The observer taking up a piece of corrugated board will become impressed at once with its extreme lightweight, and if he investigates the product at all he will very soon become convinced of its remarkable strength…. Our customers find that it saves them 10 to 25 percent on their freight bills and 10 to 25 percent on the cost over wood boxes. If the corrugated case failed to carry the goods satisfactorily, a statement as above would hardly possess the weight it really has. It might be as well to say in passing that these boxes are flat in construction being set up by the shipper very quickly without the aid of skilled worker. … The corrugated box … is easily and thoroughly sealed … and the thief cannot procure the contents or part of them without destroying the box…. In terms of safety of the corrugated box, a large shipper of glass jars testifies that claims from breakage in corrugated boxes was less then one half of one percent…. I can only repeat my confidence in the properly constructed corrugated box, a confidence supported by the testimony and actual experience of my company's customers, and to impress upon manufacturers the importance of making a good case one conforming in every particular to test and regulation.*

References

1. Coffin, D. W. (2020). Historical perspectives of corrugated box testing for 2020. Tappi J., 19(3), 161-173.
2. Bettendorf H. J. (1946). Paperboard and Paperboard Containers a History, Board Products Publishing Co Chicago IL.
3. Jones A. L. (1871) Improvement in Paper for Packing. US Patent 122023, Dec 19.
4. Twain M. and Warner C. D. (1873). The Gilded Age: A Tale of Today, Hartford, Connecticut: American Publishing Company, 1st edition. pp. 574
5. Anon. (1871). Music and Arts section, Public Opinion 19:146, Feb 4.
6. Rollerston J. D. (1933). The Smallpox Pandemic of 1870-1874, Proc Royal Soc Med., 27(2): 177–192
7. Anon. (1895). Paper has its many uses: This is the Age of Paper, The Washington Post p. 6, Aug 19.
8. Anon. (1871). Waste Paper and Rags: Value of Cast-away Trifles Precious Treasure in Refuse Magnitude of the Old-Paper and Bag Business Interesting Facts and Figs. The New York Times, p. 5, Nov 24.
9. Healy E. C. and Allen E. E. 1856. An Improvement in the preparing of veneers, paper, and other fabrics or sheets made of fibers, British Patent 1597, July 7.
10. Long O. (1874). Improvement in Packings for Bottles, Jars, &c., US Patent 150588, May 5.

11. Long O. (1874). Improvement in Packing for Bottles, &c., US Patent 154498, Aug 25.
12. Jones A. L. (1875). Improvement in Blanks for Corrugated-Paper Boxes, US Patent 163379, May 18.
13. Anon. (1902). How the 21,150,000 Paper Boxes Chicago Uses Annually Are Made. Chicago Daily Tribune pg. A4, Sep 7.
14. Schmidt T. F. W. (1893). Paper Box, US Patent 490167, Jan 1.
15. Anon. (1906). Hinde-Dauch Company. The Paper Box Maker and American Bookbinder, 24(8), Aug 14.
16. Whitcom G. W. (1921). Visit to the Sefton Manufacturing Company Plant in Chicago. Shears, 29:143-152, Oct.
17. Howell W. F. (1940). A History of the Corrugated Shipping Container Industry in the United States. Samuel M. Langston Company, Camden NJ USA.
18. M. B. K. (1910). Treatment of Paper and Cardboard for the Preservation of Food. The Inland Printer, 45, 239.
19. Cristadora C. (1907). Use Half the World's Lumber in Making Packing Boxes. Chicago Daily Tribune pg. E4, Aug 25.
20. Advertisement for Hinde & Dauch. Factory 15(3), 174, Sep. 1914
21. Anon. (1905). Packages 8(8):28, 53, 69, Aug.
22. Anon. (1909). Packages 12(7):19, July.
23. Mellinger, E. J. That Corrugated Rag. Charles H. Templeton, Sr. sheet music collection. Item number: 32278009987664: Special Collections, Mississippi State University Libraries.
24. Anon. (1902). Novelties for 1902: Corrugated-Cardboard Package for Honey. The BeeKeepers' Record 20(192): 76, May.
25. Anon. (1904). The Boxmaker and American Bookbinder 12(8):5, June.
26. Anon. (1907). Manufacturers of Corrugated Paper Cartons do a World-wide Business. The Pharmaceutical Era 38(15):359, Oct. 10.
27. Advertisement for The Sefton MFG Co. (1909). Weekly Florists' Review pg. 17, Aug 19.
28. Advertisement for Hinde & Dauch. (1910). Factory 4(3):132, March.
29. Advertisement for Hinde & Dauch. (1910). Factory 4(4):190, April.
30. Advertisement for Hinde & Dauch. (1911). Factory 5(2):82, Feb.
31. Advertisement for Hinde & Dauch. Factory 6(5):302, May 1911.
32. Cleary L. J. (1911). Better ways of Packing Goods. Factory 6(6):390-392.
33. Malcolmson J. D., (1936). The Value of the Compression Test for Corrugated Boxes. Fibre Containers 21(4):14-15, April.
34. Advertisement for Diem and Wing Paper Company. (1918). Fibre Containers 3(8):25, Aug.
35. Advertisement for Sefton Manufacturing Company (1923). Canning Age, pg. 45, April.
36. Thompson J. L. (1913). Standard Corrugated Containers Insure Safe Delivery of Package Shipments. Trade and Transportation 14(4):18, June.

Tuesday 1.9.2020 at 10:00 - 12:00

Session 2A

Compression behavior of fiber networks

Session chair: Samuel Schabel

A constitutive framework for paperboard accounting for anisotropy and compressible plasticity at finite strains

Erik Prume, Sebastian Felder, & Jaan-Willem Simon

Institute of Applied Mechanics, RWTH Aachen University, Aachen, Germany

Corresponding author: *Jaan-Willem Simon <jaan.simon@rwth-aachen.de>*

Keywords: Plasticity, anisotropy, finite strains, compressibility, paperboard

Summary

In this work, a material model for paper and paperboard has been developed. The model accounts for the material's anisotropy as well as compressible plasticity. Further, the formulation is also valid in the large deformation regime, which is crucial particularly in the out-of-plane compression loading. The yield function is based on the well-known formulation of Xia et al. making use of nine yield planes. For validation, several numerical examples have been considered, and it was shown that the model predictions and the experimental data agree.

Laminated paperboard is one of the most common packaging materials in industry due to its beneficial characteristics, such as low price, sustainability, and recyclability. This material exhibits a highly anisotropic mechanical behavior due to its manufacturing process leading to the principal directions of paper: the machine direction, cross-machine direction, and out-of-plane direction. In particular, this results in orthotropic elasticity, orthotropic initial yielding, orthotropic strain hardening, and tension-compression asymmetry.

Permanent deformations can be observed after unloading, indicating a typical elastic-plastic behavior in both in-plane and out-of-plane directions. However, the thickness direction shows several specific characteristics, particularly during the compression. It appears to evolve exponentially (see Figure 2.1) because compression results in an apparent densification effect of the underlying paper network, which is generally not found during in-plane deformation. Examples of other differences include the large

Prume, E., Felder, S., & Simon, J.W.

deformation range and the internal friction effect, which are all more significant in the out-of-plane direction.

In general, the experimentally observed mechanical behavior of paper includes: (i) elastic-plastic anisotropy, (ii) different yielding between tension and compression, (iii) pressure dependent yield behavior, (iv) densification effect in the out-of-plane compression, and (v) internal friction effect in the out-of-plane direction under combined shear and compression.
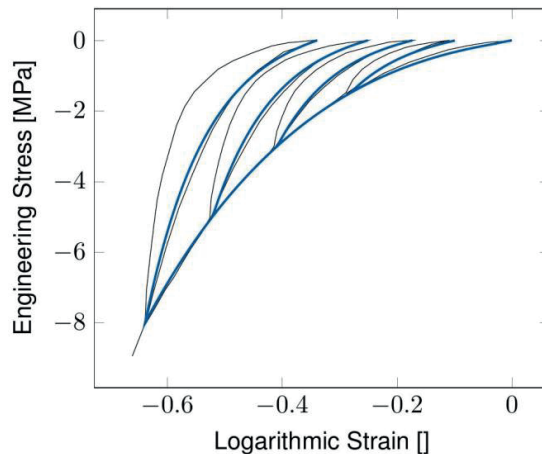
Figure 2.1. Experimental data (black) and model fit (blue) of cyclic out-of-plane compression test.

In previous works, the in-plane[1] and the out-of-plane[2] elastic-plastic behavior of paper have been modeled in an uncoupled way as suggested e.g. by Stenberg[3]. In the current work, these two models have been combined resulting in a single orthotropic model that can capture the coupling between the elastic and plastic responses in all directions.

The model accounts for all aspects mentioned above. In addition, the plastic compressibility is described in a new fashion by introducing the plastic volume change into the corresponding energy terms. Further, it is formulated within the finite strain framework such that large deformations as well as large rotations can be taken into account. Moreover, the model is proven thermodynamically consistent.

The yield function is based on the well-known formulation of Xia et al.[4], which has been extended in several more recent works such as[5,6]. In this work, the anisotropic onset and progression of yielding is defined by introducing nine yield planes.

For validation, several numerical examples have been considered. For instance, the result of the so-called punch test is given in Figure 2.2. As one can see, the model prediction and the experimental data agree.
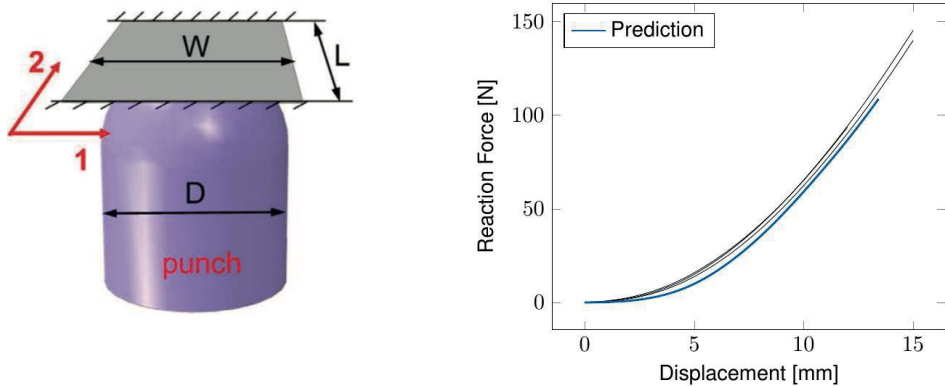
Figure 2.2. System of the punch test (left) and resulting force-displacement curves (right) from experiment (black) and prediction (blue)S

Acknowledgements

References

1. Li, Y., Stapleton, S. E., Reese, S., & Simon, J. W. (2016). Anisotropic elastic-plastic deformation of paper: In-plane model. *International Journal of Solids and Structures*, *100*, 286-296.

2. Li, Y., Stapleton, S. E., Reese, S., & Simon, J. W. (2016). Anisotropic elastic-plastic deformation of paper: In-plane model. *International Journal of Solids and Structures*, *100*, 286-296.

3. A model for the through-thickness elasticplastic behaviour of paper.

4. Xia, Q. S., Boyce, M. C., & Parks, D. M. (2002). A constitutive model for the anisotropic elastic–plastic deformation of paper and paperboard. *International journal of solids and structures*, *39*(15), 4053-4071.

5. Borgqvist, E., Wallin, M., Ristinmaa, M., & Tryding, J. (2015). An anisotropic in-plane and out-of-plane elasto-plastic continuum model for paperboard. *Composite structures*, *126*, 184-195.

6. Tjahjanto, D. D., Girlanda, O., & Östlund, S. (2015). Anisotropic viscoelastic–viscoplastic continuum model for high-density cellulose-based materials. *Journal of the Mechanics and Physics of Solids*, *84*, 1-20.

Experimental and numerical investigation of single sheet out-of-plane compression tests of different paperboards

Marcus Pfeiffer[a], Robert Götzinger[b], Benjamin Hiller[c], Stefan Kolling[a], & Samuel Schabel[b]

[a]*Technische Hochschule Mittelhessen, Giessen, Germany*
[b]*Technische Universität Darmstadt, Darmstadt, Germany*
[c]*Papiertechnische Stiftung (PTS), Heidenau, Germany*

Corresponding author: *Marcus Pfeiffer <marcus.pfeiffer@me.thm.de>*

Keywords: Out-of-plane compression, numerical simulation, viscoelasticity, plasticity

Summary

This investigation focuses on the characterisation and representation of the mechanical out-of-plane response of paperboard. Single paperboard sheets are tested and a finite element formulation accounting for viscoelastic and plastic effects is presented. Numerical simulations are conducted to investigate the sensitivity of the test setup with respect to variations in paperboard properties to improve the interpretation of test results.

Introduction

The present work focuses on determining the material behaviour of industrial paperboard sheets in the out-of-plane direction. A test apparatus with a cylindrical punch is used that enables to apply loads on single paperboard sheets perpendicular to the paperboard plane[1]. By that no adhesives are needed which might influence the material response. Exemplary results for two tested paperboard materials are shown in Figure 2.3. Out-of-plane compression tests are conducted at different load speeds in order to identify strain rate effects. Additionally, cyclic loading and relaxation tests are performed in the out-of-plane direction.
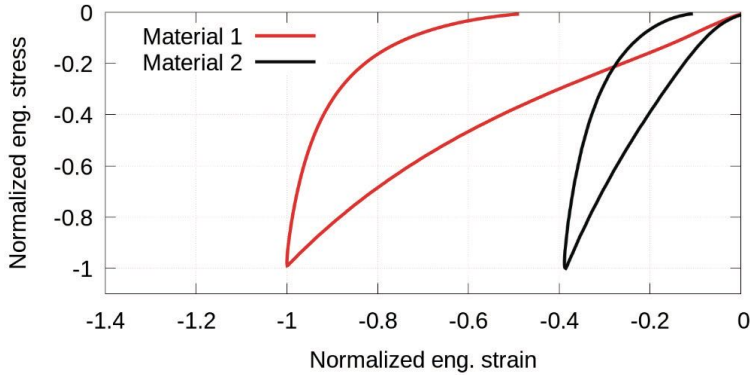
Figure 2.3. Exemplary results for the tested paperboard materials. Stress is calculated as the resulting force divided by the cross section of the indenter and strain refers to the displacement divided by the initial thickness of the material.

A finite element analysis of the experiments is conducted using a simplified material model incorporating the elastic in-plane behaviour as well as the viscoelastic-plastic out-of-plane behaviour. The simulation model enables to identify the major effects influencing the testing results. In addition, the stress distribution within the specimen can be obtained.

Material model

In contrast to previous work[2], the present material model uses a finite strain anisotropic framework. Structural tensors are used to account for the anisotropy of the material. The viscoelastic part of the model follows the approach presented in[3] where a multiplicative decomposition of the deformation gradient

$$\boldsymbol{F} = \boldsymbol{F}_i^{\infty} \boldsymbol{F}_i^{v} \tag{1}$$

into elastic parts $\boldsymbol{F}_i^{\infty}$ and viscous parts $\boldsymbol{F}_i^{v}$ is applied[4]. The subscript i denotes the ith parallel decomposition of the deformation gradient. This framework enables to account for multiple relaxation processes where an evolution equation for each relaxation process must be defined. The elastic-plastic decomposition may be performed in a similar way parallel to the decomposition given by Eq. (1)

$$\boldsymbol{F} = \boldsymbol{F}^{e} \boldsymbol{F}^{p} \tag{2}$$

and the following strain measures can be defined

$$C_i^v = (F_i^v)^{\mathrm{T}} F_i^v, \qquad C^\infty : \tag{3}$$

$$C^p = (F^p)^{\mathrm{T}} F^p, \qquad C^e = (F^e)^{\mathrm{T}} F^e. \tag{4}$$

Another possibility is to decompose the deformation gradient multiplicatively into elastic, plastic and viscous parts in contrast to the parallel decomposition given by Eq. (1) and (2)[5]

$$F = F^e F^v F^p. \tag{5}$$

Both approaches are compared in terms of their applicability to out-of-plane compression of paperboard materials. For the sake of simplicity, only the framework using the parallel decomposition is described in the following.

In the present work, the evolution of the preferred material directions follows the approach presented in[3, 6] which will be briefly summarised here. The invariants used for the free energy density are defined in the intermediate configurations. The approach is described for the elastic-plastic decomposition of the deformation gradient and is used in the same way for the viscoelastic decompositions given in Eq. (1).

It is assumed that the evolution of the preferred directions initially defined in the reference configuration is given as

$$\lambda_p^{(i)} n_p^{(i)} = F^p n_0^{(i)} \tag{6}$$

with the ith unit vector $n_0^{(i)}$ in the reference configuration and the corresponding direction in the intermediate configuration $n_p^{(i)}$ with the associated stretch $\lambda_p^{(i)}$. The mapping to the current configuration is defined in the same way using the elastic part of the deformation gradient

$$\lambda_e^{(i)} n_e^{(i)} = F^e n_p^{(i)}. \tag{7}$$

Structural tensors are defined in the intermediate configuration as

$$M_p^{(i)} = n_p^{(i)} \otimes n_p^{(i)}. \tag{8}$$

By using Eq. (6) together with Eq. (8), the structural tensors in the intermediate configuration may be expressed as[6]

$$M_p^{(i)} = \frac{F^p M_0^{(i)} (F^p)^{\mathrm{T}}}{C^p : M_0^{(i)}} \tag{9}$$

where $M_0^{(i)} = n_0^{(i)} \otimes n_0^{(i)}$. With Eq. (9), invariants in the intermediate configuration such as

$$I_{ii} = C^e : M_p^{(i)} \tag{10}$$

can be rewritten as[3]

$$I_{ii} = \frac{C : M_0^{(i)}}{C^p : M_0^{(i)}}. \tag{11}$$

The beneficial approach briefly summarized here allows to define a free energy density of the form

$$\psi = \psi_e\left(C, M_0^{(1)}, M_0^{(2)}, M_0^{(3)}\right) + \psi_{oop}\left(C, C^p, M_0^{(3)}\right) \\ + \sum_i \psi_{oop,v}^{(i)}\left(C, C_i^v, M_0^{(3)}\right) + \phi(\gamma) \tag{12}$$

with an elastic part ψ_e, an elastic-plastic part ψ_{oop} as well as viscous parts $\psi_{oop,v}^{(i)}$ for the out-of-plane direction. The specific model used in the present work can represent the strong anisotropy of paperboard materials but does not fulfil the requirements for polyconvexity.

Simulation results

Case studies are performed with a computer model based on experimental results. The finite element representation used for preliminary studies is shown in Figure 2.4. Due to the assumptions included in Eq. (12), only plastic and viscous deformations in the out-of-plane direction are considered.
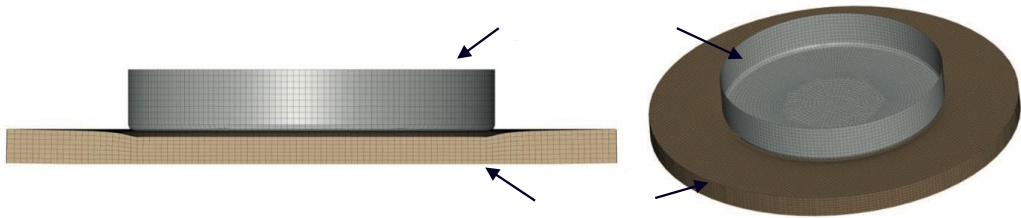
Figure 2.4. Simulation of an out-of-plane compression test showing the deformed specimen as well as the cylindrical punch with an element size of approximately 0.1 mm.

The computer model is used to investigate the impact of material parameter variations as well as variations of the testing device. Figure 2.4 shows the normalized force-displacement curves obtained from simulations for a variation of the out-of-plane shear properties. It is evident that shear deformations are present at the edge of the cylindrical punch, so that the out-of-plane shear properties influence the experimental results. From Figure 2.5 it may be concluded that the shear properties have a small impact on the resulting force, only. In this context further investigations are necessary such as convergence studies accounting for the influence of element size in numerical simulations.

$$G_{oop} = \frac{\partial^2 \psi}{\partial C_{13} \partial C_{13}} = \frac{\partial^2 \psi}{\partial C_{23} \partial C_{23}}$$
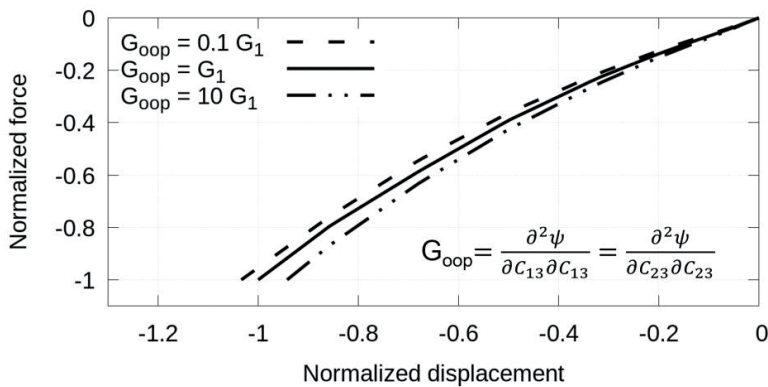
Figure 2.5: Parameter study on the influence of the out-of-plane shear properties on the force-displacement behaviour obtained from out-of-plane compression simulations.

Acknowledgements

Pfeiffer, M., Götzinger, R., Hiller, B, Kolling, S., & Schabel, S.

References

1. Chen, J. (2016). Investigation on the Mechanical Behavior of Paper and Paper Stacks in the out-of-plane Direction (Doctoral dissertation, Technische Universität Darmstadt).

2. Pfeiffer, M., & Kolling, S. (2019). A non-associative orthotropic plasticity model for paperboard under in-plane loading. International Journal of Solids and Structures, 166, 112-123.

3. Nguyen, T. D., Jones, R. E., & Boyce, B. L. (2007). Modeling the anisotropic finite-deformation viscoelastic behavior of soft fiber-reinforced composites. International Journal of Solids and Structures, 44(25-26), 8366-8389.

4. Reese, S., & Govindjee, S. (1998). A theory of finite viscoelasticity and numerical aspects. International journal of solids and structures, 35(26-27), 3455-3482.

5. Nedjar, B. (2002). Frameworks for finite strain viscoelastic-plasticity based on multiplicative decompositions. Part I: Continuum formulations. Computer Methods in Applied Mechanics and Engineering, 191(15-16), 1541-1562.

6. Reese, S. (2003). Meso-macro modelling of fibre-reinforced rubber-like composites exhibiting large elastoplastic deformation. International Journal of Solids and Structures, 40(4), 951-980.

Continuum micromechanics of transversely isotropic paper sheets: recent results for elasticity and ultimate strength

Pedro Godinho[a], Thomas Bader[b], Josef Eberhardsteiner[a], & Christian Hellmich[a]

[a]*Vienna University of Technology, Vienna, Austria*
[b]*Linnaeus University, Småland, Sweden*

Corresponding author: *Pedro Godinho <pedro.godinho@tuwien.ac.at>*

Keywords: Paper sheets, linear elasticity, ultimate strength, hierarchical organization, micromechanical representation, multiscale experimental determinations

Summary

A considerably improved, multiscale, continuum-micromechanics-based model for the elasticity and strength of transversely isotropic paper sheets; reliably reflecting an image-based description of the hierarchical, macroscopic-to-nanoscopic scale organization of such sheets and of their constituents – is briefly presented and validated

Introduction

Transversely isotropic paper sheets exhibit a distinctive, hierarchical, multiscale organization[1,2,3,4]. At a length scale of few tens of nanometers, highly aligned aggregations of circular cylindrical, molecular crystalline cellulose are embedded into a contiguous matrix made of molecular amorphous cellulose to constitute the cellulose fibril[2,3]. *At approximately the same length scale, clusters of spherical, molecular hemicellulose and lignin, as well as of water with extractives, indiscriminately interpenetrate each ot*her to form the polymer blend[2,3]. Further up, at a length scale of few micrometers, uniformly distributed assemblages of circular cylindrical cellulose fibrils are helically embedded into an adjacent polymer blend matrix to build-up the pulp fiber wall[2,3]. Finally, at a length scale of few hundreds of micrometers, oblate spheroidal pores, mirroring the in-plane orientation and out-of-plane (cross-sectional)

Gohinho, P., Bader, T., Eberhardsteiner, J. & Hemmlich, C.

shape of planarly, uniformly oriented collections of pulp fibers[1,2,3,4] of elliptical cylindrical shape[2,3,4], arbitrarily combine to materialize as a transversely isotropic paper sheet.

Model

In the framework of continuum micromechanics, we define – inspired by the hierarchical, multiscale organization of the paper sheets described above – polymer blend, cellulose fibril, pulp fiber, and paper sheet representative volume elements (or "RVEs") at appropriate length scales; before we derive expressions for the theoretically ("micromechanically") predicted (or "homogenized") stiffness tensors of respective materials, as a function of properties of corresponding RVE constituents (or "phases") [1,2,3,4]. For illustration, we present the homogenized stiffness tensor of a paper sheet, $\mathbb{C}_{pap}^{hom}$, as a function of the properties of its RVE constituents – pulp fiber and pore phases[1,2,3,4]:

$$\mathbb{C}_{pap}^{hom} = \left[{}^{V}f_{pul}^{RVEpap} \frac{1}{2\pi} \int_{\varphi=0}^{2\pi} \mathbb{C}_{pul}(\varphi) : \mathbb{A}_{pul}^{0}(\varphi)d\varphi + {}^{V}f_{por}^{RVEpap} \mathbb{C}_{por} : \right.$$
$$\left. \mathbb{A}_{por}^{0} \right] : \left[{}^{V}f_{pul}^{RVEpap} \frac{1}{2\pi} \int_{\varphi=0}^{2\pi} \mathbb{A}_{pul}^{0}(\varphi)d\varphi + {}^{V}f_{por}^{RVEpap} : \mathbb{A}_{por}^{0} \right]^{-1} \tag{1}$$

whereby $\mathbb{C}_{pul} = \mathbb{C}_{pul}^{hom}$ denotes the stiffness tensor associated to the transversely isotropic pulp fiber phase within the paper sheet RVE; $\mathbb{C}_{por} \approx 0$ corresponds to the (vanishing) stiffness tensor associated to the air-filled (or "hollow") pore phase within the paper sheet RVE; and ${}^{V}f_{pul}^{RVEpap}$ as well as ${}^{V}f_{por}^{RVEpap}$ read as the volume fractions of pulp fiber and pore phases, respectively, each with respect to the paper sheet RVE, which are identical to ${}^{V}f_{pul}^{pap}$ and ${}^{V}f_{por}^{pap}$, i.e. to the same fractions with respect to the paper sheet itself. The fourth-order tensors $\mathbb{A}_{pul}^{0}$ and $\mathbb{A}_{por}^{0}$ relate to solutions of so-called fictitious-matrix-inclusion problems[5,6], and are denoted as the Eshelby-Laws strain concentration tensors associated to the pulp-fiber-phase-like and the pore-phase-like inclusions, respectively, each with respect to the (here "self-consistent", polycrystalline, transversely isotropic) paper-sheet-like fictitious matrix of stiffness $\mathbb{C}_{pap}^{hom}$ (and compliance $\mathbb{D}_{pap}^{hom} = \mathbb{C}_{pap}^{hom,-1}$) [1,2,3,4]. They read as:

$$\mathbb{A}_{pul}^{0}(\varphi) = \left[\mathbb{I} + \mathbb{P}_{pul}^{0}(\varphi) : \left(\mathbb{C}_{pul}(\varphi) - \mathbb{C}_{pap}^{hom,3,4} \right) \right]^{-1} \tag{2}$$

$$\mathbb{A}_{por}^{0} = \left[\mathbb{I} + \mathbb{P}_{por}^{0} : \left(\mathbb{C}_{por} - \mathbb{C}_{pap}^{hom} \right) \right]^{-1} \tag{3}$$

with $\mathbb{I}$ as the identity tensor; and with $\mathbb{P}_{pul}^{0}$ as well as $\mathbb{P}_{por}^{0}$ as the Hill morphology tensors associated to the elliptical cylindrical, pulp-fiber-phase-like[2,3,4] as well as to the spheroidal, pore-phase-like[1,2,3,4] inclusions, respectively, each with respect to the

abovementioned paper-sheet-like fictitious matrix of stiffness $\mathbb{C}_{pap}^{hom}$. These latter tensors are obtained by specification of $\mathbb{P}_{ell}^{ani}$ as well as $\mathbb{P}_{spd}^{tra}$, which denote the Hill morphology tensors associated to an elliptical cylindrical inclusion embedded into an anisotropic matrix[7], as well as to a spheroidal inclusion embedded into a transversely isotropic fictitious matrix[8.] Moreover, we extend earlier work of our own on the yield strength of paper sheets[1], and derive the following expression for their in-plane, ultimate uniaxial tensile and compressive strength[2,4]:

$$\mathfrak{F}(\Sigma) = \begin{cases} \max_{\varphi} \left(\underline{n}_{pul}(\varphi) \cdot \mathbb{B}_{pul}^{pap}(\varphi) : \Sigma \cdot \underline{n}_{pul}(\varphi) \right) - \sigma_{pul}^{uut} \leq 0 \\ \min_{\varphi} \left(\underline{n}_{pul}(\varphi) \cdot \mathbb{B}_{pul}^{pap}(\varphi) : \Sigma \cdot \underline{n}_{pul}(\varphi) \right) + \sigma_{pul}^{uuc} \geq 0 \end{cases} \tag{4}$$

with $\underline{n}_{pul}(\varphi)$ the in-plane pulp fiber direction; $\Sigma_{pap,in-plane}^{hom}$ the in-plane paper sheet stress tensor (of unknown magnitude); σ_{pul}^{uut} and σ_{pul}^{uut} the pulp fiber ultimate uniaxial tensile and compressive strength, respectively; and $\mathbb{B}_{pul}^{pap}(\varphi)$, the stress concentration tensors, reading as:

$$\mathbb{B}_{pul}^{pap}(\varphi) = \mathbb{C}_{pul}(\varphi) : \mathbb{A}_{pul}^0(\varphi) : \left[{}^V f_{pul}^{RVEpap} \frac{1}{2\pi} \int_{\varphi=0}^{2\pi} \mathbb{A}_{pul}^0(\varphi) d\varphi + {}^V f_{por}^{RVEpap} : \mathbb{A}_{por}^0 \right]^{-1} : \mathbb{D}_{pap}^{hom}$$
$$\tag{5}$$

Model validation

Validation of our model is done in five steps. First, we use hundreds of experimental values on 1) mass fractions of cellulose, hemicellulose, lignin, and extractives with respect to softwood-based, unbeaten, chemical pulps; 2) mass crystallinity index of cellulose and moisture content of paper sheets, derived from the same type of pulps; 3) true mass densities of crystalline cellulose, amorphous cellulose, hemicellulose, lignin, extractives, and water; as well as 4) bulk mass density of paper sheets derived from the aforementioned type of pulps, to determine all volume fractions[2,3]. Second, we resort to theoretical and experimental values, to determine a triclinic (i.e. anisotropic) stiffness tensor for crystalline cellulose, as well as isotropic stiffness tensors for amorphous cellulose, hemicellulose, lignin, and water with extractives; all nanoscopic scale phases considered as "universal" constituents of paper sheets[2,3]. Third, we appropriately upscale these latter stiffness tensors to determine the homogenized stiffnesses of a cellulose fibril and of a polymer blend, before using these latter tensors, as well as dozens of experimental values on the mesofibril angle of softwood-based, unbeaten, chemical pulp fibers, to determine the homogenized stiffness of a mean, softwood-based, unbeaten, chemical pulp fiber[2,3]. Fourth, we employ hundreds of experimental values on the width and height, as well as on the cross-sectional area and collapse degree of such fibers[2,3] to determine the small-to-large-diameter ratio of a mean, softwood-based, unbeaten, chemical pulp fiber of

elliptical cylindrical shape – a ratio that is set equal for both pulp fiber and pore phases for symmetry reasons – before we use the aforementioned pulp fiber homogenized stiffness and a pore phase of vanishing stiffness, to determine the homogenized stiffness, as well as the associated in- and out-of-plane moduli, of the corresponding paper sheet, all as function of the latter's porosity[2,3]. In addition, we make use of two experimental values for the in-plane, ultimate uniaxial strength of paper sheets, one for tension and one for compression, to extrapolate the corresponding failure stresses of pulp fibers under tension and compression, before using these two back-fitted values to determine the homogenized, in-plane, ultimate uniaxial tensile and compressive strengths, of the corresponding paper sheet, also as function of the latter's porosity[2,4]. Fifth, we plot the abovementioned predictions as well as hundreds of respective, experiments (see Figures 2.6 and 2.7). Visual inspection of such plots shows that the model predictions for both the in- and out-of-plane moduli, as well as the in-plane, ultimate uniaxial strength of such paper sheets, agree remarkably well with corresponding experiments, as quantified by prediction errors below 5%, respectively[2,3,4].

Conclusions

We have proposed and validated groundbreaking, multiscale, continuum-micromechanics-based theoretical models for the elasticity as well as the ultimate strength of paper sheets. Predictions as a function of paper sheet porosity agree outstandingly well with a large amount of independent experiments. Further exploitation of such theoretical models could lead to more intelligent routines in production, research, development, as well as use of paper, with far reaching implications in terms of a more sustainable, future society.

Acknowledgements

Figure 2.6. Theoretically (micromechanically) predicted relations between porosity and – a) in-plane elastic modulus; b) out-of-plane elastic modulus; c) in-plane shear modulus; as well as d) out-of-plane shear modulus – of paper sheet made of mean, softwood-based, unbeaten, chemical pulp fibers; versus respective, experimentally determined relations[2,3]
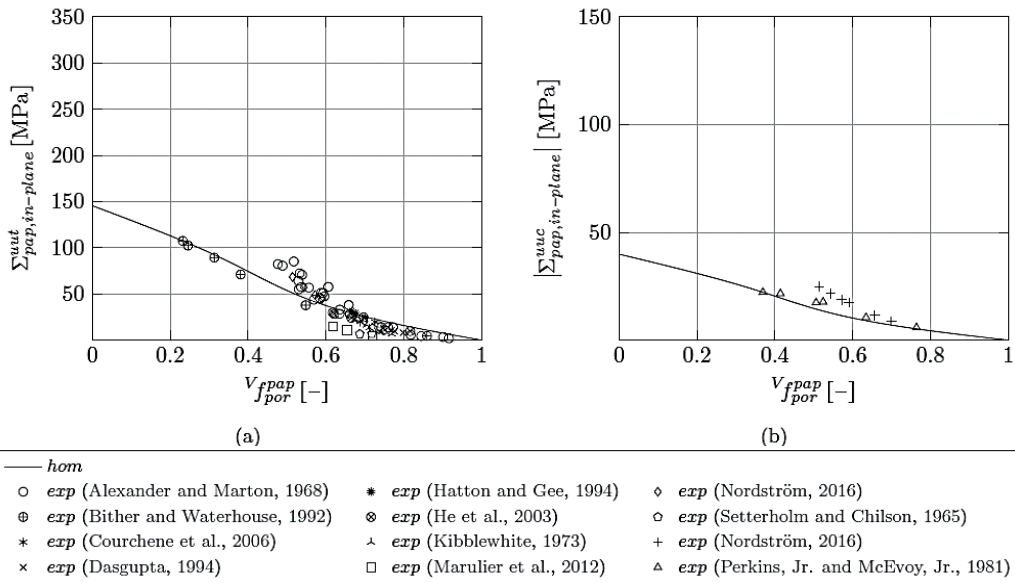
Figure 2.7. *Theoretically (micromechanically) predicted relations between porosity and – a) in-plane, ultimate uniaxial tensile strength; as well as b) in-plane, ultimate uniaxial compressive strength – of paper sheet made of mean, softwood-based, unbeaten, chemical pulp fibers; versus respective, experimentally determined relations*[2,4]

References

1. Godinho, P. M. J., Jajcinovic, M., Wagner, L., Vass, V., Fischer, W. J., Bader, T. K., ... & Hellmich, C. (2019). A continuum micromechanics approach to the elasticity and strength of planar fiber networks: Theory and application to paper sheets. *European Journal of Mechanics-A/Solids*, *75*, 516-531.

2. Godinho, P.M.J. (2020). Multiscale, Continuum Micromechanics of Paper: Elasticity and Strength. PhD Thesis. Technical University of Vienna (submission imminent), Austria

3. Godinho, P. M. J, Eberhardsteiner, J., & Hellmich, C. (2020) Towards a general, multiscale, continuum-micromechanics-based model for the elasticity of transversely isotropic paper sheets – powerful validation by means of nearly a thousand multiscale experimental measurements. Comput Method Appl M (submission imminent)

4. Godinho, P. M. J., Bader, T.K., &, Hellmich, C. (2020) The in-plane, ultimate uniaxial strength of paper sheets: a continuum micromechanics approach. Compos Sci Technol (submission imminent)

5. Eshelby, J. D. (1957). The determination of the elastic field of an ellipsoidal inclusion, and related problems. *Proceedings of the royal society of London. Series A. Mathematical and physical sciences*, *241*(1226), 376-396.

6. Laws, N. (1977). The determination of stress and strain concentrations at an ellipsoidal inclusion in an anisotropic material. *Journal of Elasticity*, *7*(1), 91-97.

7. Laws, N. (1977). A note on interaction energies associated with cracks in anisotropic solids. *Philosophical magazine*, *36*(2), 367-372.

8. Kachanov, M., & Sevostianov, I. (2018). *Micromechanics of materials, with applications* (Vol. 249). Cham: Springer. ISBN 978-3-319-76203-6

General mean-field theory to describe compression of thick porous fibre networks

Jukka Ketoja[a], Sara Paunonen[a], Elina Pääkkönen[a], Tiina Pöhler[a], Tero Mäkinen[b], Juha Koivisto[b], & Mikko Alava[b]

[a]*VTT Technical Research Centre of Finland Ltd, Espoo, Finland*
[b]*Aalto University, Espoo, Finland*

Corresponding author: *Jukka Ketoja <jukka.ketoja@vtt.fi>*

Keywords: Fibre network, compression, stress, strain, image analysis, acoustic emission

Summary

We have developed a new theory to analyse the compression-stress behaviour of foam-formed fibre materials. The experimental samples included different fibre and fines types, and they were processed with several different foaming agents. The mechanical testing was supported by simultaneous high-speed imaging and acoustic emission measurements. The theory described well the average stress behaviour upto c.a. 50% compression, despite different densities and raw materials of the samples. Moreover, the relative number of acoustic events followed the predicted proportion of buckled fibre segments for varied strain.

Introduction

Foam forming[1,2,3,4] enables the production of lightweight fibrous materials for various applications ranging from insulation and filtering to cushioning. The density of the dried material is controlled by furnish and the stability of aqueous carrier foam that is used to build up the fibre network. Typical material densities range from 20 kg/m^3 to 120 kg/m^3 in the absence of wet pressing. The pore structure can be to some extent modified by varying the mean bubble size[5]. The mechanical compression properties[6] of the material are important in many applications.

We have developed a new theory to describe the stress-strain behaviour of low-density random fibre networks under compression[7]. The theory assumes that besides bending, a part of fibre segments undergo sudden buckling failures, which effectively act as

Ketoja, J., Paunonen, S., Pääkkönen, E., Pöhler, T., Mäkinen, T., Koivisto, J., & Alava, M.

"stress sensors" during compression. We have verified predictions of the theory with compression tests on more than a hundred foam-formed trials points with varied material density and raw materials. As to the applicability of the theory, the production method as such is, however, not essential. The only requirement is that the material density is low enough so that buckled fibre segments can bend inside the network without immediate contacts with neighbouring fibres.

Model

Material compression is expected to cause significant axial stress in fibres in well-bonded networks. This takes place either as an average stress or as a peak stress outside the neutral plane of a bended heterogeneous segment. Our theory assumes that at strain ϵ, fibre segments longer than $a_0 s(\epsilon)$ (a_0 is the mean segment length) buckle within the open porous structure. Based on the exponential segment-length distribution of a random fibre network, we can derive an equation for the function s [7]:

$$[s(\epsilon) + 1]\exp[-s(\epsilon)] = \epsilon. \tag{1}$$

The mean compressive stress σ is calculated by assuming that the critical load for a buckling is proportional to the inverse square of segment length [7]:

$$\sigma(\epsilon) = \frac{\sigma_0}{[s(\epsilon)]^2}. \tag{2}$$

Here the constant σ_0 sets the absolute level of compression stress, while the stress-compression behaviour is described by the same function $s(\epsilon)$ for all low-density random fibre networks with exponentially distributed segment lengths.

Experimental verification

The fibre materials in our experiments consisted of chemical, mechanical and regenerated cellulose fibres of varied dimensions[7]. They were processed with several foaming agents and added fine particles[8], such as nanocelluloses or other types of fines. The mechanical testing was supported by simultaneous high-speed imaging[7] and acoustic emission measurements[9] to reveal underlying mechanisms and domains in which the theory was applicable.

For most of the studied samples, we found the above simple mean-field theory with one fitting parameter σ_0 to describe well the measured stress-strain behaviour at moderate, from 10% to 50% compression levels, for which strain over the whole network is quite uniform (see Figure 2.8). Moreover, high-speed imaging during compression showed abrupt bucklings and local movements of fibres under the applied stress. However, addition of fines in the furnish led to deviations from the theoretical prediction especially at low compression levels[8].
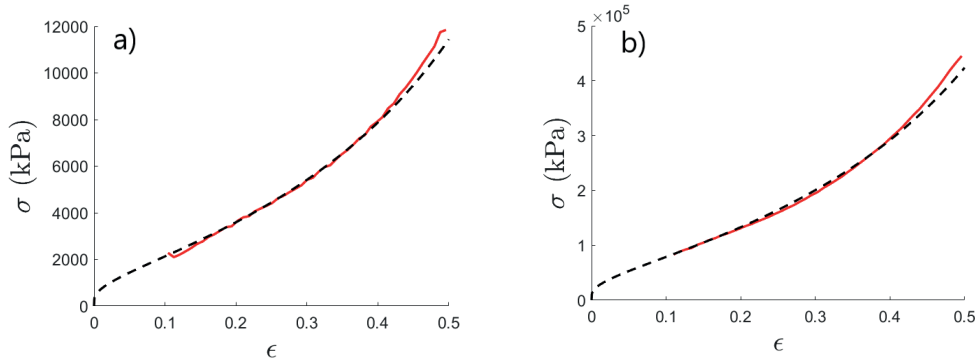
Figure 2.8. Comparison of measured (red) and predicted (dashed black) stress-strain curves of foam-formed fibre networks in the strain interval of 0.1−0.5. The measured curve is an average of five parallel compression measurements with sample area of 5 x 5 cm² and thickness of c.a. 20 mm. a) Bleached softwood kraft-fibre sample with density of 46 kg/m³ (Berol surfactant). b) CTMP sample with density of 122 kg/m³ (SDS surfactant).

In cyclic measurements, we observed significant acoustic emission only when the compressive strain exceeded the previous strains (see Figure 2.9)[9]. Because fibres bend also during unloading, this type of deformation cannot be the source of the recorded acoustic events. In fact, the number of acoustic events was directly related to the predicted proportion of buckled segments for the varied strain. Beyond c.a. 50% compression, the cumulative acoustic energy grew rapidly suggesting a crossover to collective avalanches in the network. At the same time, the compression-stress behaviour began to deviate from the mean-field prediction.
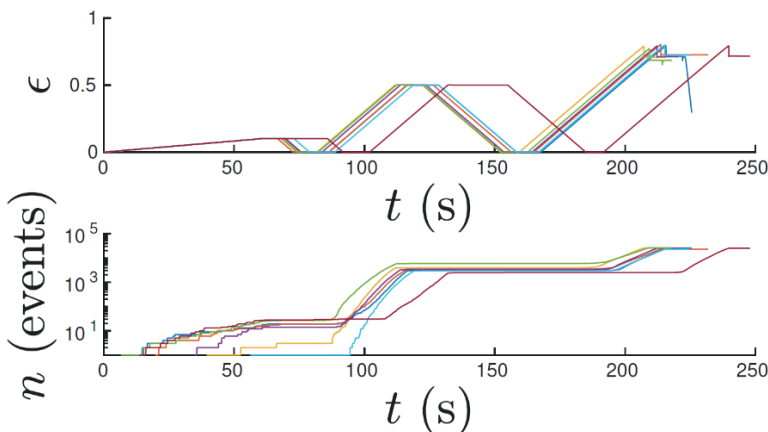
Figure 2.9. Measured number of acoustic events n in a cyclic compression test with ten parallel measurements for a CTMP sample. Significant acoustic emission is observed only when the previous compression levels are exceeded.

Ketoja, J., Paunonen, S., Pääkkönen, E., Pöhler, T., Mäkinen, T., Koivisto, J., & Alava, M.

Conclusions

The new theory, based on the statistical distribution of fibre-segment lengths, is able to predict relative stress increase for a vast range of compressed fibre materials. Moreover, by assuming that acoustic events originate from segment bucklings, the theory describes correctly the relative number of these events, as well.

Acknowledgements

References

1. Radvan, B., & Gatward, A. P. J. (1972). Formation of wet-laid webs by a foaming process. *Tappi*, *55*(5), 748.

2. Lehmonen, J., Jetsu, P., Kinnunen, K., & Hjelt, T. (2013). Potential of foam-laid forming technology in paper applications. *Nordic Pulp & Paper Research Journal*, *28*(3), 392-398.

3. Alimadadi, M., & Uesaka, T. (2016). 3D-oriented fiber networks made by foam forming. Cellulose 23, 661–671.

4. Burke, S. R., Möbius, M. E., Hjelt, T., & Hutzler, S. (2019). Properties of lightweight fibrous structures made by a novel foam forming technique. *Cellulose*, *26*(4), 2529-2539.

5. Al-Qararah, A. M., Ekman, A., Hjelt, T., Ketoja, J. A., Kiiskinen, H., Koponen, A., & Timonen, J. (2015). A unique microstructure of the fiber networks deposited from foam–fiber suspensions. *Colloids and Surfaces A: Physicochemical and Engineering Aspects*, *482*, 544-553.

6. Alimadadi, M., Lindström, S. B., & Kulachenko, A. (2018). Role of microstructures in the compression response of three-dimensional foam-formed wood fiber networks. *Soft Matter*, *14*(44), 8945-8955.

7. Ketoja, J. A., Paunonen, S., Jetsu, P., & Pääkkönen, E. (2019). Compression strength mechanisms of low-density fibrous materials. *Materials*, *12*(3), 384.

8. Pöhler, T., Ketoja, J.A., Lappalainen, T., Luukkainen, V.-M., Nurminen, I., Lahtinen, P., & Torvinen, K. (2020) On the strength improvement of lightweight fibre networks by polymers, fibrils and fines. Cellulose, https://doi.org/10.1007/s10570-020-03263-x.

9. Mäkinen, T., Koivisto, J., Pääkkönen, E., Ketoja, J.A., Alava, M.J. (2020). Crossover from mean-field compression to collective phenomena in low-density foam-formed fiber material. Submitted to Soft Matter.

Tuesday 1.9.2020 at 10:00 - 12:00

Session 2B

Novel measurement methods

Session chair: Katariina Torvinen

The use of ATR-IR spectroscopy to determine the anisotropy parameters of the structure of materials based on plant fibers

Yakov Kazakov, Anastasiia Romanova, & Dmitry Chukhchin

Northern (Arctic) Federal University, Arkhangelsk, Russia

Corresponding author: *Yakov Kazakov <j.kazakov@narfu.ru>*

Keywords: Pulp, paper, ATR-IR spectroscopy, anisotropy, fiber orientation

Summary

The dependence of the changes in the ATR IR spectra of anisotropic bleached pulp samples and cuts of wood in relation of the angle of orientation of the sample relative to the optical axis of the spectrometer was established. The method is proposed for measuring the degree of local anisotropy and the average local orientation angle of fibers in a sample.

Introduction

Paper, market pulp and wood are anisotropic materials. They are heterogeneous in their composition and structure and consist of plant fibers. The fibers have a complex multilevel structure where cellulose microfibrils in cell wall are basic elements. The strength of cellulosic materials depends on the strength of chemical and hydrogen bonds. These bonds act inside the macromolecules and in the intermolecular cellulosic crystallites. Interfibrillar bonds are located in the fiber wall, interfiber connections – into paper sheet or wood. Applying a mechanical load causes a change of energy of the bonds and, in a limiting case, - their destruction.

ATR-IR spectroscopy allows estimating bonds energy and the fractional ratio of the bonds of various energies in the cellulose-containing sample. When applying a mechanical load to the sample, it occurs a change in the intensity and width of absorption bands of spectrum, as well as a change in their position[1]. However, experiments with samples cut out at different angles to the machine direction showed

that the base spectra (spectra at zero load) are different[2]. Further comparison of the changes occurring in the spectra were difficult.

Results

We have conducted an experiment which aim was to establish how the angle between the longitudinal axis of sample and the optical axis of the spectrometer affects changes in spectra. We changed the analysis conditions by rotating the sample strip at an angle between the axes in the range of 0 ... 360 degrees with spacing 10°.

As test samples we used strips from cellulose-containing materials of 15 mm wide and radial cuts of wood of 0.1 mm thickness. The strips were cut out from sheets of hardwood kraft bleached viscose pulp and from laboratory anisotropic paper samples. We made the paper samples from the blend of kraft bleached hardwood (70%) and softwood (30%) pulp by means of TechPap SAS dynamic sheet former[3]. The radial wood cuts were got from aspen, birch and pine.

To do measurements we used Vertex 70 FTIR spectrometer (Bruker, Germany) with GladiATR attachment (Pike Tech., USA). The ATR-crystal material is an artificial diamond. IR-radiation has a strict polarization; the depth of its penetration is 10-20 microns. The recording range of the spectra was 4000-400 cm^{-1}, the resolution - 4 cm^{-1} with 128 parallel scans of the sample.

To process the obtained spectra we used the application software[4] that allows analyzing changes in a spectrum. In addition, this program makes it possible to explore the dependency of ratio of absorption intensity of the bands correspond to various functional groups on analysis conditions.

As a quantitative characteristic of watching changes in the spectra, we took ratio of the optical bands – D_{933}/D_{489} – at the wave number of 933 cm^{-1} and 489 cm^{-1}. The reason was that this ratio showed the greatest sensitivity to a rotation angle of the sample.

It was found out, there were changes of a periodic nature in the spectra, Figures 2.10 and 2.11.
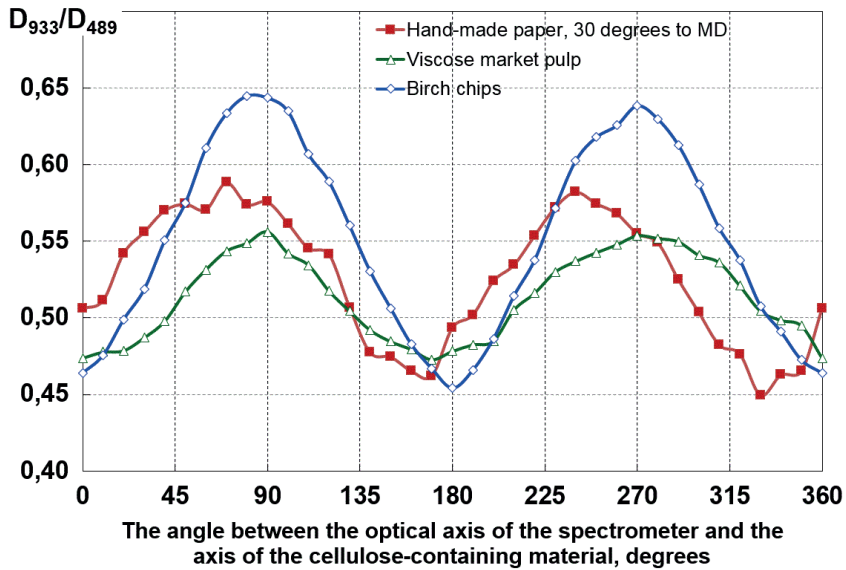
Figure 2.10. Changes in spectral characteristics of various materials based on plant fibers.
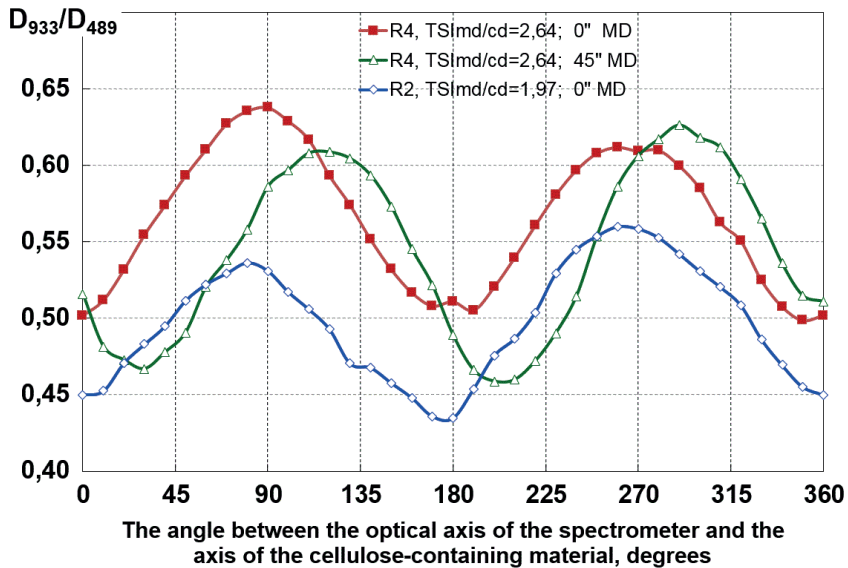
Figure 2.11. Changes in spectral characteristics of hand-made anisotropic samples.

The periodic phenomena were approximated by harmonics of the form:

$$Y = A \sin(Bx + \phi) + C,$$

where A – amplitude; B – frequency, $B = 2$; C – Y-axis displacement and ϕ – phase are coefficients of the harmonics.

The approximation results for laboratory anisotropic paper samples are presented graphically in Figure 2.12, calculation results of the harmonic coefficients – in Table 2.1, the value of ϕ – parameter is shown in degrees after converting from radians.
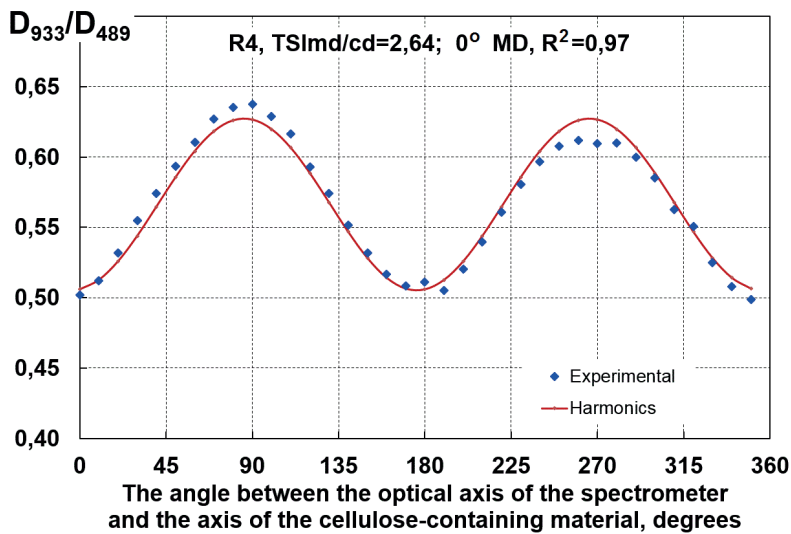
Figure 2.12. Approximating experimental data by harmonics

Table 2.1. Harmonic coefficients of anisotropic samples calculated in the analysis of ATR-IR Spectra

Material	Sample	Cutout angle to MD	Coefficients of harmonics			R^2
			A	Abs (ϕ)	C	
Wood	Pine	0	0,0847	4,0	0,639	0,947
	Birch	0	0,0870	2,0	0,553	0,992
	Aspen	0	0,0609	2,0	0,508	0,985
Market pulp	Viscose pulp sheet	0	0,0368	0,8	0,514	0,903
Hand-made paper	$TSI_{MD/CD}$ = 1,97	0°	0,0476	6,0	0,4987	0,846
		30°	0,0404	27,8	0,5391	0,783
		60°	0,0592	52,0	0,5387	0,863
		90°	0,0507	79,0	0,5143	0,850
	$TSI_{MD/CD}$ = 2,64	0°	0,0610	4,0	0,5662	0,970
		30°	0,0744	26,0	0,5443	0,957
		45°	0,0666	45,0	0,5581	0,929

Outcomes we got during experiment have shown:

A-coefficient (amplitude) for wood was higher than for paper, and higher for laboratory anisotropic paper samples than for market sheet pulp;

ϕ-coefficient (phase) for wood was close to zero, and for anisotropic paper samples – close to the angles they were cut out at (0, 30, 45, 60 and 90°) to the machine direction;

A-coefficient was higher for the samples with a greater degree of anisotropy ($TSI_{MD/CD}$ = 2.64), its average value is A_{av} = 0.0674, than for the samples with a lower degree of anisotropy ($TSI_{MD/CD}$ = 1.97), A_{av} = 0.0495; the values of ϕ-coefficient were close to the cutout angles of the tested samples. Deviations has been associated with local heterogeneity of fiber orientation in the structure.

The obtained results have confirmed that wood, as a strictly anisotropic material, had a maximum degree of structure anisotropy, market viscose hardwood bleached pulp – a minimum one, and anisotropy degree of paper structure can be varied by changing the formation parameters and paper composition.

Thus, *A*-coefficient can be used to quantify the degree of local anisotropy of a sample, ϕ-coefficient – to quantify the angle of preferential orientation of fibers in a sample.

Conclusions

1. The method to measure ATR-IR absorption spectra with the subsequent determination and analysis of changes in the spectra has been developed on anisotropic samples of wood and paper.

2. It has been shown that the dependency of D_{933}/D_{489} on an angle between the optical axis of the spectrometer and the longitudinal axis of the sample is described by the harmonic whose coefficients characterize a sample structure.

3. The proposed method allows determining quantitatively the anisotropy degree of and the average angle of fibers orientation in a cellulose-containing sample. To obtain calibration dependencies, additional series of experiments are needed.

Acknowledgements

References

1. Chukhchin, D., Mayer, L., Kazakov Y., & Ladesov, A. (2017). The use of IR spectroscopy to study the stress state of cellulosic materials. Proc 4th Int Conf in memory of Prof Valery Komarov. Northern (Arctic) Federal University (named after M.V. Lomonosov), Arkhangelsk, Russia, Sep-14–16, p. 86–91.

2. Romanova, A.N., Chukhchin D.G., & Kazakov Y.V. (2019). The study of the anisotropy of cellulose-containing materials by the ATR method of IR spectroscopy. Proc of the VIIIth Int Conf in Physicochemistry of plant polymers. Northern (Arctic) Federal University (named after M.V. Lomonosov), Arkhangelsk, Russia, July 1-5, p.118–122.

3. Kazakov, Y.V. (2013). Effect of formation conditions of hand-made anisotropic paper samples on their structure and deformation behavior. 19th Int Symp in the field of pulp, paper, packaging and graphics, Zlatibor, Serbia, June 25-28, p. 69–72.

4. Certificate Number 2018661852 of Russian Federation. Certificate of state registration of the computer program. Program for correlation analysis of a series of IR spectra / Chukhchin, D.G. The applicant and rights holder NArFU (RU). Number 2018616255; appl. 19.06.2018; publ. 20.08.2018, the Register of Computer Programs. 1 p.

Positron annihilation: A tool for paper research

Laura Resch[a], Anna Karner[a], Wolfgang Sprengel[a], Roland Würschum[a], & Robert Schennach[b,c]

[a]*Institute of Material Physics, Graz University of Technology, Graz, Austria*
[b]*Institute of Solid State Physics, Graz University of Technology, Graz, Austria*
[c]*CD-Laboratory for mass transport through paper, Graz University of Technology, Graz, Austria*

Corresponding author: *Robert Schennach <*robert.schennach@tugraz.at*>*

Keywords: Positron annihilation, pore structure, water intake, positron annihilation lifetime spectroscopy of cellulose materials during moisture intake

Summary

In this study the time evolution of the mean positron lifetime was measured in-situ during moisture intake in a paper sample. In parallel, the moisture intake was measured by monitoring the mass of the sample. The results show that the mean positron lifetime not only depends on the water content in the sample but varies on a longer timescale. This suggests that the mean positron lifetime not only indicates an increasing water content but also changes of the pore structure in the sample and variations of the chemical environment of the water molecules due to adsorption and absorption.

Both, the porous structure of paper as well as its strong interaction with water are prime properties that make paper such a unique material. While the porous structure of paper and the interaction of paper with water have been studied for a long time, there are still open questions left. Positron annihilation spectroscopy has been widely used to study pore structures in various materials so far. In this work we show the first results of positron annihilation spectroscopy on paper samples as a function of water intake from the gas phase in an attempt to get more insight into the changes of the pore structure during this process.

Positron annihilation lifetime spectroscopy is a specific and sensitive tool for the investigation of open volume defects and porosity of materials. A positron from a radioactive source (in this case ^{22}Na) is injected into the sample, where it annihilates

with an electron, emitting two γ-quants. The positron lifetime in the material is measured as time difference between the detection of a start γ-quant (β-decay of ^{22}Na) and the annihilation γ-quant. It includes sensitive information on the defect structure but is also influenced by the chemical environment of the positron annihilation site[1]. Prior to annihilation it is also possible that positron and electron form positronium with a significantly enhanced lifetime. This case indicates the presence of pores or direct interaction with water. A spectrum from which characteristic lifetime information is extracted consists of about 10^6 annihilation events.

The experimental setup of a positron lifetime spectrometer positioned on top of a closed plastic box is shown in Figure 2.13. The box includes a Petri dish either containing water (to reach 90% relative humidity at room temperature) or silica gel (to dry the sample again). The paper sample was folded 10 times to squares of around 1 cm² and placed onto both sides of the ^{22}Na source so that positrons emitted from the source to a major extend annihilate in the sample.
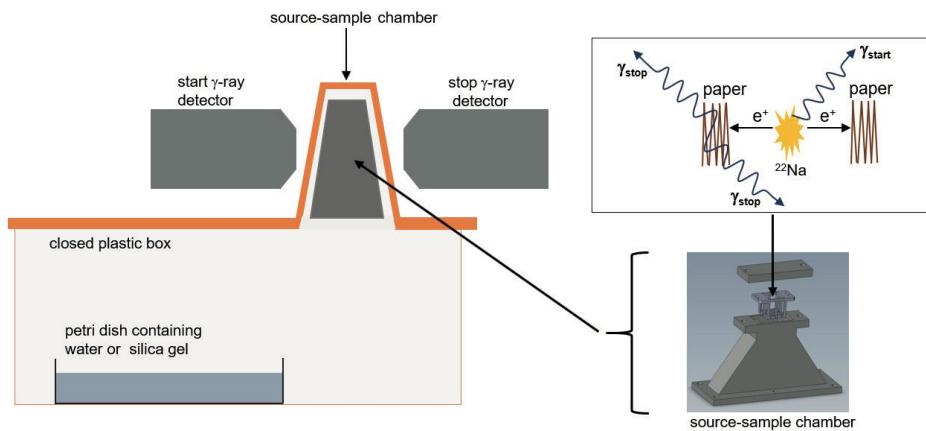
Figure 2.13. Schematic sketch of the positron annihilation lifetime spectroscopy set-up
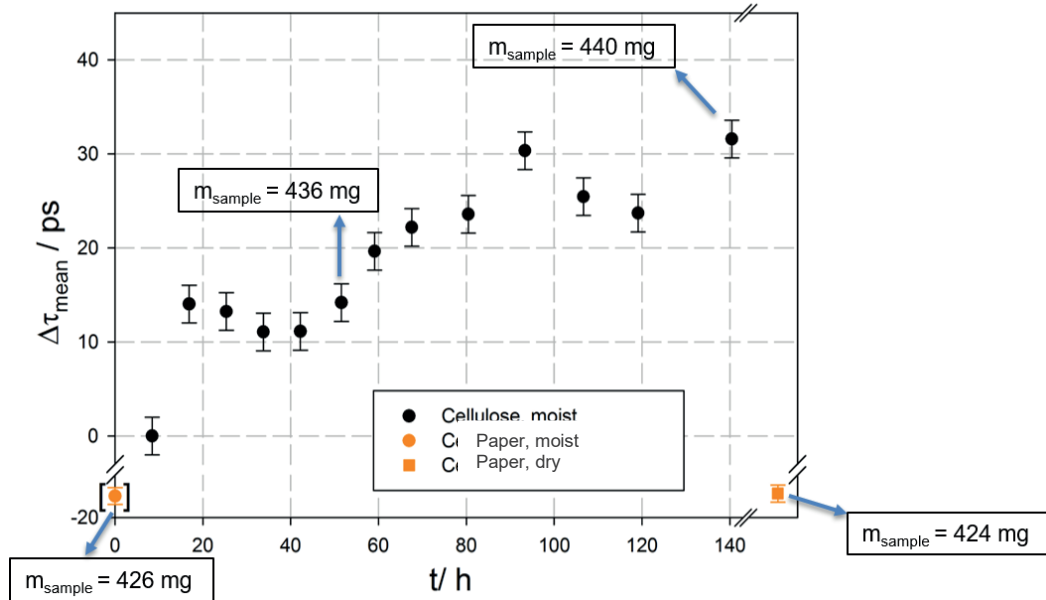
Figure 2.14. Changes of the mean positron lifetime, $\Delta\tau_{mean}$, as a function of time, t, during water intake from the gas phase. The orange point indicates the dry state, the orange square indicates the dried state of the same sample after the measurement. At selected times the mass of the sample was measured as indicated in the Figure.

First results of the study are shown in Figure 2.14. As a reference, before the measurement in humid atmosphere, the paper sample was measured in its "dry" state (see Figure 13, the petri dish in the box did not contain any water). On the other hand, for the measurements in humid atmosphere the petri dish was filled with water.

In the beginning ($t \leq 20$ h) the change of the mean positron lifetime compared to the dry sample $\Delta\tau_{mean}$ increases with time in humid atmosphere until it reaches a small plateau in the time interval between 20 h and 40 h. Subsequently, $\Delta\tau_{mean}$ increases again significantly until the end of the measurement ($t=140$ h). The overall increase of $\Delta\tau_{mean}$ after the first plateau ($40\ h \leq t \leq 140\ h$) is even higher than before ($t \leq 20$ h) which is especially interesting regarding the fact that the change of the mass of the sample Δm due to water intake seems to be more or less saturated already after 20 h.

After the measurement in humid atmosphere, the petri dish was filled with silica gel instead of water in order to dry the sample again. The measurement after drying the sample led to the same mean positron lifetime as for the dry sample, within the error of this method.

The observed increase of the mean positron lifetime can be due to several reasons: (i) At first this may be due to enhanced Ps formation probability arising from the adsorption of water at the surfaces of the cellulose pores. An increase in pore size due

Resch, L., Karner, A., Sprengel, W., Wurschum, R., & Schennach, R.

to water uptake can also lead to this behavior (ii). τ_{mean} – increase may further be caused by (iii) changes of the chemical surroundings of the water molecules due to absorption or (iv) upon water penetration into deeper pores of the sample.

The first increase ($t \leq 20$ h) of τ_{mean} is considered most likely to be due to adsorption of water molecules and an increase of pore size distribution in the paper sample (i, ii). The τ_{mean} increase at longer times (t ≥ 40 h) may be an indication for the processes (iii) and (iv), i.e., absorption or penetration into deeper pores, where process (ii) can also not be excluded.

These first results are very promising to establish positron annihilation for studies of characteristic changes of the microstructure as well as for monitoring processes in paper upon moisture intake. To distinguish possible different processes these studies are now extended to papers with varying cellulose to lignin ratios.

Acknowledgements

References

1. Dupasquier, A., & Manninen, M. J. (1979). Positrons in solids (Vol. 12). P. Hautojärvi (Ed.). Berlin: Springer-Verlag, Grmany

Adsorption of molecules on cellulose films

Elias Henögl[a,b], & Robert Schennach[a,b]

[a]*Institute of Solid State Physics, Graz University of Technology, Austria*
[b]*CD-Laboratory for Mass Transport through Paper, Graz University of Technology, Graz, Austria*

Corresponding author: *Robert Schennach <*robert.schennach@tugraz.at*>*

Keywords: Temperature programmed desorption, adsorption, desorption, cellulose films, n-decane, methanol

A study of the adsorption behavior of n-decane and deuterated methanol on cellulose films investigated by temperature programmed desorption (TPD)

In this work we present how TPD can be used to study the adsorption behavior of organic molecules (such as n-decane and deuterated methanol) on cellulose films produced from regenerated TMSC (trimethylsilyl cellulose). We show how an approximation of adsorption energy can be derived in order to make the first steps of gaining insight into the influence of adsorption to the transport kinetics of molecules through a paper-based system. We discuss further how cellulose thin films modified by ASA (alkenyl succinic anhydrides) can be distinguished from pure cellulose films by comparing TPD fingerprints.

Temperature programmed desorption (TPD) is one of the oldest methods developed in surface science to probe the interaction between gas molecules and clean surfaces. Its theoretical background is based on the assumption, that all processes where a molecule adsorbs on a surface from the gas phase are reversible and in *detailed balance*. The fundamentals of detailed balance were stated in the field of statistical mechanics inter alia in the discussion of the chapter "Boltzmann's H-Theorem and the Condition of Equilibrium" by R. C. Tolman[1]. Applying this concept on an adsorption/desorption process means, that for a given <u>constant</u> population adsorbed on a surface in thermodynamic equilibrium, each population increase by a microscopic event of a certain adsorption process is assumed to be balanced out by an equal (but reversed) process of a desorption event. Each adsorption process can then be seen as a reversed desorption process and the other way around. This fundamental

assumption and its effects have been described and investigated by Cardillo/Balooch/Stickney[2] and Steinrück/Rendulic/Winkler[3] It is essential, because it allows to learn about adsorption behavior by investigating only desorption processes.

Nevertheless, the final equilibrium population number adsorbed on a surface is depending on the temperature (the available thermal energy), which either favors the desorption or the adsorption probability by influencing the differential sticking coefficient[3]. This higher/lower desorption probability is then balanced out by building up a temperature depending (lower/higher) population number until an equilibrium of adsorption and desorption events is reached and the sample stays in thermodynamic equilibrium.

Since the number of desorption/adsorption events for a sample in thermodynamic equilibrium is very small, it is not possible to study the desorption processes of a sample at a constant temperature. Instead, a change in desorption flux by running through a constant temperature gradient after establishing an equilibrium population at the base temperature is measured.

This can be done by TPD experiments, where a sample (e.g. cellulose on a metal substrate) is placed inside a vacuum chamber, evacuated to high vacuum and cooled to the base temperature. Then, a gas flow of a substance (the adsorbate) is introduced. It fills the vacuum chamber to a certain pressure (adsorption pressure) and the sample is exposed to the adsorbate gas for a certain period of time (exposure time). Favored by the low temperature, adsorption processes into monolayers and multilayers (depending on the substrate temperature) occur. Then, the gas inflow is shut off and the remaining adsorbate gas is pumped out. Subsequently the sample is heated and undergoes a linear temperature ramp. While the rise in available thermal energy is steadily activating desorption processes, a quadrupole mass spectrometer detects the desorbing molecule flux. Different detected peaks of desorption flux are then indications of different adsorption sites and/or desorption processes with different activation energies. It was shown by Redhead[4] that one can even derive an estimation of this adsorption energy by relating the detected desorption feature to the according temperature.

The experiments for this work were done in a vacuum chamber equipped with a turbomolecular pump and a rotary vane pump with a base pressure of about 5×10^{-9} mbar (for a detailed schematic illustration see Figure 2.16.). As can be seen in Figure 2.15 the sample (a thin cellulose film on a stainless steel support) is mounted by Ta wires between two electrically isolated sample holding benches. This enables direct resistive heating of the sample only. On the left side in Figure 2.15, one can see the quadrupole mass spectrometer that is used to detect the molecules desorbing from the sample. The distance between the sample surface and the ionization space of the mass spectrometer is about 3 cm.
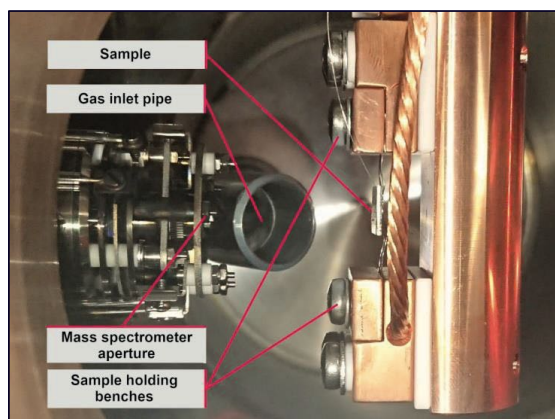
*Figure 2.15. Mass spectrometer (left) and sample holder (right)
inside the vacuum chamber.*
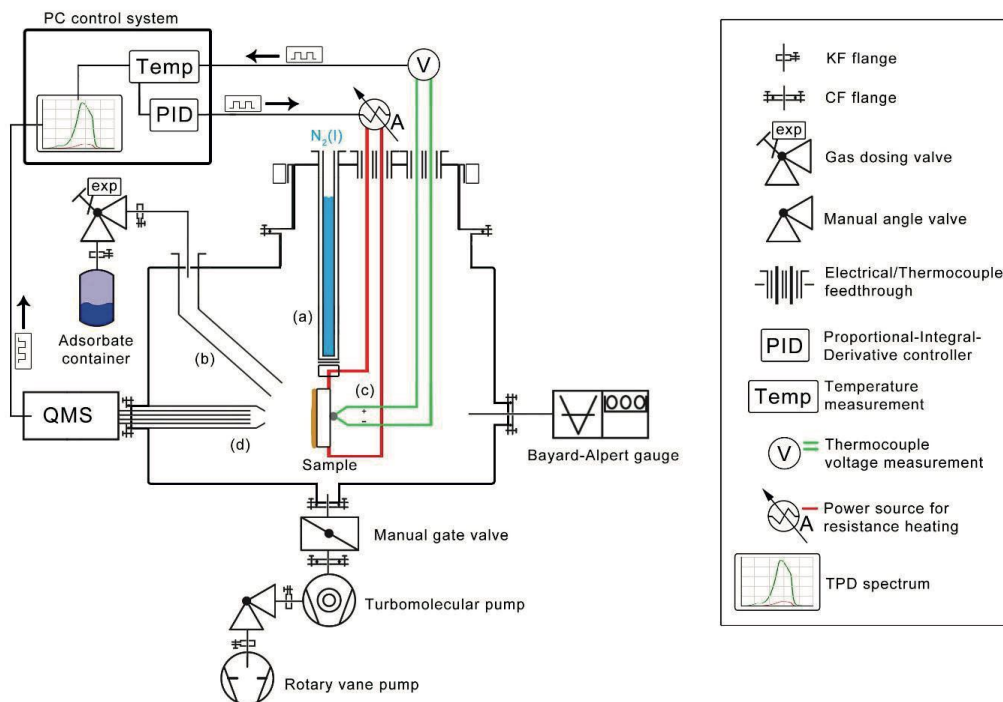
*Figure 2.16: Piping and instrumentation diagram (P&ID) of the TPD system. (a) Hollow bore inside the
sample holder for liquid N_2 cooling. (b) Adsorbate influx path: gas inlet pipe, gas dosing valve and
adsorbate container. (c) Sample: metal substrate with cellulose thin film on top, resistance heating
wires and thermocouple measurement point at the rear side. (d) Quadrupole mass spectrometer
(QMS) aperture.*

For all experiments with adsorption, the adsorbate molecule is introduced from the
adsorbate container through the adsorbate influx path (see Figure 2.16b) using the

vapor pressure of the molecule at room temperature. The influx is regulated by a manual angle dosing valve with an exponential opening characteristic to establish a constant background pressure of about 5×10^{-6} mbar during an exposure time of 6 min. The gas flow is guided directly from the valve to the surface of the sample by the gas inlet pipe (see Figure 2.15, background) in order to enhance the number of molecules that hit the sample surface. At the same time the flow of introduced adsorbate molecules is constantly detected via the quadrupole mass spectrometer (see Figure 2.16 (d) and Figure 2.15, left side). After the adsorption process is done, the gas inlet valve is closed and the background pressure goes down to the base pressure again. The sample is then heated with a linear heating rate (0.1 °C/s or 1 °C/s) and the mass spectrometer is used to measure either a series of entire mass spectra (only possible for the low heating rate) from mass 0 to 100 (as can be seen in Figure 2.18), or to trace up to 4 or 5 different masses simultaneously at higher heating rates (as can be seen in Figure 2.17).

(a)

(b)
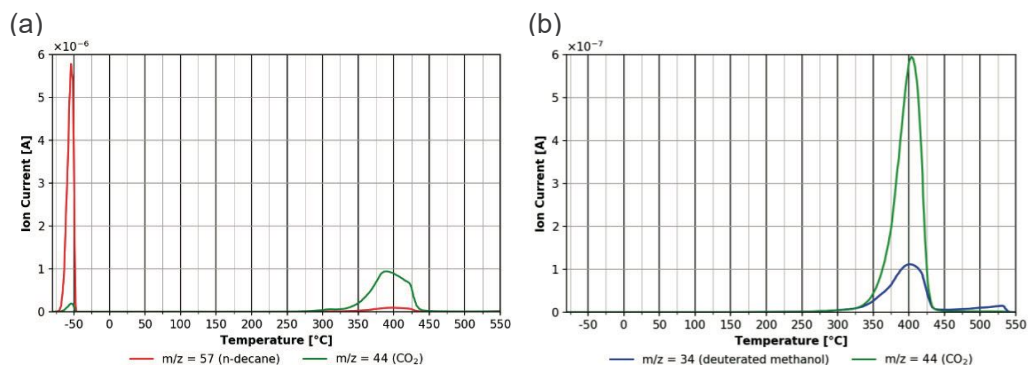
Figure 2.17. TPD desorption spectra of the intensity of the detected ion current vs. temperature of: n-decane (a), and deuterated methanol (b), from cellulose thin films. CO_2 desorption indicates thin film desorption/disintegration.

In this way the desorption of n-decane and deuterated methanol on cellulose thin films have been investigated and showed that the more polar methanol molecule (Figure 17b) adsorbs strongly on the cellulose surface, while the less polar n-decane shows a significant smaller desorption energy (Figure 2.17a[5]

In addition to desorption experiments with an external adsorbate introduced onto the surface of the thin film, TPD experiments with cellulose can also be done without introducing an adsorbate molecule in order to show the characteristic TPD fingerprint of the disintegrating thin film itself. As can be seen in Figure 2.18 (a), the cellulose film disintegrates and desorbs in a temperature range between about 300 and 400 °C with a characteristic ion m/z distribution. This characteristic distribution can also be seen in Figure 2.180 (b), where the additional peaks at about 150 °C are due to a modification of the cellulose surface by ASA.
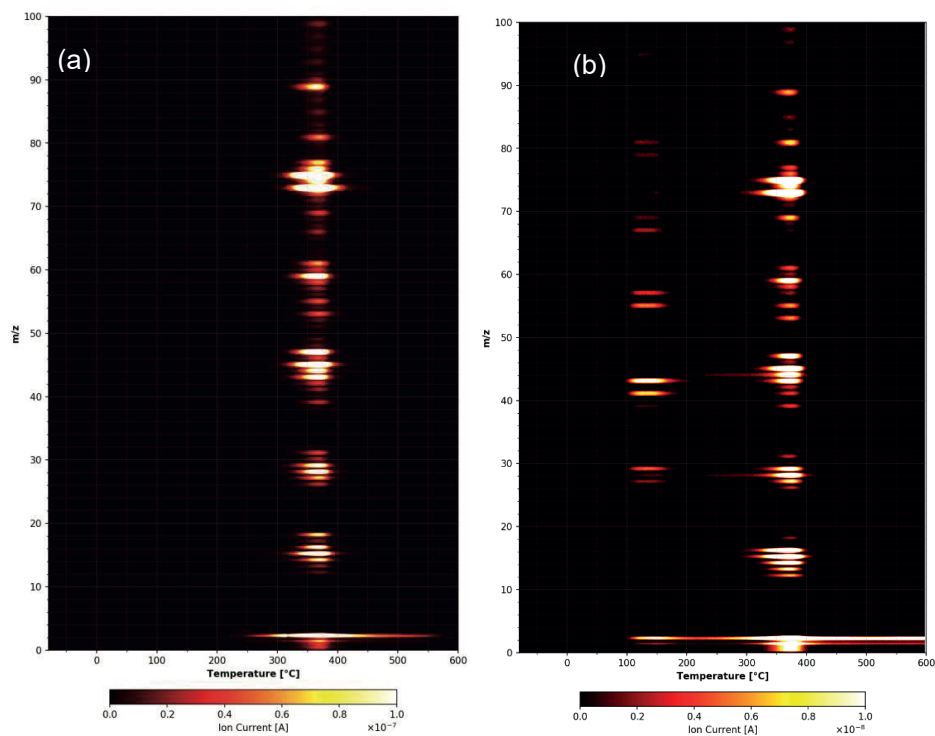
Figure 2.18. Complete TPD spectrum (ion current of desorbed molecules, color coded) in relation to the mass-to-charge ratio m/z from 0 to 100 (ordinate) as a function of temperature (abscissa). TPD fingerprint of: (a) the desorption/disintegration of a clean cellulose film and (b) desorption/disintegration of a cellulose film modified with ASA (alkenyl succinic anhydrides).

References

1. Tolman, R. C. (1979). The principles of statistical mechanics. Courier Corporation., p. 159-165

2. Cardillo, M. J., Balooch, M., & Stickney, R. E. (1975). Detailed balancing and quasi-equilibrium in the adsorption of hydrogen on copper. Surface Science, 50(2), 263-278. https://doi.org/10.1016/0039-6028(75)90024-2

3. Steinrück, H. P., Rendulic, K. D., & Winkler, A. (1985). The sticking coefficient of H2 on Ni (111) as a function of particle energy and angle of incidence: A test of detailed balancing. Surface science, 154(1), 99-108. https://doi.org/10.1016/0039-6028(85)90355-3

4. Redhead, P. A. (1962). Thermal desorption of gases. Vacuum, 12(4), 203-211. https://doi.org/10.1016/0042-207X(62)90978-8

5. Henögl, E., Haberl, V., Ablasser, J., & Schennach, R. (2019). Adsorption and desorption of organic molecules from thin cellulose films. Frontiers in Materials, 6, 178. https://doi.org/10.3389/fmats.2019.00178

Unexpected barrier properties - The interaction of the paper matrix with volatile organic compounds

Lisa Hoffellner[a,b] & Erich Leitner [a,b]

[a]*Institute of Analytical Chemistry and Food Chemistry, Graz University of Technology, Graz, Austria*
[b]*CD-Laboratory for Mass Transport through Paper, Graz University of Technology, Graz, Austria*

Corresponding author: Lisa Hoffellner <lisa.hoffellner@tugraz.at>

Keywords: Paper, food packaging, sorption, GC analysis

Summary

The aim of our study is to investigate the interaction of virgin fiber paper samples with polar and non-polar model compounds. This should help to gain a fundamental understanding of the interdependence of transport mechanisms of the paper matrix and volatile compounds. Our method is based on headspace – solid-phase-microextraction and gas chromatography (HS-SPME-GC/FID or HS-SPME-GC/MS). The results show that, especially the polar and larger non-polar compounds, are not transported through the test paper samples, i.e. they strongly sorb via the surface of the investigated virgin fiber paper samples.

Paper is one of the most important packaging materials used worldwide. Especially in the packaging sector of dry food and other granular materials, paper and board have found unique applications for fast and durable packaging. The use of paper and board in a large range of fields is highly desired because it has many favorable properties, including its economic and ecological friendly characteristics. To be suitable as a packaging material for food, paper has to fulfill certain requirements. Overall, it should protect the packaged goods from the environment. It should be sufficiently inert to preclude the transfer of substances from the packaging into the food, and it should protect the organoleptic properties of the food product[1]. As paper is a very complex three-dimensional network, with pores of different sizes and a large surface, it is often regarded as a permeable layer with limited barrier properties[2]. Complex transfer processes of compounds can occur through two ways: by migration (direct or via the

gas phase) or by permeation. Especially low molecular weight and volatile substances are of concern because they might migrate from and through the packaging into the packaged goods and vice versa.

The aim of our study is to gain a fundamental understanding of the interdependence of transport mechanisms of the paper matrix and volatile organic compounds. This may help to better understand the paper network and to predict the behavior of a selected paper for a specific use. In order to investigate the interaction of the paper matrix with different volatile substances, a set of model compounds was selected. This set consists of compounds of different structure, boiling point, molecular weight, and polarity. The polar compounds were chosen to represent aroma compounds in food products.

In a first step, we determined the sorption behavior of those compounds on our virgin fiber test paper samples. For this purpose, we developed a fast and simple method that is based on headspace – solid-phase-microextraction and gas chromatography, flame ionization detection (HS-SPME-GC/FID) or mass spectrometric detection (HS-SPME-GC/MS). Figure 2.19 visualizes such an experiment. The paper sample is placed in a HS-vial and the compounds are introduced on the wall of the vial to let the substances adsorb via the gas phase onto the paper samples. Therefore, an equilibration time of 24 h at room temperature was selected. The sorbed amounts of the compounds is then measured by HS-SPME-GC/FID. With the information from the chromatograms we can calculate how much of the compounds adsorb on the surface of the paper samples.

The obtained results indicate that the polar compounds strongly adsorb on the paper surface. Different conditions that might influence the sorption behavior of the compounds, like paper type or present humidity, were investigated. In order to determine how the addition of a sizing agent influences the sorption process, a sized and an unsized paper sample were compared. Although the polar compounds strongly interact with both paper types, the sorption on the unsized paper was, due to its more hydrophilic character, significantly higher. The results are shown in Figure 2.20.
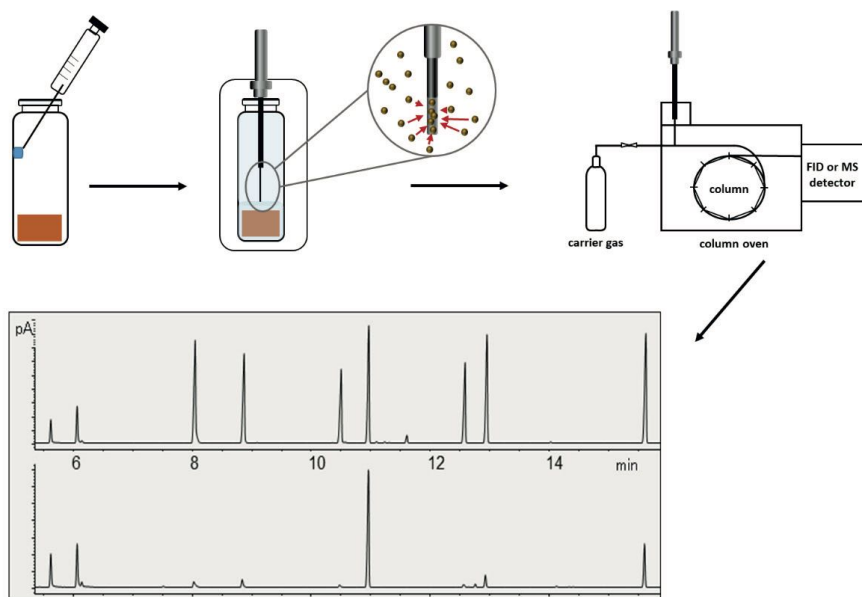
Figure 2.19. Schematic of a HS-SPME-GC/FID experiment developed in our study. First, the paper sample is placed in a HS-vial and spiked with the mixture of the model compounds. The compounds are allowed to adsorb via the gas phase on the paper. After an equilibration time of 24 h at room temperature, the sorbed amount of the compounds is measured with HS-SPME-GC/FID. The sorbed amount can be determined using the information from the chromatograms (upper: chromatogram of the pure model compounds; lower: chromatogram of a paper sample spiked with the compounds).

By increasing the humidity, the sorption of the compounds decreased, as water molecules seem to displace the model compounds on the paper samples[3].
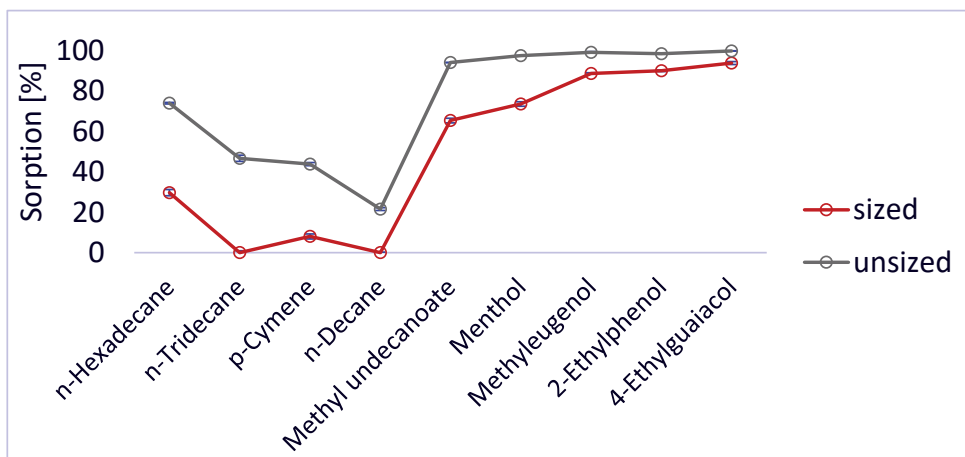
Figure 2.20. Sorption behavior of the model compounds on a sized and an unsized paper sample.

In a second step, we investigate the transfer of volatile molecules through the test paper samples with an adapted experimental setup comprising a migration cell. For this purpose, we use a modified set of model compounds that comprises a solvent-free mixture of polar and non-polar molecules. The amount of each compound transported through paper is analyzed by HS-SPME-GC/FID. The compounds are added in the lower chamber of the cell, the paper sample is placed above and the cell is closed. In order to reach equilibrium conditions, the cells are placed in a drying oven at a certain temperature for 24 h. The results show, that under the tested conditions, the model compounds did not permeate through the test paper samples. In line with the series of sorption experiments, the polar compounds seem to strongly adsorb on the paper surface.

Considering that paper fibers are composed of polar macromolecules, we distinguished between two compound classes, polar and non-polar aroma compounds. Polar volatiles exhibit a high affinity, i.e., they strongly adsorb on the surface of the investigated virgin fiber paper samples. This behavior was observed with different methods and under varying conditions. Therefore, these methods can be readily used to investigate the interaction of volatile organic compounds with paper samples.

Against the widespread theory, that paper cannot act as barrier layer, the polar aroma compounds used in our study were not transported through the test paper samples. Also, the larger non-polar molecules, that might bind via van der Waals interactions, adsorb on the paper surface. This might indicate that a food packaging made from virgin fiber paper can protect the food up to a certain degree from unwanted transfer of chemicals, depending on their polarity and their molecular size.

References

1. Regulation (EC) No 1935/2004 of European Parliament and of the Council on materials and article intended to come into contact with food and repealing directives.

2. Geueke, B. (2016). Paper and board https://www.foodpackagingforum.org/food-packaging-health/food-packaging-materials/paper-and-boar Retrieved Jan 21, 2020.

3. Hoffellner, L., & Leitner, E. (2020). Sorption behavior of organic molecules on porous paper material, Cellulose Chem. Technol., 54 (5-6), 515-522. https://doi.org/. 10.35812/CelluloseChemTechnol.2020.54.52

Session 3A

Mechanical performance of paperboard

Session chair: Anna-Leena Erkkilä

Modelling the moisture dependent elastic-plastic properties of paperboard

Gustav Marin[a], Mikael Nygårds[a], & Sören Östlund[b]

[a]*RISE Bioeconomy and Health, Kista, Sweden*
[b]*KTH Royal Institute of Technology, Stockholm, Sweden*

Corresponding author: *Sören Östlund <soren@kth.se>*

Keywords: Elastic-plastic, mechanical properties, moisture, paperboard

Summary

Mechanical tests have been performed on four types of paperboard from different manufacturers in order to verify a linear relation between normalized mechanical property and moisture ratio. The tests were performed in different relative humidity (20, 50, 70 and 90% RH) but with constant temperature (23 °C) in MD and CD, respectively.

The linear relation was confirmed for the investigated normalized mechanical properties in this study. In fact, when also the moisture ratio was normalized with the standard climate, all paperboards coincided along the same line. Therefore, each mechanical property could be expressed as a linear function of moisture ratio and two constants.

In addition, an in-plane elastic-plastic material model was suggested, based on four parameters: strength, stiffness, yield strength and hardening modulus. Since all parameters could be expressed as a linear function of moisture ratio, the model could predict the elastic-plastic behavior for any moisture content from the two constants in the linear relations and the mechanical properties at standard climate.

Introduction

In an earlier study of five multiply folding boxboards from one manufacturer, the results indicate that there is a linear relation between the mechanical properties of paperboard normalized with standard testing conditions (50% RH, 23 °C) and the moisture ratio[1], where the moisture ratio is defined as

$$m_r = m_w/m_d. \tag{1}$$

In Eq. (1), m_w is the mass of water and m_d is the mass of the dry solid content. The mass of water is calculated as

$$m_w = m_{total} - m_d. \tag{2}$$

The linear relation was formulated according

$$\frac{\text{Mechanical property}}{\text{Mechanical property at 50 \%RH}} = am_r + b, \tag{3}$$

where the constants a and b varied depending on which mechanical property that was investigated[1]. The purpose of this study was to investigate if paperboard series from other manufacturers also follow a linear relation, and if so, suggest an in-plane constitutive model that accounts for plasticity and moisture and is easy to implement in a FE-software

Materials

Paperboards, made from different types of fibers with different ply structures from four different commercial manufactures were used in this study; see Table 3.1.

Table 3.1. Paperboards used in the study.

Paperboard	Grammages [g/m²]	Description
A	235, 250, 270, 285, 320	Scandinavian duplex FBB multiply board with CTMP in the middle ply
B	280, 300, 325, 350	Recycled multiply board
C	180, 240, 300	Scandinavian multiply SBB board
D	280, 320, 350	American single ply SBB board

Method

The paperboards were tested at four different levels of relative humidity (RH): 20, 50, 70 and 90% RH at 23 °C. Short-span Compression Test (SCT) (ISO 9895:2008), and In-plane Tensile Test (ISO 1924-3:2005) was performed. The in-plane tensile tests were performed with standard test pieces of length, L = 100 mm, and width, b = 15 mm, and the tests were run in displacement controlled at a displacement rate of 100 mm/min. The force, F, and the elongation, δ, was recorded. Stresses, σ, and strains, ε, were evaluated according to

$$\sigma = F/A \text{ and } \varepsilon = \delta/L. \tag{4}$$

Young's modulus, E, was calculated following ISO1924-3:2005.

Structural parameters, such as thickness and grammage, were measured for each climate, respectively. For all tests, the equipment and the materials were conditioned for 24 hours. The thickness of the boards was measured following SCAN P88:01. Grammage was calculated following ISO 536 where the weight was measured using a Mettler AE 160 scale. At each humidity level, 10 measurements were performed in MD and CD, respectively.

Results

From the experiments results, a distinguished impact from the moisture was seen for the structural parameters, the SCT values and the in-plane tensile properties respectively. When exposed to moisture, the thickness and grammage increased. This was seen for all boards in the study, independent of thickness or density at standard climate. The density, in contradiction to thickness and grammage did not show a clear relation to the moisture change, while the mechanical properties, as expected, decreased when exposed to moisture.

Figures 3.1 and 3.2 shows Young's modulus and tensile strength, σ_f, and Figures 3.3 and S3.4 show these values normalized with the values at 50 %RH, as functions of moisture ratio. If also the moisture ratio is normalized with the moisture ratio at the standard climate, the results for the normalized Young's moduls and tensile strength in MD are shown in Figures 3.5 and S3.6, respectively.

If the same normalization procedure is performed also for the SCT-value, the yield strength, σ_Y and the hardening modulus, H, in a bilinear elastic-plastic constitutive equation (Figure 3.7) the results are shown in Figures 3.8-3.10.
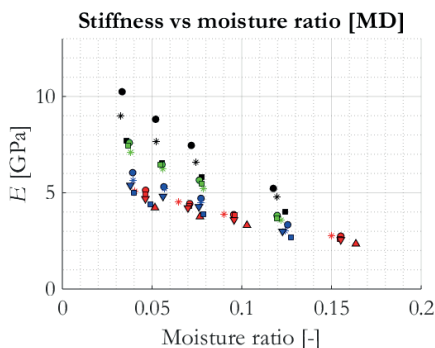
Figure 3.1. Young's modulus in MD as function of moisture ratio
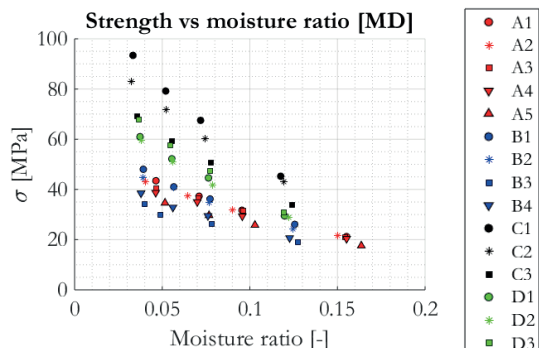
Figure 3.2. Tensile strength in MD as function of moisture ratio.
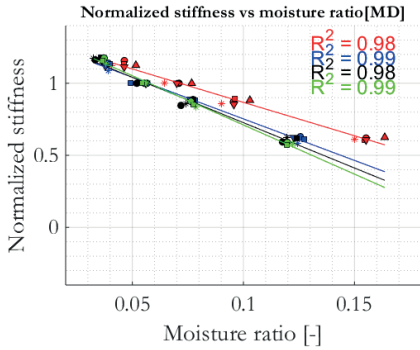
Figure 3.3 Normalized Young's modulus in MD as function of moisture ratio.
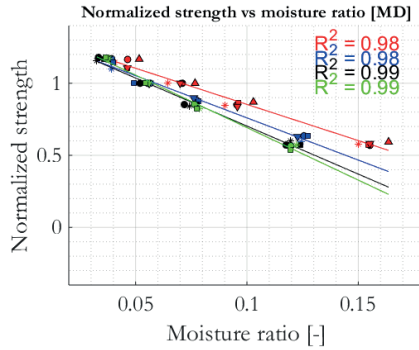
Figure 3.4 Normalized tensile strength in MD as function of moisture ratio.
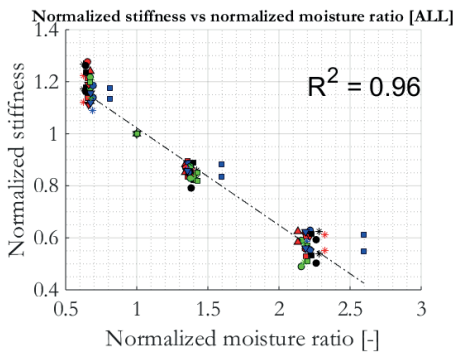
Figure 3.5 Normalized Young's modulus as function of normalized moisture ratio.
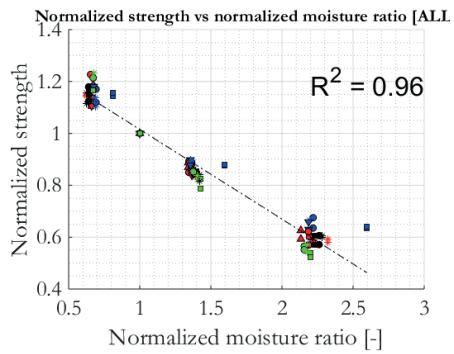
Figure 3.6 Normalized tensile strength as function of normalized moisture ratio.
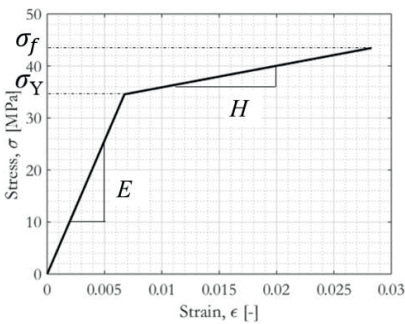
Figure 3.7 Bilinear elastic-plastic stress-strain relation.
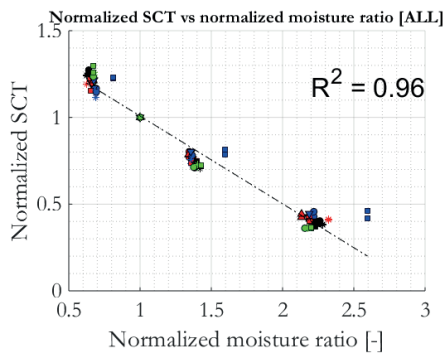
Figure 3.8 Normalized SCT in both MD and CD as function of normalized moisture ratio.
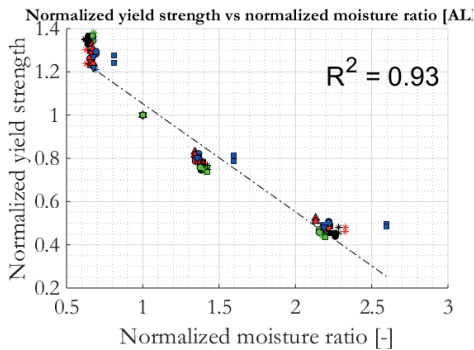
Figure 3.9 Normalized yield strength in both MD and as function of normalized moisture ratio.
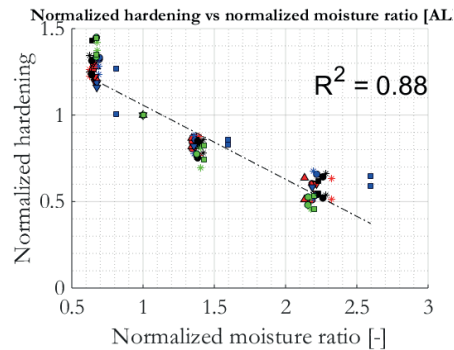
Figure 3.10 Normalized hardening modulus in MD and CD as function of normalized moisture ratio.

The results indicate that if these mechanical properties as function of moisture ratio, to a good approximation follow simple linear relations, and it would be sufficient to measure the particular property only at the standard climate. This is for example of great importance to be able to carry out accurate numerical simulations without relying on extensive testing for determination of the constitutive parameters at different moisture content, but of course also when comparing different paperboards.

Conclusions

This study shows that the mechanical properties: strength, stiffness and SCT-value exhibit a linear relation to moisture ratio if the mechanical property is normalized by the property at standard climate (50% RH and 23 °C). In addition, it has been shown that all paperboards coincide to the same linear relation for each property. Thus, the mechanical properties can be expressed by only two parameters, if the moisture ratio is normalized as well. Furthermore, an in-plane bi-linear elastic-plastic material model was suggested, based on the parameters σ_f, E, σ_Y and H, where the stress-strain relations for any moisture level can be estimated by knowing

- The mechanical properties for the standard climate (50% RH and 23 °C).
- The moisture ratio in the board for standard and preferred climate, and the two parameters describing the linear relation for each property.

Acknowledgement

References

1. Marin. G., Nygårds, M., Östlund, S. (2019) Stiffness and strength properties of five paperboards and their moisture dependency. Int. Pap. Phys. Conf., p. 14-29.

Experimental and Analytical Investigation of Paperboard Rate-Dependent Behavior

Abolhassan Nazarinezhad Giashi[a], Thomas Gereke[b], Taoufik Mbarek[a], & Chokri Cherif[b]

[a]*SIG Combibloc Systems GmbH, Linnich, Germany*
[b]*Technische Universität Dresden, Institute of Textile Machinery and High Performance Material Technology, Dresden, Germany*

Corresponding author: *Abolhassan Nazarinezhad Giashi*
<*abolhasan.giashi@sig.biz*>

Keywords: Dynamic test experiments, paperboard, rate-dependent model

Summary

Packaging converting procedures are indeed very fast with deformation times of around just some few milliseconds. For this reason, a dynamic material characterization is mandatory to precisely describe constitutive behavior during this process. The main goal of this research work has been conducted for design and development of a new high-speed dynamic test facility in order to evaluate rate sensitive mechanical properties of paperboard materials. It was shown that paperboard significantly exhibited stiffer material hardening in respect to the higher elongation rates. The mechanical constitutive models were consequently formulated based on rate dependent characteristics through the converting process simulations.

Introduction

Regarding to paperboard experimental characterization, several works have been conducted during the last decades. Tryding et al[1], Beex and Peerling[2], Nygårds et al[1,3] and Li et al[4] have performed various quasi-static uni-axial tensile and shear tests to identify paperboard material properties. The obtained experimental results have been then specifically employed to formulate material constitutive models based on Hill´s yield criterion or analytical approaches.

However, just a few works roughly addressed the dynamic characteristics of paperboard and packaging converting procedures in which the material rate sensitive properties differ from the real deformation rates observed through the real converting applications. Allaoui et al.[5] presented an experimental work about rate dependent properties of several paperboards. Based on their results, those materials significantly showed a stiffer material in respect to the higher elongation rates. In a similar work, Henry and Haslach[6] discussed the impact of deformation rate and moisture on the properties of paperboards. In this case, they have evaluated paperboard time dependent mechanical response and specifically developed analytical models to describe paperboard creep and relaxation behavior.

Most studies concerning paperboard and its converting procedures have so far been dedicated to static analyses, which are mainly suitable for low-speed converting processes. This work discusses the improvement and establishment of appropriate test facilities for experimental measurements for evaluating the rate-sensitive material properties of paperboard.

Experimental procedure

Material

For the material test procedures, a paperboard with a grammage of 240 g/m^2 was chosen. The paperboard has been selected because it was the reference material in a real packaging production process. From structural point of view, the paperboard has totally five sub-layers that include two outer plies as top and bottom layers in addition to a middle layer which is made of three thin sub-layers. In order to get a better understanding about the fundamental components of the explored paperboard, the whole carton board was firstly split into the constituent plies using one specific grinding system.

Dynamic test set-up and results

In order to find the best configuration for dynamic test procedures, several sample dimensions were thoroughly examined. After many trial tests, the gage length of 50 mm was finally fitted as the best one to reach dynamic test demands and the maximum elongation rate of 80 s^{-1} was obtained in an efficient way. For the final experiments, the test probes with 200 ×15 mm^2 were precisely cut using a laser cutting device, while the probes' extra length essentially helped to achieve a better clamping. Figure 3.11 shows an overview of the developed test facilities.
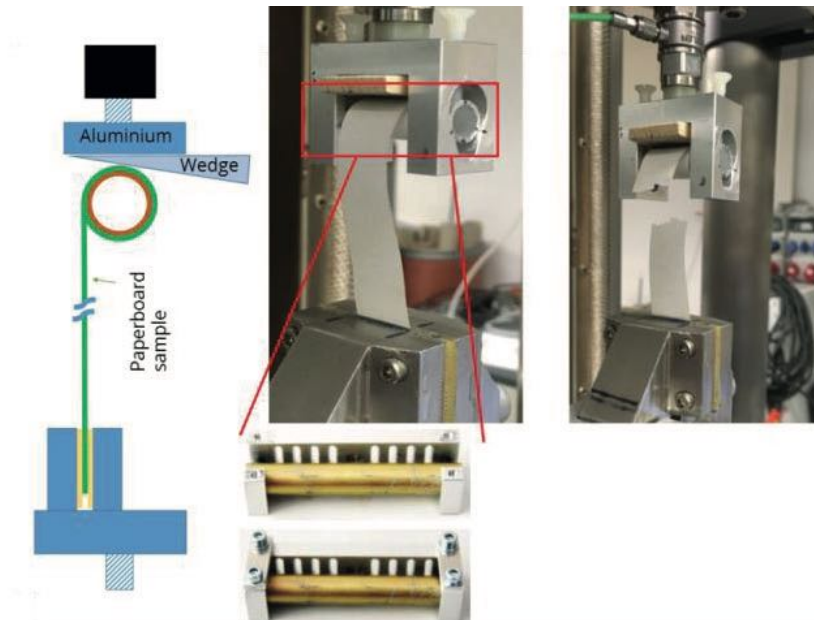
Figure 3.11. Improved dynamic experimental set-up for paperboard

The upper clamping device is fixed, while the lower clamping device is moveable in order to perform the test loads while carried out with rubber coated fixtures to prevent the relative sliding between the samples and clamps during the high speed tensile tests[7,8]. For 15 mm wide samples, a very light clamp with only 36 g aluminum tube as shown in Figure 3.11 was developed, so that the clamping force across the entire width of the sample was almost uniform. Instead of the concept of clamping between two parallel plates, the probes were inserted first through the slotted cylinder and rolled up about 1.5 turns under slight pre-tension loads. In order to reduce the local fracture effects, the outer surface of the aluminum tube is polished and all edges were perfectly rounded.

Subsequently, the high-speed test results were employed to formulate paperboard rate-dependent material properties. Two mathematical formulations based on Johnson-Cook[9] and Cowper-Symonds[10] hardening laws have been set up. The fitting process was issued for paperboard sub-layers in MATHEMATICA, and the nonlinear curve-fitting procedures were performed in least-square regression. Subsequently, the essential material parameters including both yield hardening and rate sensitive characterizations were accurately identified during material calibration procedures.

The correlation of the material models has been validated and provided a suitable model to predict material response on high-speed deformation rates. The comparison between the experimental results and obtained dynamic model based on Cowper-Symonds formulation is depicted in Figure 3.12.
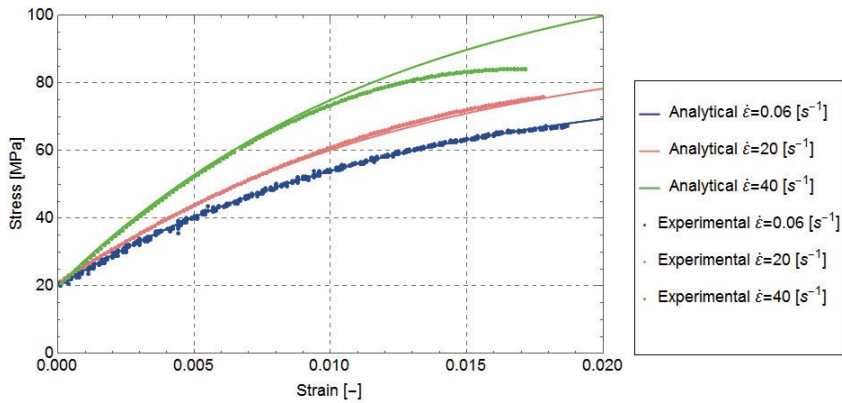
Figure 3.12. Comparison between experimental and rate-dependent model; Top layer.
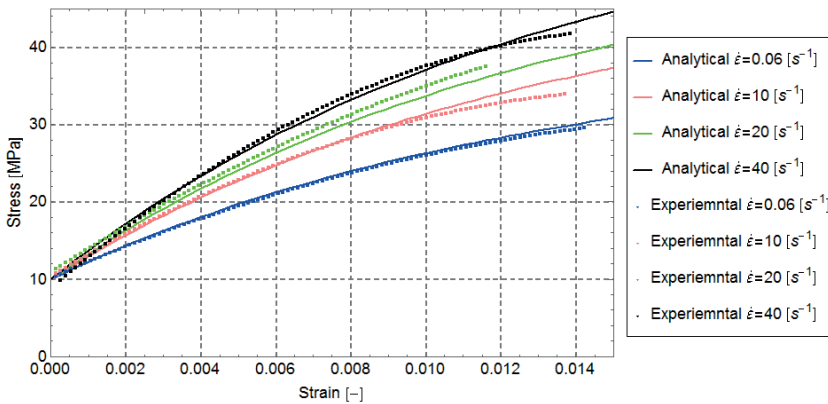
Figure 3.13. Comparison between experimental and rate-dependent model; Middle layer.
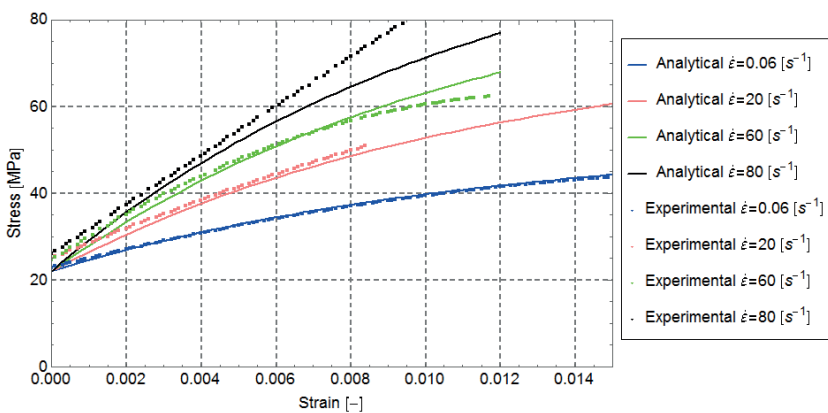
Figure 3.14. Comparison between experimental and rate-dependent model; Bottom layer.

The experimental results and further analytical models strongly exhibit the rate sensitive material properties of the paperboard sub-layers. Similar to the other conventional engineering materials, these composites represent stiffer material response at higher elongation rates as clarified through the material parameter identifications. In comparison to the quasi-static material characteristics, all of the layers exhibit about 25 % higher stresses and smaller resulting strains in respect to the higher elongation rates.

Conclusions

Experimental investigations on rate dependent material response have been conducted. Based on the experimental results, an analytical rate dependent material formulation has been elaborated for paperboard materials. Generally, packaging converting processes are carried out at very high-speed and result in enormous deformation rates and extensive nonlinearities. Therefore, it was essential to identify the rate sensitive material characteristics in order to provide a robust and reliable numerical model to simulate high speed converting processes and their impact on the paperboard response in a proper way. The implementation of dynamic tests posed a major challenge since there is no specific test standard for paperboard dynamic tensile measurements. In this reason, an improved experimental test rig was specially designed and developed to conduct high speed tensile experiments. The dynamic test results showed stiffer mechanical properties with respect to the higher elongation rates. The obtained experimental data were further employed to formulate mechanical constitutive models based on various analytical rate dependent approaches.

Acknowledgements

References

1. Nygårds, M., Just, M., & Tryding, J. (2009). Experimental and numerical studies of creasing of paperboard. International journal of solids and structures, 46(11-12), 2493-2505. https://doi.org/10.1016/j.ijsolstr.2009.02.014.

2. Beex, L. A. A., & Peerlings, R. H. J. (2009). An experimental and computational study of laminated paperboard creasing and folding. International Journal of Solids and Structures, 46(24), 4192-4207. https://doi.org/10.1016/j.ijsolstr.2009.08.012.

3. Nygards, M., Fellers, C., & Östlund, S. (2007). Measuring out-of-plane shear properties of paperboard. Journal of Pulp and Paper Science (JPPS), 33(2), 105-109.

4. Li, Y., Stapleton, S. E., Reese, S., & Simon, J. W. (2016). Anisotropic elastic-plastic deformation of paper: In-plane model. International Journal of Solids and Structures, 100, 286-296.

5. Allaoui, S., Aboura, Z., & Benzeggagh, M. L. (2009). Phenomena governing uni-axial tensile behaviour of paperboard and corrugated cardboard. Composite Structures, 87(1), 80-92. https://doi.org/10.1016/j.compstruct.2008.01.001.

6. Haslach, H. W. (2000). The moisture and rate-dependent mechanical properties of paper: a review. Mechanics of time-dependent materials, 4(3), 169-210. https://doi.org/10.1023/A:1009833415827 .

7. Cherif, C., Seidel, A., Younes, A., & Hausding, J. (2010). Evaluation of a tensile test for the determination of the material behaviour of filament yarns under high strain rates. AUTEX Research Journal, 10(4), 88-94.

8. Younes, A., Sankaran, V., Seidel, A., Waldmann, M., Cherif, C., & Hausding, J. (2012). Stress-strain behavior of carbon filament yarns under high strain rates. Textile Research Journal, 82(7), 685-699. https://doi.org/10.1177/0040517511433151 .

9. Gambirasio, L., & Rizzi, E. (2016). An enhanced Johnson–Cook strength model for splitting strain rate and temperature effects on lower yield stress and plastic flow. Computational Materials Science, 113, 231-265. https://doi.org/10.1016/j.commatsci.2015.11.034

10. Gyliene, V., & Ostasevicius, V. (2011, May). Cowper-Symonds material deformation law application in material cutting process using LS-DYNA FE code: turning and milling. In LS-DYNA® 8th European User's conference (pp. 1-12).

Prediction of ECT from SCT values including the effect of fibre furnish

Heinz-Joachim Schaffrath[a], Samuel Schabel[a], & Christopher Schmitt[b]

[a]*Technische Universität Darmstadt, Darmstadt, Germany*
[b]*University of Hamburg, Hamburg, Germany*

Corresponding author: *Heinz-Joachim Schaffrath*
<*schaffrath@papier.tu-darmstadt.de*>

Keywords: Fibre properties, corrugated board, corrugated box, modelling, compression strength

Summary

There are existing models to calculate box strength from ECT and ECT from SCT. However, this paper shows that differing between fibre sources like virgin or recovered will help to close the gap between predictions of compression strength properties form raw paper properties and measured results. Data of paper, corrugated board an boxes delivered by a big manufacturer of paper and board are investigated to see, if better fits between prediction and measurement are possible and reasonable in case clustered data-groups are examined. As a result, differentiation between altered flute types delivers no enhanced predictions. But taking the fibre source into account helps to decrease the gap between model and reality.

Introduction

Calculating ECT values for corrugated board from SCT values obtained with base papers is common practice and widely used. The existing models are based on the Maltenfort equation

$$ECT = k(\sigma_{c,L1} + \sigma_{c,L2} + \alpha\sigma_{c,Fl}) \tag{1}$$

where *L* indicates the liner, *Fl* the flute, *α* the takeup factor and σ_c a compression failure. σ_c can be replaced by RCT (ring crush test), CCT (corrugated crush test) or, as more common in the mills today, by SCT (short-span compression test) in cross direction. Published values for *k* in literature are spread over a quite wide range.

Markström offered k = 0,71 in his book[1] based on SCA Nordliner data as well as k = 0,46 based on Stora Billerud data. With Stora Billerud data the equation of Maltenfort was enhanced as- an intercept was introduced, to be regarded as an offset resulting in:

$$ECT = 0{,}71 * (SCT_{L1} + SCT_{L2} + \alpha SCT_{Fl}) \tag{2}$$

$$ECT = 0{,}46 * (SCT_{L1} + SCT_{L2} + \alpha SCT_{Fl}) + 2{,}12 \tag{3}$$

The physical meaning of the offset is not clear, and the difference between the values offered for k is of high relevance for the industry. Either equation (2) will lead to incorrect high results and the corrugated board can fail, which will lead to complaints. Or equation (3) will lead to low values with the results that the box is over dimensioned and too much material was spend for the requested purpose.

In this work, the existing models for predicting ECT from SCT-values have been applied to a wide range of data delivered by the corrugated board industry. Using this data set for creating a new fit leads to better forecasts concerning ECT. In addition, the data set has been divided into subgroups formed by fibre furnish (virgin or recovered) or flute type. With these subgroups the prediction accuracy could be improved again. The results show that it is reasonable to distinguish between fresh fibres and recycled fibres for calculating ECT from SCT measurements with empirical models.

Existing models and new fits

A set of 199 data points, consisting of corrugated boards manufactured from recycled fibres only as well as from a mixed recycled/virgin base paper and virgin base paper only, was used for an extensive analysis. ECT was determined as well as SCT in cross direction, grammage, flute type of the board and ash content.

The data set was used to calculate the ECT from the measured SCT values. The results obtained were compared with the measured ECT values and an average deviation (measured ECT minus calculated ECT) was calculated.

In a second step, the whole data set was taken to calculate a new fit using linear regression and derive a new proposal for k.

In a third step, the data has been divided into subgroups. All combinations of recycled fibres only have been evaluated separately as well as virgin fibre boards and mixed fibre boards.

It is not surprising that the new fit leads to less scattered results. No reasonable value of the average deviation could be given for virgin board grades, as the number of data available was too small. However, it is interesting to observe, that a differentiation

between virgin, mixed and recycled grades leads to better fits. Therefore, it seems to be reasonable to distinguish into subgroups. Regarding the *k*-value, it is interesting to see that the *k*-value for mixed board corresponds to the mean between the *k*-value for recycled fibreboards and the *k*-value for virgin fibreboards.

It can be concluded that the prediction of ECT values from SCT measurements can be improved significantly by taking into account the fibre source.

Table 3.2. Average deviations of calculated and measured ECT values. Different models are used.

ECT model applied	Average deviation, [%]	Remark
$ECT = 0{,}71 * (SCT_{L1} + \alpha * SCT_{FI} + SCT_{L2})$	25,8	Existing model
$ECT = 0{,}46 * (SCT_{L1} + \alpha * SCT_{FI} + SCT_{L2}) + 2{,}12$	27,5	Existing model
$ECT = 0{,}64 * (SCT_{L1} + \propto SCT_{FI} + SCT_{L2}) - 0{,}6$	5,8	New fit whole data set
$ECT = 0{,}57 * (SCT_{L1} + \propto SCT_{FI} + SCT_{L2}) - 0{,}07$	4,3	Recycled fibres only
$ECT = 0{,}64 * (SCT_{L1} + \propto SCT_{FI} + SCT_{L2}) - 0{,}81$	4,3	Mixed board only
$ECT = 0{,}71 * (SCT_{L1} + \propto SCT_{FI} + SCT_{L2})$	./.	Virgin board only

Additional work

Furthermore, the ash content of the samples was measured and the SCT data were correlated to grammage as well as fibre type. The hypothesis for this evaluation was, that only fibres are able to carry compressive load. To look after that, common SCT$_{index}$ was enhanced to an SCT$_{index\ fibre}$:

$$SCT_{index} = \frac{SCT}{grammage} \qquad (4)$$

$$SCT_{index\ fibre} = \frac{SCT_{index}}{(1 - ash\ content)} \qquad (5)$$

Figure 3.15 shows that the values for the SCT$_{index\ fibre}$ for some of the recycled papers (named R) are in the same range of compressions strength as virgin papers (named V). It may even happen, that a virgin fibre material (V4) shows less compression potential than a recycled one.

It is expected that results of ongoing work in this effect can be presented at the PPPS in Jyväskylä.

Finally, some hypotheses are tested to get an explanation what the offset in the equations could mean. Starch applied during the corrugating process has been examined and the influence of cutting the samples was taken into account. Results are also expected to be presented at the PPPS.
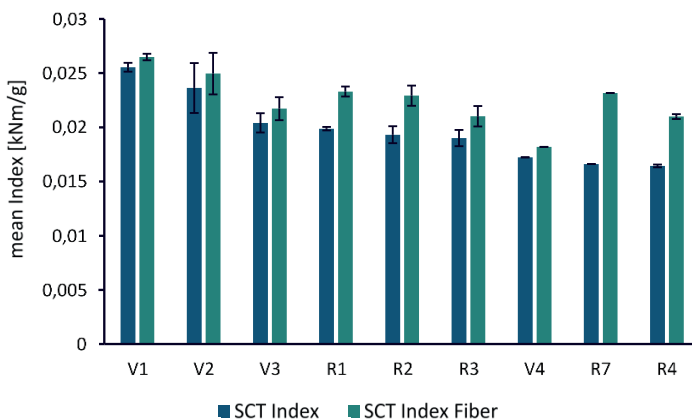
Figure 3.15. SCT related to grammage (SCT Index) and to fibre content (SCT fibre).

Conclusion

It could be shown by evaluation of extensive data that furnish type has a significant effect on the strength of corrugated board made out of them. For virgin and recycled fibre materials specific constants have been derived which improve the accuracy of the widely used Maltenfort model for predicting ECT values from SCT measurements. This reveals that it is reasonable to spend research in investigation of influence of fibre type, such as hardwood, softwood, mechanical and mechanical pulp.

References

1. Markström, H. (2005). Testing methods and instruments for corrugated board: A handbook. Lorentzen & Wettre.Howard, Kista, Sweden.

Additional literature

Fahey, D. J., & DW, B. (1982). Recycled fibers in corrugated fiberboard containers.

Zhao, L. L. (1993). Evaluation of the performance of corrugated shipping containers: virgin versus recycled boards (Doctoral dissertation, Victoria University of Technology).

Popil, R. E., Coffin, D. W., & Kaewmanee, P. (2004, June). The role of liner buckling on the edgewise compressive strength of corrugated board. In Abstract for paper presented at the 2004 Progress in Paper Physics Seminar, Trondheim, Norway (pp. 21-24).

van Eperen, R.H., & Sprague, C. H. (1983). ECT/component relationships. In: Project 3511, Progess report ECT/component relationships.The American Paper Institute and Fiber Box Association

Seth, R. S. (1985). Relationship between edgewise compressive strength of corrugated board and its components. Tappi journal, 68(3), 98-101.

Dimitrov, K. (2010). Relationship Between the ECT-strength of Corrugated Board and the Compression Strenth of Liner and Fluting Medium Papers (Doctoral dissertation, University of Pretoria).

Influence of creasing tension on reverse-side cracking of paperboard

Joel C. Panek[a] & Douglas W. Coffin[b]

[a]*WestRock, Richmond, Virginia, USA*
[b]*Miami University, Oxford, Ohio, USA*

Corresponding author: *Joel Panek <joel.panek@westrock.com>*

Keywords: Creasing, cracking, paperboard, tension

Summary

In this work, we investigate the effect of the sample width and tension on the cracking degree and critical draw. Under the same tooling, the critical draw decreases as the strip tension increases, meaning that cracking becomes greater at a shallower penetration depth. The narrower strip shows a higher critical draw than wide strip. In both cases, there is a higher amount of force on the creased region, which leads to additional cracking.

Extended abstract

In previous work, the creasing draw was shown to be an effective measure of creasing severity that causes reverse-side crease cracking (bead-side of the crease)[1]. In that work, the cracking degree for different rule and channel combinations under a constant sample width and tension was studied. The creasing draw converged the cracking degree data into a single curve. The critical draw was introduced as the draw where cracking becomes greater than 5%. In this work, we investigate the effect of the sample width and tension on the cracking degree and critical draw.

The creasing draw is a measure of the length of material that would be drawn into the channel without constraint. In reality, the material is restricted by tension. The tension may be due to 1) bending; 2) friction from passing over the channel edge; 3) strip tension; and 4) resistance to compression (for strips wider than the crease line) (Figure 3.16). Figure 3.17 shows a top view of how resistance to compression leads to tension at the end of a crease line. To clarify these effects, the tension on the strip and the width of the strip were varied for a constant set of tooling (Figure 3.18). The same

paperboard, creasing apparatus, and cracking analysis technique described previously was used[1].
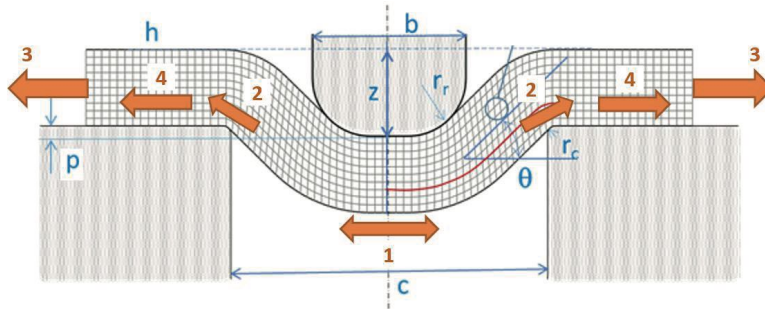
Figure 2.16. Geometry for Creasing Model with tensile forces acting on the outer surface.
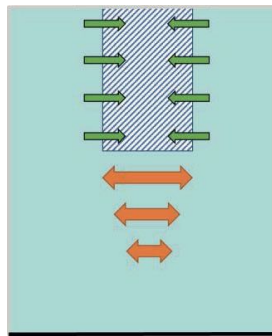
Figure 2.17 Top view of creased area where the material is wider than the crease. The hatched area represents the creased area; the single head arrows represent material being drawn into the crease; the double-head arrows represent the resistance to compression outside of the crease.
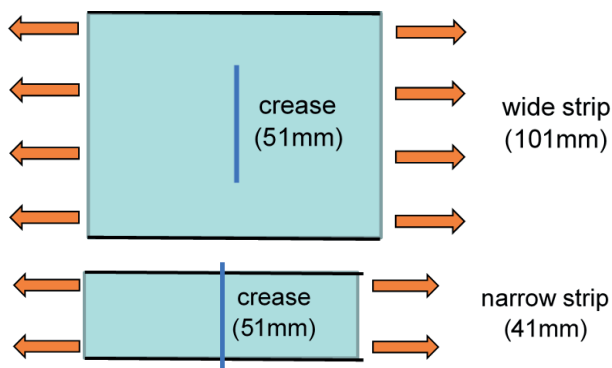
Figure 2.18. Creased area for narrow vs wide strips.

Figure 3.19 shows the cracking degree results for MD and CD creases. Note that the wide strip at 1.1 kN/m tension was the base case for the previous work. Figure 3.20 shows the critical draw (creasing draw at which the cracking length becomes greater

than 5%) as a function of strip tension. The critical draw decreases as the strip tension increases, meaning that cracking becomes greater than 5% at a shallower penetration depth. The narrower strip shows a higher critical draw than wide strip.
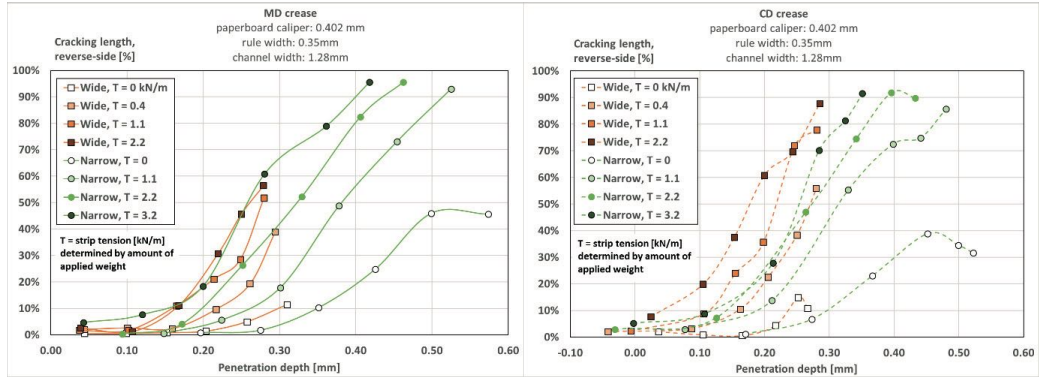
Figure 3.19. Cracking length vs penetration depth for MD (longitudinal) and CD (transverse) creases.
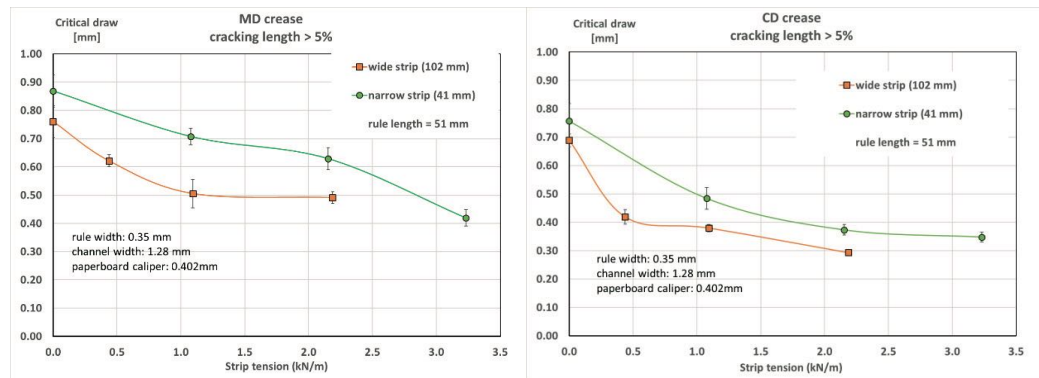
Figure 3.20. Critical draw vs strip tension for MD (longitudinal) and CD (transverse) creases. Error bars are 95% confidence intervals.

These results can be explained by the forces that are developd in the creased area (Figure 3.21). The greater forces can cause additional cracking. However, further work is still needed to develop a non-dimensional parameter to replace the creasing draw, since there is not an obvious logical way to normalize these results.
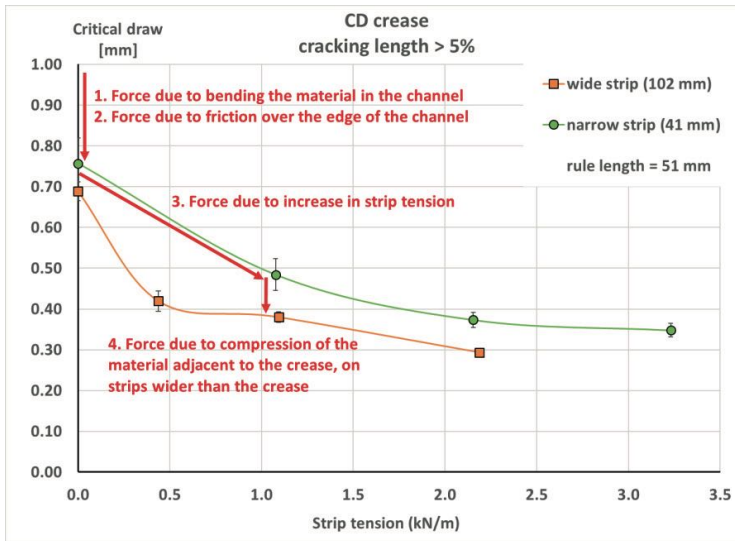
Figure 3.21. Effects that cause lower critical draw.

Acknowedgements

References

1. Panek, J. C., Smith, S. D., & Coffin, D. W. (2020). Creasing severity and reverse-side cracking. Tappi Journal, 19(4), 219-227

Tuesday 1.9.2020 at 13:00 - 15:00

Session 3B

Fiber water interactions

Session chair: Antti Koponen

Lightweight materials by tailoring foam-fiber interactions

Annika Ketola[a], Wenchao Xiang[b], Tuomo Hjelt[c], Timo Lappalainen[c],
Heikki Pajari[a], Tekla Tammelin[a], Orlando Rojas[b], & Jukka Ketoja[a]

[a]VTT Technical Research Centre of Finland Ltd, Jyväskylä, Finland
[b]Aalto University, Espoo, Finland
[a]VTT Technical Research Centre of Finland Ltd, Espoo, Finland

Corresponding author: Annika Ketola <annika.ketola@vtt.fi>

Keywords: Foam forming, cellulose, bubble-fiber interaction, model surface,
captive bubble, wetting transition

Summary

We studied surface interactions in simplified fiber-foam systems with the captive
bubble and fiber bed methods. The captive bubble technique was used to measure the
bubble interaction with different cellulose model surfaces in sodium dodecyl sulfate
(SDS) solution. The interaction of a single bubble with real fibers, submerged in SDS
solution, was investigated using the fiber bed. Bubbles had clear adhesion to fiber
surfaces in water, and the addition of SDS decreased this attraction. At high SDS
concentration, the attraction was lost due to wetting transition. However, a smooth
cellulose model surface did not attract bubbles even in the absence of surfactant. This
suggests that the observed interaction with cellulose nanofibrils and fibers was caused
by the presence of hydrophobic regions of the respective surface (e.g. lignin or
nanobubbles).

Introduction

Foam forming technology[1] enables the production of versatile cellulose fiber materials,
extending from thick, porous and lightweight structures to stiff 3D forms, thin
nonwovens and layered hybrid products[2,3]. These renewable materials can find use in
many current industrial sectors as alternatives to plastics, including packaging, high-
efficiency air filters and substrates for biocatalytic conversion. Due to these wide
application possibilities, controlling the final material properties is highly important. The

Ketola, A., Xiang, W., Hjelt, T., Lappalainen, T., Pajari, H., Tammelin, T., Rojas, O., & Ketoja, J.

stability and bubble size of the foam provide a mean to tailor the density and pore size distribution of the formed fiber network[4]. Additional effects come from surfactant chemistry and fiber surface characteristics. Thus, it is necessary to understand the interaction of bubbles with given fiber types with varied surfaces and link such knowledge with the architecture of the foam, its stability and final microporous structure.

Fiber-foams are complex systems and difficult to study in industrial processes. In this work, foam-fiber environment was simplified by using two model systems (see Figure 3.22). The first one considered a single bubble interacting with a model surface in surfactant solution[5]. The second system consisted of a bubble coming into contact with a fiber-bed in similar solution. In the first system, the model surfaces included thin films of cellulose, trimethylsilyl cellulose (TMSC) and cellulose nanofibrils (CNF) prepared by spin-coating on a silica wafer support. The captive bubble technique was used to test the interactions between the bubble and the model surfaces immersed in an anionic surfactant (sodium dodecyl sulfate, SDS) solution. SDS adsorption on the model surfaces and its possible effect on the surface wetting was determined by using the Quartz Crystal Microbalance with Dissipation (QCMD). In the second system, the complexity was increased by introducing the fiber bed. The fiber bed was prepared by letting a dilute fiber solution to settle down and form a fiber mat on the bottom of a cuvette (fibers from pine, birch and CTMP, as well as Rayon).

a) Hooked needle and a model surface **b) Fibre bed**

Captive bubble technique
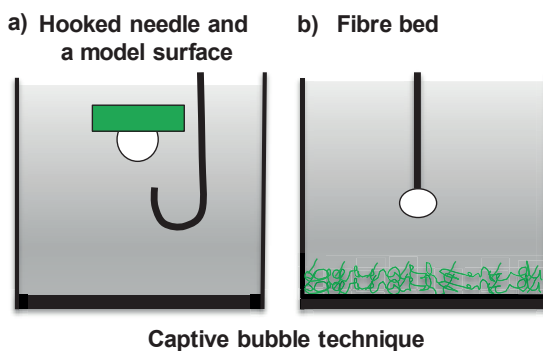
Figure 3.22. Captive bubble technique used to investigate bubble interaction with model surfaces and fibers.

Results

Results of the first system with the smooth model surfaces (Figure 3.23) generally showed that in pure water, air bubbles had a repulsive interaction with cellulose but an attractive one with TMSC. Cellulose is hydrophilic while TMSC is hydrophobic, so the interaction could be explained by the different wetting properties of the surfaces. SDS addition changed the bubble interaction with TMSC to repulsive, already at very low

concentration (0.7 g/L). According to the QCMD tests, SDS adsorbs on TMSC similarly as at the air-water interface. The adsorption changes the surface energies and turns the bubble interaction into repulsive. In addition, the critical drop contact angle of 65° for bubble attachment in water could be determined by changing the surface energy of TMSC by using partial regeneration. A simple theoretical framework was introduced to explain the experimental observations.

For rough CNF surfaces (see Figure 3.23a), the bubbles did not show any significant attraction in pure water. However, a small adhesion was observed after increasing electrolyte concentration in water. However, similar behavior was not seen with smooth cellulose surfaces. Thus, the possibility of entrapped nanobubbles in the rough CNF film and their effect on bubble adhesion was studied. When air was removed from the system, the bubble adhesion to the CNF film decreased. This suggests that entrapped nanobubbles play an important role in the bubble surface interaction with rough surfaces.

Results of the second system with the fiber-bed (see Figure 3.23b) showed that in water, bubbles have slight attraction to all fiber types. However, the probability of attachment was higher with a certain ones. The study of the effect of nanobubbles, fiber size, fiber surface morphology and SDS addition on bubble interaction with fiber surfaces is still ongoing.

a) Bubbles on model surfaces　　　　　**b) Fibre attached on a bubble**
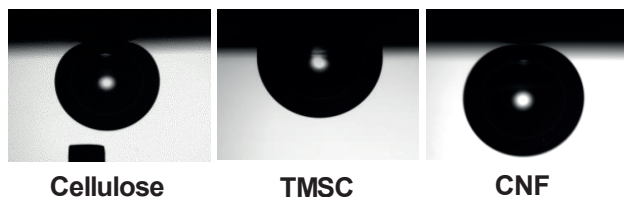
Cellulose　　　　TMSC　　　　CNF　　　　　　Birch fibre

Figure 3.23a) Bubbles on the model surfaces of cellulose, TMSC and CNF in water. Only on TMSC bubbles showed clear attachment. b) Birch fiber attached on a bubble.

Conclusions

In applications such as nonwovens with both natural and man-made fibers, the foam-formed structure is expected to be sensitive not only to the used fibers but also to the type and concentration of surfactant. Our findings can be used to understand the forming processes with smooth and rough fibers, opening ways to produce new foam-formed fiber materials.

Ketola, A., Xiang, W., Hjelt, T., Lappalainen, T., Pajari, H., Tammelin, T., Rojas, O., & Ketoja, J.

References

1. Radvan, B., & Gatward, A. P. J. (1972). Formation of wet-laid webs by a foaming process. *Tappi*, *55*(5), 748.

2. Lehmonen, J., Jetsu, P., Kinnunen, K., & Hjelt, T. (2013). Potential of foam-laid forming technology in paper applications. *Nordic Pulp & Paper Research Journal*, *28*(3), 392-398.

3. Härkäsalmi, T., Lehmonen, J., Itälä, J., Peralta, C., Siljander, S., & Ketoja, J. A. (2017). Design-driven integrated development of technical and perceptual qualities in foam-formed cellulose fibre materials. *Cellulose*, *24*(11), 5053-5068.

4. Al-Qararah, A. M., Ekman, A., Hjelt, T., Ketoja, J. A., Kiiskinen, H., Koponen, A., & Timonen, J. (2015). A unique microstructure of the fiber networks deposited from foam–fiber suspensions. *Colloids and Surfaces A: Physicochemical and Engineering Aspects*, *482*, 544-553.

5. Ketola, A. E., Xiang, W., Hjelt, T., Pajari, H., Tammelin, T., Rojas, O. J., & Ketoja, J. A. (2020). Bubble attachment to cellulose and silica surfaces of varied surface energies: wetting transition and implications in foam forming. Submitted to *Langmuir*.

Robust and precise identification of the hygro-expansion of single pulp fibers: a full-field fiber topography correlation approach

Niels Vonk, Marc G.D. Geers, & Johan P.M. Hoefnagels

Eindhoven University of Technology, Eindhoven, The Netherlands

Corresponding author: *Niels K Wonk <n.h.vonk@tue.nl>*

Keywords: Fiber swelling, full-field characterization, global digital height correlation, hygro-expansion, pulp

Summary

The dimensional stability of paper is a well-known problem, affection a range of engineering applications. The paper's repose to moisture variations is due to complex mechanisms that originate at the single fiber level. Therefore, a novel method is developed which allows precise and robust measurements of the full-field hygro-expansion of single fibers during wetting and drying in a single experiment. It involves taking consecutive fiber topographies while the relative humidity around the fiber is changed, subsequently correlating these topographies allows determination of the average strains (both longitudinal and transverse). The method is further extended to measure the dynamic hygro-expansion of single pulp fibers showing an overall relaxation trend in transverse surface strain.

Introduction

Softwood and hardwood pulp fibers are widely used in a range of paper-based products. Due to their hydrophilic nature, an imposed change in moisture content due to a change in relative humidity, wetting, printing, etc. results in swelling of the fibers, this greatly affects the geometric and mechanical properties. During printing applications, a moisture gradient throughout the thickness of the paper sheet causes unwanted out-of-plane deformations to occur, which are generally manifested as cockling, waviness or curling, greatly reduces the quality of the printed sheet. These macroscopic deformations are governed by the physical phenomena that occur in the

fibrous micro-structure of paper products; multi-layered cardboard is visualized using computed tomography in[1].

To progress in understanding the above-mentioned unwanted out-of-plane deformations, better understanding of the complex micro-structure during printing is required. The current literature shows that single pulp fibers tend to swell 20-30 times more in transverse direction compared to longitudinal direction, however, none of the current works were able to directly measure the longitudinal and transverse hygroscopic strains in one experiment. Therefore, in this work we developed and applied a new method for measuring the continuous full-field hygro-expansion of single pulp fibers during wetting and drying.

A Novel Method for Full-Field Single Fiber Hygro-Expansion Measurements

The considered method is divided into three sections, all schematically shown in Figure 3.24[2]:

Single fiber boundary conditions and patterning (a):
- two nylon threads to delicately fixate the single fiber providing complete freedom for the hygro-expansion of the fiber while only reducing the fiber's rigid body motion,
- a pattern of micro-particles is applied using a dedicated mystification setup[3] for a Global Digital Height Correlation (GDHC) algorithm to track.

Hygroscopic changes and measurements (b):
- an external climate box is used to regulate and log the relative humidity and temperature inside the climate chamber underneath an optical height profiler,
- change in relative humidity inside the climate box (30% < *RH* < 90%), while taking consecutive fiber topographies.

Full-field fiber topography correlation (*c*):
- the topographies are correlated using a GDHC algorithm dedicated to fiber swelling, capturing rigid body motion, homogeneous hygroscopic swelling, fiber rotation, fiber bending, obtaining full-field fiber surface displacement data, subsequently converted to full-field strain data,
- an average fiber surface strain in longitudinal (ϵ_{ll}) and transverse (ϵ_{tt}) direction is obtained from the strain data and is plotted versus the relative humidity or time.
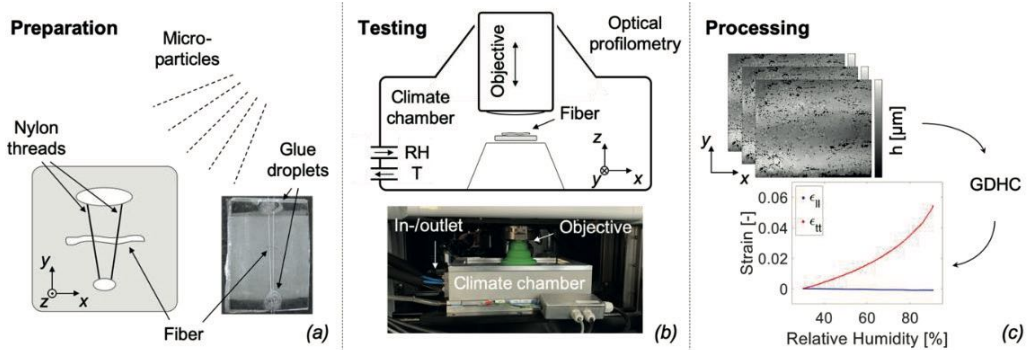
Figure 3.24. Schematic representation of the experimental procedure with: (a) the dedicated clamping method (by means of two nylon threads) of a single fiber which is sprayed with micro-particles using a dedicated mystification setup, (b) climate chamber placed underneath an optical profiler, allowing in-situ single fiber testing and (c) topographies obtained from the optical profiler are processed using Global Digital Height Correlation (GDHC) to obtain the average longitudinal and transverse surface strains of a single fiber.

Each softwood (Aspen and Fir) and hardwood (Eucalyptus) fiber is tested with a relative humidity cycle of 30 – 90 – 30 – 90 – 30 – 90 – 30 – 90 – 30, each setpoint is kept constant for 2 h and a ramp of +/- 30 %/h is used to reach the next setpoint as is shown in Figure 3.26.

The topography changes of a single softwood fiber for the first step in relative humidity (30% to 90%) is shown in Figure 3.25.
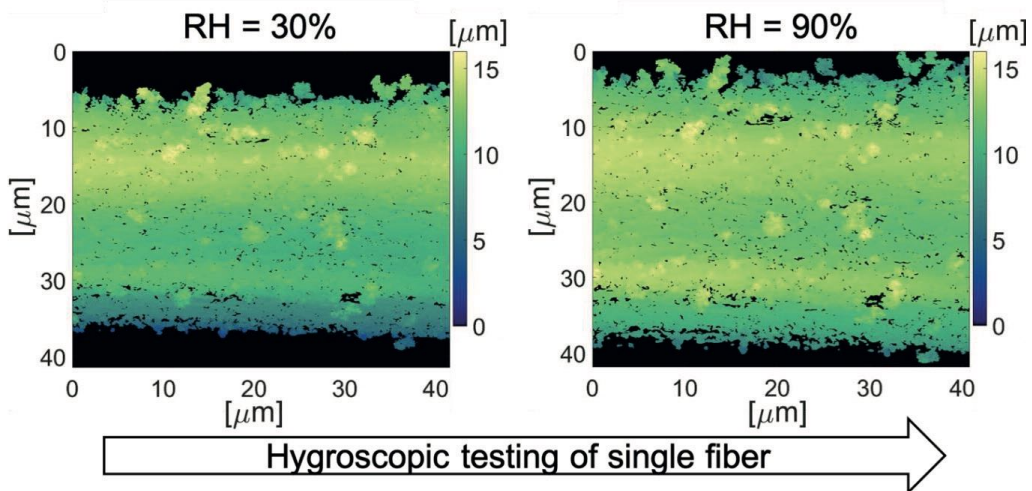
Figure 3.25. Hygroscopic testing of a single softwood fiber using optical profilometry combined with climate control. Fiber swelling is visible due to an increase in relative humidity.

Fiber swelling, because of the increase in relative humidity around the fiber, is visible. Subsequently correlating the intermediate topographies (typically 240 per setpoint change) allows identification of the continuous full-field hygro-expansion.

Results and Conclusion

Figure 3.26 shows an example of a measurement of the dynamic full-field hygro-expansion of a single softwood pulp fiber during wetting and drying.
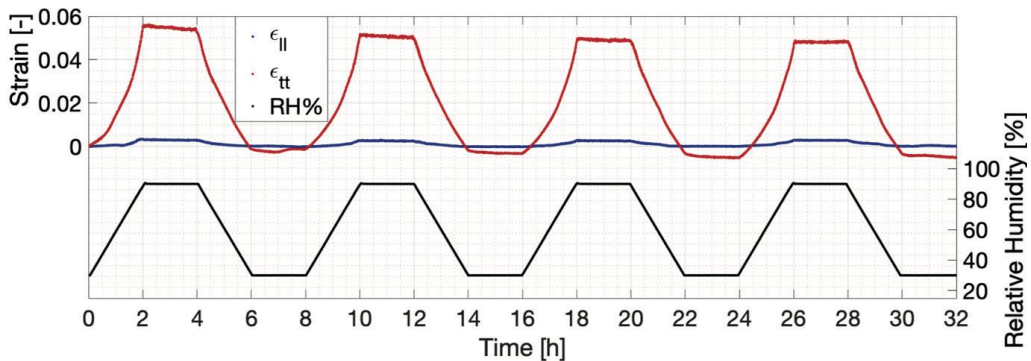
Figure 3.26. Hygroscopic strain in longitudinal and transverse direction and relative humidity as a function of time. An overall relaxation trend is visible in transverse direction.

As expected, the magnitude of hygro-expansion in transverse direction (ϵ_{tt}) is much larger than in longitudinal direction (ϵ_{ll}). Furthermore, at a relative humidity of 90%, the method allows a strain precision in, respectively, longitudinal and transverse direction of $1 \cdot 10^{-4}$ and $2 \cdot 10^{-4}$, making this method applicable to a wide range of fibers types as shown in[2].

Additionally, an overall strain relaxation trend in transverse direction is visible, possibly due to a release of internal dried-in strain, allowing the cellulose chains to order themselves.

The conducted experiments allow determination of the transverse-longitudinal hygro-expansion coefficient factor (β_t/β_l) during each wetting or drying step. Since full-field data is obtained from the experiments, a major-minor strain angle (θ) can be determined. These angles seem to correspond to the micro-fibril angle while they are in good agreement with the micro-fibril angle ranges reported in the literature[4]. All fibers show an overall relaxation trend of which a half-time (τ) value can be determined. Afterwards, a comprehensive comparison between the obtained quantities for softwood and hardwood fibers is done.

In summary, a method has been developed allowing precise full-field identification of single fibers during swelling and shrinkage, which is applied to single softwood and

hardwood fibers, giving novel insight in their hygroscopic behavior and parameter identification.

References

1. Vonk, N. H., Dekkers, E. C. A., van Maris, M. P. F. H. L., & Hoefnagels, J. P. M. (2019). A multi-loading, climate-controlled, stationary ROI device for in-situ X-ray CT hygro-thermo-mechanical testing. *Experimental Mechanics*, *59*(3), 295-308.

2. Vonk, N.H., Verschuur, N.A.M., Peerlings, R.H.J., Geers M.G.D., & Hoefnagels, J.P.M. Robust and Precise Identification of the Hygro-Expansion of Single Fibers: a Full-Field Fiber Topography Correlation Approach. Submitted for publication in 2019.

3. Shafqat, S., & Hoefnagels, J.P.M. Cool, dry, straightforward, sub-micron nebulization, DIC patterning of delicate, heterogeneous, non-planar specimen. Submitted for publication in 2019

4. Donaldson, L. (2008). Microfibril angle: measurement, variation and relationships – a review. Iawa Journal, 29, 345-386.

Wall investigations of pulp of paper flow in pipes - New model of pulp of paper flow behaviour

Salaheddine Skali Lami

Lorraine University- LEMTA, Vandoeuvre-lès-Nancy cedex, France

Corresponding: *Salaheddine Skali Lami <salaheddine.skali-lami@univ-lorraine.fr>*

Keywords: Pulp flow, shear stress, experimental flow, flow modelling

Summary

The pulp of paper is characterized by several regimes (piston flow, mixed flow and turbulent flow) during flow in the pipes. These regimes are described experimentally in the literature and are linked to the evolution of flocculation of the fibres characterizing these different regimes. However, the theoretical descriptions of these regimes are limited. We do not find a model in the literature describing the behaviour of the pulp paper flow from the plug flow at low velocities towards a behaviour identical to that of water (turbulent Newtonian flow) at high velocities passing through a drag reduction at intermediate velocities.

We give experimental studies of the pulp flow for several concentrations of fibres in two pipe diameters (assessment of confinement effects). The results are comparable to a model describing the behaviour of paper in all regimes.

The proposed model is based on the calculation of an average shear stress, which takes into account both the elastic moduli of the flocs, and of the network of fibres (agglomerates of flocs) and on the other hand, the viscosity of the modified fluid (water) with dispersed fibres.

Introduction

The investigations of the pulp of paper flow in pipes have been subject of numerous studies since the 50s[1,2,3,4] to understand various regimes of paper pulp including drag reduction. Other objectives are the description of the friction coefficients of the flow of the pulp of paper. Moller[5], on the basis of an elastic behaviour of the network of fibres

and a Newtonian behaviour of the liquid film which surrounds, showed that the evolution of the wall shear stress changes with the bulk velocity to power1/3. Current investigations are moving towards determining the rheological characteristics of the pulp of paper as the apparent viscosity, the yield stress and the elastic moduli (see summary of different works[6]). Despite the difficulties of measurements (non-homogeneous suspensions, containment ...) the authors give orders of magnitudes of these properties and their evolution as a function of the concentration and nature of the fibres. In these rheological investigations the measuring device, where the torque linked to the wall shear stress and the shear rate linked to the velocity, gives the constitutive law. This is valid for a homogeneous fluid but for pulp of paper, we encounter many problems due to the heterogeneity of the suspension. In the case of pipe flow, the wall shear stress can be deducted from the pressure loss against the etermination of the wall shear rate must use electrochemical techniques[7,8]. The measurements obtained by the authors show that the behaviour of the paper pulp close to the wall is Newtonian whatever the flow rate and whatever the concentration. In fact, the two variables vary non-linearly with the flow rate, but remain a constant ratio in average over time. This suggests that in the modelling approaches must, near the wall area, to consider the viscosity of water modified by dispersed fibres.

Experimental

Materials
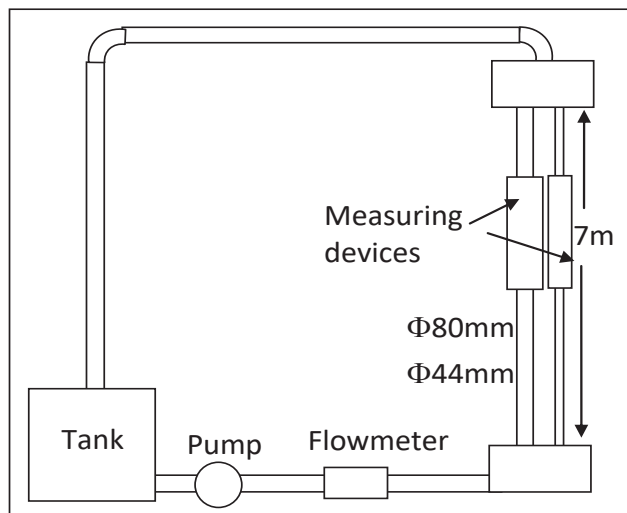
Figure 3.27. Experimental setup

The experimental setup (Figure 3.27) is composed of a tank, pump, flow meters, and two vertical pipes 7m in length and 80mm and 44mm diameters.

Each of the pipes is equipped with an instrumented element by wall platinum electrochemical probes ($\varnothing$ 0.5mm).

Method

The fibre suspension is realized in an electrochemical solution of water, potassium ferricyanide (Co = $2 \cdot 10^{-3}$ M/l), potassium ferrocyanide (2 * Co) and potassium chloride 1/3 M/l.

Determining the wall shear rate is obtained from the mass transfer equation of a potassium ferricyanide on the parietal microelectrode:

$$\frac{\partial C}{\partial t} + \vec{U}.\vec{\nabla}\,C = D\,\Delta C \quad where \begin{cases} * \; C \; is \; the \; concentration \; of \; potassium \; ferricyande \\ * \; U \; velocity : Ux = \gamma\,y \; ; \; and \; Uy = -\frac{y^2}{2}\frac{\partial \gamma}{\partial x} \\ * \; \frac{\partial^2 C}{\partial x^2} \ll \frac{\partial^2 C}{\partial y^2} \\ * \; x \; is \; the flow \; direction \; and \; y \; is \; the \; normale \; to \; the \; wall \\ * \; \gamma \; is \; the \; local \; wall \; shear \; rate \end{cases}$$

This equation to determine the mass flux was solved by Hanratty[9] and therefore the electrical current collected at a microelectrode in the case of a high Schmidt number. $I \approx \gamma^{\frac{1}{3}}$ The measurement of current gives the instantaneous value of the local wall shear rate.

Theoretical analysis

We use theoretical approach to the calculation of the average stress resulting from that of a Newtonian fluid σ_{ij}^{w} in the liquid film of thickness δ and an elastic stress σ_{ij}^{f} in the radius of fibers of network (R-δ):

$$\sigma_{ij} = -\frac{\delta_{ij}}{V}\int_{V-\Sigma Vo} p\,dV + \sigma_{ij}^{f}\left(1 - \frac{\delta}{R}\right)^2 + \sigma_{ij}^{w}\left(2 - \frac{\delta}{R}\right)\frac{\delta}{R}$$
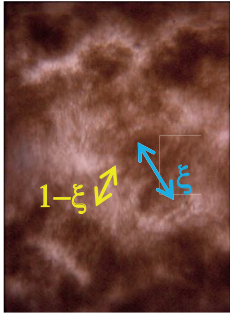
The elastic stress in the network can be described by a portion due to the splats and another portion surrounding floc because the elasticises are not the same:

$$\sigma_{ij}^{f} = \sigma_{ij}^{f1}(1-\xi) + \sigma_{ij}^{f2}\xi$$

We can deduct from this equation the mean shear elasticity modulus:

$$G = G_{\infty} + (G_0 - G_{\infty})\xi$$

Figure 3.27. Network

This expression is similar to the Zener elasticity model, where ξ can be modelled by a kinetic 1 order according to the Reynolds number and a critical Reynolds number

Also at the interface of the network of fibres, we can write the continuity of the tangential stresses where the network is assumed as a viscoelastic behaviour:

$$\tau = \tau_0 + \mu(c)\frac{V}{\Delta} = \tau_0 + \mu(c)\frac{V}{R\frac{\Delta}{R}}$$

and

$$\tau_0 = \tau\left(1-\frac{\Delta}{R}\right) \text{ and } N = E\frac{\Delta}{R} = 2\left(\frac{\tau}{G}\right)^2$$

Where τ_o : yield stress, N:normal stress E : elastic modulus $\approx$ G and Δ: mean thickness of liquid film (large deformation of the network

$$\frac{\Delta}{R} = \int_0^{\frac{\delta}{R}} \frac{d\left(\frac{\delta}{R}\right)}{\left(1-\frac{\delta}{R}\right)})$$

and μ(c) is the shear viscosity in liquid film. We use theoretical approach given by Dinh & Amstrong[10]:

$$\mu(c) = \mu_w\left(1 + \frac{4C\left(\frac{l}{d}\right)^2}{90\,Ln\sqrt{\frac{\pi}{C}}}\right)$$

Where μ_w: viscosity of water, l/d: aspect ratio of fibre ($\approx$ 100) and C the concentration of fibres (0.3 % $\leq$C$\leq$ 2 %).

Solving all these equations allows establishing the evolution of wall shear stress as a function of the mean velocity for various concentrations of fibres and for the two pipe diameters. The comparison between experimental results and this model is given in Figure 3.28.
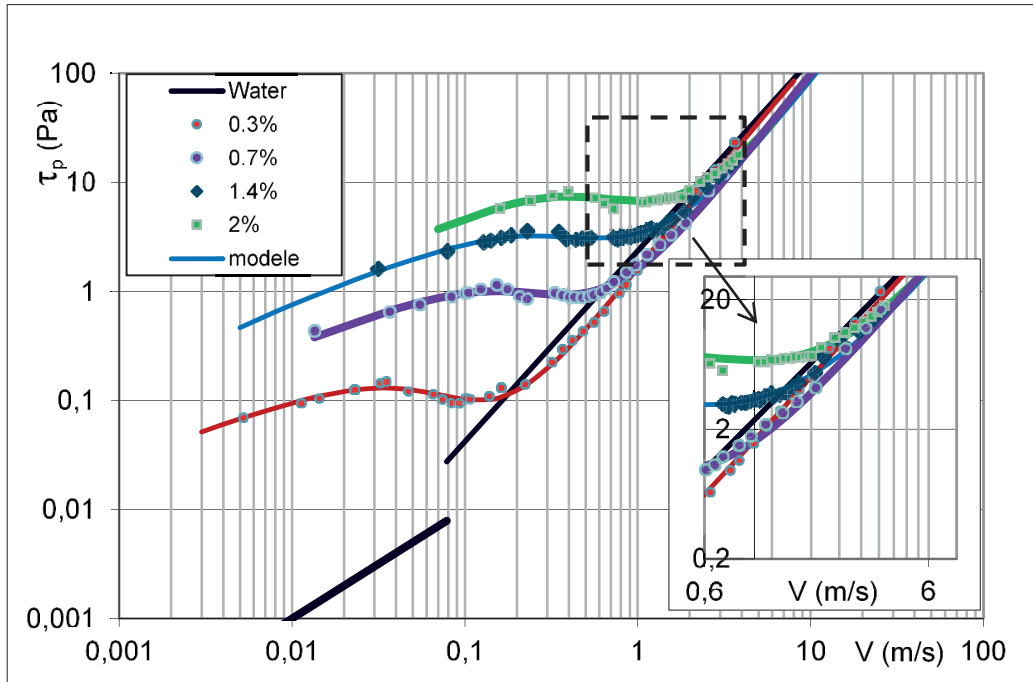
Figure 3.28. Wall shear stress vs mean velocity (pipe ϕ 80mm)

In Table 3.3, we postponed, versus the fibre concentration, the values of elasticities obtained by identification and those viscosities calculated by Dinh&Amstrong[10] equation. The critical Reynolds number is take equal to 5000 and the values of G_∞ and G_o obtained by identification to the experimental values. These elasticities change with the concentration to the power 3, and allow an estimate the number of fibre-fibre bonds[11].

Table 3.3. Elasticities G_∞ and G_o and viscosities used

C %	0,3	0,5	0,56	0,73	1,1	1,35	1,7	2
G_o (Pa)	1,39	2,20	6,09	13,36	15,84	44,88	82,47	177,85
G_∞ (Pa)	0,15	0,33	0,91	2,18	3,00	9,47	16,14	19,44
fibre-fibre bonds	0,2	0,4	0,5	0,9	2,0	3,2	5,1	7,0
μ (C) *10^3 (Pa.s)	1,33	1,58	1,68	1,93	2,45	2,96	3,52	4,05

Conclusions

The proposed model is highly nonlinear but allows describing all the behaviour of the flow of pulp with three adjustable parameters, which are the thickness of the liquid film at rest, the elasticity of flocs and the elasticity of dispersed fibres. These values allow an estimate the number of fibre-fibre bonds and gives "matton formation" at a fibre

concentration of 10%. The viscosity in the liquid film is take equal to that water modified by dispersed fibres. This model allows, according to the concentration and the flow velocity, to evaluate the characteristics of the turbulence in the flow.

References

1. Mason, S. G. (1948). The flocculation of cellulose fibre suspensions. Pulp Paper Mag. Can, 49(3), 99-104.

2. Takeuchi, N., Senda, S., Namba, K., & Kuwabara, G. (1983). Formation and destruction of fibre flocs in a flowing pulp suspension. Appita, 37(3), 223-230.

3. Kerekes, R. J., & SCHELL, C. (1983). Pulp flocculation in decaying turbulence: a literature review. Journal of Pulp and Paper Science, 9(3), 86-91.

4. Duffy, G. G. (2006). Measurements, mechanisms and models: Some important insights into the mechanisms of flow of fibre suspensions. Annual Transactions-Nordic Rheology Society, 14, 19.

5. Moller, K., Duffy, G. G., & Titchene. Al. (1971). Laminar plug flow regime of paper pulp suspensions in pipes. Svensk Papperstidning-Nordisk Cellulosa, 74(24), 829.

6. Derakhshandeh, B., Kerekes, R. J., Hatzikiriakos, S. G., & Bennington, C. P. J. (2011). Rheology of pulp fibre suspensions: A critical review. Chemical Engineering Science, 66(15), 3460-3470.

7. Skali-Lami, S. (1991). Contribution à l'étude de l'écoulement de pâte à papier: einteraction floculation turbulence (Doctoral dissertation).

8. Ogawa, K., Yoshikawa, S., Suguro, A., Ikeda, J., & Ogawa, H. (1990). Flow characteristics and circular pipe flow of pulp-suspension. Journal of chemical engineering of Japan, 23(1), 1-6.

9. Hanratty, T.J., & Campelle, J.A. (1983). Measurement of wall shear stress. Fluid mechanics measurements Goldstein R.J. (ed.), Hemisphere Publishing Corp. Ch. 11 p 559.

10. Dinh, S.M., Amstrong, R. G. (1984). A rheological equation of semi-concentrated fiber suspension. J. Rheol. 28(3), 207-227.

11. Hirn, U., & Schennach, R. (2015). Comprehensive analysis of individual pulp fiber bonds quantifies the mechanisms of fiber bonding in paper. Sci*entific reports*, *5*(1), 1-9. https:doi.org/10.1038/srep10503

Dynamics of capillary rise in sinusoidal corrugated channels

Amin Shobeiri, & Mauricio Ponga

Department of Mechanical Engineering, The University of British Columbia, Vancouver, Canada

***Corresponding author:** Amin Shobeiri <aminshobeirie@gmail.com>*

Keywords: Paper towels, embossing patterns, corrugated channel, capillary rise

Summary

We develop an analytical model for the dynamics of capillary rise in sinusoidal corrugated channels with variable separation of the plies as an extension to Washburn's equation of capillary action, and consequently investigate the effect of corrugation on the height and rate of meniscus rise. Validation is made with the known Washburn solutions for a flat channel. The model is suitable for simultaneous structural coupling of the walls to model the deformation of the plies observed during the absorption in paper towel products, where a complicated interplay of ply expansion and elastocapillary coalescence is observed in the experiments.

Introduction

The need for low cost, high-performance consumer products such as towel and hygiene products, based on sustainable materials, is strong and growing due to an increased sensitivity to the environment, the industrialization of densely populated countries, and the growing global population[1]. New uses of, and markets for paper towel products, including adult incontinence in the aged, are emerging in Canada and worldwide[2]. Paper towel products are a strategic and rapidly growing market worldwide for Canadian industry[2], with \$1.7B revenue in 2016 and projected to grow at 1.5% in 2017 with increasing long-term demand. Innovating the next generation of absorbent products requires a fundamental scientific understanding on how novel material compositions (furnishes and additives) and modern processes influence the properties such as enhanced bulk, absorption, and wet-strength properties. Also, minimizing the environmental impact through the use of new biomaterial alternatives for petroleum-based super-absorbent polymers is desired.

Paper towels, introduced in North America in the 1920s, are replacing textile-derived products world-wide as low-cost alternatives, and saving water in some developing countries[1]. They are environmentally sustainable, easily degradable, and recyclable products. Low density (< 300 kg/m^3) and grammage (< 50 g/m^2), low strength and stiffness, high tensile stretch, and high bulk compared to office-grade printing paper are some of the features of these products. However, unlike textile products, paper towels have limited wet strength and have to be used initially dry. The absorption rate (how fast a spill is absorbed) and the absorbency (retained sucked volume of liquid) set the market price[2,3]. Hence, understanding how microscopic features in paper towels affect these properties could provide valuable information in the design of new ultra-absorbent paper towel-related products. In this work, we seek to understand the effect of the corrugation of the paper plies in the capillary rise in paper towels[4,5,6,7]. To do so, we develop an analytical model where the fluid flow is controlled by the capillary pressure that appear between plies and at the liquid-air interface. The goal is to compare the height and rate of fluid rise between the flat, tapered, and corrugated channels.
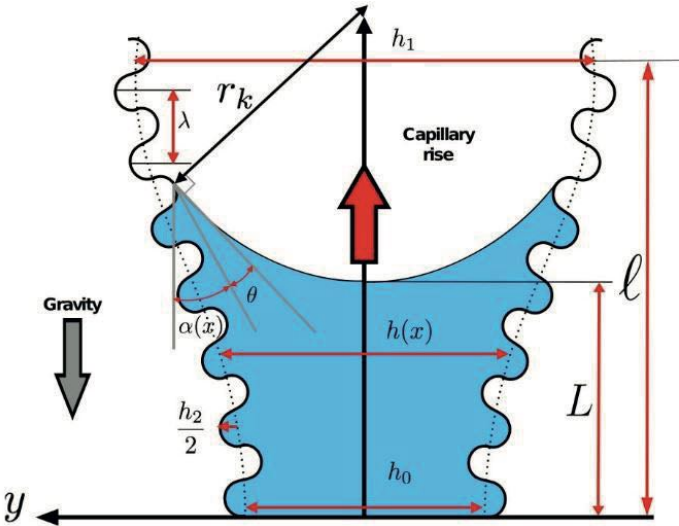
Figure 3.29 Schematic of the problem considered.

Methodology

Let us now consider a channel bounded by some impermeable and sinusoidal solid walls as shown in Figure 3.29. The sinusoidal profile can be used to model the embossing pattern that is performed on paper towels. We distinguish several quantities of interest in the schematic picture. Particularly, we observe that the separation of the channels is a function of the vertical coordinate which we arbitrarily have selected to coincide with the *x*-axis. The varying separation between the walls due to the wicking in the paper towel can be simplified as a prescribed linear tapering of a sinusoidal profile, expressed as:

$$h(x) = h_0 + (h_1 - h_0)\frac{x}{\ell} + h_2 \sin(\frac{\pi x}{\lambda}) \tag{1}$$

where h_0 and h_1 are the wall separation at the origin and at the free end, respectively (thereby being able to model either positive or negative tapering), ℓ is the total length of the channel capable of liquid absorption, h_2 is the amplitude of the sinusoidal corrugations used to represent the roughness of the channel, and λ is the periodic length of this sinusoidal profile. In Figure. S3.29 two angles are shown, i.e., θ which is the liquid-solid contact angle between the free surface of the liquid and the wall, and $\alpha(x)$ which is the angle between the channel and the vertical axis. One may now find the relation between the curvature of the meniscus and the geometry of the wall. In order to do so, we draw the triangle that contains the wall, the meniscus, and the radius of curvature, r_k. It is easy to notice that:

$$\cos(\alpha(x) + \theta) = \frac{h(x)}{2r_k}, \qquad r_k = \frac{h(x)}{2\cos(\alpha(x) + \theta)}. \tag{2}$$

The tangent to the surface of the wall can be expressed as a function of the channel separation length with respect to the mid-plane, i.e.

$$\tan(\alpha(x)) = \frac{1}{2}\frac{dh(x)}{dx} = \frac{(h_1 - h_0)}{2\ell} + \frac{h_2 \pi}{2\lambda}\cos(\frac{\pi x}{\lambda}). \tag{3}$$

Using Eq. 3 and the formula for the sum of two angles, after some algebraic manipulation, we obtain a closed-form solution for the radius of curvature:

$$r_k = \frac{h_0 \left(1 + d_3\xi + d_4 \sin(\frac{\pi x}{\lambda})\right)\left[1 + (d_1 + d_2\pi \cos(\frac{\pi x}{\lambda}))^2\right]^{\frac{1}{2}}}{2\left(\cos(\theta) - \sin(\theta)\left[d_1 + d_2\pi \cos(\frac{\pi x}{\lambda})\right]\right)}, \tag{4}$$

where $d_1 = \Delta h/\ell$, $d_2 = h_2/\lambda$, $d_3 = \Delta h/h_0$, $d_4 = h_2/h_0$, and $\xi = x/\ell$ are dimensionless geometrical features. Next, we find the capillary pressure in the sinusoidal wall profile for any arbitrary point x through Young-Laplace equation ($P_{sc} = \sigma_l(\kappa_1 + \kappa_2)$, with κ_i being the principal curvatures of the surface). For a cylindrical meniscus surface, one of the principal radii is r_k and the other converges to infinity for wide enough channels. This eventually leads to:

$$P_{sc} = \frac{\sigma_l}{r_k} = \frac{2\sigma_l \left[\cos(\theta) - \sin(\theta)(d_1 + d_2\pi \cos(\frac{\pi x}{\lambda}))\right]}{\left[h_0 \left(1 + d_3\xi + d_4 \sin(\frac{\pi x}{\lambda})\right)\right]\sqrt{1 + [d_1 + \pi d_2 \cos(\frac{\pi x}{\lambda})]^2}}, \tag{5}$$

where σ_l is the liquid-air surface tension at the interface. Before analyzing the results of the corrugated channel, we ensure that the asymptotic behavior of Eq. 5 converges to known solutions. For instance, for a flat channel, the capillary pressure, as computed with the previous equation, reduces to the known solution $P_{sc} = (2\sigma_l \cos\theta)/h_0$.

The behavior of the capillary pressure is seen in Figure 3.30 left. Let us now examine the *dynamics* of the capillary rise in the sinusoidal channel. The movement of liquid in the channel can be calculated with Poiseuille's equation of 1-D flow in a channel, in the form of:

$$Q = \iint_A u(y, h(x))dA = \int_{-h(x)/2}^{h(x)/2} \frac{b}{8\eta} \frac{\partial P}{\partial x}[h(x)^2 - 4y^2]dy, \tag{6}$$

where Q is the volumetric flow, b is the width of the channel, and $A = bh(x)$ is the cross-sectional area of the channel. $u(y, h(x))$ is the vertical upward velocity field for a given point (x, y). Integration of the right-hand side of the Eq. 6 leads Eq. 7. Details can be find in[8].

$$Q = \frac{b}{12\eta} \frac{\partial P}{\partial L} h(L)^3 = \frac{b}{12\eta} \frac{\Delta P}{\int_0^L \frac{dx}{h(x)^3}}. \tag{7}$$

The volumetric flow within the channel is equal to the rate of change of the absorbed volume of liquid. Since the upper bound of the integral is a function of time, using Leibniz rule of integration with varying bounds yields another expression for the volumetric flow:

$$Q = \frac{d}{dt}V = \frac{d}{dt}\int_0^{L(t)} bh(x)dx = bh(L)\frac{dL}{dt}, \tag{8}$$

Equating the right-hand side of Eqs. 7 and 8 leads to an expression for the rate of the rise in the meniscus height (L) (Figure 3.30 right):

$$\frac{dL}{dt} = \frac{\Delta P}{12\eta h(L) \int_0^{L(t)} \frac{dx}{h^3(x)}}. \tag{9}$$

Having found the rate in Eq. 9, the interest in evaluation of the meniscus height as a function of time eventually leads to a non-linear *integro-differential* equation, given below:

$$12\eta \dot{L}h(L)\int_0^L \frac{dx}{h^3(x)} = \Delta P(x, L). \tag{10}$$

Eq. 10 is notoriously difficult to solve for $L(t)$. However, the ever-upward driving capillary force and neglecting the effect of inertia which is inherently applied through Washburn's assumptions[9], leads to the fact that the meniscus height is a one-to-one function of time, hence an inverse exists. If there is no gravity involved, the driving pressure difference $\Delta P(x, L) = P_{sc} - \rho g L$ equates with the capillary pressure (P_{sc}) itself, thereby being independent of the meniscus height (L). With recourse to this necessary simplification, the the problem could be reformulated in an inverse way to find the elapsed time as a function of the meniscus height:

$$t(L) = \int_0^L \frac{12\eta}{P_{sc}(x)} h(x)I(x)dx, \tag{11}$$

where $I(x) = \int_0^x dX/h(X)^3$ is a nested integral function within the main integral and X represents its dummy variable. Eq. 11 is evaluated through numerical integration in this work.

$$P_{sc} = \frac{2\sigma_t\left[\cos(\theta)\ \sin(\theta)(d_1 \mid d_2\pi\cos(\frac{2x}{\lambda}))\right]}{\left[h_0\left(1+d_3\xi+d_1\sin(\frac{2x}{\lambda})\right)\right]\sqrt{1+[d_1+\pi d_2\cos(\frac{4x}{\lambda})]^2}}.$$

- $h_2 = 0$
- $h_2 = 50\ \mu m$
- $h_2 = 100\ \mu m$
- $h_2 = 150\ \mu m$
- $h_2 = 200\ \mu m$
- $h_2 = 250\ \mu m$
- $h_2 = 300\ \mu m$
- $h_2 = 0,\ h_1 = h_0$

$$\frac{dt}{dL} = \frac{12\eta h(L)}{\Delta P}\int_0^L \frac{dx}{h(x)^3}.$$

$dt/dL\ (x)$

- $h_2 = 0$
- $h_2 = 50\ \mu m$
- $h_2 = 100\ \mu m$
- $h_2 = 150\ \mu m$
- $h_2 = 200\ \mu m$
- $h_2 = 250\ \mu m$
- $h_2 = 300\ \mu m$
- $h_2 = 0,\ h_1 = h_0$
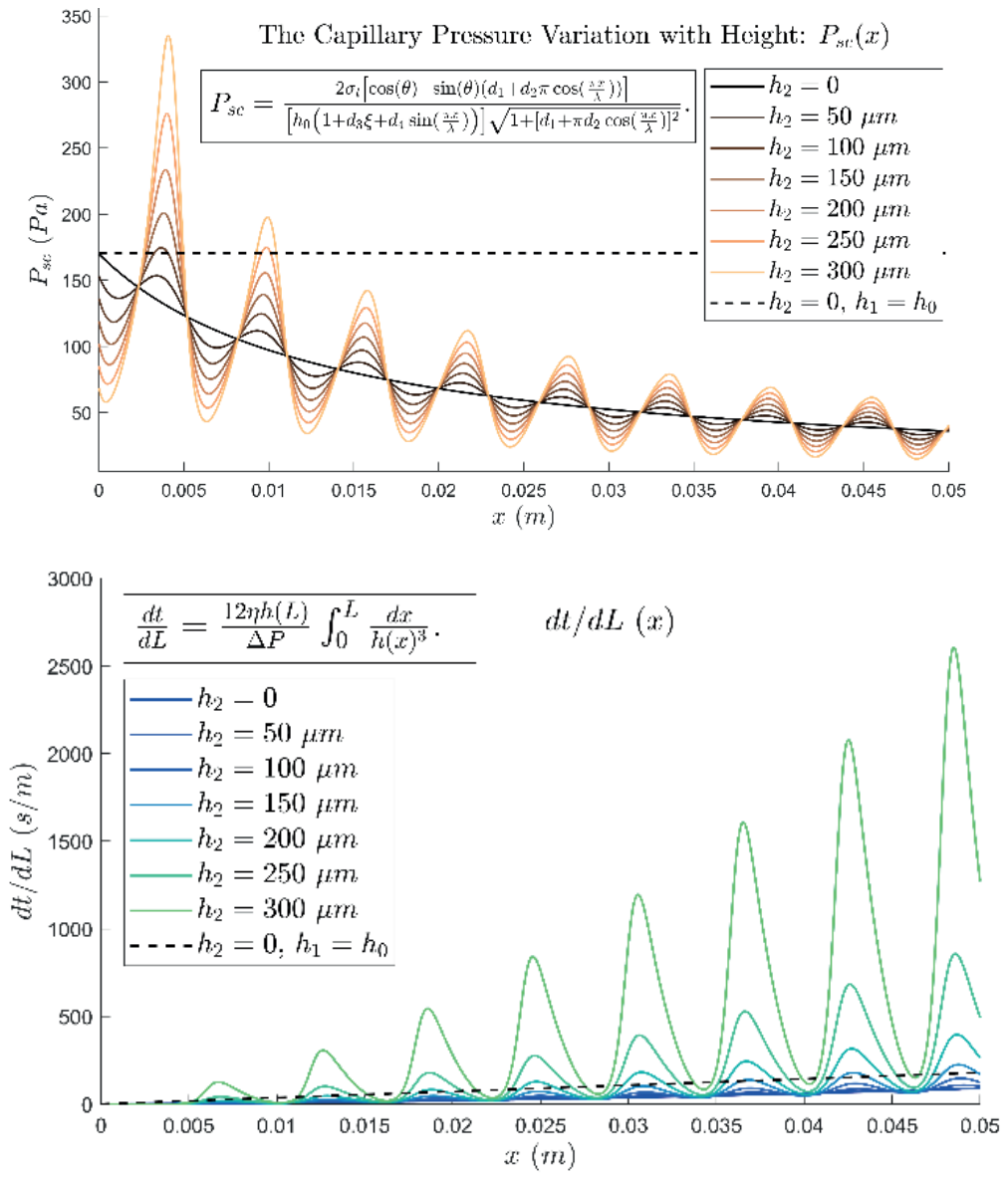
Figure 3.30. From top to bottom, capillary pressure (P_{sc}), plotted against length (x) for various corrugation amplitudes and inverse rise rate of meniscus height (dt/dL). In both plots, $h_2 = 0$ indicates that the channel is flat, i.e. no corrugation, but steel tapered ($h_1 \neq h_0$). The dashed line, on the other hand, in both plots represents the non-corrugated, non-tapered flat channel, where $h_1 = h_0$ and $h_2 = 0$. This special condition verifies the known Washburn's solutions constant for capillary pressure and linear variation of the inverse rate for a simple channel.

Figure 3.31 shows the meniscus rise as a function of time. The results indicate that corrugation of the channel slows down the rise rate. This is explained by looking at Figure 3.30 (bottom)

where the inverse rate is significantly larger for a corrugated channel in comparison with a flat one. Moreover, the osmotic pressure will tend to compress the channel, even with corrugations, leading to an *elastocapillary coalescence.*
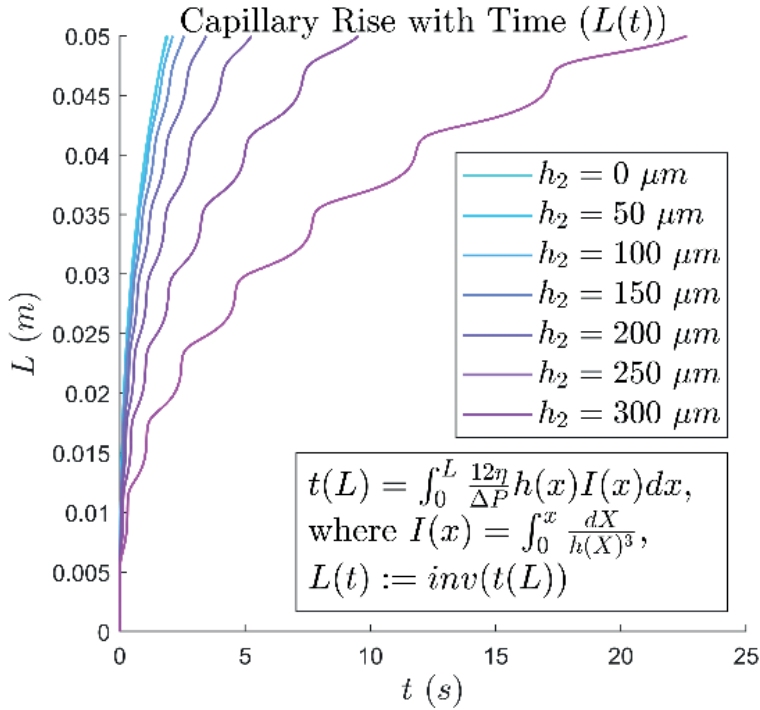
Figure 3.31. The height of the meniscus as a function of time, plotted for various corrugation amplitudes.

Conclusions

Our results indicate that corrugated and tapered channels show reduction in the rate of raise of the meniscus high in comparison with flat channels. Future work may include investigating the effects of the residual stresses in the plies of paper towels and the coupled interplay of the capillary rise and ply expansion[10,11], when the plies are considered – differently from this work, permeable as a poroelastic material. Thus, the problem then constitutes a fluid-structure interaction problem, the fact that is observed in the experiments during the liquid absorption process that might be the reason behind the positive effect of the embossing patterns on the absorbency.

Acknowledgement

References

1. Karnik, M. (2016). Forget the mug. Toilet paper is not on a roll in India. Quartz. Available at: https://qz.com/india/655977/forget-the-mug-toilet-paper-is-on-a-roll-in-india/

2. Uuhela, E. (2016). IBIS World Industry Report. RISI Global Tissue outlook.

3. IBIS World Industry Report (2019)

4. Rice, J. R., & Cleary, M. P. (1976). Some basic stress diffusion solutions for fluid-saturated elastic porous media with compressible constituents. Reviews of Geophysics, 14(2), 227-241.

5. Selvadurai, A. P. S. (1996). Mechanics of Poroelastic Media, Springer.

6. Skotheim, J. M., & Mahadevan, L. (2004). Dynamics of poroelastic filaments. Proceedings of the Royal Society of London. Series A: Mathematical, Physical and Engineering Sciences, 460(2047), 1995-2020.

7. Biot, M. A. (1964). Theory of buckling of a porous slab and its thermoelastic analogy.

8. Staples, T. L., & Shaffer, D. G. (2002). Wicking flow in irregular capillaries. Colloids and Surfaces A: Physicochemical and Engineering Aspects, 204(1-3), 239-250.

9. Washburn, E. W. (1921). The dynamics of capillary flow. Physical review, 17(3), 273.

10. Kvick, M., Martinez, D. M., Hewitt, D. R., & Balmforth, N. J. (2017). Imbibition with swelling: capillary rise in thin deformable porous media. Physical Review Fluids, 2(7), 074001.

11. Mirzajanzadeh, M., Deshpande, V. S., & Fleck, N. A. (2019). Water rise in a cellulose foam: By capillary or diffusional flow?. Journal of the Mechanics and Physics of Solids, 124, 206-219.

.

Wednesday 2.9.2020 at 8:45 - 9:45

Session 5
Plenary talk by
Anna Suurnäkki

Towards circular forest-based bioeconomy: case Bioproduct mill

Session chair: Tero Tuovinen

Towards circular forest-based bioeconomy: case Bioproduct mill

Anna Suurnäkki

Metsä Fibre, Espoo, Finland

Corresponding: *Anna Suurnäkki <anna.suurnakki@metsagroup.com>*

Keywords: Bioproduct mill, industrial ecosystem, circular bioeconomy

Globally, there is a growing need of food, energy, water and materials. This need combined with the raw material scarcity and climate change issues calls for major change in the current economic model. Circular bioeconomy targeting to recycling and long-living use of bio-based materials could be part of the solutions when tackling these challenges. Wood from sustainably managed forests is a potential raw material basis for circular bioeconomy. All parts of the wood need to be used efficiently into added-value products. Wood logs can be converted to sawn timber and wood products for use in e.g. construction. Pulpwood can be used for pulp and other bioproducts and bark, branches and top can be converted to renewable energy.

Efficient and added-value utilization of all the wood material entering the pulp mill has been the basis when Metsä Group has developed its Bioproduct mill concept. In the heart of this concept is a most modern kraft pulp mill with high energy efficiency, low emissions and minimal specific water consumption. The mill is not using fossil fuels and it generates maximum amount of bioelectricity. The first of a kind Bioproduct mill was started in Äänekoski, Finland, in 2017[1].

The Bioproduct mill concept includes the possibility to enlarge the mill product portfolio. In addition to current pulp applications such as different papers, paperboard and tissue, pulp is a potential starting material for various other value chains such as textiles and biocomposites. Part of the lignin and other side stream components could also be applied to material or chemical applications. A living industrial ecosystem is an important part of the Bioproduct mill concept. It makes it possible to efficiently exploit the all the mill streams for value added end-uses and contributes thus to the circular bioeconomy.

Active basic and applied research carried out globally in both bio-based materials and chemicals is expected to open up opportunities for new applications for pulp fibres and other wood based components in the future. When aiming at reuse and recycle and from single use to multiuse products the important aspect of ecodesign should be included in all the stages of development. New wood-based product innovations taking into consideration technical, economic, environmental and regulatory aspects will promote the sustainable and circular forest-based bioeconomy.

Reference:

1. MetsäFibre, Äänekoski bioproduct mill. https://www.metsafibre.com/en/about -us/Production-units/Bioproduct-mill/Pages/default.aspx

Session 6A

Nanofibrillated cellulose

Session chair: Heinz-Joachim Schaffrath

Do wet kraft fibres have a gel-like surface?

Annika Ketola[a], Miika Leppänen[b], Tuomas Turpeinen[a], Petri Papponen[b], & Elias Retulainen[a]

[a]*VTT Technical Research Centre of Finland Ltd, Jyväskylä, Finland*
[b]*University of Jyväskylä, Jyväskylä, Finland*

Corresponding author: Elias Retulainen <*elias.retulainen@vtt.fi*>

Keywords: Fibre surfaces, gel-like layer, nanofibrillated cellulose, microfibrillated cellulose, helium ion microscope

Summary

The mechanical properties of refined wet fibre surface was studied by assuming that the fibre surface is basically composed of micro- and nanofibrillated cellulose. The dynamic mechanical properties of microfibrillated cellulose show that already at consistencies below 2% it is clearly gel-like material. Comparison of wet fibre surface and CMF by using helium ion microscopy revealed their structural similarity and make possible to conclude that the fibre surface is gel-like material.

Background and approach

Cellulose fibres are a biomaterial extracted from green plants that possess high strength and tendency to form networks. They have drawn a lot of attention during the past few years in the field of biomaterial development as they are potential environmental friendly alternative for plastics and could be used in applications, such as extensible packaging materials, filtering and insulation[1,2,3,4]. Intensive material development is ongoing and the understanding of the material properties is essential. Even though cellulose fibres have been studied for decades, some fundamental questions remain open. One of these questions concerns chemical and physical state of fibre surface in water; what it looks like and how does it behave? The importance of the question relates to the ever-interesting phenomenon of fibre-fibre bonding and how they are created during papermaking. Fibre-fibre bonds are the main structural component of the formed network and the nature and number of the bonds determines the final strength and flexibility of the material[5,6,7]. A better understanding of the conditions on fibre surface in wet state would provide new insights to the molecular

and fibril level mechanisms behind the creation of fibre bonding and new tools for material development.

It has been generally concluded that fibres surfaces are rough and porous, consisting of a gel-like layer of hydrated fibrils and hemicelluloses (Figure 6.1.) [8,9,10,11]. It has also been proposed that bonding between fibres are caused by macrofibrils, micro- and nanofibrils, and chains of cellulose molecules of various lengths[12]; and that the cellulose surface affects the arrangement of water molecules in its vicinity. However, the gel-likeness of the fibre surfaces is challenging to study with microscopy. Most imaging techniques demand dry conditions, and the drying process completely alters the state of the fibre surface. Luckily, imaging and sample preparation methods have developed during the recent years. New methods enable both the preservation of the original sample structure and the high resolution imaging without conductive coating.

In this study, we made an assumption that the surface of a beaten kraft pulp fibre is basically made of micro and nanofibrillated cellulose. By studying the dynamic mechanical properties of the CMF and CNF we can obtain information of the mechanical properties of the fibrillated fibre surface and its potential gel-likeness. By using microscopy we can visually compare the characteristics of the wet fibre surface and wet CMF. A new powerful imaging technique, i.e. Scanning Helium Microscopy (HIM) was used for the imaging.
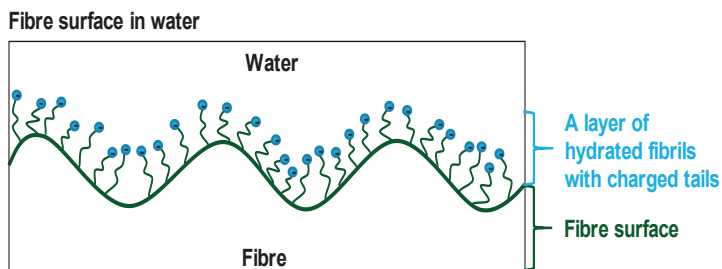
Figure 6.1. Illustration of a rough fibre surface in water. Surface is covered with hydrated fibrils with charged end groups pointing towards the water forming a gel-like layer[8].

Bleached softwood kraft fibres (refined to SR 25), fibrillated cellulose-materials (CNF and CMF) and carboxymethyl cellulose (CMC) were dried with mild drying techniques: critical point drying and cryofixing in liquid-propane followed by freeze drying. This way the fibril structure was preserved as it is in the wet state. Dried samples were imaged with HIM and images of CNF and CMF were compared with images of fibre surfaces. In addition, dynamic mechanical analysis under oscillatory shear was conducted to characterize viscoelastic properties of fibrillated cellulose-materials. In terms of rheology, gel is a viscoelastic material, which possess both viscous and elastic component under a stress. In the experiment, the storage modulus (G') and loss modulus (G") of the material were determined and the ratio between G' and G'' was

used to characterize the material properties. A dispersion can be assumed to be a gel when the elastic properties dominate over the viscoelastic behaviour, i.e. G' > G'' and phase angle (δ) 45° > δ > 0° degrees[13].

Results

The phase angle for fibrillated celluloses was around 10°, meaning that they behaved like gels under the applied stress (Figure 6.2a). The gel like behaviour was also observed in frequency sweep measurements where G' was higher than G'' and did not depend on the used frequency (Figure 6.2b). The materials were measured at 1.1% and 1.7% consistency (CNF and CMF, respectively). The gel point of oxidised CNF has been measured to be as low as 0.4%[14]. When the dry solid content of the material is increased, the storage modulus increases and the gel becomes more solid[15]. In the consistencies used in this study, the materials were clearly gel-like and well above the critical gel-point.
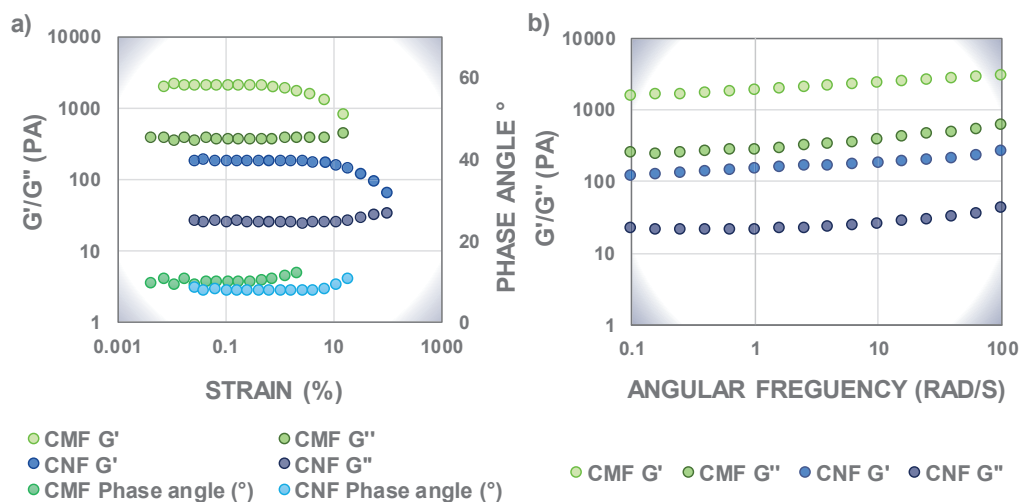
Figure 6.2. The gel like behaviour of fibrillated cellulose materials. The definition of a gel is: G' > G'' and phase angle (δ) 45° > δ > 0°. a) Oscillation amplitude-sweep of CMF (green) and CNF (blue). b) Frequency sweep of CMF (green) and CNF (blue).

HIM was successfully used to image fibrillated cellulose materials, fibres and CMC without coating. Very loose fibrillated material was observed on the refined fibre surfaces being unevenly distributed so that part of the fibre surfaces were fully covered with it and part being just bare S2 layer. The loose fibril material had clear similarities with CMF. This indicates that in wet state, fibre surfaces behave similarly that CMF and can be considered to be gel-like (Figure 6.3.). Already a low amount of fibrils could result gel-likeness on the fibre surface due to their low gel point[14]. However, the fibril consistency affects the storage modulus of the fibril gel. It can be also concluded that

local variations in the fibril consistency causes variations also in the rheology and gel-likeness of the fibre surfaces.

In addition, one batch of fibres was treated with CMC and HIM was used to detect the adsorbed CMC on fibres. The detection of CMF on fibre surface with HIM was not obvious, but according to visual estimation, the loose fibril material on fibre surfaces was more gauze-like with CMC addition and seemed to increase the fine fibril content. CMC is defined as gel-like material, which could indicate that CMC adsorption increases the gel-likeness of the fibre surface.

Refined kraft fibre
with fibrillated surface

CMF

CMF gel

Scale 10 µm

Scale 10 µm
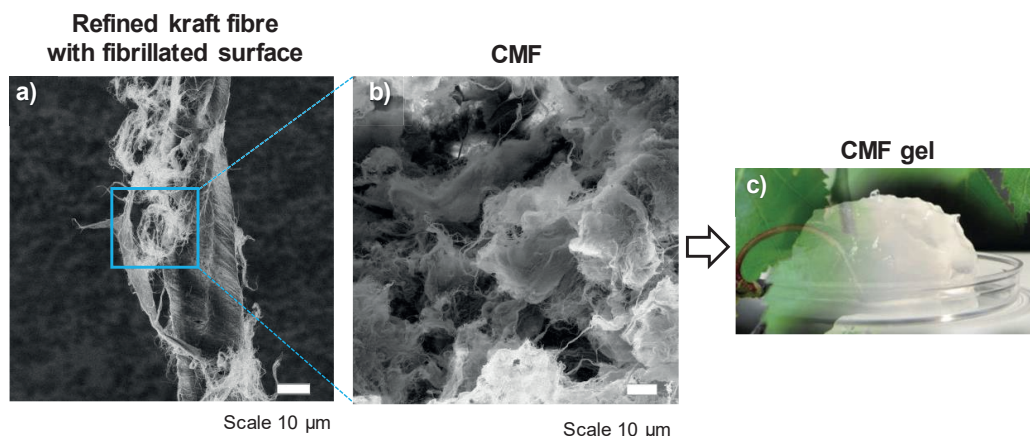
Figure 6.3. Refined kraft fibre surfaces and cellulose microfibrils (CMF) are very similar when dried with critical point drying and imaged with Helium ion microscope (HIM). HIM images of a) refined kraft fibres and b) CMF. c) CMF is a gel-like material, which could indicate that fibre surfaces are as well.

Even though HIM was successfully used to image fibrillated cellulose materials there were some challenges in sample preparation and imaging[16]. During preparation with cryofix, samples needed to be placed into the cryo-liquid without excessive drying during the transfer. With CPD, there were multiple solvent exchange steps that needed to be conducted without affecting the sample surface. Samples showed some surface waviness in the images, which was most probably caused by sample handling and liquid fluctuations during the drying. In addition, cellulose fibrils tended to degrade easily under ion beam when imaging with high magnification. This problem was severe especially with CNF. CMC seemed to be more resistant to the ion beam than fibrillated cellulose.

Conclusions

1. Surface of beaten kraft pulp fibres have a close resemblance to fibrillated cellulose materials (CNF and CMF), which can be used as model materials for approximating the dynamic mechanical properties of fibrillated fibre surface.

2. CMF and CNF materials have low gel point, meaning that already a low amount of fibrils can result gel-likeness on the surface.

3. HIM studies show large local variations in the gel-likeness along fibre surface.

4. Cationic polymer (CMC) has an increasing effect on the gel-likeness.

5. Oxidised CNF and CMC gels after cryofixation show a great resemblance.

6. There is a limit for imaging of wet fibrillated cellulosic structures with HIM at high magnifications because the required dehydration process and cellulose degradation under the ion beam may limit the detection of finest structures.

Acknowledgement

References

1. Khakalo, A., Vishtal, A., Retulainen, E., Filpponen, I., & Rojas, O. J. (2017). Mechanically-induced dimensional extensibility of fibers towards tough fiber networks. *Cellulose*, *24*(1), 191-205.

2. Vishtal, A., Retulainen, E., Khakalo, A., & Rojas, O. J. (2015). Improving the extensibility of paper: Sequential spray addition of gelatine and agar. *Nordic Pulp & Paper Research Journal*, *30*(3), 452-460.

3. Heydarifard, S., Nazhad, M. M., Xiao, H., Shipin, O., & Olson, J. (2016). Water-resistant cellulosic filter for aerosol entrapment and water purification, Part I: production of water-resistant cellulosic filter. *Environmental Technology*, *37*(13), 1716-1722.

4. Pöhler, T., Jetsu, P., & Isomoisio, H. (2016). Benchmarking new wood fibre–based sound absorbing material made with a foam-forming technique. *Building Acoustics*, *23*(3-4), 131-143.

5. Borodulina, S., Kulachenko, A., Galland, S., & Nygårds, M. (2012). Stress-strain curve of paper revisited. *Nordic pulp & paper research journal*, *27*(2), 318-328.

6. Page, D. H. (1969). A theory for the tensile strength of paper. *Tappi*, *52*, 674-681.

7. Page, D. H. (1971). The structure and properties of paper, Part II. Shrinkage, dimensional stability and stretch. Trens 18(13-19, 6-11

8. Pelton, R. (1993). A model of the external surface of wood pulp fibers. *Nordic Pulp & Paper Research Journal*, *8*(1), 113-119.

9. Kibblewhite, R. P. (1973). Effect of beating on wet web behaviour. Appita 26(5), 341-347

Ketola, A., Leppänen, M., Turpeinen, T., Papponen, P., & Retulainen, E.

.

10. Belle, J., & Odermatt, J. (2016). Initial wet web strength of paper. *Cellulose*, *23*(4), 2249-2272.

11. Myllytie, P., Holappa, S., Paltakari, J., & Laine, J. (2009). Effect of polymers on aggregation of cellulose fibrils and its implication on strength development in wet paper web. *Nord Pulp Pap Res J*, *24*(2), 125-134.

12. Clark, J. D. A. (1984). New thoughts on cellulose bonding. *TAPPI journal*, *67*(12), 82-83.

13. Goodwin, J. W., & Hughes, R. W. (2008). *Rheology for chemists: an introduction*. Royal Society of Chemistry.

14. Arola, S., Ansari, M., Oksanen, A., Retulainen, E., Hatzikiriakos, S. G., & Brumer, H. (2018). The sol–gel transition of ultra-low solid content TEMPO-cellulose nanofibril/mixed-linkage β-glucan bionanocomposite gels. *Soft matter*, *14*(46), 9393-9401.

15. Pääkkö, M., Ankerfors, M., Kosonen, H., Nykänen, A., Ahola, S., Österberg, M., ... & Lindström, T. (2007). Enzymatic hydrolysis combined with mechanical shearing and high-pressure homogenization for nanoscale cellulose fibrils and strong gels. *Biomacromolecules*, *8*(6), 1934-1941.

16. Ketola, A. E., Leppänen, M., Turpeinen, T., Papponen, P., Strand, A., Sundberg, A., ... & Retulainen, E. (2019). Cellulose nanofibrils prepared by gentle drying methods reveal the limits of helium ion microscopy imaging. *RSC advances*, *9*(27), 15668-15677.

The effect of consistency on the shear rheology of aqueous suspensions of cellulose micro- and nanofibrils

Antti Koponen

VTT Technical Research Centre of Finland Ltd, Jyväskylä, Finland

Corresponding author: *Antti Koponen <Antti.Koponen@vtt.fi>*

Summary

While the raw material type and the production method of cellulose micro- and nanofibrils (CMNF) strongly affect the absolute values of the rheological parameters of their aqueous suspensions, the dependence of these parameters on consistency, c, is uniform. The reason behind this is the strong entanglement of fibrils; the flow dynamics of typical CMNF suspensions is dominated by interactions between fibril flocs and not by interactions between individual fibrils.

Cellulose micro/nanofibrils (CMNFs), or micro/nanofibrillated cellulose, has been a topic of academic interest since the 1980's due to their unique properties, such as mechanical robustness, barrier properties, high specific surface area, lightness, and complex rheology. More recently, CMNFs have also been perceived as a versatile, sustainable, and biodegradable material that enables developing eco-friendly all-cellulose products. The industrial interest in CMNFs has recently increased also due to the rising number of commercially available CMNFs grades and due to innovations that have lowered the production costs of these materials.
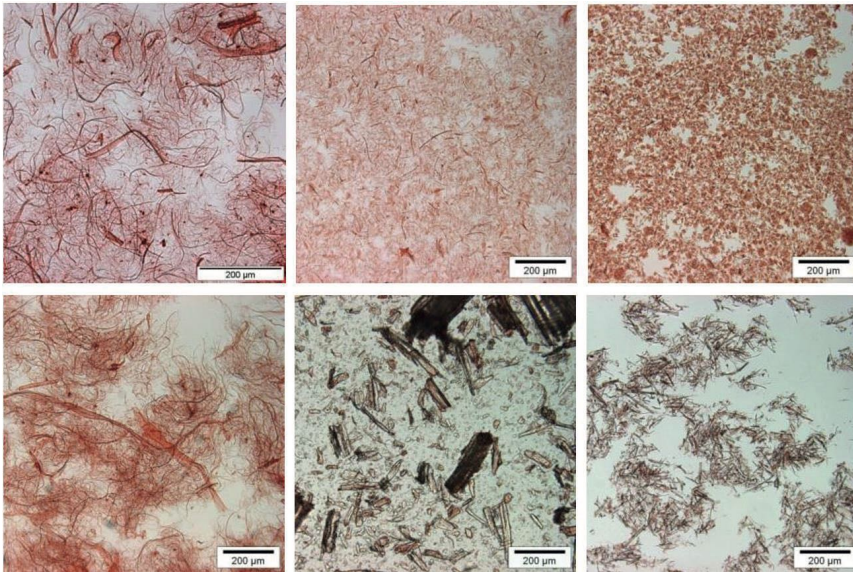
Figure 6.4. Examples of various types of CMNF fibrils. Top row from left to right: Celish (commercial grade), fluidized Celish, in-house grade 1. Bottom row from left to right: in-house grade 2, Arbocel C100 (commercial grade), fluidized Arbocel C100.

CMNFs fibrils can be isolated from wood or plant cell walls with a purely mechanical or chemical treatment, or with a chemical or enzymatic pretreatment followed by a mechanical treatment. The fibrils may greatly differ in size and morphology depending on the fibrillation method used (see Figure 6.4). Typically, the lateral dimension of fibrils is on the nanometer scale, and the length is up to several micrometers. The aspect ratio and the number of fibril-fibril contacts can, thus, be very high. The specific surface area is also much higher than for regular cellulose fibers. For these reasons, CMNF suspensions can form yield-stress gels already at approx. 0.1 - 0.3% consistency. Above the gel point CMNF suspensions are shear thinning materials, and their viscous behavior is usually well described by the power law

$$\mu = K\dot{\gamma}^{n-1}.$$

(Above parameter K is called consistency index and parameter n flow index.)

Factors that affect the rheological properties of CMNF suspensions fall into several categories. One is morphology, which includes fibril flexibility and shape, length and diameter distributions, aspect ratio, fibrillation, and network/floc structure. Another factor is the surface-chemical composition of the fibrils, which can affect surface charge and the colloidal interactions between them. Both morphology and surface composition can depend on the processes of treatments used to prepare the material.

The most universal parameter that affects CMNF rheology is indisputably mass consistency. While the values of parameters K and n have been reported for CMNF suspensions in numerous studies, there are few studies where the dependence of the consistency index, the flow index and the yield stress on consistency has been studied systematically. This review aims to fill this gap[1].

The shear rheology of various CMNF suspensions was found to be surprisingly similar. This suggest that the shear rheology of CMNF suspensions is more universal than has previously been realized. While the raw material type and the production method of CMNFs strongly affected the absolute values of the rheological parameters of their aqueous suspensions, the dependence of these parameters on consistency, c, was uniform. The consistency index and flow index followed generally the scaling laws $K \sim c^{2.4}$ and $n = 0.3 \times c^{-0.4}$, respectively. Moreover, the yield stress of CMNF suspensions scaled as $\tau_y \sim c^{2.3}$.

The variability of the scaling law parameters of CMNF suspensions found in the literature is obviously not so much due to real differences in the physical behavior of the suspensions rather than due to experimental uncertainties and to general difficulties in measuring the rheological behavior of these suspensions rigorously[2,3]. Here the biggest source of uncertainty is slip flow at the walls of the flow geometry. The reason behind the universal rheological behavior at mesoscopic and macroscopic scales might be the strong entanglement of fibrils; the flow dynamics of typical CMNF suspensions is dominated by interactions between fibril flocs and not so much by interactions between individual fibrils.

References

1. Koponen, A. I. (2020). The effect of consistency on the shear rheology of aqueous suspensions of cellulose micro-and nanofibrils: a review. Cellulose, 1-19. https://doi.org/10.1007/s10570-019-02908-w

2. Turpeinen, T., Jäsberg, A., Haavisto, S., Liukkonen, J., Salmela, J., & Koponen, A. I. (2020). Pipe rheology of microfibrillated cellulose suspensions. Cellulose, 27(1), 141-156. https://doi.org/10.1007/s10570-019-02784-4

3. Haavisto, S., Salmela, J., Jäsberg, A., Saarinen, T., Sorvari, A., & Koponen, A. (2015). Rheological characterization of MFC using optical coherence tomography. Tappi Journal, 14(5), 291-302.

.

.

Laminated high strength cellulose structures

Vesa Kunnari[a], Jaakko Pere[a], Kirsi Kataja[a], Ali Harlin[a], & Heidi Turunen[b]

[a]*VTT Technical Research Centre of Finland Ltd, Espoo, Finland*
[b]*Aalto University, Espoo, Finland*

Corresponding author: *Vesa Kunnari <Vesa.Kunnari@vtt.fi>*

Keywords: Laminated, nanocellulose, all-cellulose, solid structure

Summary

An up-scalable method to produce laminated high strength cellulose structures combining nanocellulose and cellulose was developed. To demonstrate the method interior design elements were produced. Bending strength of produced samples were measured and compared to properties of reference materials with superior results. Surface of structures was finished using patters, 3D-forms or pictures.

All material components in these novel cellulose structures were derived from wood and were bio-based. Thus structures are sustainable omitting no hazardous components and hence are completely recyclable and biodegradable.

Introduction

Formaldehyde containing adhesive systems are commonly used in wood based board production due to simple and well-known processing routes, low cost of raw materials and manufacturing. Environmental aspects and consciousness of consumers have increased the research and interest towards alternative systems and even biomaterial originating glues.

Wood based cellulose is the largest cellulose source on earth, and it has been used in paper and board manufacturing dating back for centuries. Cellulose nanofibrils (CNF) are one of the most interesting nanoscale biomaterial available from nature. Cellulose nanofibrils have different characteristics depending on the fibre origin and processing method. CNF can be liberated from various plant fibers using mechanical forces, chemical treatment, enzymes or combinations of these. The most typical mechanical methods include homogenization, microfluidization, microgrinding or cryocrushing.

Kunnari, V., Pere, J., Kataja, K., Harlin, A., & Turunen, H.

After fibrillation the width of micro/nanofibrils is typically between 5 to 20 nm and length from hundreds of nanometers to several micrometers, even exceeding 5 µm. The aspect ratio may therefore exceed 250. The aspect ratio contributes to high strength of nanocellulose network structure and possible to composite materials containing nanofiber networks[1,2,3]

Nanocellulose is typically in the form of water suspension and shows gelation at concentrations as low as 1 or 2%. Normally cellulose nanosuspensions have been used to make films by filtering the suspension using vacuum to obtain a wet gel followed by evaporation of water[4,5,6.] Fibrils are mechanically tangled and as the water evaporates capillary forces attract individual nanofibers together followed by secondary attraction forces, including hydrogen bonding. Films and structures made from CNF in general have comparable tensile strength to aluminium although the surface appearance is paper-like.

Particle board and MDF production adhesives based on natural resources have no significant commercial importance. Main research interest have concentrated on soy-based adhesives as well as lignin and tannin based adhesives. The main adhesive systems used in the European wood-based panels industry today are UF, MUF, PF and PMDI adhesives[7].

Alternative for bio-based adhesive and traditional boards could use all-cellulose structure based on combining carton board using special type of nanocellulose as glue. The approach is able to produce structures having superior bending strength compared to chip board and MDF. Even slightly higher bending strength compared to softwood veneer can be reached.

Nanocellulose fibrils are impregnated into carton board structure during manufacturing to produce a hybrid-structure consisting of cellulose fibres and nanoscale fibres within the board structure. Impregnated nanocellulose suspension softens the carton board enabling surface patternng of the structure.

This study focused on a novel manufacturing technology to produce solid structures from carton board and nanocellulose. Structures may find use as alternative for domestic dividing walls instead of gypsum and chip board, office separation walls being light and sound absorbing, furniture frames. Surface finishing could take advantage of embossed patters, printed pictures or regular painting.

Nanocellulose used was made using a novel manufacturing technology[8] to produce nanocellulose suspension showing much higher solids content, up to 10%, compared to typical nanocellulose water suspensions of 1 or 2%[1]. The high solid nanocellulose suspension was used to coat individual carton board layers followed by stacking of layers, wet pressing and drying.

Experimental section

Preparation of high consistency CNF

Bleached softwood pulp from a Finnish pulp mill (MetsäFibre, Äänekoski, Finland) was used as the raw material for producing CMF at high consistency (HefCel). The enzymatic treatment was carried out at a consistency of 25% (dw) for 6h at 70°C, pH 5 using a two shaft sigma mixer (Jaygo Incorporated, NJ, USA) running at 25 rpm. The pulp batch size was 300g (dw). After the treatment enzyme activity was stopped by increasing temperature of the mixer to 90°C for 30min. The fibrillated material was diluted with deionised water, filtered and washed thoroughly with deionised water. Finally, the fibrillated material was dewatered to a consistency of 18% by filtration. Yield of the fibrillated material was 90%. The material was stored at +4°C until used.

Preparation of CNF used as glue

Fibrillated CNF material was diluted with deionized water to a concentration of 100 g/L. The fibril suspension was dispersed for 60 minutes using Diaf-mixer at 3000 rpm. After 60 minutes a sorbitol plasticizer, D-sorbitol CAS 50-7-4 (30% from amount of dry fibrils) was added and dispersion continued for 30 minutes.

When preparing the all-cellulose structure nanocellulose was applied to individual carton board layers having thickness of approximately 500 microns. Applied wet layer of nanocellulose for single side of each carton board used in the study was approximately 500 microns. To produce structures used in strength measurements having 12 mm final thickness after pressing, 24 individual carton board sheets were stacked. Stacking was followed by wet pressing for 10 minutes. Drying was done in heat cabinet at 105 °C for at least 12 h under 10 kg weight. After drying structures were cooled in ambient conditions under weight to prevent curling caused by re-absorbing air moisture

Results and discussion

An up-scalable method to produce novel structures combining nanocellulose and cellulose was developed. To demonstrate the method interior design elements were produced. Bending strength properties surpassed the reference materials. Surface of structures was finished using patters, 3D-forms and pictures.

All material components in these novel cellulose structures are derived from wood and are bio-based. Thus structures are sustainable omitting no hazardous components and hence completely recyclable. At the end of life structures are bio-degradable and compostable.

CMF produced in high consistency can be used as glue once diluted to ~ 100 g/L consistency. The viscosity at this consistency level is comparable to the viscosity of homogenized and microfluidized nanocellulose at a concentration of 0.5%. The difference in viscosity is due to lower aspect ratio of high consistency CMF. High solids make it possible to add the CMF on carton boards without excess water. During wet pressing stage normally only water containing very little amount of nanocellulose is existing the stacked structure.   Drying time was not evaluated during this study but a time long enough (12 hours) to evaporate all water in the cellulose structures was applied. By incorporating proper industrial scale methods the drying time should be suitable for production scale implementations.

Cross-section microscopic images showed at least partial saturation of nanocellulose into stacked carton boards. The coated surfaces were recognizable in the structure as well. The carton boards acted as a carrier for the nanocellulose and enhanced the ductility of the whole structure while nanocellulose provided the strong intermediate layers.

No limit for the amount of stacked layers was identified in the study. However since drying water evaporation during lab scale study was occurring under weights water evaporation was occurring only from the sides. Therefore water evaporation is much slower compared to condebelt type of drying or drying happening between moving wires. Up to one hundred individual layers were stacked on top of each other resulting in 50 mm thick pile when dried nanocellulose experiences high shrinkage forces. Sorbitol plasticizer was added to nanocellulose to decrease shrinkage forces. When working without plasticizer the structures were more easily twisted after drying.

Finished laminated structures were finished using woodworking tools such as drilling, milling and sawing. The surface finishing quality was close to MDF. Following finishing to correct size some structures were printed using ink-jet printing. Printing quality and properties were comparable to paper.

Conclusions

Novel, up-scalable method to produce structures combining nanocellulose and cellulose was developed. To demonstrate the method interior design elements were produced. The strength properties surpassed the reference materials. Surface of structures was finished using patters, 3D-forms and pictures.

Laminated structures produced combining may provide interior architecture and building a new eco-friendly option that is bio-based and fully recyclable. Technology will be developed further to provide enhanced water tolerance for structures and even higher bending strength.

References

1. Pääkkö, M., Ankerfors, M., Kosonen, H., Nykänen, A., Ahola, S., Österberg, M., ... & Lindström, T. (2007). Enzymatic hydrolysis combined with mechanical shearing and high-pressure homogenization for nanoscale cellulose fibrils and strong gels. *Biomacromolecules*, *8*(6), 1934-1941.

2. Saito, T., Kimura, S., Nishiyama, Y., & Isogai, A. (2007). Cellulose nanofibers prepared by TEMPO-mediated oxidation of native cellulose. *Biomacromolecules*, *8*(8), 2485-2491.

3. Wågberg, L., Decher, G., Norgren, M., Lindström, T., Ankerfors, M., & Axnäs, K. (2008). The build-up of polyelectrolyte multilayers of microfibrillated cellulose and cationic polyelectrolytes. *Langmuir*, *24*(3), 784-795.

4. Taniguchi, T., & Okamura, K. (1998). New films produced from microfibrillated natural fibres. Polymer International, 47(3), 291-294.

5. Dufresne, A., Cavaillé, J. Y., & Vignon, M. R. (1997). Mechanical behavior of sheets prepared from sugar beet cellulose microfibrils. *Journal of applied polymer science*, *64*(6), 1185-1194.

6. Yano, H., & Nakahara, S. (2004). Bio-composites produced from plant microfiber bundles with a nanometer unit web-like network. *Journal of Materials Science*, *39*(5), 1635-1638.

7. Mantanis, G. I., Athanassiadou, E. T., Barbu, M. C., & Wijnendaele, K. (2018). Adhesive systems used in the European particleboard, MDF and OSB industries. *Wood material science & engineering*, *13*(2), 104-116.

8. Hiltunen, J., Kemppainen, K., & Pere, J. Process for producing fibrillated cellulose material, WO2015092146., https://patentscope.wipo.int/search/en/detail.jsf?docId=WO2015092146

Drying of cellulose nanofibrils without losing its functionality and fibrillary structure

Jani Lehmonen[a], Aayush Jaiswal[b], Kirsi Immonen[c], & Tuomo Hjelt[b]

[a]*VTT Technical Research Centre of Finland Ltd, Jyväskylä, Finland*
[b]*VTT Technical Research Centre of Finland Ltd, Espoo, Finland*
[c]*VTT Technical Research Centre of Finland Ltd, Tampere, Finland*

Corresponding author: *Tuomo Hjelt <*Tuomo.Hjelt@vtt.fi*>*

Keywords: Nanocellulose, drying, film, thermoplastic

Summary

All current drying methods of cellulose nanofibrils (CNF) create aggregates leading difficulties in re-dispersion. We have developed method to dry fibrillary nanocellulose without losing the functionality of the nanofibrils. Dried CNF can be re-dispersed to water or it can be used as a dry powder in processes that do not tolerate water.

Introduction

Nanocellulose have a wide range of applications. In the short term, the biggest usage will be in paper and board industry but in the longer terms, composites start to dominate. Other large application areas will be in paints and coatings[1].

In order to boost the expected growth in these applications, drying of cellulose nanofibrils should be tackled because typically this material contains a lot of water (up to 98%). If drying of CNF will not be solved, it might be the bottleneck for the growth of nanocellulose-based businesses.

The main benefit of our method is producing re-dispersible cellulose nanofibril material that maintains its functionality after drying and re-dispersing phases. Some application areas require materials to be dry. Extra water ruins easily the production process. One such area is composite materials, which is predicted to be one of the major areas for nanocellulose utilization[1]. Thus, this drying method opens up new application areas for cellulose nanofibril materials.

Drying method

The drying method works as follows (Figure 6.5). Foaming agent is first added to the CNF solution, which is then transferred, with a pump to a foam generator. In addition, application related additives to functionalize the CNF surface can be added in this stage. The generator applies pressurized air and high shear forces to the solution producing high air content foam (70%-90%). Foam is transferred to a foam applicator, which spreads foam to the moving felt. The felt material is such that CNF does not stick to it during drying. The felt is then run through driers. After CNF is dried, it can be collected from the felt. The structure of the foam prohibits the filming of the CNF. For that reason, dried CNF is re-dispersible without losing its functionality.
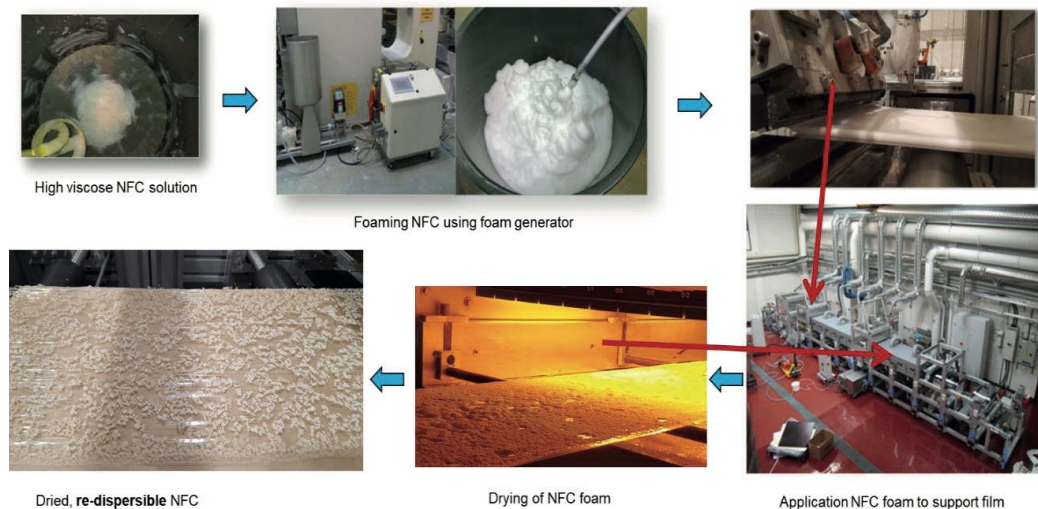
Figure 6.5. The CNF drying process using VTT pilot facilities.

Application proof of concepts

In the current study, the dried and re-dispersed cellulose nanofibrils was used to increase strength of a board structure and as an additive material in composite material. In addition, dried nanocellulose was used in film casting.

Dispersion to water

2 wt% suspensions of foam dried CNF were made by re-dispersing the powders into water using an Ultra Turrax disperser for 10 minutes at 10 000 rpm. Before mixing with the Ultra Turrax, antifoam chemical was added in order to prevent foaming. 0.5 ml of

1% Congo red dye was mixed with 0.5 ml of each suspension to dye the fibers and make them visible with an optical microscope.
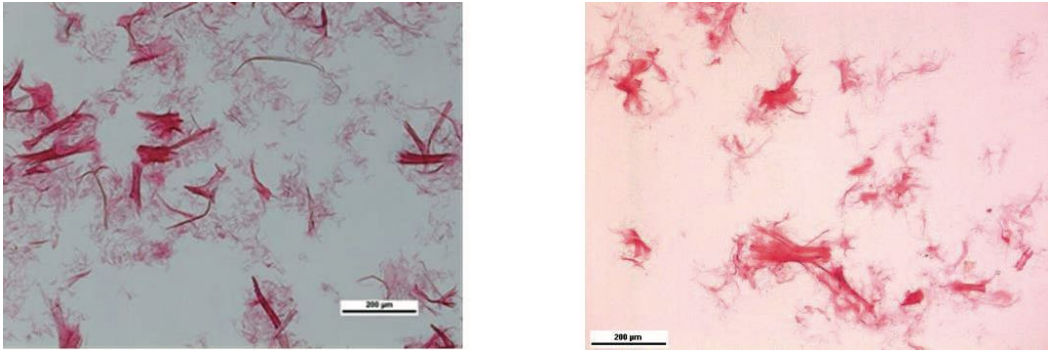
Figure 6.6 Never dried reference CNF (left) and dried and re-dispersed CNF

As seen in Figure 6.6 dispersion to water works very well. In right hand side picture one sees only bigger particles, thus all fibrillary material is dispersed to water without making aggregates detectable with optical microscope.

Increasing the strength of board material

We used the re-dispersed CNF to increase Z-strength of laboratory paper sheets. For comparison, we used also never dried wet CNF. The results are shown in Figure 6.7, which shows that the functionality of CNF was maintained during drying: the re-dispersed CNF gave roughly the same increase in Z-strength as never dried wet CNF compared to the reference sheet without CNF addition.
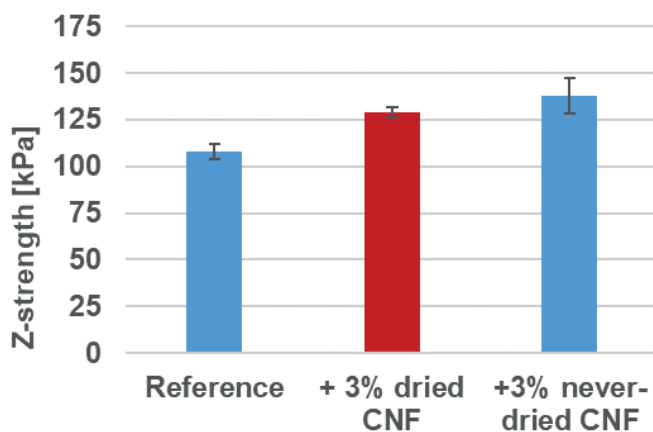
Figure 6.7 Dried CNF gave the same increase in Z-strength as same never dried wet CNF.

Film casting using re-dispersed MFC

The second proof of concept is film casting using same pilot coating line as was used to dry the CNF[2]. In Figure 6.8 is the result our trials. We were able to make CNF film in dynamic roll-to-roll environment. Making a film is a very tough test for re-dispersed CNF. The filming of the CNF is based on self-alignment of individual fibrils, thus filming requires very good re-dispersion properties of dried CNF.

Figure 6.8 CNF film made of re-dispersed CNF

Increasing the impact strength of composite

The third proof of concept is the manufacturing of composites. We used pilot scale compounder and injection molding devises[3]. This method tolerates only very small amount of water, thus dried CNF is the only option for this kind of composite manufacturing. We were able to use dried CNF as such, without any pre-treatment of it. The CNF was compounded with PLA (30% CNF / 70% PLA). From the resulting pellets, samples were made using injection molding device.
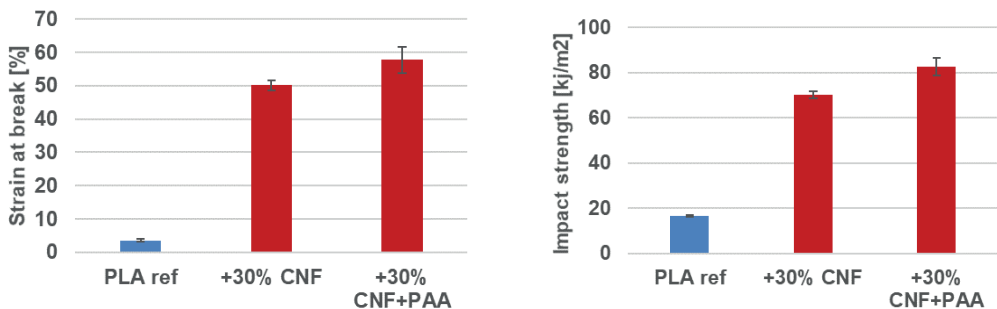
Figure 6.9 The strain at break (left) and the impact strength[4] (right) for the pure PLA samples and samples containing 30% CNF. In the third test point dispersion aid PAA was added before drying phase.

In Figure 6.9 is shown the strain at break and the impact strength of the prepared samples. The added CNF clearly changes the properties of composite. PLA as such is hard and brittle material. When CNF is added, it becomes very flexible. These results are very different compared to previous results of freeze-dried CNF where only tensile strength was slightly improved[3].

Conclusions

We have developed method to dry fibrillary nanocellulose without losing the functionality of the nanofibrils. Dried nanocellulose can be re-dispersed to water or it can be used as a dry powder in processes that do not tolerate water. The latter open up new application areas to fibrillary nanocellulose.

The developed process is an environmentally friendly water-based process. Furthermore, the solution uses only existing technologies with commercially available additives. This enable fast upscaling of the technology from the pilot scale to industrial scale.

Acknowledgements

References

1. Future Markets (2018). The Global Market for Nanocellulose 2018-2027, Feb.

2. Orelma, H., Korpela, A., Kunnari, V., Harlin, A., & Suurnäkki, A. (2017). Improving the mechanical properties of CNF films by NMMO partial dissolution with hot calender activation. Cellulose, 24(4), 1691-1704.

3. Immonen, K., Lahtinen, P., & Pere, J. (2017). Effects of surfactants on the preparation of nanocellulose-PLA composites. Bioengineering, 4(4), 91.

4. ISO, B. (2010). 148-1: 2010 Metallic Materials. Charpy pendulum impact test. Part 1, Test method.

.

Wednesday 2.9.2020 at 10:00 - 12:00

Session 6B

Fibres and fibre bonds

Session chair: Atsushi Tanaka

Decoupling the effect of fiber orientation and drying conditions on the anisotropy of the mechanical properties of paper

Mossab Alzweighi[a], Rami Mansour[a], Jussi Lahti[b,c], Ulrich Hirn[b,c], & Artem Kulachenko[a]

[a]*KTH Royal Institute of Technology, Stockholm, Sweden*
[b]*Institute of Paper, Pulp and Fibre Technology, Graz University of Technology, Graz, Austria*
[c]*CD Laboratory for Fiber Swelling and Paper Performance, Graz, Austria*

***Corresponding author:** Artem Kulachenko <artem@kth.se>*

Summary

In this work, we investigate the contribution of the fiber anisotropy and drying conditions to the overall anisotropy of mechanical properties of the commercially produced sheet. Detailed experimental measurements were performed to define the local structural properties, namely thickness, density, fiber orientation angle, and anisotropy of sack paper specimens. To establish a relationship between the anisotropy and the constitutive response of fiber network a micromechanical simulation tool was employed. Using the experimental measurements and the constitutive response of the simulated fiber network, we were able to decouple the effect of the anisotropy and orientation of the sample with respect to the drying. The results suggest that the impact of the drying conditions on the mechanical performance of fibers is larger compared to the local structural properties.

Introduction

Paper properties are inherently anisotropic. The anisotropy of the mechanical properties depends on the fiber orientation, the degree of anisotropy, and drying conditions. Due to the producing process, there are more fibers oriented in the Machine Direction (MD) compared to the Cross Direction (CD), and at the same time, during

papermaking, the paper is dried under tension in the MD. The drying process is known to affect mechanical properties considerably. The tensile and compression strength as well as the bending stiffness increase when the shrinkage is decreased during the drying, meanwhile, in contrast, the toughness properties increase. The reason for this change in the mechanical properties due to the restrained and free drying can be established with linkage to the changes in the microstructure of the fibers and the micro-compression phenomenon. Decoupling the influence of anisotropy and drying on the mechanical properties in different directions is an elusive using experimental approach due to the difficulties in separating the effect of the anisotropy, drying as well as the local structural properties such as density and thickness.

In this work, we combined experimental measurement of local properties, micromechanical simulation, and continuum model to assess the influence of restrained drying on the constitutive response of fibrous materials.

Method

Experimental measurements

Specimens of sack paper with 70 g/m^2 were used as the material of study with a size of 40x65 mm^2. Region of Interest (RoI) of 32x56 mm^2 is defined inside these samples. The local structural properties namely, thickness, density, fiber orientation, and anisotropy, as well as the local strain filed, was measured with a resolution of 1 mm/pixel. The specimens were strained by 2.2% and the local strain was measured in MD with digital image correlation[1]. The local thickness was measured with a twin laser profilometer[2]. Local basis weight was determined with a β-radiographic transmission method[3]. Finally, the density was calculated by dividing the basis weight map by thickness map. The local fiber orientation was measured with a sheet splitting method[4]. Fiber orientation is described with two parameters, i.e. angle and anisotropy, derived from an ellipse-like local fiber orientation distribution. The angle (θ) is defined as the deviation of local major orientation direction from the MD. The anisotropy is in turn calculated as, $\lambda = 1 - b/a$ where a and b the major and minor axes of the local fiber orientation distribution ellipse, respectively.

Micromechanical simulation of fiber network

Herein, the direct simulation which represents a detailed micromechanical tool is used to quantify the influence of the anisotropy and the fiber orientation angle on the constitutive response. Based on the deposition technique of[5] random generation of the fiber network with size 4×4 mm^2 was used, see Figure 6.10a). Each one of the numerically generated fiber networks will have a unique degree of anisotropy through controlling the orientation of the fibers during the deposition phase. Consequently, it will present different mechanical response as in Figure 6.10b), The anisotropy is

computed by measuring the fiber orientation distribution and fit it to an ellipse Figure 6.10c). Furthermore, in the direct simulation tool, the constitutive behavior of fibers is isotopic elastic with bilinear plastic. The effect of restrained drying is implemented by modeling the fiber properties as a function of their fiber rotational position θ_f with respect to MD. Considering a drying restraint in MD and free shrinkage in CD, the fibers oriented in MD are stiffer than that in CD. The angular dependency of the fiber elastic modulus $E_f(\theta_f)$ is then presented by

$$E_f(\theta_f) = E_f^{MD} cos^4\theta_f + E_f^{CD}(1 - cos^4\theta_f)　\tag{1}$$

where E_f^{MD} and E_f^{CD} are fitting parameters representing the elastic modulus of the fiber when it is oriented in MD and CD, respectively. The selection of this function, although being empirical, is motivated through the analytical transformations presented by[6]. The same relation is assumed to describe the fiber shear modulus $G_{xy,f}(\theta_f)$, yield strength $\sigma_{s,f}(\theta_f)$ and tangent modulus $E_{tan,f}(\theta_f)$. These are found by matching the constitutive response in three different directions of the kraft paper to that from the fiber network.
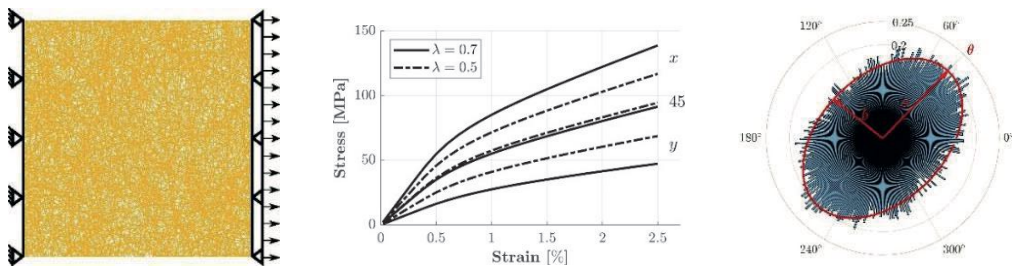
Figure 6.10 a) simulated fiber network with size 4×4 mm², b) constitutive response of fiber networks for different fiber orientations and degrees of anisotropy, c) determination of the degree of anisotropy of the fiber network.

Continuum model

The constitutive response used in the continuum model is the orthotropic linear elastic coupled with anisotropic plasticity. In this model, each element with the size 4×4 mm² has local properties derived from the local structural properties. The measured local density was used to scale the elastic moduli, the yield stress, and the power hardening constant. The local thickness is used to specify the local thickness of the element in the FE model. The angle orientation angle θ is used to orient the local coordinate system of the element in the FE model with the same value. And the relation between the constitutive response and the degree of anisotropy which was derived from the micromechanical model is used to scale the elastic and plastic properties.

Results

Figure 6.11a) shows the quality of the fit to the uniaxial physical tests perform in MD, CD, and 45 degrees direction obtained after adjusting the parameters in Equation 1 and using them in the micromechanical model. Neglecting the angular from Equation 1 dependency, i.e. assuming the same fiber properties regardless of orientation, reveals the influence of the fiber anisotropy alone Figure 6.11b). This result shows the importance of including the effect of drying as well as the impact it has compared to the anisotropy alone. The effect of the drying has a greater contribution to the anisotropy in the mechanical properties of the sheet compared to the effect of the fiber anisotropy alone.
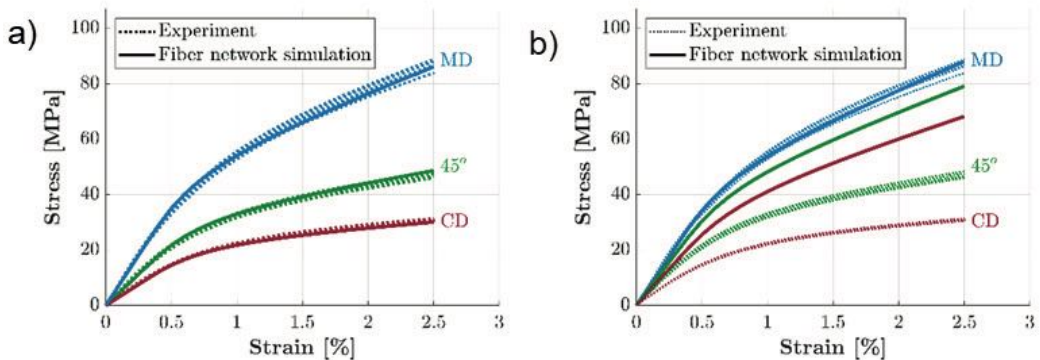
Figure 6.11. Defining the fiber properties by matching the constitutive response from experiment to that from the direct simulation: with a) combined effect of restrained drying and anisotropy, b) with the influence of restrained drying is omitted.

To validate the suggested approach the experimentally measured structural variations were integrated into a continuum macroscopic model and the measured strain field, as well as the constitutive response, was compared to the simulated ones (Figure 6.12).
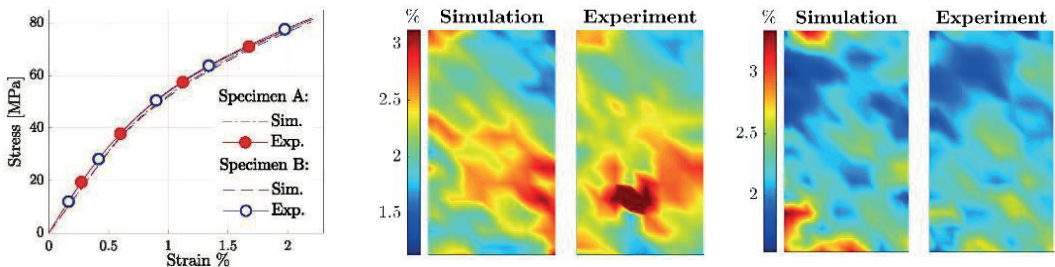
Figure 6.12. Comparison of experimental measurement and FE-simulation using the proposed approach for the two specimens, a) the stress-strain response, b, c) strain filed for Specimen A and Specimen B, respectively.

From Figure 6.12a), an excellent agreement between the stress-strain curves from the macromechanical simulations and the experiments is observed for both specimens. The corresponding strain fields at 2.2% strain level are shown in Figure 6.12b, c. Visually, it can be noticed that the simulated strain field presents a good agreement with the measured strain field for both specimens. The quantitative point-wise correlation coefficient of measured and simulated strain fields is $R = 0.617$ for Specimen A and $R = 0.596$ for Specimen B. Therefore, the model is capable to capture the regions with higher strains and the regions which are almost intact, relatively well.

Conclusions

By using a combination of the experimental and numerical tools, we were able, for the first time, to separate the contribution of fiber and drying anisotropy onto the anisotropy of the mechanical properties of a commercially produced paper. We verify the approach by incorporating the effect of structural anisotropy into a multiscale computational framework and comparing the computed strain fields with the experimentally acquired. The results of the comparison show good agreement and paves the way for investigating the effect of structural variabilities on the strain localization and failure.

Acknowledgments

References

1. Christoph, E. (2006). Digital Image Correlation and Tracking-File Exchange-MATLAB Central. Mathworks File Exchange Server FileID-12413. [Online]. Available: https://www.mathworks.com/matlabcentral/fileexchange/12413-digital-image-correlation-and-tracking. [Accessed: 16-Mar-2020].

2. Keller, D. S., Branca, D. L., & Kwon, O. (2012). Characterization of nonwoven structures by spatial partitioning of local thickness and mass density. Journal of Materials Science, 47(1), 208-226.

3. Keller, D. S., & Pawlak, J. J. (2001). b-Radiographic imaging of paper formation using storage phosphor screens. Journal of pulp and paper science, 27(4), 117-123.

4. Hirn, U., & Bauer, W. (2007). Evaluating an improved method to determine layered fibre orientation by sheet splitting. In 61st Appita Annual Conference and Exhibition, Gold Coast, Australia 6-9 May 2007: Proceedings (p. 71). Appita Inc.

5. Motamedian, H. R., Halilovic, A. E., & Kulachenko, A. (2019). Mechanisms of strength and stiffness improvement of paper after PFI refining with a focus on the effect of fines. Cellulose, 26(6), 4099-4124.

6. Cox, H. L. (1952). The elasticity and strength of paper and other fibrous materials. British journal of applied physics, 3(3), 72-79.

Twisting in the hierarchical fibre structure and its effects on bound water

Antti Paajanen[a], Sara Ceccherini[b], Thaddeus Maloney[b], & Jukka Ketoja[a]

[a]*VTT Technical Research Centre of Finland Ltd, Espoo, Finland*
[b]*Aalto University, Espoo, Finland*

***Corresponding author:** Antti Paajanen <antti.paajanen@vtt.fi>*

Keywords: Microfibril, macrofibril, fibre, twist, bound water, molecular dynamics

Summary

We have used molecular simulations to investigate the structure of a cellulose microfibril bundle, and evaluated the model against experimental evidence, including thermoporosimetry on the bound water of the fibre wall. Our simulations predict the spontaneous formation of a twisted ribbon-like bundle, the structure of which is in agreement with several experimental indicators. Specifically, the amount of freezing and non-freezing bound water are observed to correspond with molecular water layers surrounding the fibrils.

Chiral order in the structure of cellulosic fibres

The structure of cellulosic fibres involves a chiral order that appears on several length scales. The lowest level is that of the twisting of microfibrils, followed by their helical bundles as observed in transmission electron tomography studies[1]. At higher levels, one observes the helical winding of macrofibrils around wood cells[2], the twisting of cellulosic fibres[3], and finally that of fibre networks[4]. The relationship between the behaviours at the different levels is not obvious. Chirality transfer from cellulose macrofibrils to fibres and fibre networks has been proposed based on continuum models[3,5]. On the other hand, the twisting of individual microfibrils has been observed in atomistic simulation studies (reviewed by Paajanen (2020)[6]).

Molecular simulations and thermoporosimetry

We have extended atomistic molecular dynamics (MD) simulations of cellulose to involve microfibril bundles[6,7], a structural level beyond that of individual microfibrils. In particular, we show how the twisting of microfibrils is transferred to their bundles, and how this behaviour is affected by interactions with water. Our microfibril model consists of 24 cellulose chains, each 40 glucose units long. The particular arrangement is based on evidence from small and wide-angle X-ray scattering, nuclear magnetic resonance spectroscopy and Fourier transform infrared spectroscopy experiments[8].

Model visualization			SEM	
Cellulose chain	Microfibril	Microfibril bundle	Bundle network	Fiber
~1 nm	~3 nm	~10 nm	~1 μm	~10 μm
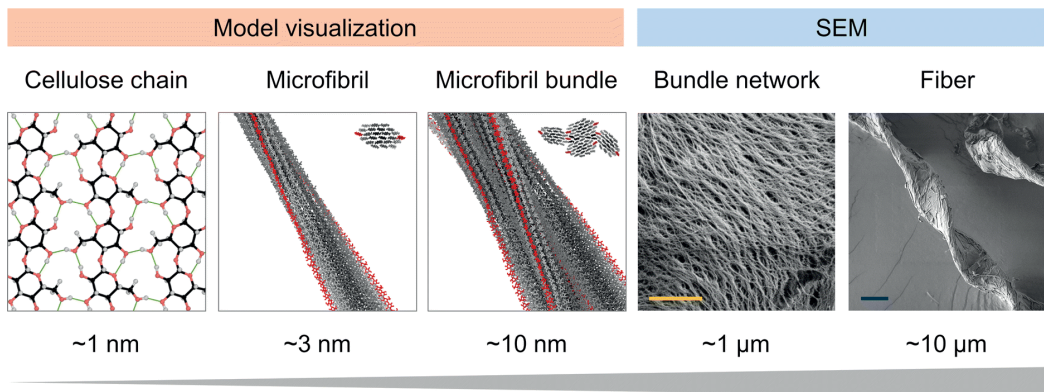
Figure 6.16. Structural hierarchy of a cellulosic fibre. Adopted from[7] and used under CC BY 4.0 (https://creativecommons.org/licenses/by/4.0/).

The simulations were compared against various experimental quantities at different levels of the structural hierarchy. Firstly, the bound water content of bleached birch kraft and dissolving pulps was determined by means of thermoporosimetry. The measurement of non-freezing (NFW) and freezing bound water (FBW) involved both never-dried and heat-treated pulps. For the birch kraft pulp, the twist rate distribution of isolated air-dried fibres was also determined. This was based on image analysis of scanning electron micrographs. Secondly, previously published measurements on the same pulps were also considered[9]. This included porosity measurements using a two-point solute exclusion method with dextran probes, as well as a method based on solvent exchange, critical point drying and nitrogen sorption. Lastly, certain experimental quantities were obtained from the literature. This included measurements on the fraction of water-accessible hydroxyl groups[8,10], the twist rates of isolated cellulose nanofibrils and their bundles[11,12] the twist rates of microfibril bundles in the native cell wall[1], as well as the type and amount of conformational disorder of the primary alcohol groups[8].

Hierarchical twisting and its structural consequences

The simulations show a coupling between the twisting behaviour of the bundle and that of its constituent fibrils. Moreover, they suggest a connection between the twisting and the conformational disorder and the water interactions. The twist rates of the fibrils and that of the bundle were observed to follow an inverse-diameter scaling law. Such behaviour has been predicted using continuum models[5] and observed in atomistic simulations of individual fibrils[13]. This happens even though the fibrils that constitute the bundle have their own, almost independent, twist rate. Interestingly, the twisting behaviour at the level of fibres seems to follow the same scaling law despite the length scale difference of two orders of magnitude. The simulations on the fibrils and the fibril bundle could be used to extrapolate the twist rate to a fibre of diameter 25 µm, which results in a value of 4.1×10^{-3} °/nm. This is surprisingly close to the experimental value of 3.5×10^{-3} °/nm.

Significant structural variation is visible in the simulated fibril bundle due to the twisting of its constituent fibrils. Mismatch in the twist rates of the bundle and its fibrils prevents co-crystallisation and results in openings along the bundle. Some diffusion of water into the bundle interior could be observed, but the amount was negligible compared to the amount of bound water measured in the experiments. By contrast, a good agreement was found when the bound water was interpreted as molecular water layers at the fibril surfaces. In the simulations, the amount of water within hydrogen bonding range was 0.19 g/g. This corresponds to roughly one monolayer of water, and it is close to the NFW content of the never-dried pulps, 0.22−0.23 g/g. The amount of water within the next two molecular layers was 0.49 g/g, which is close to the FBW content of the never-dried pulps, 0.42−0.46 g/g. Indeed, it has been shown that the hydration of cellulose nanocrystals involves the adsorption of roughly three monolayers of water[14].

Lastly, specific surface areas determined from the simulations were compared against ones determined from the nitrogen sorption experiments[9]. Here, the specific surface area of the never-dried bleached birch kraft pulp was obtained by extrapolating values from the nitrogen sorption experiments to the fibre saturation point. The resulting value, 470 m^2 g^{-1}, is reasonably close to the specific surface area of the bundle model, 520−630 m^2 g^{-1}.

Conclusion

In summary, our work reveals interesting connections between the chirality and bound water in cellulose microfibril bundles. The molecular dynamics simulations reproduce various experimental observations with reasonable accuracy. These include not only the magnitude of the twist rates at the different structural levels, but also the mass fractions of non-freezing and freezing bound water and specific surface areas.

Paajanen, A., Ceccherini, S., Maloney, T., Ketoja, J.

References

1. Reza, M., Bertinetto, C., Ruokolainen, J., & Vuorinen, T. (2017). Cellulose elementary fibrils assemble into helical bundles in S1 layer of spruce tracheid wall. Biomacromolecules, 18(2), 374-378.

2. Barnett, J. R., & Bonham, V. A. (2004). Cellulose microfibril angle in the cell wall of wood fibres. Biological reviews, 79(2), 461-472.

3. Burgert, I., Frühmann, K., Keckes, J., Fratzl, P., & Stanzl-Tschegg, S. (2005). Properties of chemically and mechanically isolated fibres of spruce (*Picea abies* [L.] Karst.). Part 2: twisting phenomena. Holzforschung, 59(2), 247-251.

4. Yu, M., Abitbol, T., & Gray, D. G. (2004). Evidence for a chiral internal stress in paper sheets. Journal of pulp and paper science, 30(4), 91-94

5. Ten Bosch, A. (1996). On the chirality of paper. Macromolecular Theory and Simulations, 5(2):225–230.

6. Paajanen, A. (2020). Computational studies on cellulose: pyrolysis, nanostructure and hydrodynamic behavior, Doctoral dissertation, University of Helsinki.

7. Mehandzhiyski, A. Y., Rolland, N., Garg, M., Wohlert, J., Linares, M., & Zozoulenko, I. (2020). A novel supra coarse-grained model for cellulose. Cellulose, 1-14.

8. Fernandes, A. N., Thomas, L. H., Altaner, C. M., Callow, P., Forsyth, V. T., Apperley, D. C., Kennedy, C. J., & Jarvis, M. C. (2011). Nanostructure of cellulose microfibrils in spruce wood. Proceedings of the National Academy of Sciences, 108(47):E1195–E1203.

9. Lovikka, V. A., Khanjani, P., Väisänen, S., Vuorinen, T., & Maloney, T. C. (2016). Porosity of wood pulp fibers in the wet and highly open dry state. Microporous and Mesoporous Materials, 234, 326-335.

10. iVäisänen, S., Pönni, R., Hämäläinen, A., and Vuorinen, T. (2018). Quantification of accessible hydroxyl groups in cellulosic pulps by dynamic vapor sorption with deuterium exchange. Cellulose, 25:6923–6934.

11. Usov, I., Nyström, G., Adamcik, J., Handschin, S., Schütz, C., Fall, A., ... & Mezzenga, R. (2015). Understanding nanocellulose chirality and structure–properties relationship at the single fibril level. Nature communications, 6(1), 1-11.

12. Ding, S. Y., Zhao, S., & Zeng, Y. (2014). Size, shape, and arrangement of native cellulose fibrils in maize cell walls. Cellulose, 21(2), 863-871.

13. Hadden, J. A., French, A. D., & Woods, R. J. (2013). Unraveling cellulose microfibrils: a twisted tale. Biopolymers, 99(10), 746-756.

14. Niinivaara, E., Faustini, M., Tammelin, T., & Kontturi, E. (2015). Water vapor uptake of ultrathin films of biologically derived nanocrystals: quantitative assessment with quartz crystal microbalance and spectroscopic ellipsometry. Langmuir, 31(44), 12170-12176.

Quantification of the impact of each, fibre flexibilization and secondary fines on tensile strength gain after refining

Daniel Mandlez, Sarah Koller, René Eckhart, Wolfgang Bauer, & Ulrich Hirn

Institute of Biobased Products and Paper Technology, Graz University of Technology, Graz, Austria

***Corresponding author:** Daniel Mandlez <daniel.mandlez@tugraz.at>*

Keywords: Refining, beating, strength properties, PFI, disc refiner, fines

Summary

Within this research activity unbleached softwood kraft pulp was refined with a lab scale disc refiner and a PFI-Mill by use of different refining intensities. After refining, the fines fraction was separated by a lab scale pressure screen. For each refining configuration and intensity hand sheets were built with and without fines to obtain values for the breaking length. Thereby it was possible to calculate and quantify the tensile gain achieved on one hand by secondary fines and on the other hand by internal and external fibrillation of the fiber itself.

Introduction

Refining of pulp is an indispensable process step in the stock preparation of any paper machine. During the refining process the fiber is modified through internal and external fibrillation. Internal fibrillation represents delamination of the cell wall, which leads to flexibilization of the fiber[1]. Therefore, fibres are prone to collapse during sheet formation allowing a flatter conformation yielding a denser network with increased bonded area. External fibrillation represents fibrils torn from the surface during the mechanical impact[1]. Therefore, fibres are prone to collapse during sheet formation allowing a flatter conformation yielding a denser network with increased bonded area. External fibrillation represe[2], leading to an increase in fibre surface area which also enhances relative bonded area and leads to increased mechanical interlocking[1].

Besides these described effects, so called secondary fines are produced during refining. In contrast to primary fines generated during the pulping process[3] which have due to their origin a more blocky or flake like character[2] they show a strong fibrillar nature[3,4] due to being torn from the fibrillar fibre wall structure[2,3]. Depending on the refining aggregate/treatment the result is different when it comes to fibrillation and fines production. The laboratory PFI mill for example is known to mainly yield internal fibrillation[5], while an industrial disc refiner shows stronger external fibrillation, fiber shortening and fines production[5,6].

The main driver for refining is the corresponding increase in mechanical strength of the paper which is the result of the described fibrillation and the generated secondary fines [6]. While this effect is described in literature extensively[4,6,7,8], it is not fully understood to what extent the fibrillation on the one hand and the secondary fines on the other contribute to the gain in e.g. tensile strength.

Recently published investigations regarding the effect of fines on strength mechanisms[1], led to the initiation of this work. The goal of this ongoing research activity is the quantification of the impact of fiber flexibilization and secondary fines on the gain in tensile strength due to refining. To get a better picture, both the PFI-mill as well as a disc refiner are being investigated within this work.

In our work, an industrial once dried unbleached softwood kraft pulp (kappa 40) was used. The primary fines content in the stock was approximately 5%. The pulp was refined in a PFI mill and in a pilot scale 12 inch single disc refiner with varying intensities. The pulp at each refining intensity was analyzed as is, as well as after a separation step where the fines (combination of primary and secondary fines) were removed. For this separation step a lab scale pressure screen implemented at the Institute of Biobased Materials and Fiber Technology at Graz University of Technology was used.

Refining

The refining in the PFI mill was done according to ISO 5264-2 with 4000, 7000 and 10000 revolutions. In case of pilot scale refining with the single disc refiner, specific refining intensities of 100 kWh/t and 250 kWh/t were applied for 60 kg(bd) pulp with a consistency of 3,9 %.

Separation

For the separation of fines, the lab scale pressure screen was equipped with a 150 µm hole screen. The pulp suspension was fed with a consistency of 1 %-wt. to the separator. Since the removal of the complete fines material is not possible in a single

step, the pulp was recirculated in a closed loop to achieve sufficient fines removal below 1 % residual fines content.

Analytics

Hand sheets of 80 g/m² were prepared for each configuration on a Rapid-Köthen hand sheet former with white-water recirculation (ISO 5269-3). To ensure a fines equilibrium in the white-water, the first four sheets were discarded. The fines content was determined using the Britt Dynamic Drainage Jar (BDDJ) according to SCAN-CM 66-05 equipped with a 200 Mesh screen. Testing of hand sheets was done after at least 24 hours storage in the climate room at 23°C and 50 % relative humidity. Apparent density (ISO 534) and tensile strength (ISO 1924-2) were determined.

Results

Figure 6.17 shows the correlation of tensile strength represented by breaking length (BL) and fines content (w_{fines}) for all the investigated samples with and without fines. Based on the example of the unrefined reference pulp, the breaking length gain induced by the primary fines (ΔBL_{prim}) can be calculated according to equation (13). The total gain in breaking length (ΔBL_{tot}) for each refined sample is derived according to equation (14). The gain due to the fines of the refined samples in comparison to the corresponding samples without fines (ΔBL_{fines}) is calculated according to equation (15).
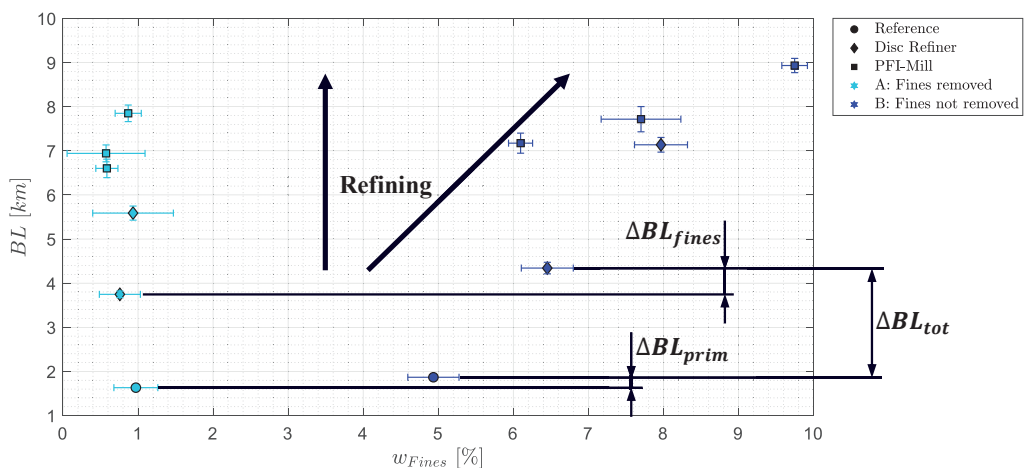
Figure 6.17. Diagram: Fines content (w_{fiber}) vs breaking length (BL) dark blue datapoints for pulp including fines ($BL_{with\ fines}$) leight blue datapoints pulp where the fines were removed ($BL_{without\ fines}$)

Based on these results the breaking length gain obtained by the secondary fines produced during refining can be calculated according to equation (16).

$$\Delta BL_{prim} = BL_{ref,with\ fines} \\ - BL_{ref,without\ fines} \tag{13}$$

$$\Delta BL_{tot} = BL_{beating,with\ fines} \\ - BL_{ref,with\ fines} \tag{14}$$

$$\Delta BL_{fines} = BL_{beating,with\ fines} \\ - BL_{beating,without\ fines} \tag{15}$$

$$BL\_Gain_{sec} = \frac{\Delta BL_{fines} - \Delta BL_{prim}}{\Delta BL_{tot}} \\ \cdot 100\% \tag{16}$$

Figure 6.18 shows the results for the breaking length gain due to secondary fines produced in the refining process. Approximately 6 to 25 % of the breaking length gain is generated by the secondary fines. The corresponding rest is attributed to the fiber modification in terms of external and internal fibrillation. The linear regression in Figure 6.18 corresponds to the impact of the PFI-Mill and the disc refiner respectively. The contribution of the secondary fines grows with higher refining intensity in both cases, but to a higher extent in case of the disc refiner. This corresponds to literature[5,6]. As already mentioned, the PFI-mill generates mainly internal fibrillation compared to disc refiner, which is known to rely more on external fibrillation and fiber shortening and therefore more production of secondary fines[5,6].
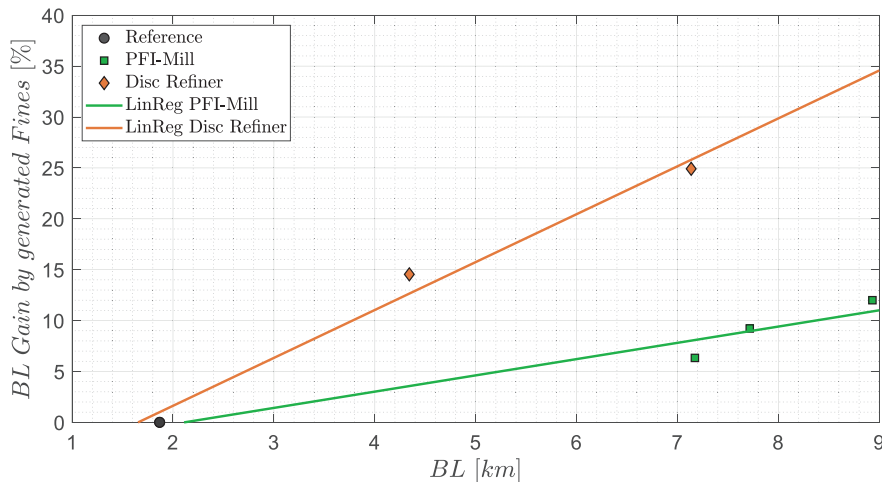
Figure 6.18. Diagram: Breaking length vs breaking length gain by generated fines

Besides this analysis focusing on the secondary fines produced we also looked into the impact of the entire fines fraction including the primary fines. Therefore, samples with fines and without fines are compared, by calculating the slope between in refining configuration related points drawn in Figure 6.15. This calculation is done according to equation (17).

$$
BL\_Impact_{fines} = \frac{BL_{with\ fines} - BL_{without\ fines}}{w_{with\ fines} - w_{without\ fines}} \tag{17}
$$

Figure 6.19 shows the efficiency of the fines fraction on the breaking length. This Impact on breaking length (BL_Impact_{sec}) gives the increase of breaking length per weight percentage fines in the pulp. The impact of the fines fraction on the tensile properties rises with increased breaking length for both refining aggregates. This might be explained by taking the development of sheet density and pore structure into account. For samples of lower tensile strength showing a more bulky structure with larger pores within the network the available fines may not be capable of closing these pores like they can in case of a denser sheet with smaller voids. Thereby the impact on RBA may be higher in case of already denser sheets which will also affect the tensile strength to a higher extent. However secondary fines produced by a disc refiner have a stronger effect on the breaking length per given amount of fines, which may lead to the second reason why the gain on breaking length in case of disc refining is higher compared to the PFI-mill.
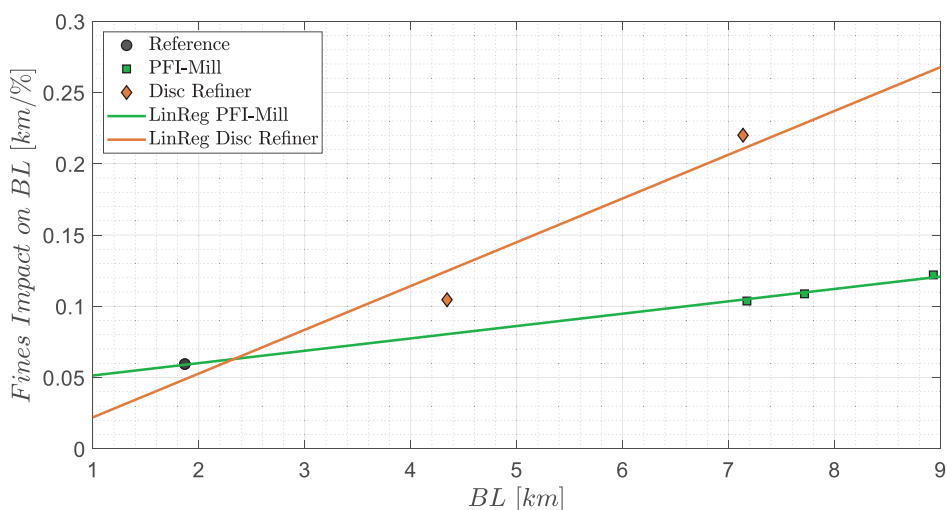
Figure 6.19. Diagram: Breaking length vs fines impact on breaking length

Mandlez, D., Koller, S., Eckhart. Bauer, B., & Hirn, U.

Conclusions

Within this re refining process. It is shown that the search activity it was possible to obtain quantitative information on the tensile gain through the generation of secondary fines in the contribution of the secondary fines to the gain in tensile strength lies – depending on the used refining aggregate – between 5 and 25%. The differences reflect the already well known differences in treatment between a PFI-mill and a disc refiner where the disc refiner shows less internal fibrillation and a higher production of secondary fines. The impact of the fines fraction to the tensile properties rises for higher refining intensities in both cases. We attribute this to the higher impact on the RBA in an already denser network, where the introduced fines may close some already small voids to produce additional bonded area.

Acknowledgements

References

1. Motamedian, H. R., Halilovic, A. E., & Kulachenko, A. (2019). Mechanisms of strength and stiffness improvement of paper after PFI refining with a focus on the effect of fines. Cellulose, 26(6), 4099-4124.

2. Ferreira, P. J., Martins, A. A., & Figueiredo, M. M. (2000). Primary and secondary fines from Eucalyptus globulus kraft pulps. Characterization and influence. Paper & Timber, (6), 403-408.

3. Odabas, N., Henniges, U., Potthast, A., & Rosenau, T. (2016). Cellulosic fines: Properties and effects. Progress in Materials Science, 83, 574-594.

4. Mayr, M., Eckhart, R., & Bauer, W. (2017). Improved microscopy method for morphological characterisation of pulp fines. Nordic pulp & paper research journal, 32(2), 244-252.

5. Yasumura, P. K., D'Almeida, M. L. O., & Park, S. W. (2008). Refining actions in PFI mill and in industrial disc refiners. O Papel, 69(8), 63-72.

6. Kerekes, R. J. (2005). Characterizing refining action in PFI mills. Tappi journal (2002), 4(3), 9-13.

7. Fahey, M. D. (1970). Mechannical treatment of chemical pulps. Tappi Journal 53(11), 2050-2064.

8. Dasgupta, S. (1994). Mechanism of paper tensile-strength development due to pulp beating. Tappi journal, 77(6), 158-166.u

Ptychographic X-ray computed tomography study of the paper pulp fiber to fiber bond

David Prochinig[a], Georg Urstöger[b], Elisabeth Müller[c], Mirko Holler[c],
Manuel Guizar-Sicairos[c], Roland Resel[a,d], Robert Schennach[a,d],
& Eduardo Machado-Charry[a,d]

[a]*Institute of Solid State Physics and NAWI, Graz University of
Technology, Graz, Austria*
[b]*Institute of Bioproducts and Paper Technology, Graz University of
Technology, Graz, Austria*
[c]*Paul Scherrer Institut, Villigen PSI, Switzerland*
[d]*Christian Doppler Laboratory for mass transport through paper, Graz University of
Technology, Graz, Austria*

Corresponding author: *David Prochining <david.prochinig@student.tugraz.at>*

Keywords: Ptychography, cellulose fiber, fiber to fiber bond, relative contact area, radiation damage

Summary

We have measured the relative contact area between two cellulose fibers using the relatively new technique called Ptychographic X-ray Computed Tomography. From these experiments, we were able to resolve this area with a spatial resolution between 50 to 100 nanometers. Moreover, we have studied the response of the fibers to radiation damage. From this study, we have determined the optimal conditions for future measurements using this technique.

Relative Contact Area

The strength of paper depends strongly on both the strength of the individual cellulose fibers and the bonded area between cellulose fibers[1]. For the latter, we must make a distinction between the intersection area and the actual bonded area. The intersection area is the optically overlapping area between two bonded fibers. The actual bonded area is the region in which the two fibers are in molecular contact. Admittedly, it is impossible to resolve the whole Fiber to Fiber (FtF) bond to the molecular regime, thus,

Prochinig, D., Urstöger, G., Mûller, E., Holler, M., Guizar-Sicairos, M., Resel, R., Schennach, R., & Machado-Cherry, E.

it is necessary to use the term relative contact area (RCA). The RCA describes the portion of the intersection area, which is measured to be in contact with the achieved experimental resolution[2].
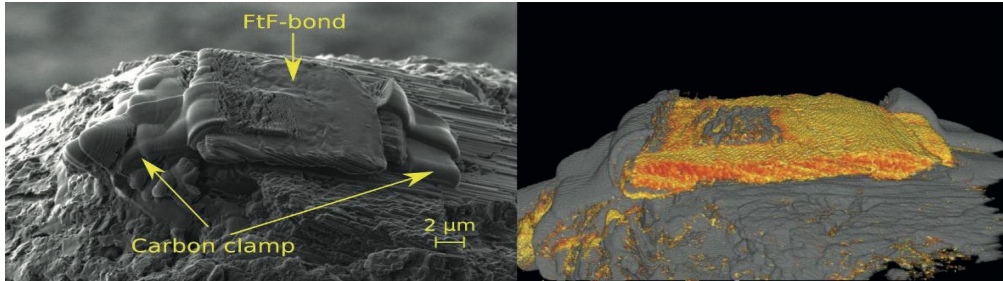
Figure 6.20. Hardwood sample on graphite pin. Left: SEM image at the end of sample preparation. The FtF-bond sits on top of a graphite pin and is clamped with carbon. Right: PXCT 3D image (voxel size: 37.6 nm). The graphite pin and the carbon clamps are displayed in grey, and the FtF-bond is displayed in yellow.

Ptychography

A novel technique called Ptychographic X-ray Computed Tomography (PXCT) has shown to provide 3D electron density maps with nanometer resolution[3]. PXCT is a coherent diffractive imaging technique. The main advantage of PXCT is that it can reconstruct the phase information from the intensity of the diffraction patterns. Having the phase is advantageous because it is the primary source of contrast in weakly scattering samples like cellulose[4]. Moreover, it is possible to calculate the refractive index and the electron density. This information allows us to acquire quantitative high-resolution 3D electron density maps[5]. Nowadays, these high-resolution 3D images from PXCT are only possible by using highly brilliant, coherent X-rays from a synchrotron source.

Radiation Damage and Image Analysis

To evaluate the fibers' response to radiation damage, we have considered two different experimental setups available at the cSAXS beamline at the Swiss Light. The first setup, the so-called "flexible tOMography Nano Imaging" (flOMNI) [6], operates at ambient conditions. In contrast, the second one works at cryogenic conditions, and it is known as "tOMography Nano crYo" (OMNY) [7].

For these experiments, we used FtF-bonds made of soft-to-softwood and hard-to-hardwood. By using Focused Ion Beam (FIB), we cut two hardwood samples and one softwood sample. Then, we mounted each of them on the top of the pin used in the PXCT setup. Finally, we fixed the sample to the pin through FIB deposited carbon clamps (Figure 6.20, left).

For the first experiment, we used the softwood sample with the flOMNI stage and a high photon flux. The tomographic reconstructions revealed that the photon flux was too high, and the sample morphology started to change significantly due to radiation damage, leading to a low resolution and artifacts in the reconstructions.

Consequently, we made some modifications for the second experiment. First, we used FtF-bonds made of thinner fibers, i.e., of hardwood. This choice led to a smaller volume and thus to shorter measurement time compared to the softwood sample. Secondly, we made use of the OMNY setup, at a temperature of 90 K. And finally, we took some measures to reduce the radiation dose. These measures included detuning the undulator, decreasing the exposure time per scanning point, changing the number of scanning points (step size), and decreasing the width of a slit in the X-ray beam's pathway. The cryogenic conditions and the lowered radiation dose turned out to be beneficial for a radiation-sensitive sample like cellulose. The tomographic reconstructions provided a resolution between 50 and 100 nm and did not show significant changes in sample morphology (Figure 6.20, right).

Thus, we are now able to make statements about the maximum bearable radiation dose and the ideal parameters and setup for future PXCT experiments with cellulose samples from combining both experiments.

We have done a proper image segmentation to analyze the 3D electron density maps concerning RCA. We tested several algorithms (Otsu's method[8], Image Thresholding by Indicator Kriging[9], but they failed to detect small non-contact regions between the two fibers. Thus, we used a machine learning-based method implemented in Fiji – ImageJ, called *Trainable Weka Segmentation 3D*[10]. This method has proven to show consistent results. With this method, a classifier is trained on small, representative subsystems of the whole 3D image, which can then be applied to the entire system. Finally, we calculated RCA on the segmented images, and generated quantitative opening thickness maps like those in the work of Sormunen et al. [11].

In summary, Ptychographic X-ray Computed Tomography provides high-resolution 3D electron density maps, which allow quantitative analysis of the contact region between cellulose fibers. On the other hand, our findings of those experiments suggest that radiation damage to cellulose samples is a crucial factor when using experimental methods with X-ray radiation. Therefore, we have obtained the ideal parameters and setup for future PXCT experiments with cellulose samples.

References

1. Page, D. H. (1969). A theory for the tensile strength of paper. *Tappi*, *52*, 674-681.

2. Sormunen, T. (2018). Measuring the contact area in cellulose fibre bonds using X-ray nanotomography. MSc Thesis. University of Jyväskylä. Department of Physics.

3. Holler, M., Diaz, A., Guizar-Sicairos, M., Karvinen, P., Färm, E., Härkönen, E., ... & Bunk, O. (2014). X-ray ptychographic computed tomography at 16 nm isotropic 3D resolution. Scientific reports, 4(1), 1-5. https://doi.org/10.1038/srep03857

4. S Sala, S., Batey, D. J., Prakash, A., Ahmed, S., Rau, C., & Thibault, P. (2019). Ptychographic X-ray computed tomography at a high-brilliance X-ray source. Optics express, 27(2), 533-542. https://doi.org/10.1364/OE.27.000533

5. Diaz, A., Trtik, P., Guizar-Sicairos, M., Menzel, A., Thibault, P., & Bunk, O. (2012). Quantitative x-ray phase nanotomography. Physical Review B, 85(2), 020104. https://doi.org/10.1103/PhysRevB.85.020104

6. Holler, M., Raabe, J., Diaz, A., Guizar-Sicairos, M., Quitmann, C., Menzel, A., & Bunk, O. (2012). An instrument for 3D x-ray nano-imaging. Review of Scientific Instruments, 83(7), 073703. https://doi.or/10.1063/1.4737624

7. Holler, M., Raabe, J., Diaz, A., Guizar-Sicairos, M., Wepf, R., Odstrcil, M., ... & Maag, S. (2018). OMNY—a tOMography nano crYo stage. Review of Scientific Instruments, 89(4), 043706. https://doi.org/10.1063/1.5020247

8. Otsu, N. (1979). A threshold selection method from gray-level histograms. IEEE transactions on systems, man, and cybernetics, 9(1), 62-66. https://doi.org/10.1109/TSMC.1979.4310076

9. Oh, W., & Lindquist, B. (1999). Image thresholding by indicator kriging. IEEE Transactions on Pattern Analysis and Machine Intelligence, 21(7), 590-602. https://doi.org/10.1109/34.777370

10. Arganda-Carreras, I., Kaynig, V., Rueden, C., Eliceiri, K. W., Schindelin, J., Cardona, A., & Sebastian Seung, H. (2017). Trainable Weka Segmentation: a machine learning tool for microscopy pixel classification. Bioinformatics, 33(15), 2424-2426. https://doi.org/10.1093/bioinformatics/btx180

11. Sormunen, T., Ketola, A., Miettinen, A., Parkkonen, J., & Retulainen, E. (2019). X-ray nanotomography of individual pulp fibre bonds reveals the effect of wall thickness on contact area. Scientific reports, 9(1), 1-7. https://doi.org/10.1038/s41598-018-37380-2

Session 7A

Transport phenomena

Session chair: Annika Ketola

Contact angle measurement on absorbing paper – influence of absorption rate and drop size

Sarah Krainer[a,b], & Ulrich Hirn[a,b]

[a]Institute of Bioproducts and Paper Technology, Tehnical University of Graz, Graz, Austria
[b]CD Laboratory Fiber Swelling and Paper Performance, Graz, Austria

Corresponding author: Ulrich Hirn <ulrich.hirn@tugraz.at>

Keywords: Contact angle, absorption, drop ize

Summary

Liquid absorption into the paper is affecting the contact angle measurement. In this work we have investigated the influence of liquid penetration, residence time of the drop on the paper and drop size over a large range of volumes (30pl to 4µl). We find that the combined influence of all these parameters on the measured contact angle can be conveniently described by the absorbed drop volume, which turns out to be a comprehensive state variable for the measured contact angle.
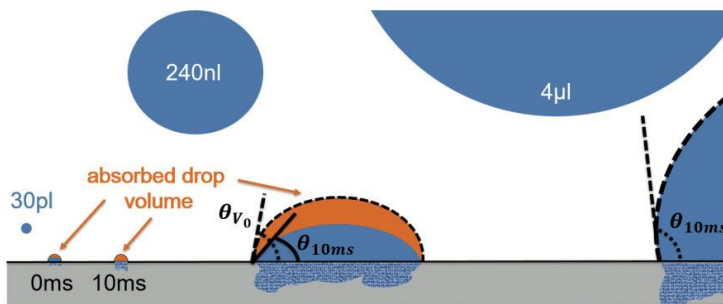
Figure 7.1. Drop sizes used for contact angle measurements on paper (drawing to scale). It can be expected that liquid absorption has a large effect on the measures contact angle.

Introduction

The contact angle θ is a key parameter indicating the wetting and penetration behavior of liquids on paper. The contact angle therefore is a good parameter to predict e.g. the

spreading of printing ink on the paper surface[1]. Furthermore the contact angle θ is one of the driving forces for liquid penetration into capillary pores, as described in the Lucas-Washburn equation[2], hence a low contact angle is also promoting liquid absorption. Contact angle measurements therefore are standard for evaluating paper-liquid interaction in printing, sizing, coating and converting of paper.

Often it is necessary to measure the contact angle of liquids on papers that are absorbing the liquid. In printing for example the paper is supposed to take up the ink solvent or the fountain solution. After touching the surface the drop is at the same time spreading on the paper surface and penetrating into the paper bulk. It can be expected that the drop absorption into the paper is reducing the contact angle of the drop and thus altering the measurement result. Figure 7.1 shows the situation in contact angle measurements drawn to scale. Commonly contact angle is measured with 1-4 µl drop size, these drops are so large that they fully saturate the paper with liquid. For applications like inkjet printing the contact angle is measured with picoliter drops, i.e. in the size range of inkjet droplets. Such drops penetrate into the paper substrate with 50-200 milliseconds. In this work we have investigated the influence of drop size and liquid absorption rate of the paper on the measured contact angle. We will demonstrate that the combined influence of drop size, drop residence time on the surface and paper absorption rate is comprehensively described by the relative absorbed liquid volume of the drop, which turns out to be a useful parameter to compare contact angle measurements with different drops sizes and different drop residence times on the paper.

Materials and methods

We used four types of office-type hardwood papers with different absorption characteristics. The water absorption rate of these paper was measured with an ASA direct absorption tester[3].

- Strongly absorbing paper. An uncoated, unsized and untreated paper with a water absorption rate of 710 ml/m^{2}s.
- Moderately absorbing paper. The same uncoated, unsized and untreated paper like above, only calendered for a reduction of porosity. Liquid absorbency is 470 ml/m^{2}s.
- Weakly absorbing paper. 4 g/m² of surface starch and clay were applied in a size press to create a more homogeneous surface, reducing liquid penetration to 380 ml/m^{2}s.
- Almost non - absorbing paper. This paper was AKD bulk sized, water absorption rate was
  8 ml/m^{2}s.

Contact angle measurements were made with deionized water, spanning a large range of drop sizes. Minimum was 30pl, maximum was 4µl which is 130 000 times larger than

the smallest drops. The drop sizes measured were: 30 pl, 60 pl, 120 pl, 240 pl, 480 pl, 960 pl, 5 nl, 15 nl, 30 nl, 60 nl, 120 nl, 240 nl, 480 nl, 1µl, 2µl and finally 4µl. The contact angle was measured with a Dataphysics OCA 200 contact angle device and a STFI contact angle tester. For all measurements the contact angle was measured from images of the drop on the surface. The OCA 200 is equipped with a high speed camera, delivering a frame every 0.5ms. In this way for each measurement the change of contact angle over time is recorded.

Results and discussion

Figure 7.2 shows the results in a condensed form. The red graphs in the left column give the absorbed drop volume (in % of initial drop volume) measured directly after impact (0ms) and 10ms after impact. For the non absorbing paper there is no liquid penetration, the drop sizes are equivalent. With increasing absorptivity of the paper (from top to bottom) one can see an increasing difference between the drop volume at 0ms and 100 ms. For the highest absorbing paper (bottom) the smallest picoliter drops have fully disappeared after 10 ms (i.e. 100% absorbed drop volume) whereas the volume of the largest microliter drops is virtually unaffected after 10 ms. We can identify 3 regions in the plots. Region ① is where significant penetration was taking place between 0ms and 10ms, in region ③ no penetration at all has occurred (i.e. 0% absorbed drop volume). In region ① the drops are small and/or the paper is highly absorbing and in region ③ the drops are large and/or the paper is non absorbing.

The blue/green graphs in the right column of Figure 7.2 are giving the contact angle measured directly after impact (0ms) and 10ms after impact. One can clearly see that the contact angle between 0ms and 10ms is changing considerably in region ①, it is changing moderately in region ② and it is virtually identical in region ③. Furthermore it is evident that the contact angle decreases in accordance with the absorbed liquid volume: The drops with a large volumedifference between 0 and 10 ms (pink vs. red squares left column) also have a large difference in contact angle between 0 and 10ms (blue vs. green squares right column).

This confirms the idea that the contact angle is systematically reduced due to liquid penetration. Please note that there are huge differences in measures contact angle for different drop sizes on the same paper. For the moderately absorbing paper the contact angle measured after 10 ms varies from 30° at the smallest drop size to 85° at the largest drop size.

This variation decreases when the measurements at 0ms are considered. For the strongly absorbing paper the contact angle values are reasonably stable for the 0ms measurements, however they show a systematic increase for the 10 ms measurement. The conclusion to draw here is that the contact angle should be measured at the earliest possible moment the drop has stabilized after falling on the surface.

The relationship between penetration of the drop into the paper and its effect on the contact angle is shown Figure 7.3. It gives the change in contact angle over the absorbed drop volume (in % of initial drop volume) for the smallest (60 pl, black) and the largest (4µl, blue) drops. The plot covers several seconds of time. As the liquid penetrates into the paper the contact angle decreases. We see a stable trend, there is a stable, fairly linear decrease of contact angle with increased penetration of the drop into the paper. Please note that this stable for a large time scale (less than 5 milliseconds for the smallest drops and a few seconds for the largest drops) and a large size scale (60pl to 4µl), for highly absorbing and non-absorbing papers. We find that the critical parameter to be observed for contact angle measurements on absorbing materials is the relative absorbed drop volume (in %).

Conclusions

Our results demonstrate that the drop volume as well as the absorption rate of the substrate substantially affect the measured contact angle. Thus, for a correct and stable measurement, it is necessary to use high drop volumes and capture θ immediately after drop application, eliminating the penetration impact. If the absorption rate is too high or the drop size is restricted to a specific value, however we recommend calculating the relative absorbed drop volume V_a and obtaining the contact angle always at same values for V_a. In this way the relative absorbed drop volume V_a captures the combined effect of drop volume, contact time and substrate absorption rate.

Acknowledgements
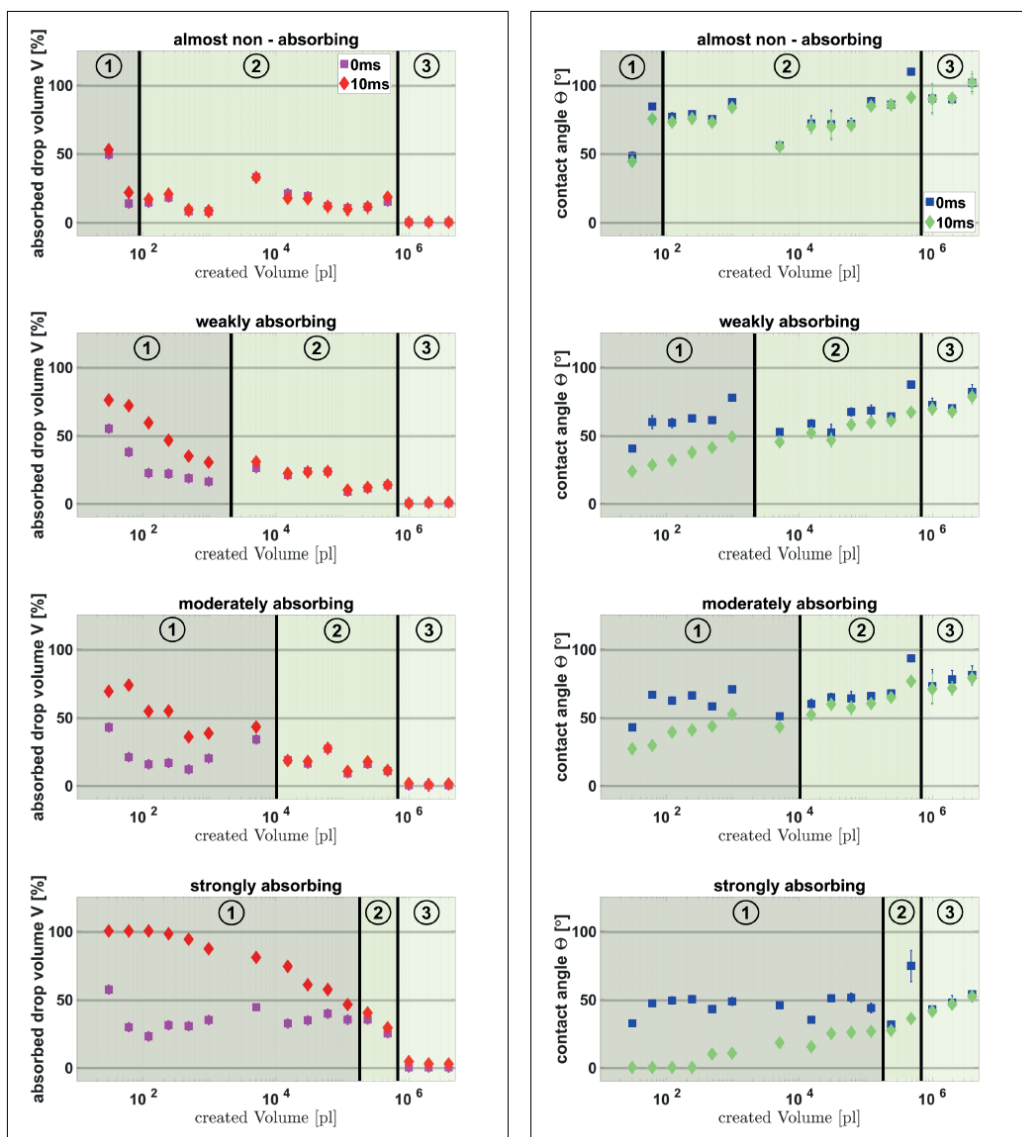
Figure 7.2. Absorbed drop volume (left column) and contact angle (right column) over drop volume. From top to bottom row: no liquid absorption (top) to high liquid absorption (bottom) of the paper
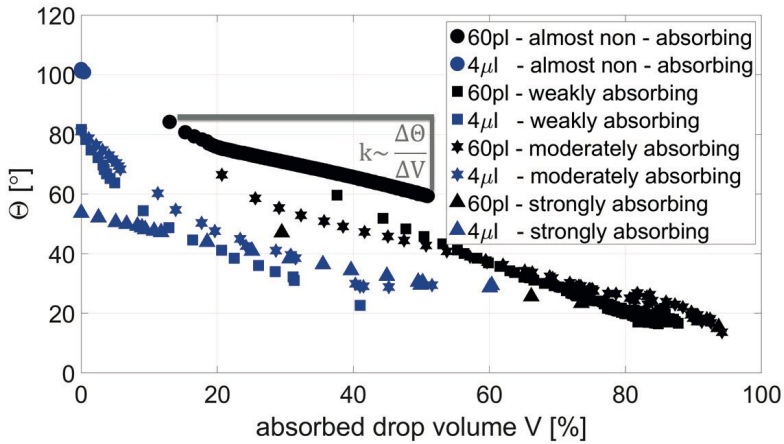
Figure 7.3 Contact angle over absorbed drop volume. The plot shows the behavior of the smallest (60 pl, black) and the largest (4µl, blue) drops. The change in contact angle from 0ms to 10s is plotted.

References

1. Krainer, S., Saes, L., & Hirn, U. (2020). Predicting inkjet dot spreading and print through from liquid penetration-and picoliter contact angle measurement. Nordic Pulp & Paper Research Journal, 35(1), 124-136.

2. Ovaska, S. S., & Backfolk, K. (2018). The versatility of the Bristow absorption tester–a review. Nordic Pulp & Paper Research Journal, 33(2), 279-296.

3. Sarah, K., & Ulrich, H. (2018). Short timescale wetting and penetration on porous sheets measured with ultrasound, direct absorption and contact angle. RSC advances, 8(23), 12861-12869.

Modelling ink penetration, hygro-expansion and curl in digital inkjet printing

Nik Dave[a,b], Ron Peerlings[a], Thierry Massart[b], & Marc Geers[a]

[a]*Eindhoven University of Technology, Eindhoven, The Netherlands*
[b]*Université Libre de Bruxelles, Brussels, Belgium*

Corresponding author: *Nik Dave <N.Dave@tue.nl>*

Key Words: Water transport, hygro-expansion, curl

Summary

Ink-induced deformation of paper sheets is one of the factors limiting the quality of new-age ink-jet printing systems. In this work, a phenomenological model for water transport in an unsaturated porous-fibrous material and the resulting hygro-mechanical behaviour of paper is presented.

Introduction

New-age digital printing systems use inkjet technology on plain paper sheets. The inks used are often water-based. Paper, a hydrophilic material, is notably susceptible to deformations due to variations in moisture content, which develop over time[1]. These deformations may result in instabilities and out-of-plane displacements such as curl (Figure 7.4a), which could affect the performance of these printers[2].

Modelling the moisture transport through the thickness of a paper sheet and the time-dependent mechanics allows us to study the curling behaviour of paper.
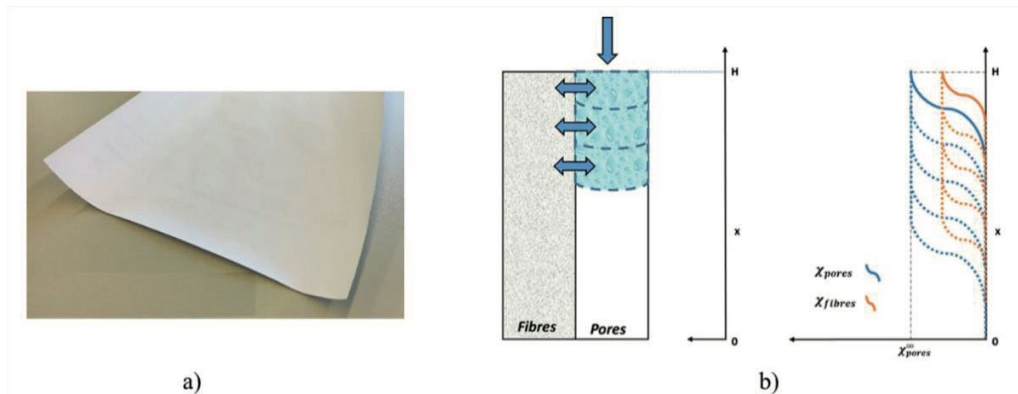
Figure 7.4 a) Curl developed in a paper sheet b) 1D through-thickness moisture transport model in a fibrous material.

Modelling

The water transport model considers the paper sheet as a variably-saturated porous medium and employs the Richards equation[3]. The Richards equation is extended to incorporate the water exchange between the pores and fibres. For this purpose, the model distinguishes the volumetric water content into a mobile and immobile fraction, where the fibres can exchange or store the immobile water by swelling, and contribute towards the hygro-expansion.

The immobile water fraction in the fibres also affects the elastic as well as plastic properties. For solving the mechanical part of the problem, we assume a constant curvature along the length of the paper strip and and solve the equilibrium for the mean strain and curvature along the thickness direction.

As a constitutive material model, the current study considers a linear elastic material model for the paper strip and could be extended to include the behaviour of visco-elasticity and visco-plasticity[1].
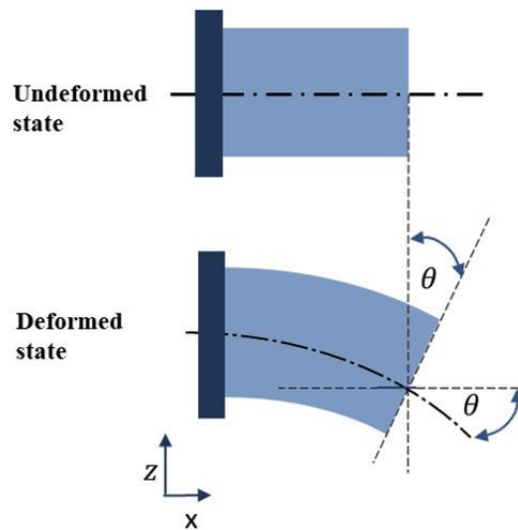
Figure 7.5: Undeformed and deformed bending state of a paper strip under the simple beam theory.

Conclusion

The developed theoretical model enables us to study the effect of time-scale difference, introduced by the aforementioned processes, on the predicted curling response of paper sheet to a wetting-drying cycle. In this study, the interaction between a paper-sheet and water is analysed, taking into account the moisture dependent elastic and inelastic response of the paper. The bending response of the paper strip triggered due to the hygroscopic strain (i.e. moisture-induced strain) is simulated in a one-way coupled manner for various boundary-value problems.

References

1. Bosco, E., Peerlings, R. H. J., Lomans, B. A. G., van der Sman, C. G., & Geers, M. G. D. (2018). On the role of moisture in triggering out-of-plane displacement in paper: from the network level to the macroscopic scale. International Journal of solids and Structures, 154, 66-77.

2. Niskanen, K. (Ed.). (2011). Mechanics of paper products. Walter de Gruyter.

3. Richard, L. A. (1931). Capillary conduction of liquids through porous mediums. Physics, 1(5), 318-333.

.
.

Quantification of the interdependence of local porosity and local tortuosity that determine the airflow in paper

Karin Zojer[a,b], Peter Leitl[b,c], Eduardo Machado Charry[a,b],
Matthias Neumann[d], Ulrich Hirn[e], & Volker Schmidt[d]

[a]*Institute of Solid State Physics, NAWI Graz,Graz University of Technology, Graz, Austria*
[b]*Christian Doppler Laboratory for mass transport through paper, Graz University of Technology, Graz, Austria*
[c]*Bionic surface technologies GmbH, Graz, Austria*
[d]*Institute of Stochastics, Ulm University, Ulm, Germany*
[e]*Institute of Bioproducts and Paper Technology, Graz University of Technology, Graz, Austria*

Corresponding author: *Karin Zojer <*karin.zojer@tugraz.at *>*

Keywords: µ-CT, tortuosity, computational fluid dynamics, statistical data analysis, copula

Summary

Multiple properties of the pore space determine the airflow through a sheet of paper. Our analysis of the simulated airflow through the microstructure of a model paper nicely illustrates that the tortuosity of pathways is as crucial as the porosity and that these two properties markedly vary across a paper sheet. As generally porosity and tortuosity do not vary independently, we introduce the parametric Copula approach as a convenient method to quantify the correlation between them under consideration of their local variations.

The porosity of paper is a crucial quantity for most applications. As a prominent example, the air permeance of paper is strongly governed by the porosity. The relation between air permeance and porosity is regarded sufficiently unambiguous so that the paper porosity is indirectly inferred from standardized air permeance measurements, i.e., the Gurley method[1.] Moreover, paper can be markedly heterogeneous up to the centimeter scale due to, e.g., the formation of flocs. A global, sheet-averaged value of

the air volume flux likely fails to capture the nature of the pore space offered by paper. Hence, it is highly desirable to establish the extent of local variations in porosity and further descriptors of the pore space and to quantify how these variations locally modify the air permeance.

In this contribution, we combine a statistical analysis of the 3D porous microstructure of paper with a simulation of airflow utilizing Computational Fluid dynamics (CFD) to determine the degree of local airflow variations. These simulations instruct us that besides the porosity, the tortuosity is a suitable quantity to rationalize the local variations in airflow. As a result of the interdependence between tortuosity and porosity, a rationalization of the variations in terms of the pore microstructure requires us not only to quantify (i) the local variation in the porosity and mean geodesic tortuosity from the microstructure, but also (ii) their degree of correlation.

We utilize CFD to simulate the airflow for the standardized conditions related to the Gurley test[1] The underlying microstructure has been acquired from X-ray computed microtomography (µ-CT) measurements at a voxel resolution of 1.5 µm. Subsequent postprocessing to determine pore and fiber contributions[2] yielded a total investigated area of $A = 2.8125 \times 1.666$ mm^2, which is further subdivided into non-overlapping cutouts. For each cutout, the CFD simulations yield the mean air velocity (and mean volume flux) as a measure for the permeance and the spatial evolution of the air pressure, and the air velocity (cf. Figure 7.6a). Alongside the local porosity available for airflow (i.e., pores continuously connected to the exterior air volume), the local thickness of each cutout is extracted from the CFD simulations. Figure 7.6b shows that the local air velocities appear to correlate linearly with the local porosity.

Nevertheless, knowing the local porosity is not sufficient to infer the air velocity, as the velocities profoundly spread for practically equal porosities (filled symbols in Figure 7.6b). With a further analysis in terms of the Carman-Kozeny equation, we can rule out that this spread arises from variations in the local thickness.

Rather, the evolution of the streamlines through the microstructure, illustrated in Figure 7.6a, indicates important pathways that do not straightly connect the bottom and top surfaces. To account for the nature of these pathways, our statistical analysis of the pore space ought to account also for the mean geodesic tortuosity, which measures the windedness of pathways through the pore space, i.e., captures the length and the orientation of the shortest local pathways. The tortuosity is known to be an important morphological descriptor for mass flow and conduction phenomena in porous media in general, cf. e.g.[3,4,5], and in paper, cf., e.g. [6,7]. We can readily expect that the tortuosity, similar to the porosity, is going to exhibit local variations.
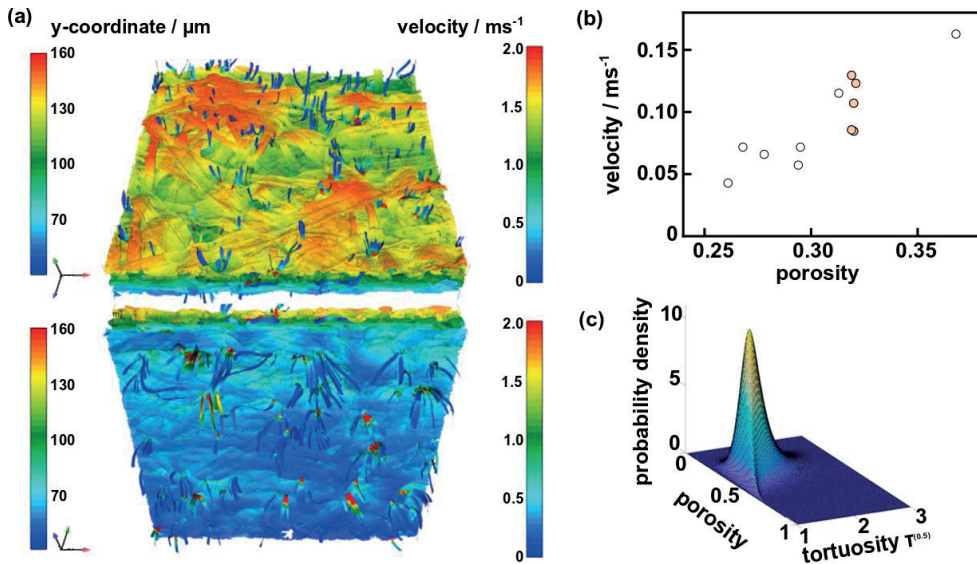
Figure 7.6 (a) Top and bottom view on the streamlines of the airflow obtained from the CFD simulations under Gurley conditions for a selected cutout. (b) Mean air velocity of the cutouts obtained from the CFD simulations under Gurley conditions vs. the cutout porosity. The lightly shaded symbols represent cutouts with comparable porosity but distinctively different velocities. (c) Joint distribution of porosity and tortuosity of a voxel-sized intruder for a cutout size of 60 µm.

As the tortuosity cannot be tuned or established independent from the porosity[3,4,5,6,7] also the local variations of these quantities ought to be related. We propose that the use of so-called copulas offers an elegant and convenient route to track the combined impact of porosity and tortuosity and their local variations[8] We statistically analyze the local geometry in two consecutive steps. First, we analyze the variations of each quantity separately. To do so, we extract sets of cutouts from the microstructure and analyze them in terms of the local porosity and the mean geodesic tortuosity. We obtain an analytical representation of our porosity distribution by fitting the parameters determining a beta-probability distribution function to the data via maximum likelihood estimation. Alike, the distribution of local mean geodesic tortuosities can be well modeled by a shifted gamma-distribution[9] An asymmetric Gamma distribution nicely illustrates that local variations are not necessarily normally distributed, see also, e.g.[10], With this step, we gained analytical "models" that approximate the distributions obtained from the geometry data very wel[8].

To quantify inter-relationships between porosity and tortuosity in a second step, we turn to the copula approach. In essence, copulas allow one to decompose a joint probability distribution, here consisting of the local porosities and local tortuosities, into the above-obtained individual, univariate probability distributions of porosity and tortuosity. Copulas couple these univariate probability distributions (uncorrelated by definition) and allow one, hence, to specify their correlation separately. Formally, a

copula is a distribution function on the unit cube, which can be used to model the (multivariate) joint distribution of random variables provided their univariate distributions are available.

In this contribution, we use the parametric family of Gumbel copulas[11] to model the joint distribution of local porosity and local mean geodesic tortuosity; the Gumbel copula has only one parameter, which readily quantifies the correlation between local porosity and local mean geodesic tortuosity. Our analysis clearly shows a negative correlation between local porosity and tortuosity for the considered sample, in line with the findings for tortuous flow in a 2D pore space in a crafted virtual material[3] Thus, the larger the porosity, the shorter the shortest path lengths through the pore space. As our statistical analysis relying on copulas quantifies the porosity-tortuosity correlation, we can even predict conditional distributions of local tortuosities for a given value of local porosity and vice versa. In essence, this conditional tortuosity distribution is obtained by "slicing" such a joint distribution, which is exemplarily shown in Figure 7.6c, at the porosity value of interest, e.g., at 0.4. The resulting conditional distribution of the local mean geodesic tortuosity readily rationalizes why the air velocity attains a marked spread at a given porosity (cf. Figure 7.6b). The large spread in the values of the mean geodesic tortuosity readily causes also the air velocity value to spread. The proposed copula approach can be readily applied to other pairs of quantities, including, for example, the air permeance. Likewise, the approach can be transferred to related, yet mathematically distinct pore space descriptors.

As possible examples may serve here, a porosity restricted to the interconnected (i.e., flow-relevant) pore space, the mean geodesic tortuosity related to pathways of a minimal path diameter[8] pore size distributions[10], mass density distribution, and thickness distributions[12,13]. As parametric copulas model the distribution of each quantity analytically, the approach inherently retains the complete information on each distribution stored in just a few parameters. In doing so, each suitable distribution can be accounted for, rather than just tracking mean values or widths of not-necessarily justified normal distributions. The coupling of the individual distributions in a copula formalism just introduces one or a few more parameters to indicate the degree of correlation between them. Thus, copulas are particularly attractive as they can statistically characterize large three-dimensional microstructures by using few parameters.

References

1. Tappi (2017). Air resistance of paper (Gurley method), Jan.

2. Machado Charry, E., Neumann, M., Lahti, J., Schennach, R., Schmidt, V., & Zojer, K. (2018). Pore space extraction and characterization of sack paper using μ-CT. Journal of microscopy, 272(1), 35-46.

3. Koponen, A., Kataja, M., & Timonen, J. V. (1996). Tortuous flow in porous media. Physical Review E, 54(1), 406.

4. Matyka, M., Khalili, A., & Koza, Z. (2008). Tortuosity-porosity relation in porous media flow. Physical Review E, 78(2), 026306.

5. Neumann, M., Stenzel, O., Willot, F., Holzer, L., & Schmidt, V. (2020). Quantifying the influence of microstructure on effective conductivity and permeability: virtual materials testing. International Journal of Solids and Structures, 184, 211-220.

6. Holmstad, R., Gregersen, Ø. W., Aaltosalmi, U., Kataja, M., Koponen, A., Goel, A., & Ramaswamy, S. (2005). Comparison of 3D structural characteristics of high and low resolution X-ray microtomographic images of paper. Nordic Pulp & Paper Research Journal, 20(3), 283-288.

7. Holmstad, R., Goel, A., Ramaswamy, S., & Gregersen, O. W. (2006). Visualization and characterization of high resolution 3D images of paper samples. Appita: Technology, Innovation, Manufacturing, Environment, 59(5), 370.

8. Neumann, M., Charry, E. M., Zojer, K., & Schmidt, V. (2020). On variability and interdependence of local porosity and local tortuosity in porous materials: a case study for sack paper. Methodology and computing in applied probability, 1-15. https://doi.org/10.1007/s11009-019-09761-1.

9. Johnson, N. L., Kotz, S., & Balakrishnan, N. (1995). Continuous univariate distributions. John Wiley & Sons, Ltd., New York.

10. Dodson, C. T. J., & Sampson, W. W. (1997). Modeling a class of stochastic porous media. Applied Mathematics Letters, 10(2), 87-89.

11. Nelsen, R. B. (2007). An introduction to copulas. Springer Science & Business Media.

12. Dodson, C. T. J., & Sampson, W. W. (1999). Spatial statistics of stochastic fiber networks. Journal of statistical physics, 96(1-2), 447-458.

13. Dodson, C. T. J., Oba, Y., & Sampson, W. W. (2001). Bivariate normal thickness-density structure in real near-planar stochastic fiber networks. Journal of Statistical Physics, 102(1-2), 345-353.

.

Computer simulation of liquid wetting in low density fibrous networks

D. Steven Keller

University of Miami, Oxford, Ohio, USA

Corresponding author: *Steven Keller <kellerds@miamioh.edu>*

Keywords: Tissue, towel, wetting, tomography, numerical simulation

Summary

The absorption characteristics, including the rate of wetting and volumetric holding capacity of aqueous solutions, are important quality metrics for retail and away from home paper towels. The spreading of liquid is a function of the surface energetics of the liquid-fiber system, as well as the heterogeneous distribution of fiber density within the structure. Kitchen towels incorporate structural features that cause a wide variation in the local web density that spans dimensions from the fiber scale (10-6 m) to embossments and multi-plies (10-3 m). Most standard absorption test rely on the bulk absorption behavior of the products in attempt to simulate end use performance[1]. Recent studies[2,3] have explored the meso-scale wetting behavior, with interest in observing how structural features and liquid chemistry influence wetting. The modeling of liquid wetting up to now has focused on the use of the traditional wetting theory, such as that of Lucas-Washburn[4].

This paper describes a new approach for numerically modelling the wetting behavior of paper towel structures using 3D X-ray microscopic (3D-XRM) data sets as the volumetric structure within which the movement of the liquid is tracked. The approach is based on a modified Ising Model[5] and recent implementations thereof[6,7] that model the wetting of simulated fibers and fibrous structures. The model uses the surface energetic parameters of the liquid and solid surfaces to predict the spreading of the liquid into the heterogeneous fibrous structure.

Introduction

In the study of the meso-scale (10-2-101 mm) wetting of kitchen and away-from-home hand towels, the spreading of the liquid, either by pressurized flow or wicking due to

low liquid-solid interfacial energy, is generally irregular due to heterogeneity in the structure resulting from the induced features, such as creping embossing or structured drying. The characteristics of the fiber morphology as well as the web density have significant influence on wetting rate and capacity. The size and spacing of features, as well as the interfiber spacing and fiber alignment all affect wetting behavior. The surface chemistry of the fibers, and its uniformity, also impact the rate of wetting at the scale of individual fiber surfaces. Fiber shape and the presence of microfibrils and other surface asperities will all affect the advancing of liquids along the internal surfaces. The properties of the liquid and any dissolved chemicals that can change the liquid or the surface will also affect the rate of spreading. Investigation of the effects of mesoscale structure are ongoing, as reported recently by Keller[2]. Those experiments have observed the non-uniform rate of liquid wicking in retail kitchen towels that results from density and thickness heterogeneity. The in-plane spreading was imaged using infrared imaging and observed to advance within the structure and along the external surface of densified regions, depending on the rate of liquid injection.

Kitchen towels, other hygienic papers and nonwovens generally have exceedingly complex structures that are not easily modeled using simulated web structures, although a few examples exist in the literature. The most common approach has been to observe the macro scale behavior through standard tests[1,4] and the mesoscale behavior[8], and consider the fibrous solid as the continuous phase and the void space as distributed open pores of a given size or distribution. Capillary dynamics theories, such as Lucas-Washburn[4] and modified forms of such, are then applied to ascertain how structural modification, such as changes to fiber morphology[9,10] or imparted features, affect pore structure and hence bulk wetting behavior.

This investigation represents a compliment to the meso-scale examination of wetting rate and capacity previous described[2], by using XR-uCT data sets from retail kitchen towels in numerical computer simulation of liquid advancement through solid fibrous structures. The approach establishes a three-phase system where the fibrous structure is static, and the liquid and air are moveable, depending on minimization of the local energy balance. The surface energetics of the liquid and fiber, in this case water and cellulose, determine the extent to which the liquid advances within the structure. The objective was to replicate the intricacies of wetting observed in experiments, using no other inputs than the mesoscale structure and the surface energy parameters of the constituents.

Theoretical

Simulation based on the Ising Model

The Ising model, in either 2D or 3D, was first used to describe the behavior of a ferrous material by describing the magnetic dipole moments of cells within a structural lattice

as having one of two "spin" states[5]. Any two cells within the lattice will have a mutual interaction energy that exists only if the cells differ in spin state. It was developed to describe the thermal dependency of magnetism and is essential a discrete treatment of the system that considers a lattice of cells that possess properties independent of the bulk system, but dependent on neighboring cells. Specific application to the phase transition experienced when liquid advances in the presences of fibers, or with a fibrous web was first introduced in a series of papers by Lukas et al. [11,12,13,14,15]. While the Ising model considers the system to be binary with either +1 or -1 polarity, Lukas et al. [14] postulated that unit cells could be ascribed multiple parameters useful in describing an energetic state with neighbors. From that starting point, they demonstrated the application of numerical computer simulations of the transport of moisture within model systems, such as along cylindrical rods[11] and wicking through oriented rod bundles[12], and computer-generated fibrous structures with different levels of fiber anisotropy[13]. The interaction energies of the simulations used to calculate phase exchanges were either approximated[14] or obtained from the literature for the liquids and solids involved[16]. While some of his work delved into the concept of a distance function where the parameters of a unit cell are a function cells of a neighborhood beyond nearest neighbors, for this investigation only the 6 or 27 nearest neighbors that contact the unit cell were considered. In order to determine if the liquid advances into the structure, the energetic state of all "liquid" cells is considered before and after a unit cell of liquid is advanced to fill an adjacent "void" cell. If the energy of the system is reduced, then the advancing of the liquid occurs. Otherwise, the liquid remains static until the next iteration. For tomographic data sets with as much as 109 cells, and 85% void space, calculation efficiency is a significant consideration.

In their investigation of ink seepage into paper, Cheriet et al. [7,17] presented an algorithm to increase calculation efficiency by reducing the redundancy of exchange energy determination for nearest neighbors, and focused exchange calculations on only the cells at the liquid / air interface. Once again, that work was limited to computer-generated fibrous structures stochastically distributed in a virtual space.

Simulated Liquid Flow in Kitchen Towels

The Ising based, energy exchange minimization approach seemed ideally suited to simulate the non-pressurized advancement of liquid through the discrete data sets obtained from 3D-XRM imaging. The binarized data sets provide a rigid porous structure that closely represents the variation in local density and local fiber segment orientation that exists in actual towel samples. To implement the simulation, a margin is generated at one edge of the data set by assigning void voxels as the probe liquid, e.g. water. Figure 7.7 illustrates a small region of a 3D lattice, where white voxels are the fiber derived from 3D microscopy, and blue voxels represent the liquid in the initial state. The red voxel represents a test cell, where the interaction energy between it and its neighbors is compared with that after a phase change. Energy minimization

determines if the liquid advances or recedes, especially along the surface of the rigid fiber network depending on the liquid/solid interfacial energy.

The simulation is initiated by iteratively testing each voxel at the liquid/air interface. Figure 7.8 illustrates the initial state (A) and the advancement of the liquid after numerous iterations (B). It is evident that the fluid advances along the fibers and is transferred to adjacent fibers without consideration of directionality. Gravitational forces are considered negligible in this model, since the volumes of the pixels are so small, i.e. 10-9 g, and spreading occurs within the plane that is perpendicular to the gravitational vector. One may also notice that the liquid transports along fibers and is especially promoted in bridges between multiple fibers, where liquid is draw into crevasses by wetting on multiple surfaces of the cell.
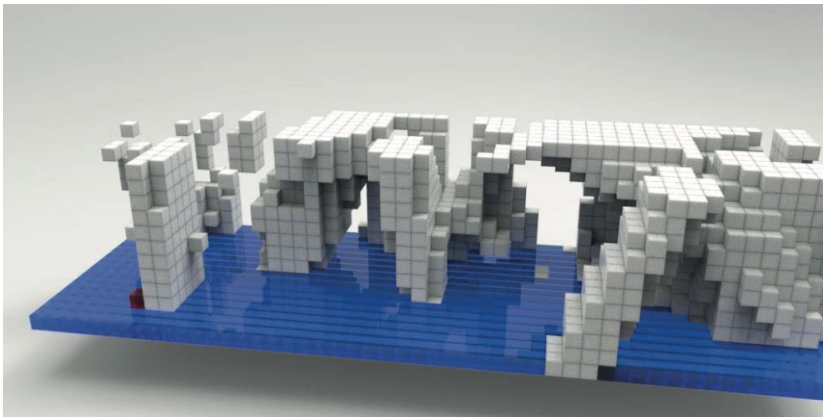
Figure 7.7. Representation of a region of a XR-µCT data set shown solid-fibers (white) and a liquid-water surface (blue). Each void voxel that potentially intersects both solid and liquid (red) is tested to determine if the energy of the system is reduced if it converts to liquid. If this is the case, then it represents the advancing of the liquid along the surface of the solid. Once all voxels are tested and action is taken, then the process is repeated. Each iteration represents a step in time. It is not possible to determine flow rate using this model.

Results

The liquid wetting simulation was implemented using a custom MATLAB routine. The routine loads 3D-XRM data sets and performs the iterative comparative process of surface voxels to determine if the liquid advances or remains. Once all surface voxels are tested, the data set is stored, and the cycle repeated. Thus, each data set represents a frame in time to visualize the wetting process. The limitations of this approach are fully recognized, as the units of time are not defined. The velocity of fluid flow requires the introduction of liquid viscosity and adding a force term dependent on the proximity of the liquid to the solid surface, establishing a shear gradient. An example of a single frame from a simulation series is shown in Figure 7.8 (left). In that Figure, water is shown as blue and fibers are white. The advancing of the water into

the structure along the fiber surfaces causes progression in certain directions, while others remain unwetted. This corresponds well with what is observed in actual wetting experiments. In Figure 7.8 (right) the fibers have been hidden so that only the water voxels appear. Notice the preponderance of large void spaces in the lower left and upper right wetted regions.

A second limitation was observed in the first implementation of this model. Consideration was not given to energy minimization for neighbors extending beyond those nearest to the center voxel. This produces an artifact in the liquid phase that appears as a pyramid geometry as the liquid advances along a fiber. This is especially visible where liquid at the initial level is in contact with that which has advanced along a fiber. What is absent is a minimization of the surface energy of the liquid expanse where no fiber is in contact.

Conclusions

In summary, the Lukas-Ising approach for simulating wetting remains viable, although development will require significant computational power as proper implementation should include calculation of energy of both surface and bulk phase liquid voxels. It should also involve a more robust energy calculation that
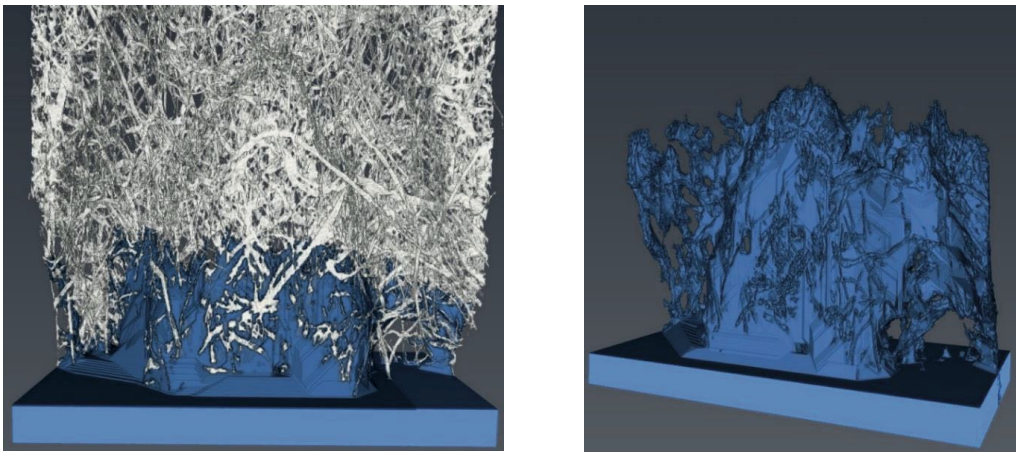
Figure 7.8. Eaxmple of the simulated wetting of a bounty TAD feature using the Lukas-Ising model after 255 iterations. The combined fiber and water system is shown left. Illustrated at the right, the fiberous structure is hidden.

includes a larger neighborhood with an appropriate distance decay function. The method would significantly benefit from increasing the resolution of surface curvature by subsampling the liquid voxels by at least a factor of 10. This action that would increase calculation time by at least a factor of 100, a proposition not unreasonable considering the potential for advancement in computational power that GPU processing provides.

References

1. Beuther, P. D., Veith, M. W., & Zwick, K. J. (2010). Characterization of absorbent flow rate in towel and tissue. Journal of Engineered Fibers and Fabrics, 5(2), 155892501000500201.

2. Keller, D.S., & Abedsoltan, H. (2019). Mesoscale liquid Absorption properties of towel papers. Int. Paper Physics Conf., Indianapolis. Tappi, Atlanta, USA

3. Gabrielsson, A., Vomhoff, H., & Tysen, A. (2014). Investigation of the Dynamic Liquid Absorption Properties of Kitchen Towel. TAPPI PaperCon 2014 (ed) pp. 3137-3160, TAPPI Press, Nashville, TN, USA.

4. Chatterjee, P. K., & Nguyen, H. V. (1985). Mechanism of liquid flow and structure property relationships (Vol. 34). Elsevier, Amsterdam.

5. McCoy, B. M., & Wu, T. T. (2014). The two-dimensional Ising model. Courier Corporation.

6. Lukas, D., Kostakova, E., & Sakar, A. (2006). Computer simulation of moisture transport in fibrous materials. Thermal and Moisture Transport in Fibrous Materials, Woodhead Publishing Limited, Cambridge, 469-541.

7. Bakhta, A., Leclaire, S., Vidal, D., Bertrand, F., & Cheriet, M. (2019). Multiscale simulation of ink seepage into paper: A mesoscopic variational model. Computer Physics Communications, 239, 1-13.

8. Vomhoff, H., Gabrielsson, A., & Tysen, A. (2014). Investigations into dynamic liquid absorption properties of kitchen towel. In Tissue World Americas Conference 2014.

9. Hodgson, K. T., & Berg, J. C. (1988). The effect of surfactants on wicking flow in fiber networks. Journal of colloid and interface science, 121(1), 22-31.

10. Hodgson, K. T., & Berg, J. C. (2007). Dynamic wettability properties of single wood pulp fibers and their relationship to absorbency. Wood and fiber Science, 20(1), 3-17.

11. Lukas, D., Pan, N., Sarkar, A., Weng, M., Chaloupek, J., Kostakova, E., ... & Amler, E. (2010). Auto-model based computer simulation of Plateau–Rayleigh instability of mixtures of immiscible liquids. Physica A: Statistical Mechanics and its Applications, 389(11), 2164-2176.

12. Lukas, D., & Pan, N. (2003). Wetting of a fiber bundle in fibrous structures. Polymer composites, 24(3), 314-322.

13. Zhong, W., Pan, N., & Lukas, D. (2004). Stochastic modelling of tear behaviour of coated fabrics. Modelling and Simulation in Materials Science and Engineering, 12(2), 293.

14. Lukas, D., Soukupova, V., Pan, N., & Parikh, D. V. (2004). Computer simulation of 3-D liquid transport in fibrous materials. Simulation, 80(11), 547-557.

15. Zhong, W., Pan, N., & Lukas, D. (2004). Stochastic modelling of tear behaviour of coated fabrics. Modelling and Simulation in Materials Science and Engineering, 12(2), 293.

16. Weng, M., & Lukas, D. (2012). A Stochastic Study on the Wicking Phenomena. Journal of Donghua University (Eng. Ed.) Vol, 29(2).

17. Moghaddam, R. F., Moghaddam, F. F., & Cheriet, M. (2013). Computer Simulation of 3-D Finite-Volume Liquid Transport in Fibrous Materials: a Physical Model for Ink Seepage into Paper. arXiv preprint arXiv:1307.2789.

Wednesday 2.9.2020 at 13:00 - 15:00

Session 7B

Numerical modelling of deformation and fracture

Session chair: Jukka Ketoja

Moisture induced instability in paper analysed with incremental deformation theory

Eric Borgqvist[a], Bo Li[b], & Xi-Qiao Feng[b]

[a]*Tetra Pak Packaging Solutions AB, Lund, Sweden*
[b]*Institute of Biomechanics and Medical Engineering, Tsinghua University,
Beijing, China*

Corresponding author: *Erik Borgqvist <Eric.Borgqvist@tetrapak.com>*

Keywords: Incremental deformation theory, instability, wrinkling, moisture, swelling

Summary

Incremental deformation theory is used to analyze the onset of wrinkling induced by constrained swelling. An ordinary differential equation is derived which is used to study at what increase of moisture content the instability is triggered. The critical wavelength and moisture content have been identified when the length and web force is varied.

Introduction

Wrinkling in paper induced by moisture has been investigated in this work using incremental deformation theory, see Biot (1965)[1] and Odgen (1984)[2]. In this framework, a pre-deformed state of a body is assumed and new non-trivial solutions to the incremental boundary value problem is sought. We will in particular investigate the case of tension wrinkling type instabilities induced by moisture. During the ink-jet print process, wrinkling induced by moisture can occur, see Maharajan (2007)[3]. Fluting is also a wrinkling phenomena, which can happen for paper during the offset printing process, see Kulachenko et al., (2007)[4], and Erkkilä et al., (2016)[5], and is related to the moisture content in the board.

In this work, incremental deformation theory is used to analyze the onset of wrinkling induced by constrained swelling. Growth deformation tensors were included into the incremental deformation theory in[6] and is adopted in this work. The theory has been widely adopted and successful for analyzing many aspects of growth induced wrinkling phenomena for different materials, e.g. In[7] esophageal mucosa was studied using the

framework. Until now the incremental deformation theory has not yet been applied to paper materials to the authors' knowledge.

An ordinary differential equation is derived which is used to study at what increase of moisture content the posed incremental field is triggered. It is rather straight forward to make parametric studies since the ODE can be solved using standard solvers, while it can be comparably more difficult with FEM-simulations due to sensitiveness to meshing and perturbations fields. However, there are limitations related to what boundary value problems that is possible to solve with this method, and therefore FEM-simulations have also been performed in this work to verify the model.

Incremental boundary value problem

The material is assumed to be hyperelastic and the existence of a potential (the free energy) ψ, is assumed for the constitutive law. The free energy from[8] has been adopted to model the paper. To simulate swelling of paper a multiplicative split of the deformation gradient is assumed, i.e.

$$F = F^e F^G \tag{1}$$

Where F^e is the elastic part of the deformation and $F^G(\Delta m_c)$ is the deformation induced by the swelling through a change in moisture content of the material. It is assumed that the swelling in the paper will be controlled externally by increasing or decreasing the moisture content from a reference moisture state, m_c^0 e.g.
$\Delta m_c = m_c - m_c^0$

The incremental BVP can be formulated as

$$\text{div}(\mathcal{L} : \dot{F}_0) = 0 \tag{2}$$

where the instantaneous moduli tensor $\mathcal{L}$ can be identified from

$$\mathcal{L} : \dot{F}_0 = F^e \left(\frac{\partial \psi}{\partial F^{eT} F^{eT}} : (\dot{F}_0 F^e)^T \right) \tag{3}$$

The boundary conditions at the traction free surfaces and the boundary with prescribed displacements are respectively given by

$$\dot{S}_0^T n = 0 \qquad \dot{x} = 0 \tag{4}$$

The moisture content will be increased from a pre-stressed state and non-trivial solution for a given Δm_c will be sought for when solving (2)

The particular boundary value problem that is studied is given below. We will assume that the paper is initially loaded in tension in according to Figure 7.9a. After the pre-tension step, the paper is wetted uniformly and it is assumed that all the edge boundaries are kept fix, cf. Figure 7.9b.

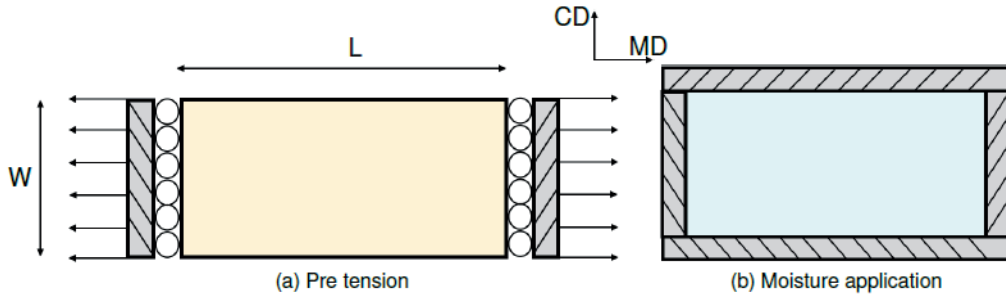(a) Pre tension   (b) Moisture application

Figure 7.9. Sketch of the boundary conditions used in analysis. First a pre tension is applied and then moisture is applied uniformly on the paper with constrained boundaries.

Inspired from the out-of-plane displacement described in [9], the onset of instability from the following incremental deformation field is investigated:

$$
\begin{aligned}
u(x, y, z) &= U(z) \cos(ny) \cos(\pi x/L) \\
v(x, y, z) &= V(z) \sin(ny) \sin(\pi x/L) \\
w(x, y, z) &= W(z) \cos(ny) \sin(\pi x/L)
\end{aligned}
\tag{5}
$$

This field is inserted into the incremental boundary value problem (2). After quite some linear algebra , the following six degree differential equation can be derived

$$
-b_5 b_1 V + \left(c\frac{a_{11}a_{24}}{a_{13}a_{21}} - c\frac{a_{14}}{a_{13}} + \frac{a_{39}}{a_{32}}b_1 - b_5 b_2\right)V'^{(2)} + \left(c\frac{a_{11}a_{26}}{a_{13}a_{21}} + c\frac{a_{35}}{a_{32}} + \frac{a_{39}}{a_{32}}b_2 - b_5 b_3\right)V'^{(4)} + \frac{a_{39}}{a_{32}}b_3 V'^{(6)} = 0
\tag{6}
$$

The coefficients in the differential equation $\mathcal{L}$ 6) correspond to different linear combinations of the components of the instantaneous moduli tensor

Results

The differential equation (6) is integrated with a standard ODE-solver and the moisture content difference Δm_c which provides a non-trivial solution to (6) and fulfills the boundary conditions (4) is found by applying the shooting method. This procedure is repeated for a number of wavelengths, n, and the moisture content that triggers the instability for the different wavelengths can be computed. The results from a specific simulation with dimensions L = 200 mm and thickness, t=0.05 mm is shown in Figure 7.10a

(a) Moisture content vs wave length from incremental deformation theory

(b) Finite element simulation
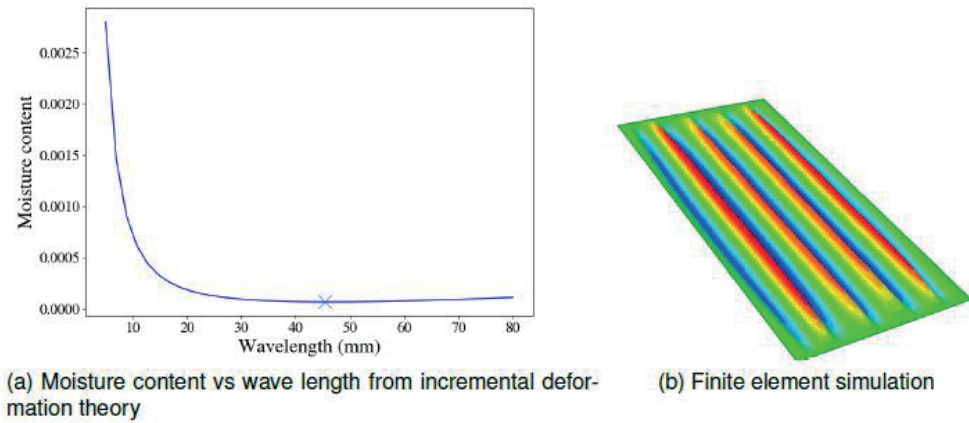
Figure 7.10 The moisture content difference that gives a non-trivial solution to (6) for different wavelengths. The length of the paper has been set to L=200 mm. b) The boundary value problem solved with Finite Element Method and where the displacements have been magnified 100 times

A location at wavelength 45.4 mm and moisture content $6.7 \cdot 10^{-5}$ is marked with an $\times$ in Figure 7.11a. This marks the lowest moisture content necessary to trigger the instability, e.g. providing the critical wavelength. The critical moisture content corresponds to an compressive CD-stress that is approximately 30 kPa. A FEM simulation has been performed with the boundary conditions outlined above. The resulting post-buckling deformation fields are shown in Figure 7.11b where the out-of-plane displacements have been magnified 100 times. The wavelength and moisture content is matching well that obtained with the incremental deformation theory.

(a)

(b)
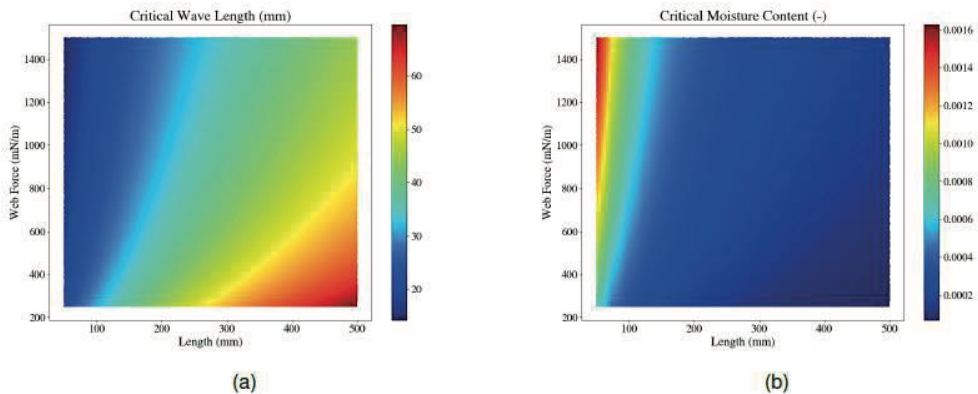
Figure 7.11. Influence of length and web force of paper on the critical wavelength and moisture content difference

Parametric studies have been performed with the model. As an example, the length and the web force have been varied simultaneously and the critical wavelength and

moisture content have been identified. From Figure 7.11 one can clearly see that an increasing web force leads to a decrease in the critical wavelength and increase in critical moisture content difference. While an increasing length provides larger critical wavelength but lower critical moisture content. This is in line with previous studies performed in the literature.

Acknowledgements

References

1. Biot, M. A. (1965). Mechanics of incremental deformations. John Wiley & Sons, Inc. New York/London/Sydney.

2. Ogden, R. (1984). Non-linear elastic deformations. Dover Publications, inc, dover edition edition.

3. Maharajan, R. K. (2007). Investigation of the effect of swelling and shrinkage on the wrinkling response of locally wetted papers subjected to tension with application to web-fed ink-jet printing (Doctoral dissertation, Miami University).

4. Kulachenko, A., Gradin, P., & Uesaka, T. (2007). Basic mechanisms of fluting formation and retention in paper. Mechanics of materials, 39(7), 643-663.

5. Erkkilä, A. L., Leppänen, T., & Tuovinen, T. (2016). The curl and fluting of paper: the effect of elasto-plasticity. Proc. ECCOMAS Congress 2016: VII Eur Cong Computat Meth Appl Sci Eng., Vol III, ISBN 978-618-82844-0-1. National Technical University of Athens, Greece

6. Amar, M. B., & Goriely, A. (2005). Growth and instability in elastic tissues. Journal of the Mechanics and Physics of Solids, 53(10), 2284-2319.

7. Li, B., Cao, Y. P., & Feng, X. Q. (2011). Growth and surface folding of esophageal mucosa: a biomechanical model. Journal of biomechanics, 44(1), 182-188.

8. Borgqvist, E., Wallin, M., Tryding, J., Ristinmaa, M., & Tudisco, E. (2016). Localized deformation in compression and folding of paperboard. Packaging Technology and Science, 29(7), 397-414.

9. Cerda, E., & Mahadevan, L. (2003). Geometry and physics of wrinkling. Physical review letters, 90(7), 074302.

.
.

Numerical investigation of paper using the concept of representative volume elements characterized by single fiber behavior and fiber-fiber interaction

Greta Kloppenburg[a], Hagen Holthusen[a], Yujun Li[b], Jean-Francis Bloch[c], Ulrich Hirn[d], & Jaan-Willem Simon[a]

[a]RWTH Aachen University, Aachen, Germany
[b]Northwestern Polytechnical University, Shaanxi, China
[c]Grenoble Institute of Technology, Grenoble, France
[d] Institute of Bioproducts and Paper Technology, Technical University of Graz, Graz, Austria

Corresponding Author: Jaan-Willem Simon <jaan.simon@rwth-aachen.de>

Summary

In this work, paper has been investigated numerically on the scale of the fiber network taking into account the single fiber mechanical behavior as well as the fiber-fiber interactions. The implementation of a random distribution of fibers and a statistical distribution of fiber geometries enabled the resulting network model to yield realistic results. As a result, a representative network size of $L = 12L_H \approx 420 \mu m$ has been identified in accordance with the requirements of numerical homogenization.

The material paper is actually indispensable in daily life and will gain further importance due to its sustainability and recyclability. Therefore, a comprehensive understanding of its mechanical behavior is essential. For this purpose, both the macrostructure on the sheet scale and the microstructure, which ranges from the network to individual fibers, must be investigated.

The macrostructural behavior of paper is highly affected by the characteristics of its microstructure. Furthermore, the microstructural network behavior is mainly influenced by the single fiber material behavior, which is additionally influenced by the microfibrils (see e.g.[1]), and by the bonding behavior between the fibers. The prediction of the

network behavior is difficult due to (i) the properties of fibers (variety of geometries and mechanical properties) and contacts and (ii) the non-periodic distribution of the interwoven fibers. A further difficulty is the determination of representative subsections of the microstructure.

The use of numerical models is a helpful tool to deal with this challenge, since it allows a separate examination of the microstructural components. A fiber network model representing the microstructure of paper using the principle of numerical homogenization is presented, based on a previous study[2].

In the current work, realistic network models (see Figure 7.12) were (i) generated based on a single fiber model and a fiber-cross model and (ii) investigated in the framework of the Finite Element Method (FEM).

The single fiber material behavior was experimentally determined using a testing setup, described in[3]. Furthermore, microfibril angles were determined by curve fitting. The bonding behavior between the fibers was investigated by a fiber-cross model, utilizing a cohesive contact formulation. In a parameter study, the influence of both material and structural properties was determined, performing peeling and shearing tests inspired by[4,5].

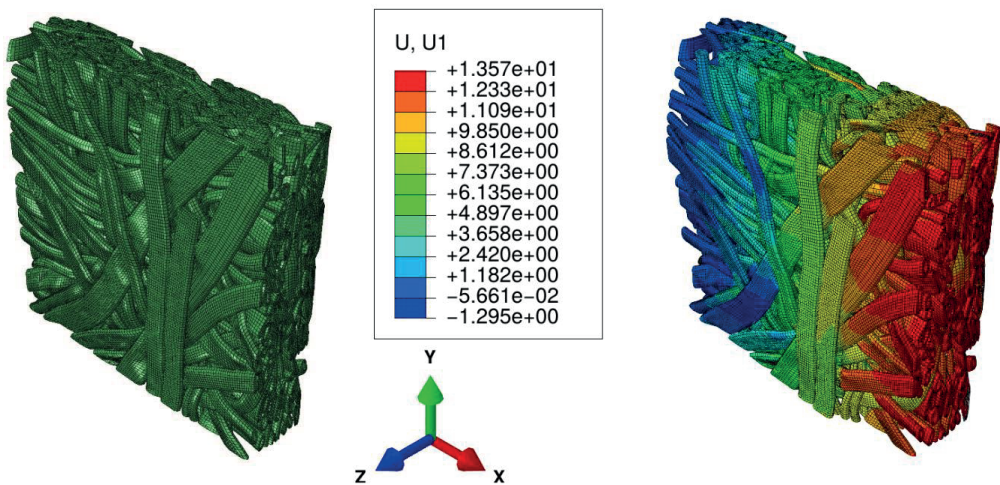Figure 7.12. Undeformed (left) and deformed (right) network (network length L = 420μm) with loading in x-direction.

According to the principle and the requirements of numerical homogenization, a study was performed to find a network size that could be considered representative for the microstructure of paper. In accordance with the approach presented in[6], it was

assumed that the network size L could be expressed through a multiple N of a heterogeneity size L_H consisting of the mean fiber width and the mean pore size, $L = N \times L_H$, where $L_H \approx 35\,\mu m$.

Moreover, the approach of averaging the material response of several realizations of smaller networks to obtain a representative result in the framework of homogenization was applied. As a result, it was found that network sizes with $N = 12$ were representative for the investigation of mechanical characteristics if at least three realizations were considered. Smaller networks showed a strong dependence on the fiber orientation even for higher numbers of realizations.

To summarize, a microstructural fiber network, based on separately investigated material and contact parameters, is presented. Thanks to the implementation of a random distribution of fibers and a statistical distribution of fiber geometries, the resulting network model has been proven to yield realistic results. Finally, a representative network size of $L = 12L_H \approx 420\mu m$ has been identified in accordance with the requirements of numerical homogenization.

Acknowledgements

References

1. Vishtal, A., & Retulainen, E. (2014). Boosting the extensibility potential of fibre networks: A review. BioResources, 9(4), 7951-8001.

2. Li, Y., Yu, Z., Reese, S., & Simon, J. W. (2018). Evaluation of the out-of-plane response of fiber networks with a representative volume element model. Tappi Journal, 17, 329-339.

3. Jajcinovic, M., Fischer, W. J., Hirn, U., & Bauer, W. (2016). Strength of individual hardwood fibres and fibre to fibre joints. Cellulose, 23(3), 2049-2060.

4. Magnusson, M. S., Zhang, X., & Östlund, S. (2013). Experimental evaluation of the interfibre joint strength of papermaking fibres in terms of manufacturing parameters and in two different loading directions. Experimental mechanics, 53(9), 1621-1634.

5. Magnusson, M. S., Fischer, W. J., Östlund, S., & Hirn, U. (2013). Interfibre joint strength under peeling, shearing and tearing types of loading. Adv Pulp Pap Res. Cambridge, 103-124.

6. du Roscoat, S. R., Decain, M., Thibault, X., Geindreau, C., & Bloch, J. F. (2007). Estimation of microstructural properties from synchrotron X-ray microtomography and determination of the REV in paper materials. Acta Materialia, 55(8), 2841-2850.

.

Simulated fracture and tensile strength of paper

Anna-Leena Erkkilä[a], Teemu Leppänen[a], & Tero Tuovinen[a,b]

[a]*University of Jyväskylä, Jyväskylä, Finland*
[b]*JAMK University of Applied Sciences, Jyväskylä, Finland*

Corresponding author: *Anna-Leena Erkkilä <anlejoer@gmail.com>*

Keywords: Paper, fiber orientation variation, tensile strength, fracture, simulation, FEM

Summary

Linear elastic material model with a softening step was constructed to study fracture behavior of paper. Measured and artificial fiber orientation structures and moisture contents were considered in the simulations.

Methods

Linear elastic orthotropic material model is used to describe paper behavior under external tension. A plane stress state is assumed. Tensile strength $\sigma^t(\xi, \beta)$ (MPa) and breaking strain $\varepsilon^b(\xi, \beta)$ (-) under tension are determined using function

$$f(\xi, \beta) = a_1\xi + a_2 e^{a_3\beta} + a_4\xi\beta + a_5 \tag{1}$$

where ξ (-) is the fiber orientation anisotropy, β (%) is the moisture content and a_i are the fitted parameters for $\sigma^t(\xi, \beta)$ and $\varepsilon^b(\xi, \beta)$ for the main (subscript 1 in Table 7.1) and the transverse (subscript 2 in Table 7.1) directions. The dependence is based on the measurements presented in reference[1]. Figure 7.13 (left) demonstrates the behavior of tensile strength σ_1^t in the main direction. Elastic moduli for main and transverse directions are defined as

$$E(\xi, \beta) = \frac{\sigma^t(\xi, \beta)}{\varepsilon^b(\xi, \beta)} \tag{2}$$

and formulas for Poisson ratios μ_{12} and μ_{21} and shear modulus G_{12}

$$\mu_{12} = (1.65 - 0.015\beta)\sqrt{\xi} \tag{3}$$

$$\mu_{21} = (1.65 - 0.015\beta)/\sqrt{\xi} \tag{4}$$

$$G_{12} = \frac{E_2\sqrt{\mu_{12}/\mu_{21}}}{2 + 2\sqrt{\mu_{12}\mu_{21}}} \tag{5}$$

are adopted from referenc[2]. When the tensile strength (Equation 1) in a particular location is reached in the main or transverse direction, in that location the elastic modulus in same direction and the shear modulus drops to 1 MPa and the transverse deformation due to axial strain goes to zero.

Table 7.1. Fitted parameters for Equation (1).

	a_1 (-)	a_2 (-)	a_3 (1/%)	a_4 (1/%)	a_5 (-)
σ_1^t	-4.006	6.081e-3	7.400e-2	9.525e-2	-2.003
σ_2^t	-1.581	1.360e-4	1.100e-1	2.667e-2	1.204
ε_1^b	-3.180e-3	2.939e-1	-3.800e-2	5.000e-5	-5.930e-3
ε_2^b	1.807e-2	5.321	-8.400e-2	-1.700e-4	-8.700e-4
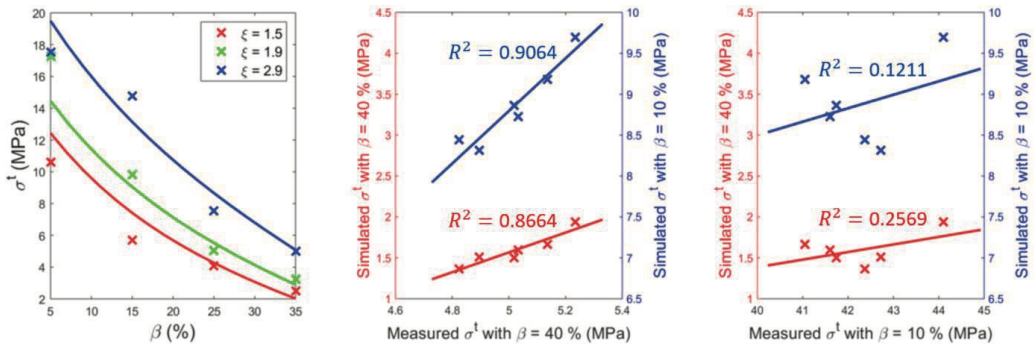
Figure 7.13. Left: Measured MD tensile strengths (markers) with different anisotropies (ξ) and moisture contents (β) and fitted behavior according to Equation (1) for σ_1^t. Middle and right: Correlations between measured and simulated MD tensile strengths with different moisture contents.

Results

The simulations in this study use measured structures of news sheets as well as artificial structures. The simulations were performed via finite element method (FEM) using Abaqus/Standard. The in-plane size of the elements was 2 mm × 2 mm, and in the thickness direction, the element was divided into 10 layers of equal thickness. Main and transverse directional material parameters of each layer of each element is connected to a fiber orientation anisotropy and angle, determined by the layered fiber orientation measurements[4] or by generated artificial structures. Figure 7.14 demonstrates different stages of the simulated fracture behavior in a news sample under MD strain.

For six news samples (thickness of 65 µm and basis weigh of 45 g/m^2), the tensile strength measurements were conducted with AHMA runnability pilot device[3] by using re-wetted and dry paper webs. The web width for AHMA was 250 mm. In fiber orientation measurements and simulations, the in-plane size of the news samples was 120 mm in machine direction (MD) and 180 mm in cross machine direction (CD). Figure 7.15 (middle and right) shows the correlations between simulated and measured MD tensile strengths under external MD strain with two different moisture contents β = 40 % and β = 10 %. High correlations are obtained when comparing simulated tensile strength results with those measured from the high moisture content papers, whereas comparison with tensile strengths measured from the dry papers (β = 10 %) results in low correlations. The effect of the moisture content distribution in the thickness direction on the MD tensile strength is shown in Figure 7.15. The correlation between measured and simulated decreases when the bottom side moisture content is higher. Figure 7.15 demonstrates that the fracture initiation location may depend on the through thickness moisture content distribution.

In Figure 7.16, the fracture behavior is investigated by artificial fiber orientation structures. The results show how the arrangement of low anisotropy streaks influences the simulated fracture behavior. The main angle of local orientation in both the streak and other areas is towards MD. In the case of horizontal streaks, the fracture originates from the area of streaks whereas in the case of vertical streaks, the initiation location is in non-streak area. The tensile strengths are 22.3 MPa and 25.5 MPa in the cases of horizontal and vertical streaks, respectively.

Discussion

A high correlation was found between simulated and measured tensile strengths when measurements were made on samples with high moisture content. The difference in scale between the simulations and the AHMA measurements, the chosen scale of the fiber orientation variation, and the simplicity of the model, all together imply that fracturing behaviour in high moisture content paper is quite insensitive to local small-scale noise-like variations. On the other hand, in the simulations, the structure of one relatively small sheet was sufficient to provide a good response when compared to measured tensile strength of high moisture content paper determined using much larger amount of material. Simulation tests suggest that larger patterns and their arrangement as well as through thickness moisture content distribution can have a significant effect on the fracture behavior and tensile strength.
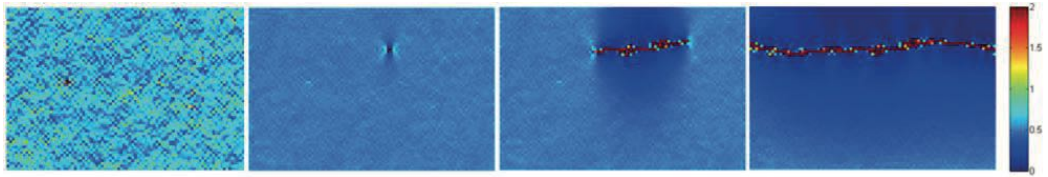
Figure 7.14. Simulated MD strain (%) during fracturing process. In figures,
the MD is parallel to the vertical direction.
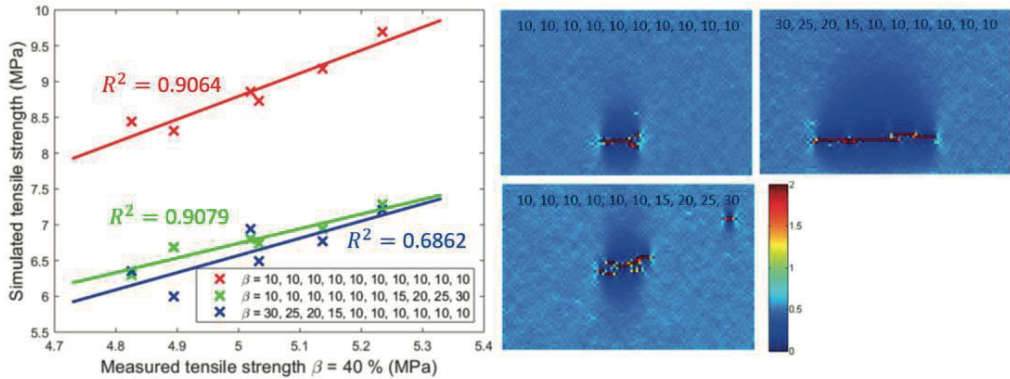
Figure 7.15. The effect of the through thickness moisture content distribution on the simulated fracture.
The numbers in legends represent the moisture content (β) of the layers from bottom side to top side.
Left: Correlations between measured and simulated MD tensile strengths. Right: Example of fracture
initiation presented by MD strain (%) images. The MD is parallel to the vertical direction.
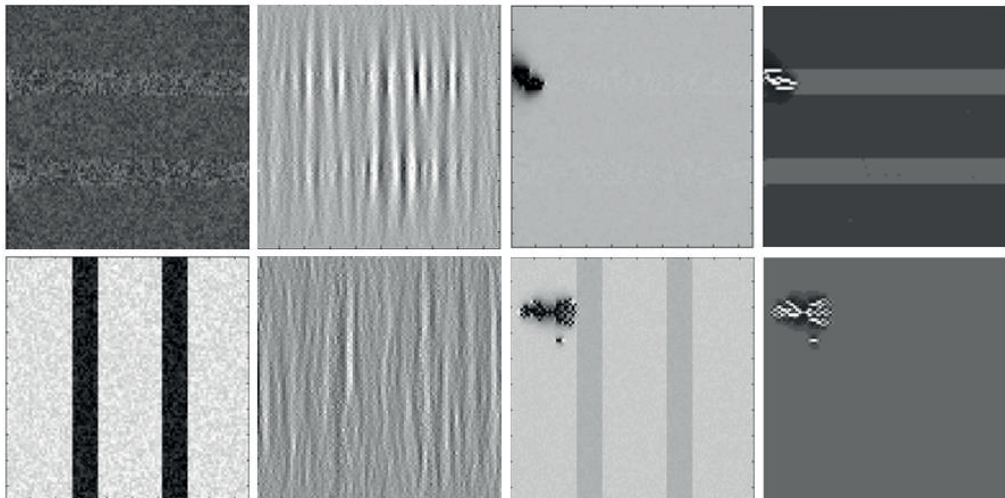
Figure 7.16. In Figures, the MD is parallel to the vertical direction. A sample (192 mm × 192 mm) is
generated with randomly varying anisotropy ξ from 2.5 to 2.7 otherwise but in the two through-
thickness streaks (width 20 mm) where ξ varies between 1.5 and 1.7. In the top row, the through-
thickness streaks are horizontal and in the bottom row, the streaks are vertical. From left to right: MD
tension and out-of-plane deformation before fracture and MD tension and MD strain after fracture
initiation. In MD tensions and strains, darker color corresponds to the lower values.

There is no correlation between tensile strengths measured from dry and high moisture content samples. In addition, the correlation between simulated and measured tensile strengths, when measured from dry paper, is poor. This diversity can be caused by basis weight variation, drying-related factors, moisture content irregularities, etc. It should also be noted that the model's moisture content dependence has been derived using another material: fine paper sample measurements instead of newsprint. The different nature of the fracture behavior of dry and high moisture content samples remains unresolved in this study. However, the presented fracture model proved to be a suitable tool for studying the fracture phenomenon and its complexity.

References

1. Lipponen, P., Leppänen, T., Kouko, J., & Hämäläinen, J. (2008). Elasto-plastic approach for paper cockling phenomenon: On the importance of moisture gradient. International Journal of Solids and Structures, 45(11-12), 3596-3609.

2. Leppänen, T. (2007). Effect of fiber orientation on cockling of paper. Kuopio, Finland: University of Kuopio.

3. Niskanen, K., Makinen, J., Ketoja, J., Kanenen, J., & Wathén, R. (2003). Paper industry invests in better web runnability. Paperi ja Puu-Paper and Timber, 85(5), 274-278.

4. Erkkilä, A. L. (2015). Hygro-elasto-plastic behavior of planar orthotropic material. Lappeenranta University of Technology, Doctoral thesis

.

Predicting Strength characteristics of paper in real time using process parameters

Shivamurthy Modgi, & Kamala Rajan

Alsip Minimill LLC, Alsip, Illinois, USA

Coresbonding author: *Rajan Kamala <kgrajan@alsipminimill.com>*

Summary

In this paper we have made an attempt to predict sheet strength properties in real time using the process parameters to ensure that the paper being manufactured is within the customer specifications. Multivariate analysis was performed using an online data management software from BrainCube on process parameters (1600) from the old corrugated waste paper pulper to the reel. This enabled us to identify the major impact process parameters that affect sheet strength tested using offline bench top equipment and autoline from ABB. Regression models developed with the top impact process parameters for Ring Crush Test (RCT - Refer TAPPI T818 Ring Crush Test),Concora Flat Crush of Corrugating Medium TAPPI T809 (CMT-Refer: https://www.tappi.org/content/SARG/T809.pdf), Short Span Compression Strength (SCT) TAPPI T826, Tensile Stiffness Index (TSI) showed a very good correlation. These models will help operators to monitor process changes and make process adjustments in real time thereby making good quality paper all the time.

Abstract

On-line paper testing methods are currently unavailable and papermakers have to wait for a complete reel to be manufactured to assess quality. The current methodology is to test a very small sample of data (less than 0.005%) of the reel to confirm that the entire reel meets the specifications. This paper attempts to predict paper properties on a running paper machine so that papermakers can see the test values predicted while changing various process parameters. This study was conducted at Alsip MiniMill (a subsidiary of Corrugated Supplies Company of Chicago), a recycled container board

mill located at Alsip IL, using the multivariate analysis method. The program provided by Braincube was used to identify all parameters that affect strength characteristics. Nearly 1600 parameters were analyzed using regression modeling to identify the major parameters to predict sheet strength characteristics. The coefficients from the regression model were then used in real time data to predict sheet strength characteristics while paper makers made adjustments to various parameters. Comparing the prediction with test results showed good correlation (95% in some cases). The process parameters identified related well to the papermaking process thereby validating the model. If this method is used, it may be possible to predict in the future various elastic moduli (E11, E12, E22, etc.) as the next step - rather than the traditional single number "strength" tests used in the containerboard industry Ring Crush Test (RCT), Concora CMT, Short Span Compression Strength (SCT), Tensile Stiffness Index (TSI), etc.).

Methodology

The offline testing of paper was conducted using bench top equipment for RCT, Concora and STFI. The TSI Machine Direction (MD) to Cross Direction (CD) ratio was obtained through our Autoline supplied by Lorentzen and Wettre (L&W) products (now ABB). Figure 7.17 shows the autoline equipment installed in the mill to measure basic paper properties. Figure 7.18 shows the concora tester along with the fluter for the flat crush test of corrugating medium. TAPPI T809 om-06 is used to measure concora. The same tester is also used to measure RCT using TAPPI T818 test method. The SCT is tested using L&W compressive strength tester that measure compressive strength of the corrugating medium using the TAPPI T826 test method.

A very simplistic method was used to develop the predictive models for sheet strength properties. Data from each strength property that was tested using a bench top equipment or ABB Autoline was collected against all the variables in the process. There are almost 1600 variables in the process that is used to conduct a multivariate analysis using Braincube software. The multivariate analysis provides process parameters that highly impact the sheet property being analyzed. Some data cleaning is required based on missing numbers from certain process parameters. The data collected was for a duration of 6 months. The high impact process parameters are selected based on papermaking knowledge and statistics. These parameters are then transferred to Microsoft excel to perform multivariate regression analysis. From the statistics it is now possible to identify the parameters that have a linear relation to the sheet property under study. With this information it is now possible to arrive at an equation that will help to predict the sheet property. The predicted sheet property equation was then used to calculate the predicted value and compared to the actual value to determine the R^2 value to validate the accuracy of the model.

Figure 7.17. Autoline Supplied by Lorentzen & Wettre Products (now ABB).

Figure 7.18 RCT & Concora Tester from Lorentzen & Wettre Products (now ABB).

In addition we also calculated the error percent. The error percent tells us when the predicted model moves away from the actual value there by showing when the model needs to be carefully examined. These equations were then entered into our live database to examine if it can predict the properties accurately. Trending the calculated sheet property with the operator tested property it was evident that we had a model that could predict the sheet properties accurately. In fact, observing the parameters that were used to predict the sheet properties were indicative of whether the paper will meet the specifications for the grade. Initially this was validated when we made lower strength or exceptionally high strength. The process parameters identified were examined in each case to understand their impact.

Results and Discussion

Ring Crush Test Prediction (TAPPI T826)

RCT is one of the main parameters that is measured in our process to grade paper. The mill would benefit greatly if we were able to control and predict this sheet property.

The operators perform RCT every reel and enter into the mill quality system with the timestamp. The process data during the manufacture of the reel in real time is used to predict the RCT. Figure 7.19. show the correlation between the actual value tested by the operator and the predicted value. This shows that the model used to predict RCT was reliable.
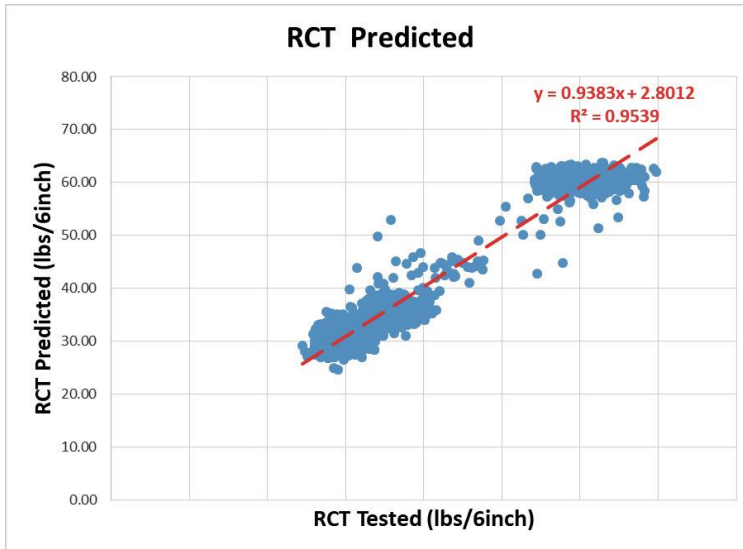

Figure 7.19. Correlation between RCT tested in the lab vs RCT predictedusing the model

The few parameters that showed the effect on RCT were basis weight, head box static head, rush/drag and vacuum on #5 low vacuum box on our paper machine. The #5 low vacuum box is situated critically on our Fourdrinier table where sheet consolidation happens. The other parameters are well understood by papermakers and how they play an important role in sheet manufacturing process. The one parameter that we were expecting was the refiner freeness but our study showed it was not relevant in our multivariate analysis. This also points out that the process parameters on a given machine and process might be different in different machines and mills. So it is very important to have a good reliable database that can collect data to develop models that can predict sheet properties.

Using the model in the database and plotting it we can see from Figure 7.20 that the model predicts the RCT accurately. This accuracy is enough to guide the operators in real time to control and make changes in the process. They can troubleshoot the problem before the entire reel is manufactured and then make changes. Also the model guides them if the changes made are in the right direction. This type of prediction helps the mill to meet grade specification all the time and make prime paper.

Figure 7.20. Trend between RCT tested in lab vs RCT predicted

Conclusions

Multivariate data analysis tool was used to identify the major paper making parameters that affect sheet properties. The data base included test results from the mill's bench top equipment that includes an Autoline. The parameters were then used in a regression analysis to identify the coefficients to predict the sheet strength properties.

RCT was found to be dependent on basis weight, headbox pressure, jet/wire speed difference, low vacuum in suction box and Pick-up roll vacuum. R^2 value of 0.95 was achieved using the model.

Concora was found to be dependent on bone dry weight, headbox pressure SCT was dependent on the bone dry weight and speed difference between jet/wire. R^2 value of 0.76 was achieved using the model.

TSI MD/CD ratio was found to be dependent on basis weight, headbox pressure, jet/wire difference, press draws, low vacuum in suction box and PU roll vacuum. R2 value of 0.62 was achieved using the model.

Sheet properties derived from the model correlate closely to the properties tested using the bench top equipment in real time

.

Wednesday 2.9.2020 at 15:30 - 16:15

Session 8

Plenary talk by Tom Lindström

The world of nanocellulosic material applications

Session chair: Elias Retulainen

The world of nanocellulosic material applications

Tom Lindström[a,b]

[a]*KTH Royal Institute of Technology, Stockholm, Sweden*
[b]*Stony Brook University, Stony Brook, New York, USA*

Corresponding author: *Tom Lindström <*[*toml@kth.se*](mailto:toml@kth.se)*>*

Keywords: Nanocellulose, applications, commercialization

Summary

There is a whole family of different nanocellulosic nature-based materials, which may be divided into, nanocrystalline cellulose (CNC), nanofibrillar cellulose (CNF) and bacterial nanocellulose (BNC) and algal (Cladophora) nanocellulosics (ANC). The history of these nanocellulosics goes back, at least, to the 1940s.

All of these materials have widely different applications, ranging from large-scale papermaking applications to high-end use in, for instance, the medical and electronic materials sector.

The presentation will focus on the manufacture and applications of NFC in the commodity materials sector and is a personal account of the evolutionary patterns and challenges on the road to practical commercial applications.

There have been extensive research and development activities in the field of nanofibrillar cellulose (CNF) materials during the past decades, although microfibrillated cellulose (MFC) was developed already during the late 1970s at ITT-Rayonier in USA. The developments, however, run to a stand still after ITT Rayonier abandoned their development efforts, but R&D was taken up in the late 80s and in the 90s by efforts in Japan (e.g. Daicel and Japanese scientists), who also became leaders of the current developments in the field of CNF materials, particularly in the areas of TEMPO-oxidation pre-treatments, but also in the area of composite applications and in a vast area of high end applications.

The presentation will give a current perspective on nanocellulose developments. The hurdles to be alleviated in order to secure a successful commercialisation of these materials will be highlighted in the presentation.

Thursday 3.9.2020 at 8:45 - 9:45

Session 9

Influence of moisture on paper performance

Session chair: Vesa Kunnari

Influence of wood extractives on the performance of packaging papers

Jussi Lahti[a,b], Werner Schlemmer [a,b], Roman Poschner [a,b], Andrea Walzl[c], Erich Leitner [c], Stefan Spirk [a,b], & Ulrich Hirn [a,b]

[a]*Institute of Bioproducts and Paper Technology, Graz University of Technology, Graz, Austria*
[b]*CD Laboratory for Fiber Swelling and Paper Performance, Graz University of Technology, Graz, Austria*
[c]*Institute of Analytical Chemistry and Food Chemistry, Graz University of Technology, Graz, Austria*

Corresponding author: *Jussi Lahti <*[*jussi.lahti@tugraz.a*](jussi.lahti@tugraz.a)*>*

Keywords: Wood extractives, carry-over, kraft pulp, paper strength

Summary

The objective of this work was firstly to investigate which extractive (pitch) compounds after kraft pulping are efficiently carried over to paper mill. Secondly, the aim was to find out how these compounds influence on paper performance. It became apparent that all major pitch compounds, *i.e.* fatty acids, resin acids, sterols and other unsaponifiables, are harmful for kraft paper strength. Fatty acids can be considered to be especially harmful as their portion in the carry-over pitch was the highest.

Introduction

Wood extractives (also called pitch) entering the paper mill along with mechanical pulp are well known to cause various problems, such as deposition issues, reduced paper machine efficiency and decreased paper quality[1]. In the case of kraft pulping many of these problems can be expected to occur to a considerably lesser extent due to efficient washing of the extractives dissolved during cooking[2]. However, it has been previously shown that the strength of softwood kraft pulp handsheets is sensitive to the extractive content, *i.e.* a severe drop in mechanical properties has been observed with the addition of wood extractives[3]. In order to better understand the effect of extractives on the performance of packaging papers the objective of our work was as following:

- Investigate which softwood extractive compounds, *i.e.* fatty acids, resin acids, sterols and other unsaponifiables[4], are efficiently carried over with unbleached kraft pulp to paper mill.
- Study the harmfulness of these extractive compounds carried over to paper mill on packaging paper performance.

Experimental and results

The composition of extractives carried over to paper mill was investigated by separating the extractives from unbleached kraft pulp by acetone extraction and analysing them by two-dimensional comprehensive gas chromatography-mass spectrometry (GCxGC-MS) after silylation. The following composition was determined: 35% fatty acids, 13% resin acids, 18% sterols and 34% other unsaponifiables.

Based on the composition analysis of the extractives, abundant compounds from each group, *i.e.* stearic and oleic acid (fatty acids), abietic acid (resin acids), β-sitosterol (sterols) and docosanol (other unsaponifiables), were chosen to laboratory papermaking trials to investigate the effect of pitch on paper performance. Figure 9.1 shows the scheme for preparing the handsheets. Unbleached kraft pulp was first beaten in a PFI mill (ISO-5264-2) followed by a preparation of the handsheets with a Rapid Köthen method (ISO 5269-2). The process chemicals, *i.e.* dispersed pitch (model compounds and industrial process water), alum (pitch retention aid) and NaOH (pH control), were added to pulp suspension prior to forming. The tensile properties and pitch retention of the handsheets were tested according to ISO 1924-3 and ISO 14453, respectively.
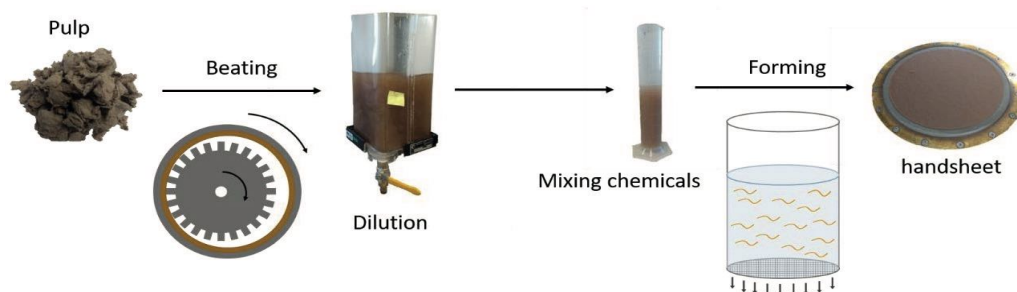

Figure 9.1 Scheme for preparing handsheets to test the effect of pitch on paper performance

Figure 9.2 shows that the added pitch (1 mg/g paper) strongly reduced the tensile index of the paper. Furthermore, the retention and decrease in tensile index were both higher for fatty acids/alcohol in comparison to resin acid and sterol. The retention and tensile index of process water were in the middle proving that the model compound dispersions simulated the effect of industrial pitch quite well.
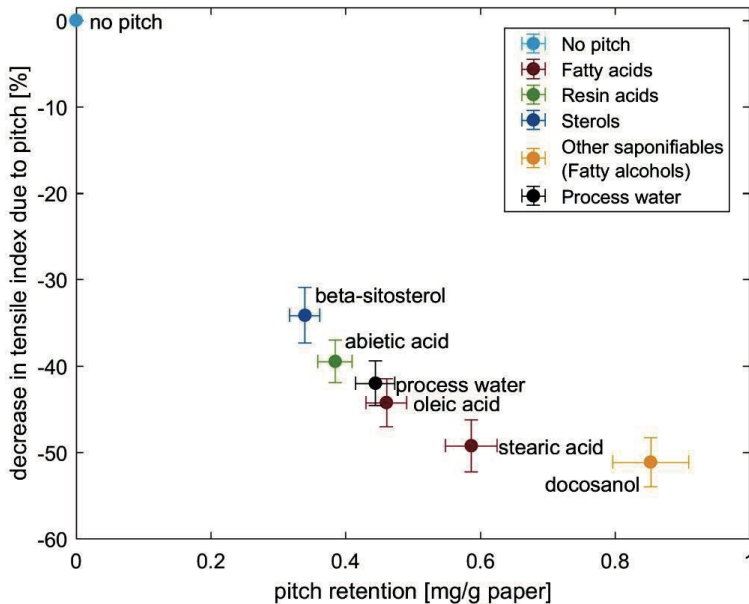
Figure 9.2. Influence of added (1 mg/g paper) pitch model compounds and industrial process water on tensile index of paper

Conclusions

All major pitch compounds revealed to be harmful for unbleached kraft paper strength. Special attention should be paid on the fatty acids due to their high abundance and harmfulness when developing novel strategies to overcome the harmful effect of pitch.

References

1. Hubbe, M. A., Rojas, O. J., & Venditti, R. A. (2006). Control of tacky deposits on paper machines–A review. Nordic Pulp & Paper Research Journal, 21(2), 154-171.

2. Hubbe, M. A., Sundberg, A., Mocchiutti, P., Ni, Y., & Pelton, R. (2012). Dissolved and colloidal substances (DCS) and the charge demand of papermaking process waters and suspensions: A review. BioResources, 7(4), 6109-6193.

3. Sundberg, A., Holmbom, B., Willför, S., & Pranovich, A. (2000). Weakening of paper strength by wood resin. Nordic Pulp & Paper Research Journal, 15(1), 46-53.

4. Vikström, F., Holmbom, B., & Hamunen, A. (2005). Sterols and triterpenyl alcohols in common pulpwoods and black liquor soaps. Holz als Roh-und Werkstoff, 63(4), 303-308.

Influence of moisture content and additives on the fracture toughness of recycled paper

Pablo González-Miguel[a], Sandra Roche[a], Elías Liarte[a], Iciar Serrano[2], Naiara Sánchez[b], Noemí Gil-Lalaguna[b], Alberto Gonzalo[b], & Cristina Crespo[a]

[a]*Aragon Institute of Technology ITAINNOVA, Zaragoza, Spain*
[b]*Aragón Institute of Engineering Research (I3A), Zaragoza, Spain*

***Corresponding author:** Pablo González-Miguel <pablog@itainnova.es>*

Keywords: Fracture toughness, recycled fibres, mechanical properties, nanocellulose, polyelectrolytes

Summary

The aim of this work is the analysis of fracture toughness in different moisture conditions for several samples of reinforced recycled paper, either by synthetic additives and other additives produced from agricultural residues. We propose the fracture toughness evaluation by a modification/adaptation of the standardized test SCAN-P 77:95, by using a dynamic mechanic analyzer equipped with a small chamber with humidity control. The results obtained showed significant improvements in fracture toughness, above 25%, which spread the possibilities of new uses for recycled paper.

Introduction

The use of recovered paper is becoming more influential in the paper industry, with a substantial increase in the percentage of paper produced from secondary (recycled) fibres.

During physical operation, such as disintegration, refining and drying, fibres degrade and pulp and paper properties are worse than those obtained originally with virgin fibres. Fibre beating, refining, or the use of starch, are usually implemented in the paper mills to increase secondary fibres properties[1,2].

Fracture toughness (FT) of paper is an important property since conventional structural properties (tensile and compression strength) have often demonstrated to be

Gonzales-Miguel, P., Roche, S., Liarte, E., Serrano, I., Sánchez, N., Gil-Lalaguna, N., Gonzalo, A., & Crespo, C.

insufficient to evaluate paper web breaks in its manufacturing and end-use related processes[3]. Currently, the industry is able to provide recycled papers with similar structural properties to virgin fibre, and manufacturing cardboard boxes with similar characteristics, mainly increasing the grammages of the recycled papers. However, for some of the novel and potential applications of the paper, such as bags for supermarkets, bottles, six-pack ring soda cans, pre-cut paperboard packs. Improved FT is needed for converting process and service performance, and not just the structural properties as in cardboard boxes. In addition, due to the implementation of sustainability goals in the industry, an improvement in the efficiency of the processes in terms of resources, raw materials and energy is expected. Therefore, production and converting losses must be minimized, which again makes the FT a key parameter to analyze.

Generally, some additives are incorporated along with the recycled fibres to improve the properties, as synthetic resins or, to a greater extent, starch, mostly for tensile/compression properties[4,5]. However, their contribution to FT when they reinforce recycled paper has not yet been studied in depth[6], especially in the case of analysis in different humidity conditions. The replacement of these additives, either non-natural or edible products, by others produced from agricultural or forestry residues would result in an increase of the process sustainability.

The objective of this work is to analyse as easy as possible the fracture toughness in different moisture conditions of reinforced recycled paper, either by synthetic additives and other additives produced from agricultural residues. The standardized test allows the determination of this value on paper[7], but doing so in different humidity conditions requires the provision of a large conditioned space, which can generate higher costs and extra time.

Results

We propose the FT evaluation by a modification/adaptation of the standardized test, by means of a Metravib +450 dynamic mechanic analyzer (DMA, different geometry, different stiffness) equipped with a small chamber with humidity control (Figure 9.3), which allows the tests to be accelerated in time at a reasonable cost.
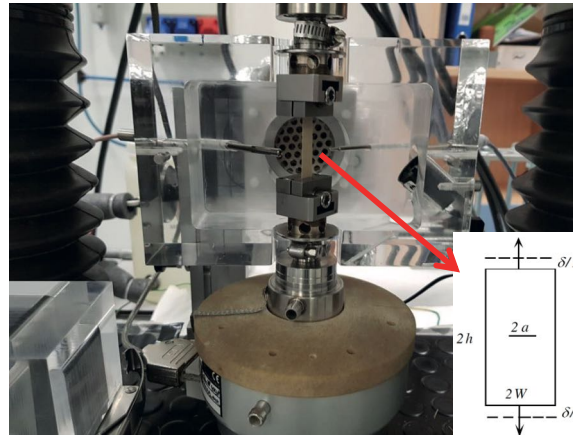
Figure 9.3 Test piece mounted in the DMA equipped with humidity control chamber.

The geometry of the test piece was slightly different of those in the standardized test: the test span length (2h in Figure 9.3) was 35 mm and the test pieces width (2W in Figure 9.3) was 10 mm, for both tensile and fracture toughness test pieces. The central notch length (2a in Figure 9.3) was 4 mm for the fracture toughness test pieces.

We use Equation 1 for FT calculation, J_{Ic}^{b}, and the rest of equations as indicated in the standard SCAN-P 77:05, with the exception that we recalculated the coefficients of functions f_1 and f_2, for the geometry of our test pieces, and validated by FEM:

$$J_{Ic}^{b} = \frac{(\bar{\beta})^2 \cdot E_2^b}{h \cdot (1 - \nu_{12} \cdot \nu_{21})} f_1 + \frac{2p \cdot h}{p+1} \Phi \cdot \sigma_0^b (\varepsilon_0)^p \left(\frac{\bar{\beta}}{\varepsilon_0 \cdot h}\right)^{p+1} f_2 \qquad (1)$$

We established 3 test levels for relative humidity (R.H.): 5%, 25% and 50%. Conditioning of test pieces before test was as follows: first, we completely dried the test piece by means of a halogen moisture analyzer (HG63 Mettler Toledo); then we mounted the test piece on DMA, selected the minimum R.H. level on moisture chamber (5%), and let the test piece reach the equilibrium moisture for 20 minutes. For those test pieces tested at 25 % R.H., we follow the same steps and we add 20 minutes at 25% R.H. Samples analyzed at 50% R.H. were tested without the chamber, due to the DMA equipment was placed in a conditioned room at 50% R.H. After each test, we measured the moisture content of the sample with the halogen moisture analyzer.

We studied FT at different moisture contents in laboratory sheets (Figure 9.4) reinforced with different additives.
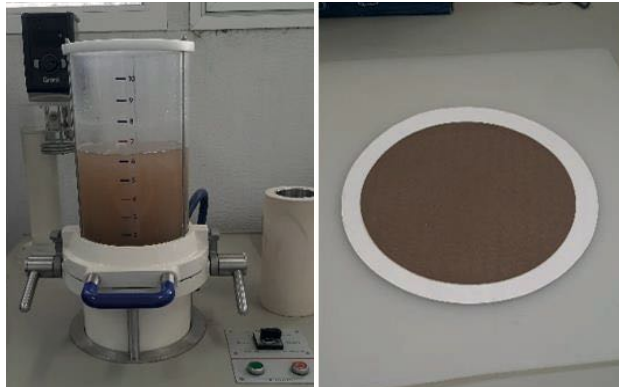
Gonzales-Miguel, P., Roche, S., Liarte, E., Serrano, I., Sánchez, N., Gil-Lalaguna, N., Gonzalo, A., & Crespo, C.

Figure 9.4. Laboratory sheet former and handsheet.

Our starting material was 1.05.01 grade, according to the European list of standard grades of paper and board for recycling (EN-643 standard). We reinforced OCC pulp with nanofibrils (Figure 9.5) obtained from semichemical wheat straw pulp (N-SCWS) following a method similar to that described by Delgado-Aguilar et al. [8]. We also produced laboratory paper by reinforcing OCC with layers of cationic and anionic polymers: Polyacrylamide-PAM (PAM(+)/PAM(-)); Polyvinylamine-PVAm and carboxymethyl cellulose-CMC (PVAm/CMC), Polyethyleneimine-PEI and carboxymethyl cellulose-CMC (PEI/CMC).

The results obtained showed significant improvements in tensile results and in FT, above 25%, which spread the possibilities of new uses for recycled paper (Figure 9.6a). We also analyzed changes due to moisture content (Figure 9.6b), observing the typical trend in tensile curves due to moisture content. The effect of moisture on FT value was also investigated for each additive.
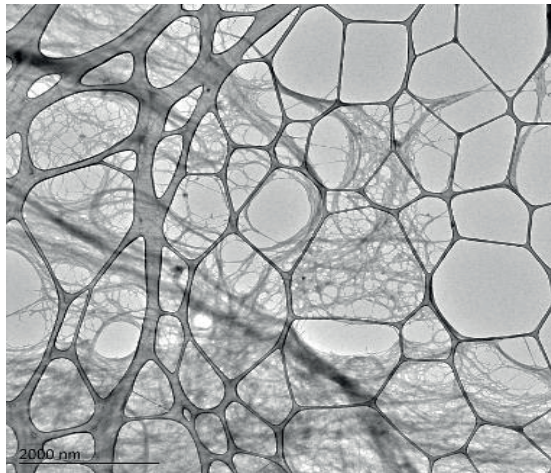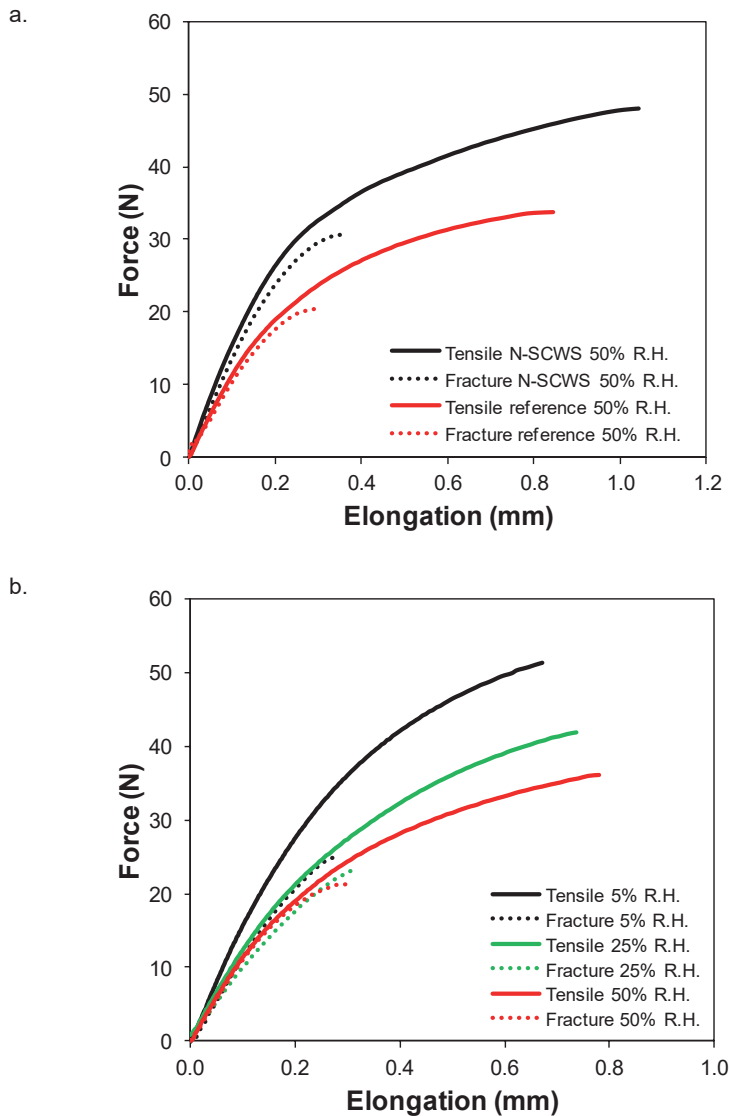

Figure 9.5. TEM image of N-SCWS.

a.

b.

Figure 9.6. Stress vs. elongation curves for tensile and fracture toughness test. a) 5% N-SCWS and reference paper at 50% R.H. b) Reference paper at 5% R.H., 25% R.H. and 50% R.H.

References

1. Howard, R.C., &, Bichard, W. (1992). The basic effects of recycling on pulp properties. J Pulp Pap Sci 18(4), J151–J159.

2. Thorn, I., & Brander, J. (1997) Surface application of paper chemicals. Blackie Academic & Professional.

3. Wanigaratne, D. M. S., Batchelor, W. J., & Parker, I. H. (2002). Comparison of fracture toughness of paper with tensile properties. Appita J. 55, 369–385.

4. Lindström, T., Wågberg, L., & Larsson, T. (2005, September). On the nature of joint strength in paper-A review of dry and wet strength resins used in paper manufacturing. In 13th fundamental research symposium (Vol. 1, pp. 457-562). Cambridge, UK: The Pulp and Paper Fundamental Research Society.

5. Hubbe, M. A. (2006). Bonding between cellulosic fibers in the absence and presence of dry-strength agents–A review. BioResources, 1(2), 281-318. Larsson P T, Lindström T, Carlsson L A, Fellers C (2018) Fiber length and bonding effects on tensile strength and toughness of kraft paper. J Mater Sci 53, 3006–3015.

6. Scandinavian Pulp, Paper and Board Testing Committee (1995) Scan Standard P 77:95 Fracture toughness.

7. Delgado Aguilar, M., González Tovar, I., Tarrés Farrés, Q., Alcalà Vilavella, M., Pèlach Serra, M. À., & Mutjé Pujol, P. (2015). Approaching a low-cost production of cellulose nanofibers for apermaking applications. © Bioresources, 2015, vol. 10, núm. 3, p. 5435-5355.

Session 10

New cellulose based applications

Session chair: Kristian Salminen

Fibre Printer: A Machine to apply 3D printing principles on paper production

Frederic Kreplin, & Samuel Schabel

Technische Universität Darmstadt, Darmstadt, Germany

Corresponding author: *Frederic Kreplin <kreplin@papier.tu-darmstadt.de>*

Keywords: Additive manufacturing, paper structure, fibre printer

Summary

Current trends show an increasing demand for individualized products. These trends are related to terms as Industry 4.0. Therefore, flexible manufacturing processes are required. In recent years, there has been great progress in the field of additive manufacturing processes. 3D printing technology is now available at low cost and is increasingly used for the industrial production of goods in various fields of application, like medicine, automotive, aviation or tool manufacturing.

In contrast, paper today is a mass product. In Germany, 22.6 million tons of paper were produced in 2018[1]. But, industrial paper production is also an additive manufacturing process. Individual fibres are combined to form a fibre network. However, the fibres cannot be specifically deposited in the papermaking process. Small quantities of just a few sheets with individual profiles in terms of fibre orientation, pore structure or shape of the paper sheets cannot be produced in an industrial process. This is where the fibre printer described here comes in. The combination of 3D printing technology and paper production enables us to produce paper with individual properties in small quantities. In future, paper can be designed on a PC as a 3D CAD model with the desired shape and properties for specific requirements. The external and internal structure of the paper can be influenced by the print pattern and machine parameters. In this paper, the construction of the fibre printer will be examined in more detail. In future, influences of the model geometry, slicing and machine settings on the paper properties will be determined. The goal is, to simulate and optimize highly specialised paper and its properties before their production.

State of the art

In laboratory scale, various commercial systems are available to produce paper in small quantities, such as the Rapid-Köthen sheet former, Dynamic Sheet Former or MK Sheet Former. Some of these sheet formers can produce hand sheets with a significantly increased fibre orientation in machine direction. With these systems, fibres can only be oriented in one direction, the machine direction. The influence of highly unidirectional fibre orientation on paper properties is currently investigated at the PMV[2]. The inspiration for this new sheet forming system is based on the results of Dolatshahi and Kortschot[3]. In contrast to the laboratory sheet former mentioned above, the PMV system applies fibres as a thin jet onto a revolving fabric. The fibres are in a highly dilute suspension, so that they are deposited almost individually on the fabric. The nozzle generates a laminar elongation flow, whereby the fibres are oriented in the direction of flow. After leaving the nozzle, the fibres hit the rotating fabric with a small impact angle. Directly behind the fabric a suction device removes the water and fixes the fibres on the fabric. The velocity of the fabric is higher than the jet´s exit velocity, so that the fibres are additionally stretched when they hit the fabric. During the production process, the nozzle and suction zone traverse the fabric, so that a paper web is produced in several layers. With the help of this process, it is possible to produce paper with unidirectional oriented fibres. In addition, the system is designed to be modularly expandable to allow numbering up to a small industrial sheet forming process[2,4].

As mentioned for the PMV system, nozzles are also used in additive manufacturing processes, especially in extrusion processes, to apply material at a predetermined location. Extrusion processes, such as Fused Deposition Modelling (FDM), usually have a heated extruder moving in one plane (XY) and a platform moving orthogonally to this plane (Z). Materials as acrylonitrile-butadiene-styrene (ABS) and polylactides (PLA) or waxes are fed into the extruder as a filament. In the printing process, the material is applied in layers to build up a solid body. The material solidifies shortly after emerging from the nozzle. A layered solid body allows more degrees of freedom in designing a component. Process variants include Fused Deposition Modelling (FDM), 3-D plotter, Multiphase Jet Solidification (MJS) and Multi-Jet Modelling (MJM) [5]. Since paper manufacturing is in principle also an additive manufacturing process, the transfer of 3D printing principles to paper production is obvious.

Cellulose based or cellulose containing filament materials are already available such as "UPM Formi" or "Evolv 3D Universal Support Material". However, no systems are known that can apply fibre material in a highly dilute suspension to a fabric using 3D printing principles and thus create predetermined paper structures. The below described fibre printer is intended to clarify whether 3D printing technologies can be used to produce paper or other fibrous materials in small quantities with predefined structures.

Fibre printer

In current research, a new type of machine has been developed at PMV combining the process principle of a FDM printer with the findings from the PMV system for highly unidirectional papers[6,7]. In this machine, the Fibre Printer (Figure 10.1), a nozzle is moving in the X-Y plane, driven by stepper motors. A hose connects the nozzle with a storage tank for the fibre suspension. The fibre suspension replaces the filament of a FDM printer. A stirrer is installed in the tank to ensure the homogeneity of the suspension and to prevent sedimentation of fibres. The storage tank has an overflow so that suspension can be pumped into the tank permanently and the level remains constant. The hydrostatic pressure generated in the storage tank creates a constant volume flow through the nozzle. By changing the difference in height between nozzle outlet and suspension level in the storage tank, the volume flow can be adjusted. An electromagnetic valve controls the suspension flow. As described for the system for unidirectional papers[3], a laminar elongation flow is generated within the nozzle to orient the fibres in the direction of flow. The suspension is applied through the nozzle to a Rapid-Köthen fabric (Ø 20 cm). The nozzle can be arranged vertically (0°) or have an angle of up to +/- 45°. The mounting of the nozzle is designed in a way that the point of impact on the fabric is not changed by changing the nozzle angle. The fabric is mounted on a fabric holder, which can be rotated permanently or a certain angle by a stepper motor with variable speed. The fabric holder is mounted on a fixed intermediate level. The fabric thus forms the printing platform analogous to a 3D printer. To remove the excess water, a suction nozzle connected to a vacuum pump moves parallel to the application nozzle below the fabric. A bypass valve can adjust the intensity of the suction. The suction unit thus forms a second X-Y plane. The guide rails of the two X-Y levels and the fixed intermediate level are attached to an outer frame, which also carriess the storage tank with stirrer for the fibre suspension.
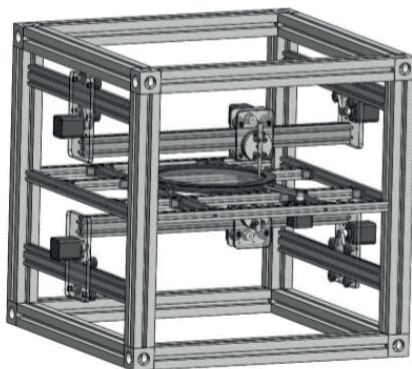

Figure 10.1. Model of the Fibre Printer.

The drives of the two X-Y levels, the drive for the fabric rotation as well as the valve are controlled by an Arduino Uno with GRBL firmware. Two CNC shields are used to control the two planes in parallel. The signal for the first CNC-shield, which controls the application nozzle, is mirrored to the second CNC-shield to control the suction nozzle. The identical design of the X-Y traversing system ensures that the application and suction nozzle move in parallel. G-Code is used to control the nozzles movement, which is standard for CNC machines such as 3D printers. G-Code can be generated from 3D CAD models by feeding them into a slicing program. The slicing program generates a layered body from a solid body. According to the settings, the routes for material application within the individual layers are generated. The G-code for system control is generated automatically from the routes. Using a freely available sending program (e.g. Universal Gcode Sender), the G-Code can be send to an Arduino after minor adjustments such as deleting the commands for the Z-axis and adding commands to control the valve. The process chain (Figure 10.2) of this fibre printer corresponds to the process chain of e.g. the FDM 3D printing process, except for minor adaptations. The printing process is accomplished by sending G-code commands to the Arduino, which translates the commands into motion signals. After the printing process, the Rapid-Köthen fabric can be removed from the system. The wet sheet can then be taken from the fabric and dried e.g. in a Rapid-Köthen dryer.
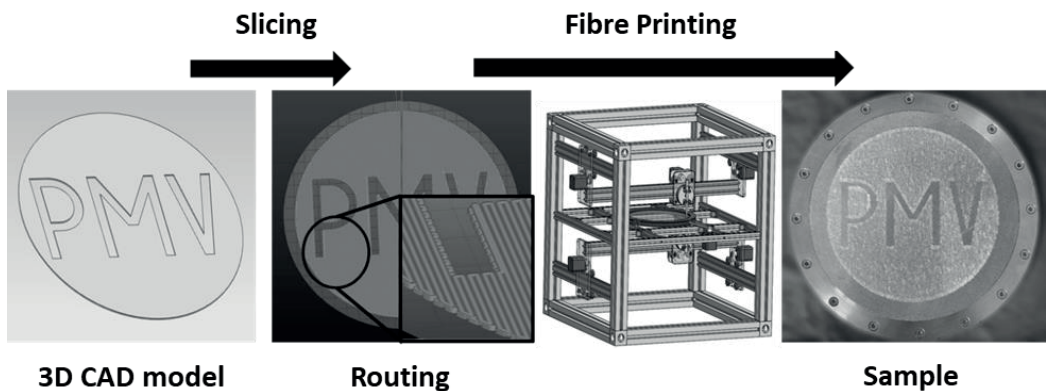

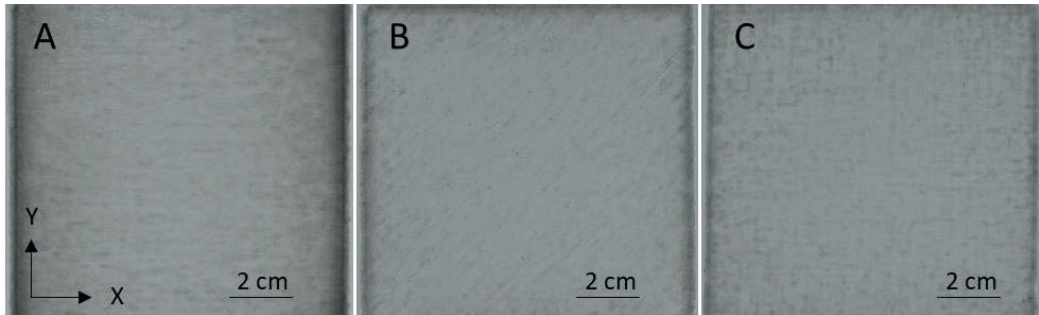Figure 10.2. Fibre printing process.

Figure 10.3. Different printing pattern unidirectional in X-direction (A) and 45° (B) and bidirectional in XY-direction (C).

Proof of concept

During commissioning, suitable slicing parameters, such as feed rate and application quantity, were identified. Using simple rectangular bodies, various infill geometries were investigated. Figure 10.3 shows a unidirectional application direction in the X-direction (A), a unidirectional with a 45° offset to the X-direction (B) and a bidirectional application direction (C). The suspension of regenerated cellulose fibres was applied with a consistency of 0.05 %. The minimum number of layers for these fibres is 20. These 20 layers are required to remove the sheet from the fabric without damage. If the number of layers is lower, the structural strength is not sufficient to remove the sheet manually from the fabric and dry it.

Application potential

In addition to the free design of contours and recesses within the paper, the internal structure can also be varied within the levels by routing, orientation of the fibres or the fibre material itself. This offers the possibility to influence microfluidics in each layer and helps to realize cost effective paper-based tests. Furthermore, the fibre orientation of the planes allows the production of a fibre material optimized for composites within one production step. In addition to pure paper products, hybrid materials can be produced by using different fibre materials. Figure 10.4 shows some examples for predefined infill geometries. Various other infill geometries optimised for specific applications can be programmed.
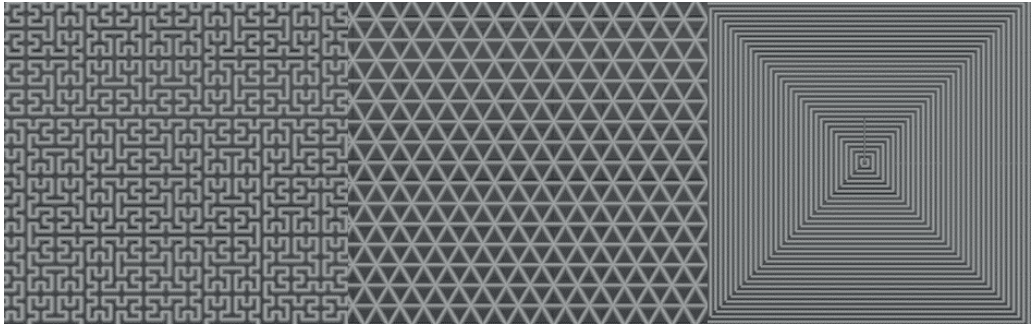
Figure 10.4. Different possible infill geometries to functionalise paper.

References

1. VDP - Verband Deutscher Papierfabriken e.V., Papier Kompass 2019. 2019, Bonn

2. Götzinge, R., & Schabe, S. (2017). Test rig for the production of highly oriented papers in the context of building with paper. Cellulose Materials Doctoral Students Conference, p. 139-140.Technische Universität Graz, Austria.

3. Dolatshahi, S., & Kortschot, M. T. (2009) The effect of fibre orientation on the zero-span testing of paper. Advances in Pulp and Paper Research, 931-946.

4. Götzinge, R., & Schabe, S. (2018). Highly oriented paper for paper based construction materials. Proceeding of the Progress in paper physics seminar. University of Technology Lodz, 26-27.

5. Kalweit, A., Paul, C., Peters, S., & Wallbaum, R. (Eds.). (2011). *Handbuch für Technisches Produktdesign: Material und Fertigung, Entscheidungsgrundlagen für Designer und Ingenieure*. Springer-Verlag, p. 608.

6. Wang, X. (2019). Konstruktion und Inbetriebnahme eines Versuchsstandes für den 2D-Druck von Papierfasern. FG Papierfabrikation u. Mech. Verfahrenstechnik, p. 107, Technische Universität: Darmstadt, Germany.

7. Sa'di, F. (2019). *Inbetriebnahme und Verbesserung eines Versuchsstandes zur Anwendung von 3D-Druckprinzipien auf die Papierherstellung*. PMV, p. 156. TU Darmstadt, Germany.

Deteriorated dispersibility of hydroentangled wetlaid wet wipes over storage time

Thomas Harter[a,b], Ingo Bernt[b,c], & Ulrich Hirn[a,b]

[a]Institute of Bioproducts and Paper Technology, Graz University of Technology, Graz, Austria
[b]Christian Doppler Laboratory for Fiber Swelling and Paper Performance, Graz, Austria
[c]Kelheim Fibres GmbH, Kelheim, Germany

Corresponding author: Thomas Harter <harter@tugraz.at>

Keywords: Flushable wipes, wet wipes, dispersibility, viscose fibres, ageing effect

Wet wipes came into public observation recently as sewage cloggings suggest these wipes take a major role in the remains that block pipes and sewer systems. In this work it will be shown that nonwoven wet wipes reduce their ability to disperse after a prolonged wet storage condition. As storing nonwovens in a liquid is part of their eponymous usage as wet wipes, the reduced dispersibility presents to be a crucial problem. A possibility to overcome this so-called ageing effect of dispersibility is to use unbleached kraft pulp which with its elevated lignin content seems to be able to prevent the ageing. With wet tensile tests it will be shown that the ageing effect is not a manifestation of increased strength as the wet strength over the wet storage time is unaffected.

Introduction

Wet wipes as a commodity product rise in usage and their usage is forecasted to increase furthermore. The problems caused with the disposal of these wipes is present in the global newsfeeds[1,2]. Agglomerations of wet wipes are part of the cloggings in big city's sewer systems although some of the wet wipes claim to be flushable. Wet wipes that strive to be truly flushable[3] must consist of biodegradable materials for which the preferable way of production is the wetlaid process in combination with hydroentanglement[4]. The fibres that are typically used when producing nonwovens for wet wipes include wood pulp and viscose fibres, but also lyocell fibres. In a current wet wipe both pulp and man-made cellulosic fibres are used in a blend according to the

required properties. The up to 14 mm long viscose fibres along with the hydroentanglement process create the ground structure of the material and entangle with each other[5] and the pulp fibres thus generating the strength properties of the material[6]. The short pulp fibres therefore determine the dispersible behaviour of the nonwovens, where a higher amount of pulp fibres lead to a more dispersible wet wipe[7].

Materials and Methods

The used wipes were produced on a laboratory scale inclined wire machine with in-line drying. Viscose fibres were used according to Table 10.1. For the nonwovens two different kraft pulps were used, one bleached (BSK) and one unbleached (UBSK).

Table 10.1. Used man-made cellulosic fibres.

Name	Length [mm]	Linear density [dtex]
Flat viscose fibre (CV)	10	2.4
Round viscose fibre (CV)	8	0.9
Round Lyocell fibre (CLY)	12	1.7

Within the possible methods that are available to determine the dispersible properties, the slosh box test asserts itself as a quick and applicable method. This procedure includes water-filled boxes where the single wet wipe is placed into. After a certain movement of the box the residues are divided with a 12.5 mm sieve. The mass of the restrained fraction is put in relation to the total mass of the wipe which results in sloshability values that can be seen in Figure 10.6. A higher sloshability value therefore indicates a better dispersibility, meaning a faster disintegration of the wet wipe after disposal.

Wet strength values were measured using a standard tensile tester using a sample length of 100 mm and a testing speed of 20 mm/min.

For the preparation of the samples the nonwovens were treated with deionized water in a ratio of 2:1 (deionized water: mass of nonwoven). To avoid dehydration the samples were sealed in plastic bags.

Results

The effect of the ageing is displayed in Figure 10.5 as residues of two samples after the slosh box test. One was tested dry (0h) whereas the other image shows a wipe that was stored for 168 hours. It is clearly visible that the 0h-sample is well dispersed and the 168h-sample already shows big remaining flakes.
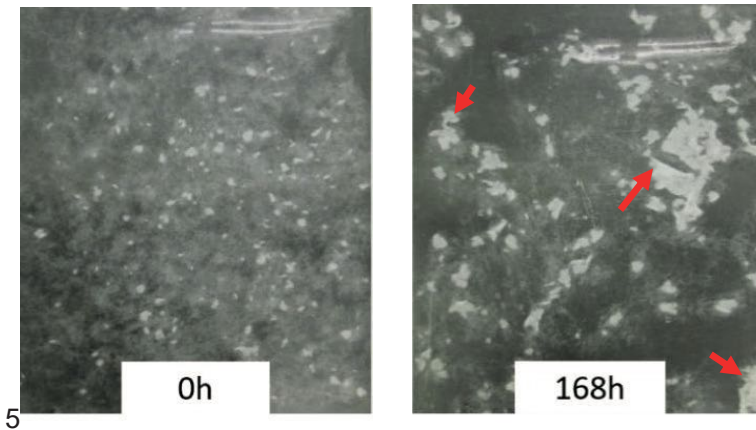
5

Figure 10.5. Reduced wet wipe dispersibility (flat viscose fibre with bleached kraft pulp) after 168h of storage (right) compared to 0h (left).

In Figure 10.6 the sloshability is plotted over the wet storage time in hours. For comparable results dry nonwovens were manually wetted with deionized water and stored before testing. The results at 0 hours represent the slosh box results of nonwovens without wet storage that attest three of the tested samples a good sloshability and therefore dispersibility.

In the diagram on the right the effect of different man-made cellulosic materials is shown. The results represent wipes that consist of bleached kraft pulp and of the fibres listed in Table 10.1. Here it is visible that over the wet storage time all wipes reduce their sloshability. This occurrence is called the ageing effect of dispersibility. In Figure 10.6 on the left are results for wipes with the same flat viscose fibre but one time with bleached and one time with unbleached kraft pulp. Using unbleached pulp seems to allow the wipe to keep a good dispersibility over the wet storage time. One possibility in the prevention of the ageing effect could be that the remaining lignin in the unbleached pulp counteract on the ageing mechanism. However, it is also possible that surface interactions in the wet wipes are altered when using unbleached pulp with its less rough surface and less flexible fibres.
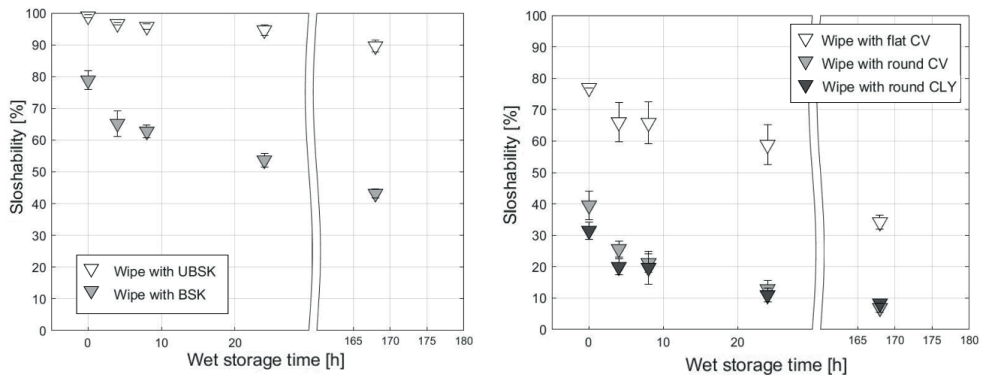
Figure 10.6 Sloshability (dispersibility) of wet wipes over wet storage time. Left: Wet wipes with bleached pulp (BSK) and unbleached pulp (UBSK) and flat viscose fibres. Right: flat CV, round CV, round CLY blended with bleached pulp. Error bars represent the standard deviation.

Figure 10.7 the results for wet strength measurements are exemplarily depicted for the same wet wipes represented in Figure 10.6. Similar to the sloshability results the wet strength is plotted over the wet storage time. Although it seems reasonable that the loss in dispersibility has its meaning in some kind of increasing mechanical resistance, the wet tensile test results in Figure 10.7 contradict this suggestion. This observation suggests that either it is not an increase in bonding mechanisms that causes the ageing effect or that the effect occurs on a very small level where standard test procedures are not able to detect it.
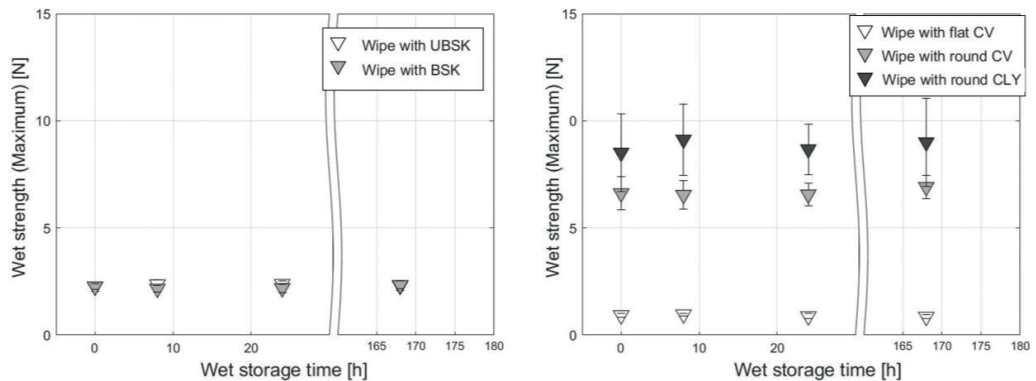

Figure 10.7. Wet strength of wet wipes over the wet storage time. Left: Wet wipe with bleached pulp (BSK) and unbleached pulp (UBSK) and flat viscose fibres. Right: flat CV, round CV, round CLY blended with bleached pulp. Error bars represent the standard deviation.

Conclusion

The term ageing effect of dispersibility is introduced to describe the continuous decrease of dispersibility over the time a wet wipe is stored in it's wet condition. It is shown that the reduction in dispersibility does not correlate with mechanical tests e.g.

wet tensile test as it shown in Figure 10.7. Pulp is suggested as the key parameter to reduce the ageing effect and to maintain good dispersible properties. Particularly unbleached kraft pulp seems, either through the elevated lignin content or the untreated surface, to counteract the ageing effect in wet wipes.

Acknowledgements

References

1. Hassan, J. (2019). Britain's latest 'fatberg,' a mass of grease and wet wipes in a sewer, is longer than 6 double-decker buses The Washington Post. [Online]. Available at: https://www.washingtonpost.com/world/2019/01/09/britains-latest-fatberg-mass-grease-wet-wipes-is-longer-than-double-decker-buses/?utm_term=.1c37fa8d2316. Retrieved May 23, 2019]

2. Flegenheimer, M. (2015). Wet wipes box says flush. New York's sewer system says don't. The New York Times, 15(4), 1849–1895.

3. Mango, P. (2004). Flushable wipes-past, present and future. Nonwovens Industry, 12, 64-71.

4. Deng, C., Liu, W., Zhang, Y., Huang, C., Zhao, Y., & Jin, X. (2018). Environmentally friendly and breathable wet-laid hydroentangled nonwovens for personal hygiene care with excellent water absorbency and flushability. Royal Society open science, 5(4), 171486.

5. Atasağun, H. G., & Bhat, G. S. (2020). Advancement in flushable wipes: Modern technologies and characterization. Journal of Industrial Textiles, 49(6), 722-7

6. Zhang, Y., Xu, Y., Zhao, Y., Huang, C., & Jin, X. (2019). Effects of short-cut fiber type and water-jet pressure sum on wet strength and dispersibility of wood pulp-based wetlaid/spunlace wipes. Eur J Wood and Wood Products, 77(1), 33-43.

7. Zhang, Y., & Jin, X. (2018). The influence of pressure sum, fiber blend ratio, and basis weight on wet strength and dispersibility of wood pulp/Lyocell wetlaid/spunlace nonwovens. J. Wood Sci., 64(3) 256–263.

Sheet structural and mechanical properties and their relationship to tissue softness

Yuhan Wang, Richard A. Venditti, Ronalds Gonzalez, & Joel J. Pawlak

North Carolina State University, Raleigh, North Carolina, USA

Corresponding author: *Joel J. Pawlak <jjpawlak@ncsu.edu>*

Keywords: Softness, volume fractions, fiber properties, friction, roughness, statistical model

Introduction

Softness, as a subjective perception, is an expression of tactile feeling related to compressibility and deformability[1]. Transitional physical aspects[1], multi-dimensional visual and haptic inputs[1] and various material properties[2,], make softness a challenge to express and measure[3,4,5]. In the tissue and textile industry, a panel test has been recognized as the most reliable method to characterize softness[3,6]

The mechanoreceptive units on humans' hands play a major role in determining the tactile sensation of objects[7]. The mechanoreceptive units, composed of Merkel disks, Meissner's corpuscle, Ruffini endings, and Pacinian corpuscles, are responsible for the perception of pressure, flutter, stretching and vibration respectively[8,9] Contact between the hand and the object results in pressure, friction, and vibration, which generates neurological signals[10] The brain combines and interprets these signals into the perception of roughness, smoothness or softness. Several studies had shown that the softness perception is related to friction-induced vibration[11,12,13,14.15]

This friction-induced vibration is a function of the surface and internal properties of both sliding components[4,16,17]. In the case of tissue paper, the surface morphology and internal structures are the two dominant variables that contribute to its physical properties. Tissue papers are typically made from cellulosic wood fibers. Its final properties are a function of manufacturing technology, fiber selection, and chemical additives[2]

In this study, relationships between various sheet properties and the softness as characterized by the Tissue Softness Analyzer (TSA) (Emtec GbHm, Leipzig,

Germany) is undertaken. Sheet properties are varied through the changes in the basis weight and fiber content of the tissue sheets.

Methodologies

Four different pulps that are typically used in tissue making were selected for this study. The pulps included two softwood pulps and two hardwood pulps. Sheets were formed via a modified handsheet making method to create low-density sheets that have been found to be reproducible and representative of a tissue sheet. The sheet were formed at a variety of basis and compositions. A total of 41 different samples were created for this study. A Hi-Res Fiber Quality Analyzer (FQA) (OpTest Equipment Inc., Hawlebury Canada) was used to characterize the dimension of the fibers.

The basis weight and caliper were measured for all of the sheets using Tappi methods. The caliper was measured using a 2kPa pressure to ensure an accurate determination of the caliper for these compressible sheets. The Tissue Softness Analyzer (TSA) was used to characterize the sheet in terms of softness response. Roughness was measured using a Kawabata Evaluation System (KES-FB4) surface tester (KatoTech, Kyoto, Japan). A 0.5 mm diameter U-shape wire probe was used to scan the surface of the sample with a contact force of 0.05 N, scanning speed of 1mm/s and scanning length 30 mm[17] (Bending stiffness was measured using a "drape" test where the length of the sample required to create 25 cm of deflection is characterized. The stiffness is then calculated using the equation:

$$D = (BW * g * b * L^4)/8W \tag{1}$$

where D is the bending stiffness of the sample, BW is the basis weight of the sample, g is the acceleration due to gravity, L is the length of the strip extending out from the platform, b is the width of the strip, and W is the height of the platform.

The surface friction was measured using a customized test to mimic the interaction of skin and the tissue sheet. A small circular sled, 1 cm in diameter and having a mass of 30 grams, was covered with synthetic skin. The sled with the skin was dragged over the surface of the sheets while the displacement forces were recorded.

A parameter call the Fiber Volume Fraction (FVF), was calculated using measured fiber dimensions, caliper and basis weight of the sheet. The fiber volume fraction can be expressed as:

$$V_f = \frac{\pi * w^2}{4 * X} * \rho_p \tag{2}$$

where V_f is FVF, w is the number average fiber width, X is number average coarseness, ρ_p is the density of the sheet. Equation 2 assumes that the cross-section of fiber is circular.
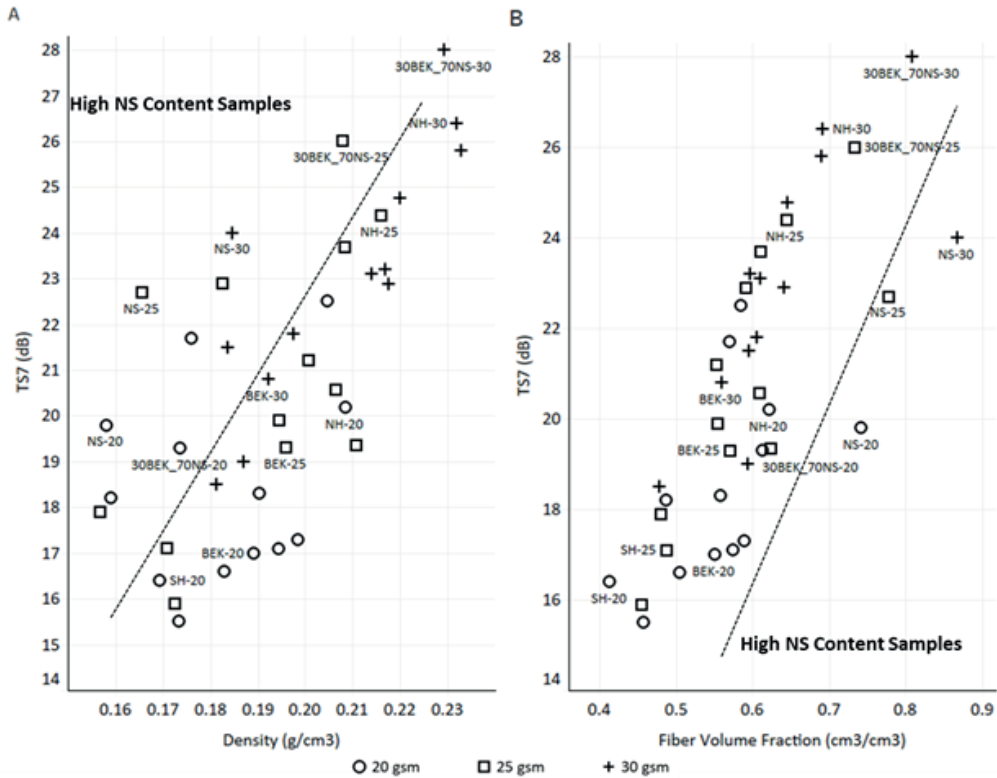

Figure 10.8. The plots of TS7 vs. (A) sheet density and (B) Fiber Volume Fraction. A group of NS content samples was separated from the majority of the samples.

Results and Discussion

Investigations into a wide variety of correlations was undertaken. It was shown that no single fiber characteristic was correlated with the measured TSA softness. Better correlations were found between density and TSA softness and even better correlations where found with FVF, cf. Figure 10.8.

Additionally, the causation for the improved correlation between FVF and TSA softness was further explored. This included developing a conceptual model of the transfer of energy through and within the tissues sheets. Each of the various sheets showed significant differences in packing which could be related to the fiber selection. Figure 10.9 shows SEM cross sections of various samples.
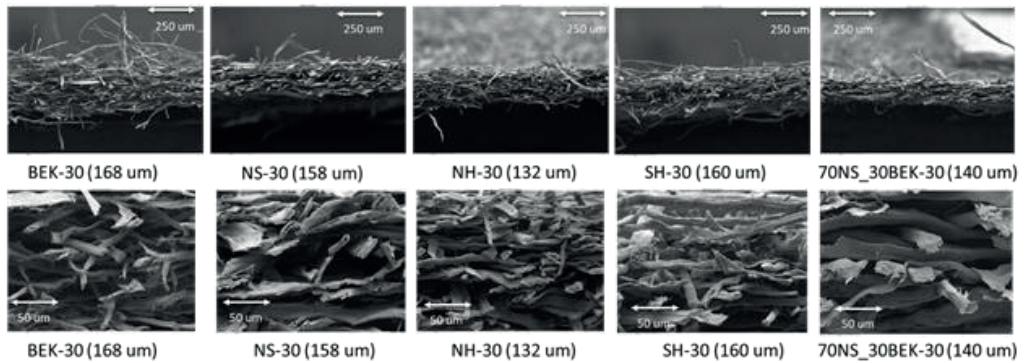
Figure 10.9. The Scanning electron images of the cross direction of selected samples.

The fiber geometry was used to predict the number of fiber-to-fiber contacts within a given area. This information was used to characterize the "fineness" of the tissue sheet surfaces. A relative few number of contacts were indicative of a less fine surface and relationships with softness were explored. Overall, there was found to be some correlation with softness, but the data indicated that there are clearly other more complicated factors involved.

The bending stiffness of the sheet was also considered in this study. The bending stiffness can be related the ability of the sheet to transmit energy elastically within the plane and through the sheet. Figure 10.10 shows relationships between softness and stiffness as well as the independence of the number of fiber contacts and stiffness. This indicates that these two factors can be used independently. By combining together the Fiber Volume Fraction, number of contacts per unit area and stiffness of a sheet, a predictive model of TSA softness was created with a R-squared of 0.78.
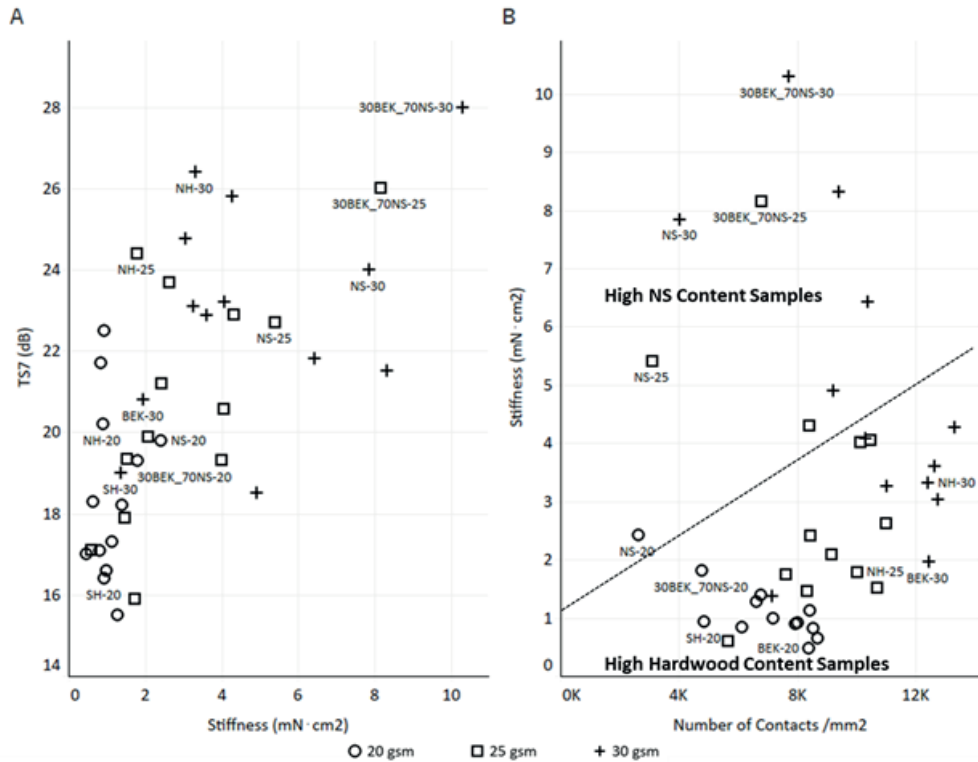
Figure 10.10. The plots of (A) TS7 vs. stiffness and (B) stiffness vs. number of contacts per mm^2. As the stiffness increased, the TS7 generally increased. As the number of contacts increased, the stiffness generally increased, whereas separation was found between high NS content and high hardwood content samples.

References

1. Tiest, W. M. B., & Kappers, A. M. (2014). Physical aspects of softness perception. Multisensory softness, Springer: 3-15.

2. de Assis, T., Reisinger, L. W., Pal, L., Pawlak, J., Jameel, H., & Gonzalez, R. W. (2018b). "Understanding the effect of machine technology and cellulosic fibers on tissue properties–A review." BioResources 13(2), 4593-4629.

3. Leporte, L. E. (1970). Project 2817 (Report 2). Institute of Paper Science and Technology. Atlanta, GA, USA.

4. Wang, Y., de Assis, T., Zambrano, F., Pal, L., Venditti, R.A., Dasmohapatra, S., Pawlak, J. J., Gonzalez, R. (2019). "Relationship between Human Perception of Softness and Instrument Measurements." BioResources 14(1), 780-795.

5. de Assis, T., Reisinger, L.W., Dasmohapatra, Pawlak, J., Jameel, H., Pal, L., Kavalew, D., & Gonzalez, R. W. (2018a). "Performance and Sustainability vs. the Shelf Price of Tissue Paper Kitchen Towels." BioResources 13(3), 6868-6892.

6. Hollmark, H., Ampulski, R.S. (2004). "Measurement of tissue paper softness: A literature review." Nordic Pulp & Paper Research Journal 19(3), 345-353.

7. Pare, M., Elde, R., Mazurkiewicz, J. E., Smith, A. M., & Rice, F. L. (2001). The Meissner corpuscle revised: a multiafferented mechanoreceptor with nociceptor immunochemical properties. Journal of Neuroscience, 21(18), 7236-7246.

8. Bolanowski Jr, S. J., Gescheider, G. A., Verrillo, R. T., & Checkosky, C. M. (1988). Four channels mediate the mechanical aspects of touch. The Journal of the Acoustical society of America, 84(5), 1680-1694.

9. Johnson, K. O. (2001). The roles and functions of cutaneous mechanoreceptors. Current opinion in neurobiology, 11(4), 455-461.

10. Lumpkin, E. A., & Caterina, M. J. (2007). Mechanisms of sensory transduction in the skin. Nature, 445(7130), 858-865.

11. Kenins, P. (1994). Influence of fiber type and moisture on measured fabric-to-skin friction. Textile Research Journal, 64(12), 722-728.

12. Lynn, B., & Perl, E.R (1996). Afferent mechanisms of pain. In: Kruger, L.(ed.) Pain and Touch. San Diego, USA, pp. 213–241.

13. Bertaux, E., Lewandowski, M., & Derler, S. (2007). Relationship between friction and tactile properties for woven and knitted fabrics. Textile Research Journal, 77(6), 387-396.

14. Fagiani, R., Massi, F., Chatelet, E., Berthier, Y., & Akay, A. (2011). Tactile perception by friction induced vibrations. Tribology International, 44(10), 1100-1110.

15. Fagiani, R., Massi, F., Chatelet, E., Costes, J. P., & Berthier, Y. (2012). Contact of a finger on rigid surfaces and textiles: Friction coefficient and induced vibrations. Tribology Letters, 48(2), 145-158.

16. Akay, A. (2002). Acoustics of friction. The Journal of the Acoustical Society of America, 111(4), 1525-1548.

17. Chen, G. S. (2014). Handbook of friction-vibration interactions, Elsevier.

18. Ko, Y. C., Park, J. Y., Lee, J. H., & Kim, H. J. (2017). Principles of developing a softness evaluation technology for hygiene paper. Journal of Korea TAPPI 49(4), 184-193.

ABSTRACTS FOR

POSTER

PRESENTATIONS

Session chair: Jani Lehto

Ionic liquid application for wood-based materials

Atsushi Tanaka, Alexey Khakalo, Antti Korpela, & Hannes Orelma

VTT Technical Research Centre of Finland, Espoo, Finland

Corresponding author: *Atsushi Tanaka <atsushi.tanaka@vtt.fi>*

Keywords: Ionic liquid, paper, sawdust, film, particleboard

Introduction

Mass consumption of fossil fuel-based plastics as packaging materials has been rising due to increased transportation. Poor waste management causes environmental pollution. They are harming animals and other living organisms, e.g. human health issues related to the microplastics problem[1], risking sea creatures by ocean plastic pollution. Thus brought to a social need to develop sustainable alternative packaging materials. One potential solution is all-cellulose materials, which have novel properties to compensate for the use of conventional package materials[2]. We have recently studied the conversion of woodfree paper into plastic-like material using the ionic liquid (IL) 1-Ethyl-3-methylimidazolium acetate ([EMIM][OAc])[3,4]. By changing the treatment intensity, IL partially or fully dissolves the cellulose component. Thus paper can be converted into transparent film or composite materials. Here we further applied chemical crosslinking for IL-treated papers. Influences of drying condition was studied as well. In addition, similar approach was applied for other wood-based materials, i.e. IL-treated sawdust to make particleboard or strand.

IL-treatment for woodfree paper

Laboratory handsheets (100 g/m^2) were prepared with bleached pine kraft pulp according to ISO 5269-1:05. Each sheet (~2 g) was dipped into the aqueous solution of [EMIM][OAc] (75 wt% concentration) to impregnate 10 ± 0.5 g of IL solution, then heated in an oven. Altogether 6 samples were prepared as shown in Table P1, i.e. varying heating conditions, chemical crosslinking, and drying method. As for crosslinking, final washing (before wet-pressing) was performed for 120 minutes with water containing 4.0 wt% glyoxal and 1 wt% aluminium sulfate-14-hydrate. The sheets were dried and heated in L&W rapid dryer at 135 °C for 10 minutes for full curing of the crosslinking chemicals.

Table P1. IL-treatment conditions for woodfree paper.

	Heat treatment		Crosslink
	Temperature	Time	
#1	80 °C	50 min	
#2	80 °C	50 min	x
#3	95 °C	7 h	
#4	95 °C	7 h	x

Increased intensity of IL-treatment promoted sheet transparency and density, and in more substantially in-plane shrinking. Samples #1, #2 still had somewhat paper-like feel and appearance, whereas #3, #4 resembled stiff plastic film. More severely treated papers also shrank more substantially. Chemical crosslinking (#2, #4) turned out to make stiffer and more fragile sheets. In addition, less water absorption were achieved for them (Table P2).

Table P2. Weight gain in immersion test. Original handsheet as Ref.

	Weight gain, %								
	0 min	5 min	10 min	20 min	40 min	80 min	160 min	360 min	1440 min
REF	0,0	101,3	102,7	105,5	105	104,9	102,4	104,5	101,8
#1	0,0	94,0	93,4	98,8	97,7	102,8	104,7	103,8	105,7
#2	0,0	47,3	50,4	49,1	56,7	58,2	64,3	68,8	66,3
#3	0,0	67,2	74,1	77,8	78,1	77,8	81,1	82,0	82,8
#4	0,0	0,6	0,7	0,9	0,9	10,4	20,6	26,3	32,3

IL-treatment for sawdust

Scotch pine sawdust (< 36-mesh size) was treated by [EMIM][OAc] in two ways: Compression molding; and Extrusion by twin-screw extruder. Sawdust particles and IL was carefully mixed in advance. In case of molding, the mixture was compressed at 160°C, 10 MPa for 3 hours. Sawdust-IL ratio was varied from 1:0.5 to 1:3. As for extrusion, sawdust and IL mixture (1:3) was processed at 160°C for 30 min prior to extruding through 2 mm diameter outlet. In both cases, samples were rinsed in methanol and air-dried at 23°C, 50%RH.

The higher the IL dosage, the larger tensile strength of particleboards (Table P3). SEM observation confirmed that the degree of particle-merging developed accordingly.

95°C was sufficient for full dissolution of woodfree paper (#3, #4), while even higher temperature (160°C) was required for sawdust processing. This should derive from glass transition temperature of lignin. Indeed, extrusion was unsuccessful under 150°C (sawdust stuck in extruder). Dry strength of strand was three times higher than particleboard with same mixing ratio (1:3). Very uniform structure was observed by SEM.

Table P3. Strength properties of IL-treated sawdust materials.

Sample	Density	Dry strength		Wet strength	
Ratio of sawdust : IL	g/cm^3	MPa	Strain	Stress	Strain
Particleboard (1:1)	0,44	1,8	0,8	0,7	2,5
Particleboard (1:2)	0,97	4,8	0,8	2,2	19,3
Particleboard (1:3)	1,04	10,4	2,4	2,4	63,6
Strand (1:3)	1,18	30,5	14,7	4,0	16,3

Acknowledgements

References

1. Haward, M. (2018). Plastic pollution of the world's seas and oceans as a contemporary challenge in ocean governance. Nature communications, 9(1), 1-3.

2. Huber, T., Müssig, J., Curnow, O., Pang, S., Bickerton, S., & Staiger, M. P. (2012). A critical review of all-cellulose composites. Journal of Materials Science, 47(3), 1171-1186.

3. Tanaka, A., Khakalo, A., Hauru, L., Korpela, A., & Orelma, H. (2018). Conversion of paper to film by ionic liquids: manufacturing process and properties. Cellulose, 25(10), 6107-6119.

4. Korpela, A., Tanaka, A., Khakalo, A., & Orelma, H. (2020). Water Sorption Properties of Regenerated Sulfate Pulp Paper Treated with Ionic Liquid [EMIM]OAc. Submitted to J Wood Chem Technol.

Determining properties of dense stack of paper

Tero Ponkkala[a,b], Jarmo Kouko[a], Panu Mikkonen[c], Elias Retulainen[a]

[a]*VTT Technical Research Centre of Finland Ltd, Jyväskylä, Finland*
[b]*Alva-yhtiöt Oy, Jyväskylä, Finland*
[c]*Tervakoski Oy, Tervakoski, Finland*

Corresponding author: *Elias Retulainen <*elias.retulainen@vtt.fi*>*

Keywords: Density, thermal proerties, mechanical properties, paper stack

Summary

A method was developed to measure the effect of density on certain mechanical and thermal properties of a dense stack of paper. Pieces of paper were stacked in a frame and compressed to different densities by a hydraulic press. The two lateral sides of the stack were smoothened for testing. Thermal conductivity, behavior under cyclic compression loading and in ball indentation test were determined. Thermal conductivity, storage modulus, loss factor depended approximately linearly on the density of the stack.

Materials and methods

 Paper samples with basis weight of 180 g/m^2 were made of flax fibers and were cut to the desired size. High number of these paper pieces (around 100-180 pieces) were stacked in a frame and compressed to different densities by a hydraulic press, forming a compressed cuboid like samples, here called "unit cells" (Figure P15). The two sides of the unit cell were smoothened for testing by grinding. Two kinds of unit shells were made (Figure P15). The size of the larger unit cell was 20 mm (width), 24 mm (length) and the height was about 30 mm.

Thermal conductivity

Transient Plane Source method was used to determine the thermal properties of the unit cells. The sensor was placed between two identical unit cell samples. Sensor was heated by electric current. Temperature raised a few Celsius degrees above the

ambient temperature. At the same time the resistance alteration of sensor was registered which enabled calculations of heat transmission in sample.

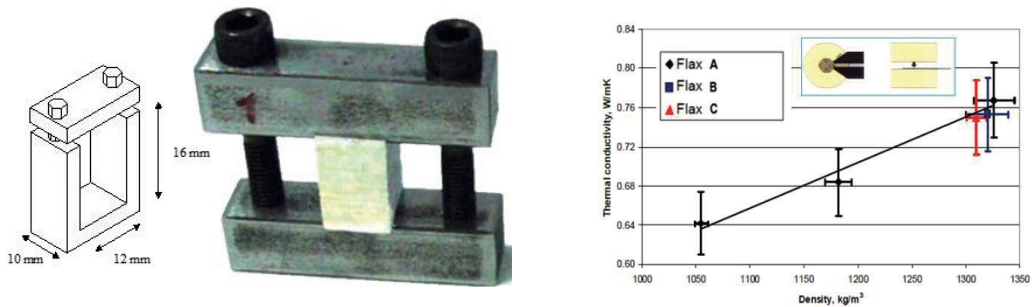Figure P15 Stacks of compressed paper samples, smaller and larger "unit cell", used for testing.

Figure P15. Effect of the density of the paper stack on the thermal conductivity.

The thermal conductivity of unit cells made of flax based paper is shown in Figure P16. The conductivity increased with increasing density of the unit cell. The measured value deviates considerably from thermal conductivity values (0.06-0.17 W/mK) measured for paper[1]. The method in principle could be used to estimate the thermal conductivity of nonporous fibre wall material. Rough extrapolation suggest that the thermal coefficient of cellulose material at 1500 kg/m^3 is around 0.85 W/mK.

Compressive properties in-plane of paper

The compressibility and hardness of the unit cell in-plane of individual paper samples was measured using a spherical measuring head (ø3 mm). Also the estimates for elastic and permanent deformations could be determined (Figure P16).

Dynamic mechanical properties were measured using a dynamic compression test rig with press platens. The structure of the measuring head can be seen in Figure P17. Cyclic compressive pulses (40 MPa) were applied onto the sample area of 78.5 mm^2 (ø10 mm).
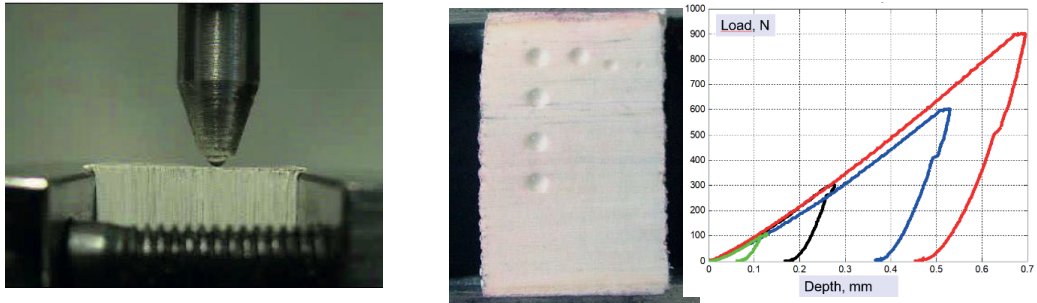
Figure P16. Side view of the measuring head (left) and the permanent marks on the sample surface (middle), and typical measured load–compression curves (right).
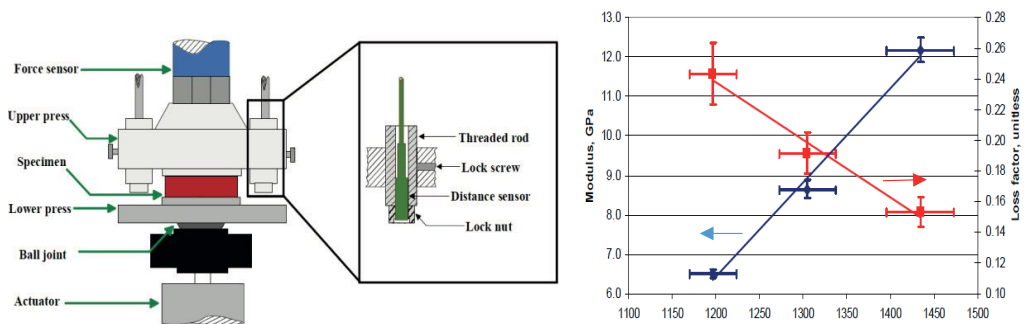
The duration of a single pulse was 50 ms.

Figure P17 (Left) Measuring head of the dynamic compression test device. (Right) Storage modulus and loss coefficient determined from the dynamic compression test as function of the stack density.

The results (Figure P17, Right) show that density has strong effect on the elastic modulus and loss factor. Due to the increase in density from 1200 kg/m^3 to 1450 kg/m^3 loss coefficient decreased by over 35% and storage modulus was increased by 90%.

Conclusions

A method was developed for physical testing of dense stack of paper mainly in-plane direction of the paper. The method made it possible to evaluate effect of the density over a wide range (from 1050 to 1450 kg/m^3). Density had a strong influence on the thermal and mechanical properties of the stack of paper. Increasing density increased thermal conductivity, hardness and storage modulus of the stack.

References

1. Bohmer, E. (2002). Thermal properties. Handbook of physical properties of paper. (Borch, J., Lyne, B., Mark, R., Haberger, C.C., eds). Marcel Dekker, NY, USA

Origami folding for structured materials

Miia Palmu[a], Kirsi Peltonen[a], & Jarmo Kouko[b]

[a]*Aalto University, Espoo, Finland*
[b]*VTT Technical Research Centre of Finland Ltd, Jyväskylä, Finland*

Corresponding author: *Miia Palmu <miia.palmu@aalto.fi>*

Keywords: Origami tessellations, folding, Miura-Ori, paperboard, packaging design

Summary

There is a pressing need to replace plastic materials used in packaging design, in which origami tessellations can offer interesting opportunities for technical applications. This requires finding suitable patterns and studying their structural and technical properties and manufacturing possibilities. Designing origami-structured, transformable and rigid packaging materials, and using cellulose based sheet materials, can provide a more sustainable solution for the packaging industry.

Introduction

What qualities are necessary in a material that needs to replace plastic? High flexibility, transformability and light-weightiness are all undisputable qualities of plastic which are extremely necessary when looking for durable and transformable solutions for packaging. The solution could lie in origami tessellation patterns, complex polygonal patterns which can be folded into structural materials[1]. The reason why origami tessellations are such a potential solution lies within the technical properties that the structuring creates: origami tessellation patterns offer high flexibility, transformability, mechanical stiffness and, depending on the material used, they can be very lightweight.

Origami tessellation patterns have inspired many artists, designers and architects, and the patterns have even been applied to fields such as astronomy[2] and medical appliances[3]. Yet, their use in packaging field has been quite rare.

Results

To demonstrate the possibilities of origami tessellation patterns, several different patterns were taken under study, to identify the qualities that different patterns have in order to determine the best usage for various purposes and production.

Figure P4. The Waterbomb base pattern and test pieces with different variations of the pattern.

The main focus was set on the Waterbomb pattern and Miura-ori pattern, which in comparison have very different properties, Miura-ori being a rigid and stable pattern with a clear folding direction and the Waterbomb pattern very flexible and transformable in shape. The patterns were studied in order to create design proposals for protective packaging solutions, such as a cushioning material for replacement of bubble wrap.

Figure P5. Different shapes of the Waterbomb tessellation pattern, designed to serve as cushioning materials. Photos by Valeria Azovskaya.

Test pieces were folded manually in order to see how each pattern behaves and to estimate the possibilities of the industrial manufacture. There are many factors that affect the industrial manufacturing possibilities of the patterns: the folding direction of the chosen pattern, material qualities (strain, thickness, etc.), and the angle in which the pattern reaches the state of energy that keeps it in its folded position.

From the design perspective origami tessellations offer a variety of possibilities to create diverse range of shapes. Thus the options for using these patterns with different functions and purposes are quite limitless.

Figure P6. Examples of cushioning materials designed to fit around a plate, based on the flexible character of the waterbomb pattern.

Conclusions

Origami tessellation patterns can offer interesting points of view to both design and technical approach. These patterns can be categorized by their structural qualities such as flexibility and mechanical stiffness and based on certain mathematical principles, the patterns can be modified by changing their parameters which affects the properties of the folded structure.

Tessellated structures that are based on origami folding provide excellent opportunity to design for example functional lightweight wrapping, cushioning and packaging structures.

References

1. Lang, R. J. (2017). Twists, tilings, and tessellations: mathematical methods for geometric origami. CRC Press. p. XV-XVI.

2. Greicius, T. (2014). Solar Power, Origami-Style. NASA. (Retrtieved: from: https://www.nasa.gov/jpl/news/origami-style-solar-power-20140814, 5.8.2019.

3. Trebbi, J. C., & Corkett, T. (2012). The art of folding: Creative forms in design and architecture. Promopress. p.17.

Measurement of curvature resistance – a method for quantifying and predicting the plastic bending and folding of cardboard composites

Toma Schneider[a], Antje Harling[a], & Frank Miletzky[b]

[a]*Papiertechnische Stiftung (PTS), Heidenau, Germany*
[b]*Technische Universität Dresden, Dresden, Germany*

Corresponding author: *Toma Schneider <*[*Toma.schneider@ptspaper.de*](Toma.schneider@ptspaper.de)*>*

Keywords: Cardboard, forming, plastic bending, folding, material model, simulation

Summary

Requirement and development of a new measuring method to determine the plastic bending and folding properties of cardboard composites. Presentation of the principle, the limitations and possible future applications.

Introduction: To realize an advantageous distribution and use behaviour of consumer goods, integral packaging structures are made of fibre composites, e.g. composite cardboards with plastic barrier. Savings of global resources is intended by efficient material use based on processes with low material damage. The development and optimization of such processes require a qualitative and quantitative description of the material behaviour as well as the resulting processing behaviour.

Requirements

Object of the work is to understand and to predict the forming behaviour of cardboard and composite materials under plastic bending stress, including local folding. There is an ongoing conflict between safe predisposing of folding lines and minimal material damage. The desired delamination (interlayer breaks) of individual layers through the conventional preparation of folding lines by creasing is often accompanied with tensile breaks (inner layer breaks) of individual layers. If these individual layers are intended to act as a barrier against gases or radiation, a crack leads to a loss of functionality of the material. Excessive creasing causes extensive mechanical damage to the material, reducing the load-bearing capacity and stiffness of the produced packages. This is

usually compensated by mechanical oversizing during material selection. This shall be overcome by developing minimally invasive pretreatment (conditioning step) of folding lines and load-appropriate packaging structures. For more accurate prediction of behaviour of a packaging structure, the mechanical preload and the influence of the filling material must be taken into account. The mechanical pre-stresses usually result from the upstream forming processes with plastic deformation. Therefore, quantifications of plastic bending behaviour are required. Essential basics like measurement methods for quantifying geometry-independent parameters to describe the plastic forming behaviour during bending are unknown.

Integral material model: The Finite Element Method (FEM) is an established tool for modelling the behaviour of macrostructures under load. For elastic deformations the clt (classical laminate theory) can be applied with restrictions. Plastic deformations, orthotropy and shear-soft cross-sections are not considered[1]. The description of a composite structure requires the mechanical material parameters of each individual layer and its connections. Due to these limitations, the following thesis is examined: the behaviour under plastic bending stress can be mapped as a substitute derived from pseudo-homogeneous replacement material behaviour. In this procedure, the entire composite structure is depicted as a homogeneous material with isotropic, plastic material behaviour. The impacts of the effects in bending and folding forming, such as displacement of the stress zero line, delamination and segmentation are reflected in the transfer behaviour. To calculate the transmission behaviour of a finite element (slab), a homogeneous material behaviour over the entire composite cross-section is used. Measurement principles and parameter libraries are available for pure plastic tensile stress and partially for compressive stress, but are not available for bending stress. Since in folded packaging, buckling (3D deformation) usually only occurs in the elastic range, the restriction to modelling plastic bending (2D deformation) is nevertheless sufficient for building macrostructure models. Consequently, a stress-strain curve is required which describes the non-linear response of curvature to bending moment.

Measurement methodology, modelling and validation: Existing measuring arrangements are dependent on the sample geometry. They record the geometric changes incompletely and deliver only derived integral parameters, e.g. measurement of two point bending stiffness and folding resistance. Furthermore, fibre materials show an inhomogeneous distribution of stiffness and strength. Due to this, a calculation of the curvature resistance based on existing principles is hardly and only possible with restrictions.

In the novel, direct measurement of the curvature resistance, a ring is formed from a strip-shaped sample. The bearing forces and torques in the clamping are recorded at one end of the sample. During the measurement, the circumference of the effective ring is continuously reduced by a deduction, thus increasing the mean curvature. At

the beginning of the measurement there is a low curvature and almost constant bending moment load for large diameters. When the effective circumference decreases, a spiral segment is formed. Based on known geometric conditions, the location and quantities of the searched transfer function can be calculated iteratively. For the prognosis an approach consisting of continuous sigmoid and potential function is used. Based on the bearing forces, local buckling of the sample is identified. Local buckling marks the transition from plastic bending to folding. A folding line can be modelled in structural models as a discrete, non-linear rotational spring. With the help of the curvature resistance measurement, the required transmission function of this rotary spring can be identified. Therefore a reference sample without and a sample with bending resistance reduction introduced close to the clamping is required.

The validation of the novel methodology is done in two steps: In step one, the new and existing measuring principles are numerically simulated by FEM and then compared with experimental measurements. The quality and the influence of the simplifications on the prediction of the forming behaviour are examined. In step two, the construction of prognosis models with complex macrostructures is planned, for which the description of the plastic compressive stress is also required. In the case of bending stress, a combined tensile and pressure stress is present in the load cross-section. The parameter curve for pure compressive loading is calculated iteratively based on the tensile test and the curvature resistance measurement. Thus one is not dependent on the geometry-related parameter curves based on ring crush test (rct) and short-span compression test (sct). The calculation is based on the geometry and the relative stiffness of the individual layers of the composite. As a result of step two, a tool for the prognosis of plastic forming processes will be created and experimentally validated. On this basis, load-bearing structures and material-conserving forming processes, including tool geometries, can subsequently be developed.

Fields of application: The geometry formation during forming is largely dependent on the local stiffness relations. Large curvature gradients are advantageous for folding and low gradients for deep drawing. The collected transfer functions for plane bending are normalized to their maximum torque. The course of the curve characterizes the geometry-independent forming behaviour between the limits of local buckling and surface creping. This means that the forming behaviour can be characterised independently of the grammage and bending stiffness for conventional, path-controlled forming processes. By this forming processes or desired material substitutions can be supported successfully.

Schneider, T., Harling, A., & Miletzky, F.

Poster 4

References

1. Schürmann, H. (2005). Konstruieren mit Faser-Kunststoff-Verbunden (Vol. 2). Berlin: Springer.

Wet strength properties of foam formed fiber materials

Tiinamari Seppänen[a], Jukka Ketoja[b], Tiina Pöhler[b], & Elina Pääkkönen[a]

[a]*VTT Technical Research Centre of Finland Ltd, Jyväskylä, Finland*
[b]*VTT Technical Research Centre of Finland Ltd, Espoo, Finland*

Corresponding author: *Tiina Seppänen <*[*tiinamari.seppanen@vtt.fi*](mailto:tiinamari.seppanen@vtt.fi)*>*

Keywords: wet strength, wet tensile strength, compression strength, foam forming

Introduction

The foam forming of natural fibers into different materials represent an increasingly applied method due to its cost-effectiveness. Various potential application areas of foam formed cellulose fiber materials, including tissue paper[1], packaging materials[2] as well as some construction materials[,3,4,5], equire wet strength. Required wet strength properties depends highly on the application type, for example toilet paper requires temporary wet strength and insulation material should not be affected by the fluctuating humidity. In this novel work polyamidoamide-epichlorohydrin (PAE) as well as potential bio-based and/or biodegradable wet strength agents are used to increase the wet strength of cellulose-based foam formed materials. The efficiency of different wet strength agents was examined by measuring wet tensile index from paper-like materials and durance against disintegration in water from low-density materials.

Results

Paper-like materials - Wet tensile strength

Figure P9a shows the tensile index results of the paper-like samples and Figure P9b shows the wet to dry strength ratio (W/D ratio) of the samples after immersion in water. The wet tensile index of the PAE sample was around 6 times higher than of the reference and the W/D ratio was around 24%. The use of 5% CMF with PAE increased the dry tensile strength significantly, but the wet tensile index was much lower than of the PAE sample. No improvements were seen with chitosan addition, but used together with poly(ethylene maleic acid) (PEMA) resulted in the highest wet tensile index of all the samples. The wet tensile index of chitosan + PEMA sample was around 11 times higher than of the reference sample, and W/D ratio was 28%.
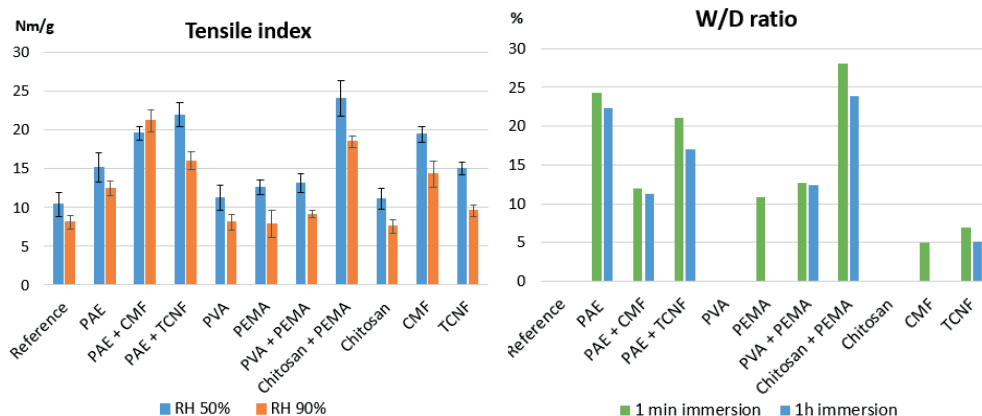
Figure P9a) Tensile index at relative humidity (RH) 50% and RH 90%. b) W/D ratio after 1 min and 1 h immersion in water. If there is no bar, the sample was too weak to be measured.

Low-density matrials -Compression strength

Figure P10a shows the compression stress of the low-density samples at relative humidity (RH) of 50% and 90%. The wet strength agents had generally only minor effect on the compression strength. Compression strength of PAE + CMF sample had increased significantly at RH 50%, but it was similar to others at RH 90%. When CMF was used alone, the compression stress at RH 90% was clearly lower compared to the other samples. The general 1.9-fold drop in compression stress with increasing RH follows the theory of Ketoja et al[6].

Low-density materials - Durance against disintegration in water

Low-density samples were stirred in water with a magnetic stirrer until disintegration or approximately for 6 hours. Sample durance can be divided into three groups based on the results: no durance (disintegrated less than 5 min), medium durance (5 min - 3h) or good durance (> 3h). As shown in Figure P10b, the reference disintegrated immediately after dropping in water. Medium durance samples included e.g. chitosan, PEMA and PAE + CMF. When PVA and chitosan were combined with PEMA, the structures withstood over 6h mixing in water, similar to PAE.
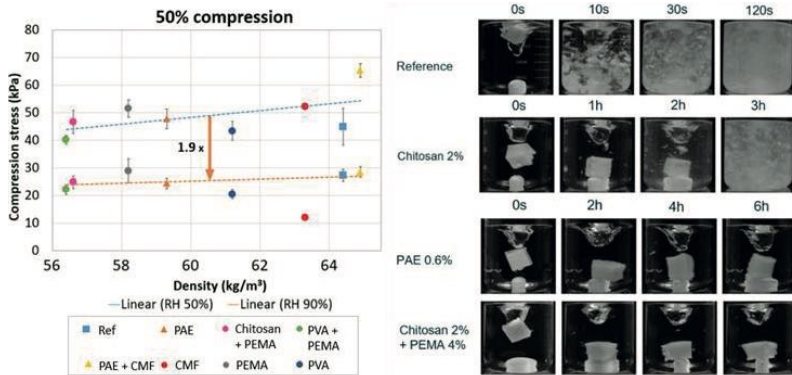
Figure P10. Compression strength of the low-density materials with 50% compression at RH 50% and RH 90%.

Conclusion and summary

Most of the studies with wet strength agents have focused on increasing the wet tensile index. In this study, the compression strength at RH 90% and durance against disintegration in water were measured as well. Overall, it can be said that PAE had significant effect e.g. on the wet tensile index and durance against disintegration in water. Bio-based and/or biodegradable options to PAE were found, especially chitosan + PEMA gave promising results in terms of wet tensile strength and durance against disintegration in water.

References

1. Hellen, E., Jetsu, P., & Lehmonen, J. (2013). Foam forming: What could it mean for tissue?. Paper Technology, 54(4), 10-12.

2. Paunonen, S., Timofeev, O., Torvinen, K., Turpeinen, T., & Ketoja, J. A. (2018) Improving Compression Recovery of Foam-Formed Fiber Materials. BioResources 13:4058–4074

3. Pöhler, T., Jetsu, P., Fougerón, A., & Barraud, V. (2017). Use of papermaking pulps in foam-formed thermal insulation materials. Nordic Pulp & Paper Research Journal, 32(3), 367-374.

4. Pöhler, T., Jetsu, P., & Isomoisio, H. (2016). Benchmarking new wood fibre–based sound absorbing material made with a foam-forming technique. Building Acoustics, 23(3-4), 131-143.

5. Jahangiri, P. (2013). Novel cellulose based foam-formed products: Applications and numerical studies (Doctoral dissertation, University of British Columbia).

6. Ketoja, J. A., Paunonen, S., Jetsu, P., & Pääkkönen, E. (2019). Compression strength mechanisms of low-density fibrous materials. Materials, 12(3), 384.

Continuous folding of origami structures

Jarmo Kouko[a], Miia Palmu[b], & Kirsi Peltonen[b]

[a]*VTT Technical Research Centre of Finland Ltd, Jyväskylä, Finland*
[b]*Aalto University, Espoo, Finland*

Corresponding author: *Jarmo Kouko <Jarmo.kouko@vtt.fi>*

Keywords: Folding, Miura-Ori, paperboard

Introduction

There use of these patterns reaches far beyond that and offer interesting opportunities for technical applications as well. Internationally, interest to the tessellation design has grown steadily for several years. Structures have scientific and technical potential to industrial breakthrough.

Protective packages are designed to withstand the many rigors of the distribution, such as sudden impact, sustained load (stacking), and vibrations. The flexible protective packaging is projected to be the fastest-growing product segment from 2015 to 2020. At present, cushioning structures that consist of folding patterns based on simple origami-based tessellation design are relatively rare.

Objective of our investigation has been development of roll-to-roll folding technique for flat paperboard web that will enable mass production of origami-type patterns. Tessellations based on origami-type folding provide excellent opportunity to design novel functional lightweight wrapping, cushioning and packaging structures. Miura-Ori pattern is already suitable for the industrial roll-to-roll folding process and enable large-scale production.

Coninuous folding of origami

A pilot scale roll-to-roll folding device shown in Figure P7 was developed at VTT. One Miura-Ori -type pattern was demonstrated with several different commercial board and paper grades. Different materials act in different ways when folded or bent, and clearly the paperboard have a large impact on foldability. Successful folding in enhanced by optimal combination of material extensibility, stiffness and strength. The required

material properties also depend on the designed pattern and on material **thickness and stiffness.**

Figure P7. A pilot for a rolling nip device was developed at VTT to demonstrate the folding of
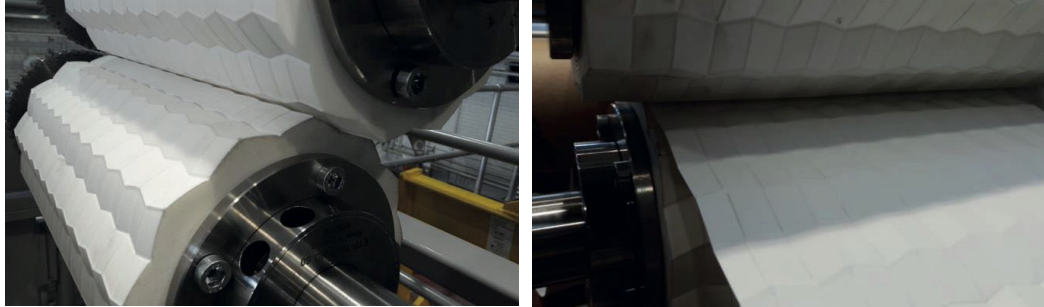
Miura-Ori pattern.

Previously there have been some efforts to utilize continuous manufacturing techniques for a new sheet material folding technology[3,4]. It is noted that when sheet materials are shaped and structurally folded, folding technology with a machine continuously producing sheet folded patterns is a very efficient process. Other production methods, such as pressing, can be costly and provide non-consistent results.

Acknowledgements

References

1. Reis, P. M., Jiménez, F. L., & Marthelot, J. (2015). Transforming architectures inspired by origami. Proceedings of the National Academy of Sciences, 112(40), 12234-12235. https://doi.org/10.1073/pnas.1516974112

2. Jackson, P. (2015). Complete pleats: pleating techniques for fashion, architecture and design. Laurence King Publishing.

3. Schenk, M. (2011). Folded Shell Structures, Doctoral thesis, University of Cambridge, Oxford, UK.

4. Basily, B. B., & Elsayed, E. A. (2004). A Continuous Folding Process for Sheet Materials. Department of Industrial and Systems Engineering, Rutgers University', New Jersey, USA.

Compensating capillary force by centrifugation during paper imbibition

Niels Postulka, Beatrice Fickel, Maximilian Hartmann, Dirk Gründing, Tobias Meckel, & Markus Biesalski

Technische Universität Darmstadt, Darmstadt, Germany

Corresponding author: *Markus Biesalski <*biesalski@cellulose.tu-darmstadt.de*>*

Keywords: Paper-based microfluidic, capillary-driven flow, centrifugal forces

Experimental analysis of spontaneous dynamic wetting processes is an ongoing challenge. As no time independent equilibrium is established, already small pinning effects lead to experimental uncertainties[1]. The situation becomes even more complicated if the observed system changes its geometry during wetting process, e.g. by swelling, as is the case with paper-based materials.[2] To address this problem, we built a device to oppose the capillary force that develops during the wetting and swelling process with a matching centrifugal force. With this, we are able to halt the progression of the imbibition and establish a quasi-stationary equilibrium. Using a camera system with exposure times in the microsecond range that is always triggered at the same pass point, we are able to image the whole process with reasonable contrast and resolution. Validation of the spinning device was achieved by analyzing meniscus shapes and capillary rise heights of water in rectangular glass capillaries at various rotation speeds and comparing the results with simulations. Afterwards, capillary driving forces within the more complex system of paper-based materials were analyzed by determining fluidic distance against rotation speed (Figure P1).

While the capillary pressure is determined by the pore radius of the porous structure, some paper intrinsic parameters lead to a pressure drop reducing the total flow distance[3-4] Notably, we are able to modulate the degree of pressure drop by changing the fiber type or by applying various fiber pretreatments, such as milling, reduction of fines content or various fiber coatings. While analyzing the change in flow distance, conclusions about the pore geometry and fiber characteristics can be drawn. Ultimately, we aim to obtain a detailed and possibly separated view on the numerous simultaneous processes (i.e. wetting, swelling, imbibition) by increasing the imaging resolution and the accuracy of the rotation control. With this, we hope to identify

Postulka, N., Fickel, B., Hartmann, M., Gründing, D., Meckel, T., & Biesalski, M.

important aspects of the dynamic interaction between water and paper fibers which are generally not taken into account in considerations based on a transport to Darcy or Lukas-Washburn, respectively.
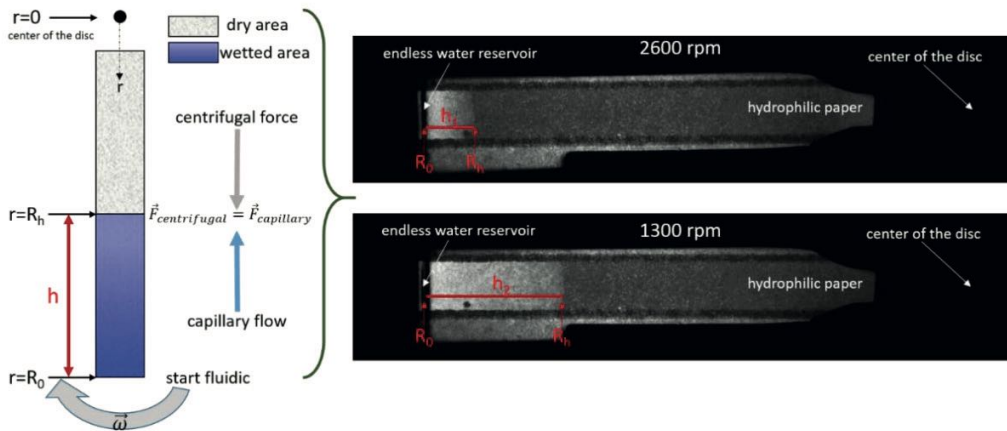

Figure P1. Left: schematic illustration of countering the capillary-driven flow within paper through centrifugal forces. Right: photography of the rotating disc at 2600 rpm (top) and 1300 rpm(botton) providing different wicking distances at the equilibrium state.

Acknowledgements

References

1. Lhermerout, R., Perrin, H., Rolley, E., Andreotti, B., & Davitt, K. (2016). A moving contact line as a rheometer for nanometric interfacial layers. Nature communications, 7(1), 1-6.

2. Hubbe, M. A., Gardner, D. J., & Shen, W. (2015). Contact angles and wettability of cellulosic surfaces: A review of proposed mechanisms and test strategies. BioResources, 10(4), 8657-8749.

3. Böhm, A., Carstens, F., Trieb, C., Schabel, S., & Biesalski, M. (2014). Engineering microfluidic papers: effect of fiber source and paper sheet properties on capillary-driven fluid flow. Microfluidics and nanofluidics, 16(5), 789-799.

4. Rosenholm, J. B. (2015). Liquid spreading on solid surfaces and penetration into porous matrices: Coated and uncoated papers. Advances in colloid and interface science, 220, 8-53.

Tensile test imaging of paper using X-ray microtomography

Tuomas Turpeinen, & Jarmo Kouko

VTT Technical Research Centre of Finland Ltd, Jyväskylä, Finland

Corresponding author: *Tuomas Turpeinen <tuomas.turpeinen@vtt.fi>*

Keywords: X-ray microtomography, tensile test, cellulose fibers

Summary

X-ray microtomography (XµCT) combined with a material testing unit (MTU) is used to obtain 3D images of fiber samples while tensile testing them. The thickness of the sample is analyzed as a function strain percentage. The results indicate thickening on fiber samples during the straining. The method has potential to provide essential new information of complex structures under forced deformation.

Introduction

XµCT is an imaging method to obtain a digital X-ray attenuation (I.e. density-based) 3D representation of virtually any material[1]. In XµCT, a collection of X-ray transmission images is converted to a digital 3D representation of the sample using an inverse radon transform[2]. The transmission images are obtained using a tomographic scanner: the sample is rotated while illuminated from one side with X-rays and imaged from other side using a combination of scintillator and a digital image sensor (see Figure P12a). XµCT devices commonly provide resulting 3D X-ray attenuation matrix with isotropic volume element (voxel) size (see Figure P12b). As the magnification is known, the conversion to metric distances is straightforward. The tomographic scanners can be equipped with a MTU which can be used for pulling or compressing a sample while obtaining 3D images of the process.
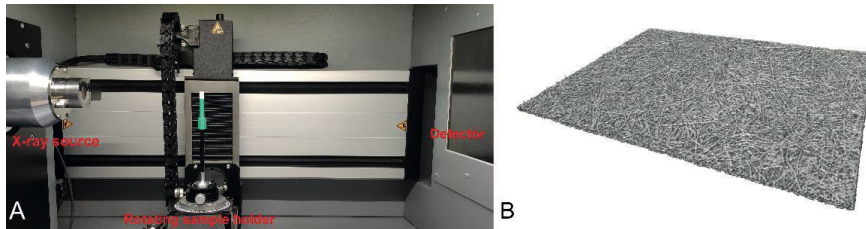
Figure P12a) Interior of a typical XµCT scanner. b) A 3D visualization of a typical X-ray attenuation field, where air is depicted transparent and higher densities are given a grey value.

The XµCT scanner used in this work is RX solutions desktom 130. The device has best spatial resolution of a 4 µm obtained with sample diameter of 7.5 mm. It is equipped with flat panel detector making it possible to obtain images in time range of minutes. The MTU used in this study is Bruker Skyscan MTS1 with maximum load of 44 N. The maximum travel of the device is 5.5 mm. As the imaging time of XµCT scanner is relatively slow the MTU is halted during the imaging.

Tensile elongation imaged by x-ray microtomography

The XµCT scanner with MTU was used to study commercial sack paper sheets with thickness 120 µm and basis weight 80 g/m^2. Small sheet of paper was cut and placed into the MTU device. The sample width was 8 mm and length of the active area was 10 mm (the actual sample size is larger as it is partially inside the sample holder clamps). The size of the MTS device limits the maximum resolution of the CT system, the images had 6 µm voxel size. The acceleration voltage used in the system was 40 kV. The imaging time per one step of the tensile test was 12 minutes. 1% (0.1 mm) steps were used stretching the sample. Figure P13 presents a XµCT visualization of few steps of the process.
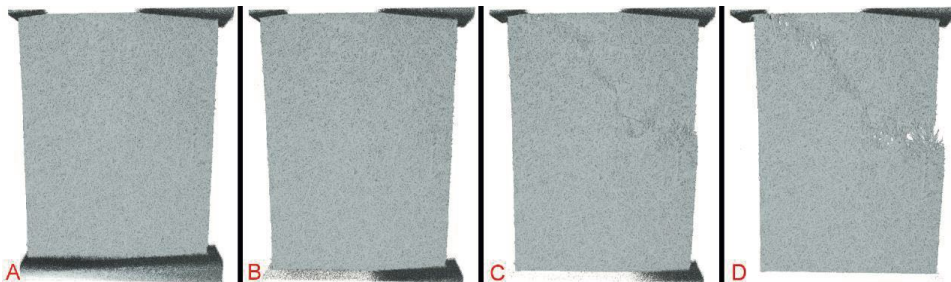
Figure P13 An example of a 3D visualization of the XµCT images while pulled in MTU, a) initial straining phase, b) maximal strain, c) breaking phase, and d) broken structure

The 3D images obtained from the process allows many kinds of analyses. Thickness of the samples was analyzed as a function of the sample elongation. To define the sample thickness, the top and bottom surface of the sample were determined using method described in [3]. The results are shown in Figure P14. Thickening of the sample

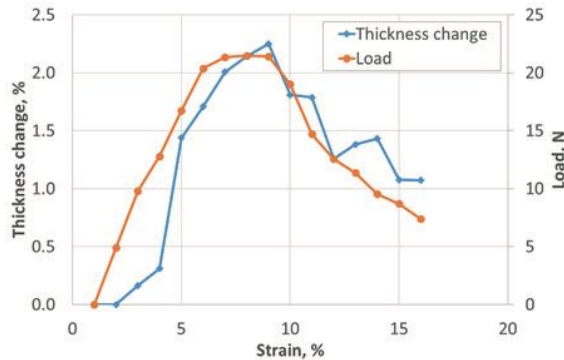was observed during the process,that has been reported also in literature for sack paper[4]

Figure P14. The strain vs sample thickness for a sample.

Conclusions

XµCT and MTU provide and interesting tool to analyze forced sample deformation in 3D. The 3rd dimension of the analysis provided new and potentially important information for understanding the dynamic behavior of such fiber structures. In this work, the thickness of the paper sample during the straining. The results indicate the sample to thicken during the process, indicating an anisotropic Poisson ratio of the fiber network.

Acknowledgements

References

1. Stock, S. R. (2019). Microcomputed tomography: methodology and applications. CRC press.

2. Kak, A. C., & Slaney, M. (2001). Principles of computerized tomographic imaging. Society for Industrial and Applied Mathematics.

3. Turpeinen, T., Myllys, M., Kekäläinen, P., & Timonen, J. (2015). Interface Detection Using a Quenched-Noise Version of the Edwards–Wilkinson Equation. IEEE Transactions on Image Processing, 24(12), 5696-5705.

4. Göttsching, L., Baumgarten H.L. (1973). Triaxial deformation of paper under tensile load. In The Fundamental Properties of Paper Related to its Uses, Trans. Vth Fund. Res. Symp. Cambridge, 1973, (F. Bolam, ed.), pp 227-249, FRC, Manchester, 2003.

The use of co-surfactant to prevent the precipitation of an anionic surfactant in foam forming

Janika Viitala, Timo Lappalainen, & Marjo Järvinen

VTT Technical Research Centre of Finland Ltd, Jyväskylä, Finland

Corresponding author: *Janika Viitala <janika.viitala@vtt.fi>*

Keywords: Foam forming, mixed micelles, sodium dodecyl sulphate, surfactant residues

Summary

The precipitation of an anionic surfactant due to hard water can cause problems in foam forming process. Addition of a nonionic or a zwitterionic surfactant as a co-surfactant with the anionic surfactant inhibits the precipitation of the anionic surfactant. 20-25 mol-% addition of the co-surfactant is recommended to prevent the precipitation of the anionic surfactant. Addition of Tween 20 with sodium dodecyl sulphate (SDS) was found to decrease the SDS residue in foam-formed paper sheets. The paper sheets produced with the surfactant mixture also exhibited higher tensile index compared to sheets made with only SDS or Tween 20.

Introduction

Small anionic surfactants, such as SDS, are suitable for foam forming applications due to the rapid foaming, good foam stability, fast biodegradability and relatively low dosage required.[1] However, anionic surfactants are sensitive to hard water, and precipitate out from aqueous solutions as salts of calcium and magnesium.[2] The hardness of the tap water varies greatly in different countries. The precipitation of an anionic surfactant has been recognised as a problem from the point of view of foam forming process, surfactant recovery and the end product quality. Anionic surfactant residues in foam-formed products increase with increasing water hardness due to the precipitated anionic surfactant, which remains in the fibre network. High surfactant residues can adversely affect the strength properties of the final product[3].

In general, the precipitation of dodecyl sulphate (DS) can cause problems in foam forming if the dosage of SDS is relatively high (above 0.5 g/l), and/or the water is hard. Precipitation of DS with Ca^{2+} can be inhibited by increasing the water temperature above the Krafft temperature of calcium dodecyl sulphate $Ca(DS)_2$ (above 50 °C).[3] Another solution to prevent the precipitation of an anionic surfactant with Ca^{2+} is to add small amount of a nonionic or a zwitterionic surfactant.

Results

The effect of three different co-surfactants on the formation of $Ca(DS)_2$ was studied by the turbidity measurement. The tested co-surfactants were non-ionic Tween 20 and Triton X-100, and zwitterionic Euroxide LO/A. The turbidity of 1.7 g/l SDS solution at the hardness of 4.1 °dH was measured with varying concentrations of the co-surfactant. In all cases, no precipitates were observed with 20 mol-% co-surfactant addition. When a non-ionic or a zwitterionic surfactant is added with anionic surfactant at a certain molar ratio, the surfactants co-operate to form mixed micelles, and Ca^{2+} ions are bound on the micelles. Due to the mixed micelle formation, the anionic surfactant stays in soluble form.

Foam-formed hand sheets were prepared from pre-refined chemical pine pulp with a consistency of 0.5% using either Tween 20, SDS, or 77/23 (mol/mol) SDS+Tween 20 mixture as a foaming aid. The target grammage of the sheets was 100 g/m^2. SDS residues were determined from the paper sheets by spectrophotometry after extraction with water. The method for SDS residue determination from solid foam-formed samples has been described earlier.[3] The tensile index of the sheets was determined from rotary drum dried sheets.

When hard water (7 °dH) was used, SDS residues were over double compared to the corresponding theoretical values (see Figure P2a). Theoretical values for SDS residues have been calculated from the water content of the sheet after formation and the SDS dosage.[3] When 23 mol-% Tween 20 was added, SDS residues decreased near the theoretical level or even below it.

Figure P2b shows that an increase in the surfactant dosage decreases the tensile index of foam-formed paper. The effect of surfactant dosage was the most significant in the case of Tween 20. SDS gave higher tensile index compared to Tween 20. The paper sheets produced with the SDS+Tween 20 mixture gave the highest tensile index, even though the SDS dosage used was high. The results suggest that surfactant can affect the strength properties of foam-formed product.
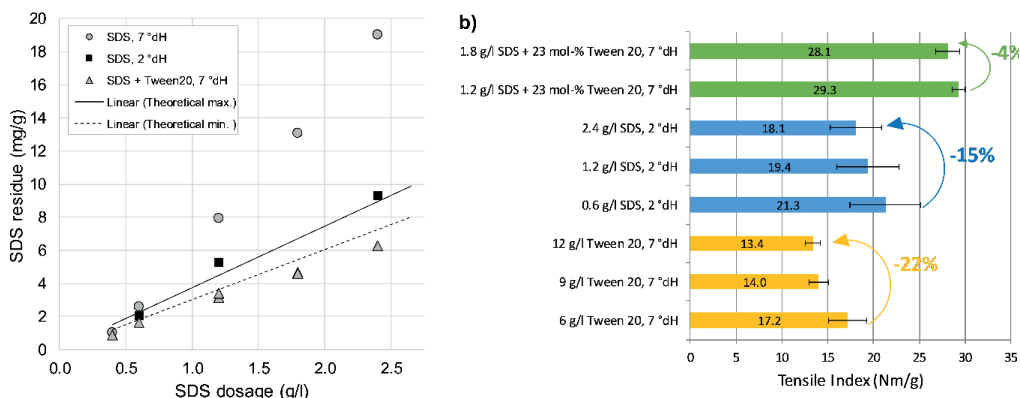
Figure P2a) The measured SDS residues in foam-formed hand sheets. Hardness of 1 °dH corresponds to 7 mg/l Ca. b) The tensile index of foam-formed hand sheets made using different surfactants. The bulk of the sheets was 3.79 ± 0.13 cm³/g.

Conclusions

SDS, like all anionic surfactants, tends to precipitate out from the aqueous solution as salts of calcium and magnesium. Due to the precipitation, anionic surfactant residues in foam-formed fibre products increase which can affect the quality of the foam-formed product. The precipitation of an anionic surfactant can be inhibited by adding 20-25 mol-% a non-ionic or a zwitterionic surfactant. When 77/23 (mol/mol) mixture of SDS and Tween 20 was used to make foam-formed hand sheets in hard water, SDS residues were significantly lower. In addition, the the SDS+Tween 20 mixture gave higher tensile index compared to the sheets produced using only SDS or Tween 20.

References

1. Lappalainen, T., Salminen, K., Kinnunen, K., Järvinen, M., Mira, I., & Andersson, M. (2014). Foam Forming Revisited. Part II. Effect of Surfactant on the Properties of Foam-Formed Paper Products. Nord. Pulp Pap. Res. J. 29 (4), 689–699.

2. Miyamoto, S. (1960). The Effect of Metallic Ions on Surface Chemical Phenomena. IV. Surface Tension Measurement on Aqueous Solutions of Metal Dodecyl Sulfates. Bull. Chem. Soc. Jpn. 33 (3), 375–379.

3. Viitala, J., Lappalainen, T., & Järvinen, M. (2020). Sodium Dodecyl Sulphate (SDS) Residue Analysis of Foam-Formed Cellulose-Based Products. Nord. Pulp Pap. Res. J. Advance online publication. https://doi.org/10.1515/npprj-2019-0058

Tension and tension relaxation of wet webs

Kristian Salminen[a], Jarmo Kouko[b], &, Elias Retulainen[b]

[a]*VTT Technical Research Centre of Finland, Tampere, Finland*
[b]*VTT Technical Research Centre of Finland, Jyväskylä, Finland*

Corresponding author: *Kristian Salminen <Kristian.salminen@vtt.fi>*

Keywords: Tension, relaxation, strain, strain rate, dryness

Summary

The increase of paper machine production speed is often limited by the mechanical properties of wet web, i.e. wet web tensile and relaxation characteristics. As a consequence of this, many paper machines are forced to run below their design speed. So far, despite the high technological importance of wet paper rheology under dynamic conditions, very few attempts have been made to systematically study the effects of different factors affecting wet web tension and tension relaxation behaviour during short time scales. In this laboratory-scale study, the effects of several variables, such as strain rate, dryness, fibre orientation, furnishes type, fibre shape and strength additives on tension and tension relaxation of paper network were examined.

Introduction

The increase of paper machine production speed is often limited by an increase of web breaks occurring in the press-to-dryer transfer and at the beginning of the dryer section caused by the speed increase (see for example[1,2,3]). In the open draw, the wet web is transferred from one surface to another without the support of any fabrics. During the open draw, the stability of the running web depends mainly on the web tension. After the open draw, the velocity of the web remains constant for a considerable time. During this time, the tension created in the open draw does not remain constant, but lowers rapidly, i.e. tension relaxation occurs. Lowered tension due to relaxation may lead to slackening of the wet paper. This causes wrinkling, bagging, fluttering and weaving of the web, which can lead to web breaks.

Materials and methods

ECF-bleached pine pulp was obtained from a Finnish pulp mill. The pulp was refined (a conical pilot-scale refiner) and dewatered at the mill. The pulp was packed as never-dried into airtight polyethylene bags, and kept at -18°C until used for testing. The Schopper-Riegler value of the pulp after dewatering and freezing was 20.

Wet and dry handsheets having grammage of 60 g/m^2 were formed without white water circulation adapting SCAN-CM 26:99. Oriented paper samples having grammage of 70 g/m^2 were produced with a pilot paper machine having production speed 900 m/min. The pilot paper machine had a gap former and a press section with three press nips. The third nip in the press section was a shoe press nip. The samples from the pilot paper machine were collected after wet pressing. The mechanical properties of samples were determined by IMPACT[6] and C-IMPAC[7] test rigs.

Main results and Conclusions

The tension relaxation behaviour of dry and wet paper is affected by similar factors; however, the effect can be inverse.

An exponential function seemed to describe well the effect of dryness on wet-web tensile strength, T.E.A., initial tension, and residual tension when the dryness of wet handsheets was varied through changes in the wet pressing pressure. However, a dependency on dryness was highly characteristic of each property.

Initial tension and residual tension of paper were shown to be greatly dependent on dryness over the dryness range of 40…95%. However, the relaxation percentage of wet paper was nearly constant over the 40…65% dryness range.

With increasing tension, the relaxation percentage of wet paper was reduced. This runs counter to general expectations and what is known to occur with dry paper. The straining of the loose structure of the wet paper activates and straightens fibre segments and increases the load-bearing ability of the network. In the pilot-machine paper, increased orientation of the fibres in the direction of strain was also found to reduce the relaxation percentage.

Initial tension increased with increasing strain rate, but residual tension decreased. Both changes were proportional to the logarithm of strain rate.

Wet web tensile strength can be significantly improved via increased strength of fibre–fibre contacts. For improved relaxation characteristics of the wet web, the number of load-bearing fibre segments in the network must be increased.

References

1. Kurki, M., Pakarinen, P., Juppi, K., & Martikainen, P. (2000). *Web handling,* Papermaking Science and Technology, Book 9, Drying, Fapet Oy, Jyväskylä, Finland

2. Mardon, J., Cutshall, K.A., Smook, G.A., Branion, R.M.R., & Michie, R.I. (1975). *Effect of wet web furnish properties on newsprint runnability,* Pulp and Paper Canada, 76, 5

3. Gûldenberg, B., Schwarz, M., & Mayer, R. (2004). *High-speed production of wood free paper grades – An on-going challenge,* PulPaper 2004, June, Helsinki, Finland.

4. Jantunen, J. (1985). *Visco-elastic properties of wet webs under dynamic conditions,* Transactions of the 8th Fundamental Research Symposium, September, Oxford, UK

5. Kekko, P., Kouko, J., Retulainen, E., & Timonen J. (2009). *Effects of strain rate on the stress relaxation of wet paper.* 6th International Symposium of Creep Effects on Paper Board and Container, July, Madison, USA

6. Kurki, M., Kouko, J., Kekko, P., & Saari, T. (2004). *Laboratory scale measurement procedure of paper machine wet web runnability: Part 1,* Paperi ja Puu, 86, 4

7. Kouko, J., Kekko, P. & Kurki, M. (2006). Effect of Strain Rate on Strength Properties of Paper. Proceedings of the progress in paper Physics Seminar, Miami University, Oct 2006, Oxford, USA

Lignocellulose enabled highly transparent nanopaper with tunable ultraviolet-blocking property and durability

Yazeng Zhang, Yudi Kuang, Yuan Wei, Yangyang Qian, Mengli Zhang, & Gang Chen

South China University of Technology, Guangzhou, China

Corresponding author: *Gang Chen <papercg@scut.edu.cn>*

Keywords: Lignocellulose, transparent film, nanopaper, UV-blocking, durability

Lignin-containing cellulose nanopaper (LCNP) has emerged as a new generation of full-biobased film material for its higher moisture stability than traditional cellulose nanopaper (CNP)[1,2] While there are also a few disadvantages appeared at the same time, like obviously decreased visible light transmission, dark color of the film, etc., which greatly hinder its application[3,4,5] To address those issues, in this study, we employed a treatment of TEMPO-mediated oxidation and sequential high-pressure homogenization treatment on lignocellulose material. The obtained lignin-containing cellulose nanofibers (LCNFs) were directly used to fabricate nanopaper by vacuum filtration. Due to a small size of LCNFs, the resultant LCNP possessed a dense inner structure and thus exhibited an ultrahigh visible light transmittance (~91%) and tunable optical haze (22 ~ 91%). At the same time, the remained large amount of lignin insures the excellent ultraviolet-blocking efficiency (~68%). Moreover, other properties like mechanical performance, water stability, and thermal stability were also improved significantly for the existence of lignin. This work would greatly contribute to extend the application of LCNP in electron devices, building material, automobile industry, etc.[6,7,8.]

Acknowledgements

Zhang, Y., Kuang, Y., Wei, Y., Qian, Y., Zhang, M., Chen, G.

Poster 11
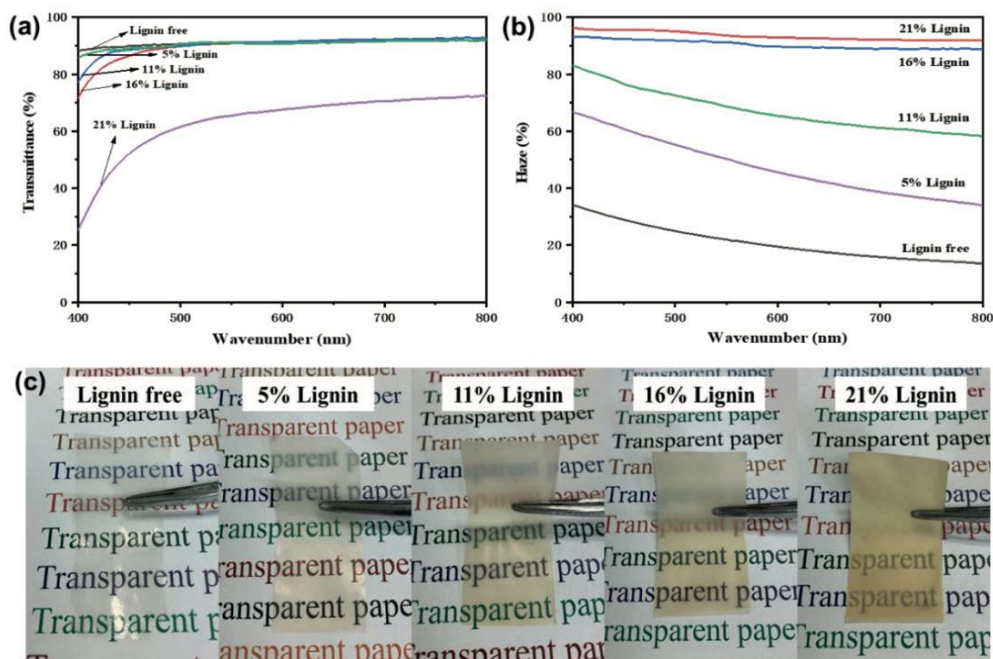
Figure P8. Optical transmittance and haze of LCNP. (a) Optical transmittance of LCNP in visible light stage. (b) Optical haze of LCNP in visible light stage. (c) Transmittance performance of LCNP

References

1. Klemm, D., Kramer, F., Moritz, S., Lindström, T., Ankerfors, M., Gray, D., & Dorris, A. (2011). Nanocelluloses: a new family of nature‑based materials. Angewandte Chemie International Edition, 50(24), 5438-5466.
2. Moon, R. J., Martini, A., Nairn, J., Simonsen, J., & Youngblood, J. (2011). Cellulose nanomaterials review: structure, properties and nanocomposites. Chemical Society Reviews, 40(7), 3941-3994.
3. Sadeghifar, H., Venditti, R., Jur, J., Gorga, R. E., & Pawlak, J. J. (2017). Cellulose-lignin biodegradable and flexible UV protection film. ACS Sustainable Chemistry & Engineering, 5(1), 625-631.
4. Wang, Q., Du, H., Zhang, F., Zhang, Y., Wu, M., Yu, G., ... & Peng, H. (2018). Flexible cellulose nanopaper with high wet tensile strength, high toughness and tunable ultraviolet blocking ability fabricated from tobacco stalk via a sustainable method. Journal of Materials Chemistry A, 6(27), 13021-13030.
5. Parit, M., Saha, P., Davis, V. A., & Jiang, Z. (2018). Transparent and homogenous cellulose nanocrystal/lignin UV-protection films. ACS omega, 3(9), 10679-10691.
6. Yang, W., Wang, X., Gogoi, P., Bian, H., & Dai, H. (2019). Highly transparent and thermally stable cellulose nanofibril films functionalized with colored metal ions for ultraviolet blocking activities. Carbohydrate polymers, 213, 10-16.
7. Liu, X., Zhang, T., Pang, K., Duan, Y., & Zhang, J. (2016). Graphene oxide/cellulose composite films with enhanced UV-shielding and mechanical properties prepared in NaOH/urea aqueous solution. RSC advances, 6(77), 73358-73364.
8. Jiang, Y., Song, Y., Miao, M., Cao, S., Feng, X., Fang, J., & Shi, L. (2015). Transparent nanocellulose hybrid films functionalized with ZnO nanostructures for UV-blocking. Journal of Materials Chemistry C, 3(26), 6717-6724.

Bio-based air-laid nonwovens

Anabela S. Santos [a], Sara Ceccherini[b], Paula C. O. R. Pinto[a],
António P. M. de Sousa[a], Paulo J. T. Ferreira[c], & Thaddeus C. Maloney[b,c]

[a]*RAIZ – Forest and Paper Research Institute, Quinta de São Francisco, Aveiro, Portugal*
[b]*Aalto University, Espoo, Finland*
[c]*University of Coimbra, CIEPQPF, Department of Chemical Engineering, Coimbra, Portugal*

Corresponding author: *Anabela Santos*
<anabela.santos@thenavigatorcompany.com>

Keywords: Air-laid nonwovens, bio-based binders, eucalyptus fibers

Summary

Nonwovens are one of the fastest growing and most technically sophisticated categories of fiber products. Unfortunately, many nonwoven products rely heavily on petrochemical-based materials as binders and synthetic fibers. In this project we target air-laid structures that utilize natural fibers and bio-based binders. Thus we attempt to a high degree of functionality *e.g.* bulk, absorption and strength for products that are highly sustainable.

Introduction

Wet-laid or paper-based technology refers to systems designed to use mainly natural pulp fibers in an aqueous production process. Webs are formed stochastically and then water is removed to allow fibers to bond together via inter-fiber hydrogen bonds. Nonwoven products are often produced with an air-laid process using synthetic binders and binder fibers to achieve the inter-fiber bonding and mechanical strength[1,2,3]. However, the environmental problems caused by the disposable nonwovens mainly made of petrochemical-based materials leads to an intense interest to develop nonwoven products which use cellulosic fibers and sustainable, compostable "green" binders, but which maintain at least the functionality of the current generation of nonwoven products[4].

Santos, A. S, Ceccherini, S., Pinto, P.C.O.R., de Sousa, A.P.M., Ferreira, P.J.T., & Maloney, T. C.

Poster 12
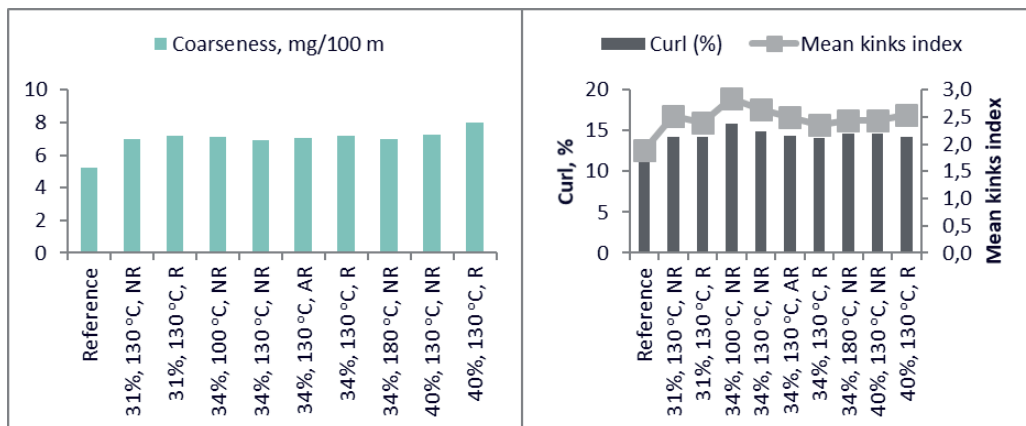
Figure P18. Results of coarseness (mg/100m), curl (%) and mean kinks index for the 9 samples of modified fibers obtained by drying in the defibration dryer, represented by the initial consistency of the pulp (%), temperature of drying (°C) and presence or absence of rotation (R or NR, respectively).

In this research, we target sustainable nonwoven products by using wood pulp fibers and binders from renewable raw materials. In the work, separated eucalyptus fibers are produced in a unique defibration dryer which allows control over some of the fiber properties and avoids the typical milling of fluff sheets in the nonwoven process. A new type of lab sheet former is being developed for the project.

At this early stage, we have concentrated on producing separated, dried pulp fibers with suitable properties for air-laid products. High consistency pulp was dried in a home built defibration dryer, obtaining 9 samples of modified fibers, by changing initial consistency, temperature and rotation. It was observed a generalized enhancement of coarseness, curl percentage and kinks index, with an increase up to 54%, 33% and 50% respectively, compared to the reference dried at open air, room temperature (no defibration dryer used) (Figure P18). Scanning Electron Microscopy (SEM) analysis of each sample of modified fibers was performed, showing accordance with the results from biometric analysis.

The first trials to obtain air-laid sheets obtained allowed to project a lab-scale air-laid sheet former. The preliminary results showed a high bulk (8-28 cm^3/g) and absorbency capacity (9-20 g water/g of sample) provided by the modified dry fibers. Bio-based binders are applied by spraying on the sheets, followed by drying to achieve higher strength.

Future work encompasses the development of bio-based air-laid structures, using bio-based binders, study of their final properties and comparison of their performance with similar commercial products.

In summary, natural fibers as hardwood pulp (eucalyptus) and bio-based binders assume a great potential for replacing petrochemical-based materials in the

manufacture of more sustainable nonwovens. New techniques *e.g.* dryer and lab air-laid sheet former, reveal as essential for fulfill the demand of "greener" products.

Acknowledgements

References

1. Pourmohammadi, A. (2013). Nonwoven materials and joining techniques. In Joining Textiles: Principles and Applications (565–581). Elsevier Ltd.

2. Russell, S. J., & Smith, P. A. (2016). Technical fabric structures – 3. Nonwoven fabrics. In Handbook of Technical Textiles (2nd ed., Vol. 1,163–188). Elsevier.

3. Russel, S. (2007). Handbook of nonwovens. Woodhead Publishing.

4. EDANA. (2018). Nonwovens industry pledges uptake in use of recycled PET. https://www.edana.org/newsroom/news-announcements/news-article/2018/12/11/nonwovens-industry-pledges-uptake-in-use-of-recyled-pet

Scientific Programme

Scientific Programme

Day 1: Tuesday 1.9.2020

8:45 – 9:00	Opening the PPPS2020 *Jarmo Kouko*
9:00 – 9:45	**Session 1 Plenary talk 1** ***Chair: Jarmo Kouko*** On the founding of the corrugated board industry and the introduction of box compression testing: 1871-1914 *Douglas Coffin*
9:45 – 10:00	Break
10:00 – 12:00	**Session 2A Compression behavior of fiber networks** ***Chair: Samuel Schabel***
10:00 – 10.30	A constitutive framework for paperboard accounting for anisotropy and compressible plasticity at finite strains *Jaan-Willem Simon*
10:30 – 11:00	Experimental and numerical investigation of single sheet out-of-plane compression tests of different paperboards *Marcus Pfeiffer*
11:00 – 11.30	Continuum micromechanics of paper: recent results for elasticity and ultimate strength of transversely isotropic paper sheets *Pedro de Sousa Godinho*
11:30 – 12:00	General mean-field theory to describe compression of thick porous fibre networks *Jukka Ketoja*
10:00 – 12:00	**Session 2B Novel measurement methods** ***Chair: Katariina Torvinen***
10:00 – 10:30	The use of ATR-IR spectroscopy to determine the anisotropy parameters of the structure of materials based on plant fibers *Yakov Kazakov*
10:30 – 11:00	Positron annihilation: A tool for paper research *Laura Resch*

11:00 – 11:30	Adsorption of molecules on cellulose films studied by TPD *Elias Henögl*
11:30 – 12:00	Unexpected barrier properties - The interaction of the paper matrix with volatile organic compounds *Lisa Hoffelner*
12:00 – 13:00	Lunch
13:00 – 15:00	**Session 3A Mechanical performance of paperboard** ***Chair: Anna-Leena Erkkilä***
13:00 – 13.30	On modelling the moisture dependent elastic-plastic properties of paperboard *Sören Östlund*
13:30 – 14:00	Experimental and analytical investigation of paperboard rate dependent behavior options *Abolhasan Giashi*
14:00 – 14.30	Prediction of ECT from SCT values including the effect of fibre furnish *Heinz-Joachim Schaffrath*
14:30 – 15:00	Influence of creasing tension on reverse-side cracking of paperboard *Joel Panek*
13:00 – 15:00	**Session 3B Fiber water interactions** ***Chair: Antti Koponen***
13:00 – 13:30	Lightweight materials by tailoring foam-fibre interactions *Annika Ketola*
13:30 – 14:00	Robust and precise identification of the hygro-expansion of single pulp fibers: A full-field fiber topography correlation approach *Niels Vonk*
14:00 – 14:30	Wall investigations of pulp of paper flow in pipes New model of pulp of paper flow behaviour *Salaheddine Skali Lami*
14:30 – 15:00	Dynamics of capillary rise in sinusoidal corrugated channels *Amin Shobeiri*
15:00 – 15:30	Break
15:30 – 17:30	**Session 4 Poster pitchings at the posters with refreshments** ***Chair: Jani Lehto***
17:30 –	Organized evening program Guided walk 1: Alvar Aalto Museum Guided walk 2: Canoening on Jyväsjärvi-lake

Day 2: Wednesday 2.9.2020

8:45 – 9:30	**Session 5 Plenary talk 2** ***Chair: Tero Tuovinen*** Towards circular forest-based bioeconomy: case Bioproduct mill *Anna Suurnäkki*
9:30 – 10:00	Break
10:00 – 12:00	**Session 6A Nanofibrillated cellulose** ***Chair: Heinz-Joachim Schaffrath***
10:00 – 10:30	Do wet kraft fibres have a gel-like surface? *Annika Ketola*
10:30 – 11:00	The effect of consistency on the shear rheology of aqueous suspensions of cellulose micro- and nanofibrils *Antti Koponen*
11:00 – 11:30	Laminated high strength cellulose structures *Vesa Kunnari*
11:30 – 12:00	Drying of cellulose nanofibrils without losing its functionality and fibrillary structure *Tuomo Hjelt*
10:00 – 12:00	**Session 6B Fibres and fibre bonds** ***Chair: Atsushi Tanaka***
10:00 – 10:30	Decoupling the effect of fiber orientation and drying conditions on the anisotropy of the mechanical properties of paper *Mossab Alzweighi*
10:30 – 11:00	Twisting in the hierarchical fibre structure and its effects on bound water *Antti Paajanen*
11:00 – 11:30	Quantification of the impact of each, fibre flexibilization and secondary fines on tensile strength gain after refining *Daniel Mandlez*
11:30 – 12:00	Ptychographic X-ray computed tomography study of the paper pulp fiber to fiber bond *Eduardo Machado-Charry*
12:00 – 13:00	Lunch

13:00 – 15:00	**Session 7A Transport phenomena** ***Chair: Annika Ketola***
13:00 – 13:30	Contact angle measurement on absorbing paper – influence of absorption rate and drop size *Ulrich Hirn*
13:30 – 14:00	Modelling ink penetration, hygro-expansion and curl in digital inkjet printing *Nik Dave*
14:00 – 14:30	Quantification of the interdependence of local porosity and local tortuosity that determine the air flow in paper *Karin Zojer*
14:30 – 15:00	Computer simulation of liquid wetting in low density fibrous Networks *Steven Keller*
13:00 – 15:00	**Session 7B Numerical modelling of deformations and fracture** ***Chair: Jukka Ketoja***
13:00 – 13:30	Moisture induced instability in paper analysed with incremental deformation theory *Erik Borgqvist*
13:30 – 14:00	Numerical investigation of paper using the concept of representative volume elements characterized by single fiber behavior and fiber-fiber interaction *Greta Kloppenburg*
14:00 – 14:30	Simulated fracture and tensile strength of paper *Anna-Leena Erkkilä*
14:30 – 15:00	Predicting strength characteristics of paper in real time using process parameters *Kamala Rajan*
15:00 – 15:30	Break
15:30 – 16:15	**Session 8 Plenary talk 3** ***Chair: Elias Retulainen*** The world of nanocellulosic material applications *Tom Lindström*
16:15 – 17:15	70th Tappi Paper Physics Committee meeting
18:00 – 19:00	The Natural History Museum of Central Finland
19:00 – 23:00	Dinner at Restaurant Vesilinna (Ihantolantie 1)
	Best presentation and poster awards

Day 3: Thursday 3.9.2020

8:45 – 9:45	**Session 9 Influence of moisture on paper performance** ***Chair: Vesa Kunnari***
8:45 – 9:15	Influence of wood extractives on the performance of packaging papers *Jussi Lahti*
9:15 – 9:45	Influence of moisture content and additives on the fracture toughness of recycled paper *Pablo González-Miguel*
9:45 – 11:15	**Session 10 New cellulose based applications** ***Chair: Kristian Salminen***
9:45 – 10:15	Fibre Printer: A Machine to apply 3D printing principles on paper production *Frederic Kreplin*
10:15 – 10:45	Deteriorated dispersibility of hydroentangled wetlaid wet wipes over storage time *Thomas Harter*
10:45– 11:15	Sheet structural and mechanical properties and their relationship to tissue softness *Joel Pawlak*
11:15 – 11:20	**Closing words by** **Jarmo Kouko, Jani Lehto and Tero Tuovinen**
11:20 – 12:00	Lunch
12:15 – 15:30	Online company presentations: Metsä Fibre (Pro Nemus), University of Jyväskylä Nanoscience Center, University of Jyväskylä Department of Physics, VTT Technical Research Centre of Finland Ltd

Author index

Author index

Title	**Progress in Paper Physics Seminar PPPS2020** Book of abstracts
Author(s)	Jarmo Kouko, Jani Lehto & Tero Tuovinen (eds.)
Abstract	The scope of the Progress in Paper Physics Seminar is to discuss the broad scope of physical properties of paper, paperboard and new cellulose containing materials. The program contain presentations reporting on the latest experimental, theoretical and computational developments. The three invited plenary speakers aim at bringing industry and academia together for in-depth discussions on selected topics in paper physics the potential impact on industry. The selected 37 oral presentations and 12 poster presentations provide opportunity to improve scientific knowledge and explore the latest outcomes and trends in the field.
ISBN, ISSN, URN	
Date	August 2020
Language	English
Pages	322 p. + app. 0 p.
Name of the project	
Commissioned by	
Keywords	Paper physics, paper chemistry, pulp and paper, nanocellulose, fibers and bonds, modelling
Publisher	

Progress in Paper Physics Seminar
Abstract book of the PPPS2020 seminar on
September 1-3, 2020 in Jyväskylä, Finland

Day 1 - Tuesday, September 1st
 8:45 - 9:00 Seminar opening
 9:00 - 10:00 Plenary talk
10:00 - 15:00 Presentations
15:30 - 17:30 Poster competion
17:30 - 20:00 Organized evening program

Day 2 - Wednesday, September 2nd
 8:45 - 9:30 Plenary talk
10:00 - 15:00 Presentations
15:30 - 16.15 Plenary talk
16:15 - 17:15 70th TAPPI Paper Physics Committee Meeting
18:00 - 19:00 The Natural History Museum of Central Finland
19:00 - 23:00 Seminar dinner at Vesilinna Restaurant

Day 3 - Thursday, September 3rd
 8:45 - 11:15 Presentations
11:15 - 12:00 Seminar closing
12:15 - 15:30 Online excursion and presentations

VTT beyond the obvious